Imperial College London

Doctoral Thesis

Understanding the Effects of Heterogeneities on Battery Pack Lifetime

Author:
Max Peter Naylor Marlow

Supervisors:
Dr. Billy Wu
Prof. Mirko Kovac

A thesis submitted in fulfillment of the requirements for the degree of Doctor of Philosophy

in the

Electrochemical Science and Engneering Group
Dyson School of Design Engineering

August 27, 2021

Authorship and Copyright

I, Max Peter NAYLOR MARLOW, declare that this thesis, *"Understanding the Effects of Heterogeneities on Battery Pack Lifetime"* and the work presented in it are my own. Where it has been included, the work of others has been acknowledged and is appropriately referenced.

Max Peter NAYLOR MARLOW (2021)

ORCID: 0000-0002-0970-4368

The copyright of this thesis rests with the author. Unless otherwise indicated, its contents are licensed under a Creative Commons Attribution-Non Commercial 4.0 International Licence (CC BY-NC). Under this licence, you may copy and redistribute the material in any medium or format. You may also create and distribute modified versions of the work. This is on the condition that: you credit the author and do not use it, or any derivative works, for a commercial purpose. When reusing or sharing this work, ensure you make the licence terms clear to others by naming the licence and linking to the licence text. Where a work has been adapted, you should indicate that the work has been changed and describe those changes.

Please seek permission from the copyright holder for uses of this work that are not included in this licence or permitted under UK Copyright Law. Some figures contained within this work are sourced from third parties whose licensing rights differ. In these instances, the specific rights are expressly given in Appendix B and take precedence.



For Peter

Imperial College London

Abstract

Electrochemical Science and Engineering Group
Dyson School of Design Engineering

Doctor of Philosophy

Understanding the Effects of Heterogeneities on Battery Pack Lifetime

by Max Peter NAYLOR MARLOW

Practical lithium-ion battery (LIB) systems require parallelisation of tens to hundreds of cells to achieve high capacities, however interconnection resistances, pack architecture and thermal gradients influence start of life (SoL) performance and subsequent degradation. The literature review found that parallel string degradation is a major underexplored area, motivating this work to develop understanding of the effects of heterogeneities on parallel-string degradation.

The tools to perform detailed investigations of the effects of heterogeneities and architecture were developed, including Peltier-based thermally controlled test benches, a quantitative diagnostic model, and an equivalent circuit network model. At SoL, thermal heterogeneities led to state of charge (SoC) deficits and reduction in accessible capacity. Interconnection overpotentials, cell open circuit voltages and cell impedance contribute to the pack current distribution. While coupled and non-linear, cell impedance is the dominant cause of heterogeneity. This study gives a detailed understanding of the coupled causes of current heterogeneities in parallel-strings.

An experimental study of parallel-string lifetime (temperature range 20-45 °C) shows thermal heterogeneities caused divergent capacity fade between parallel-connected cells. While growth of the solid-electrolyte interphase is generally quoted as the dominant degradation mechanism, for the nickel manganese cobalt oxide-graphite cells studied, impedance growth was negatively correlated with temperature, suggesting other dominant mechanisms. Consequently, increasingly heterogeneous current and SoC distributions occur during aging. Quantitative diagnostics indicate the dominant degradation mode transitions from loss of cathode active material at low temperature to loss of lithium inventory at increased temperatures. Therefore, consideration of cathode degradation is critical to understanding degradation within battery packs at intermediate temperature. A mechanistic model describing the observed degradation is proposed whilst the comprehensive aging dataset is made available.

This work thus highlights the importance of cathode polarisation resistance, which was previously not well captured, while developing understanding of lifetime behaviour in LIB packs and providing underpinning insights for developing longer lifetime packs.

Acknowledgements

Firstly, I would like to thank Dr Billy Wu for giving me with the opportunity to embark on the long and winding PhD road. It has been a pleasure working and learning under your supervision over the past 6(!) years. Thank you in particular for your unwavering confidence and support over the entire journey. It has been incredible to have been a part of the growth of the group from a couple of borrowed benches and no equipment in the RSM when I started to a fully-fledged research group with several full laboratories as I finish. I would also like to thank the Dyson School of Design Engineering and the EPSRC for providing the funding for my studentship, without this PhD would not have been possible. I am extremely grateful for the opportunity granted to me.

To the experimentalists - Alex, Yan, Ryan, Jingyi, Oisin, Harini and Teddy (and too many others to name here), you've made spending an inordinate amount of time in labs over the past 6 years a breeze. And the beers afterwards helped. Not to mention how much you've helped with the actual project! Thank you for your support, friendship and good company over the years, it's been an absolute blast. Whilst the Electrochemical Science and Engineering group has grown hugely while I have been a part of it, none of the character and fun has gone, and long may that continue.

To all everyone outside of Imperial – Theo, Dylan, Jake, Charlie, Zak and the rest. Whatever we're doing, it's a lot of fun, and London wouldn't be the same without you. Thank you all for your unwavering support and for being such an amazing bunch.

Anisha – hard to put into words how much I've relied on you over the past 4 years, and how much you've helped me. To many more (hopefully less stressful) years.

And finally, to my family – thank you for being a constant in my life. Nothing comes close to a weekend in Dungeness to forget about the stresses and worries of life. Fiona and Peter – for all the opportunities in life you've given me I cannot thank you enough. Dad – thank you for failing to talk me out of studying engineering. I miss you.

Dissemination

Journal Papers

Xinhua Liu[1], **Max Peter Naylor Marlow**[1], Samuel J. Cooper, Bowen Song, Xiaolong Chen, Nigel P. Brandon and Billy Wu, *Flexible all-fiber electrospun supercapacitor*, Journal of Power Sources, Volume 384, 2018, Pages 264-269, https://doi.org/10.1016/j.jpowsour.2018.02.081.

Xinhua Liu, Weilong Ai, **Max Peter Naylor Marlow**, Yatish Patel, Billy Wu, The effect of cell-to-cell variations and thermal gradients on the performance and degradation of lithium-ion battery packs, Applied Energy, Volume 248, 2019, Pages 489-499, https://doi.org/10.1016/j.apenergy.2019.04.108.

Mengzheng Ouyang, Antonio Bertei, Samuel J. Cooper, Yufei Wu, Paul Boldrin, Xinhua Liu, Masashi Kishimoto, Huizhi Wang, **Max Peter Naylor Marlow**, Jingyi Chen, Xiaolong Chen, Yuhua Xia, Billy Wu and Nigel P. Brandon, *Model-guided design of a high performance and durability Ni nanofiber/ ceria matrix solid oxide fuel cell electrode*, Journal of Energy Chemistry, Volume 56, 2021, Pages 98-112, https://doi.org/10.1016/j.jechem.2020.07.026.

Xinhua Liu, Mengzheng Ouyang, Marcin W. Orzech, Yubiao Niu, Weiqiang Tang, Jingyi Chen, **Max Peter Naylor Marlow**, Debashis Puhan, Yan Zhao, Rui Tan, Brankin Colin, Nicholas Haworth, Shuangliang Zhao, Huizhi Wang, Peter Childs, Serena Margadonna, Marnix Wagemaker, Feng Pan, Nigel Brandon, Chandramohan George and Billy Wu, *In-situ fabrication of carbon-metal fabrics as freestanding electrodes for high-performance flexible energy storage devices*, Energy Storage Materials, Volume 30, 2020, Pages 329-336,https://doi.org/10.1016/j.ensm.2020.04.001.

Jingyi Chen, **Max Peter Naylor Marlow** and Billy Wu, *A quantitative incremental capacity-differential voltage method for analysing degradation mechanisms inlithium-ion batteries*, 2021, Submitted for Publication

Max Peter Naylor Marlow, Jingyi Chen, and Billy Wu, *The effects of thermal heterogeneities on aging within parallel-connected Lithium Ion batteries*, 2021, In Preparation

Max Peter Naylor Marlow, and Billy Wu, *A comprehensive dataset for parallel-connected Lithium Ion batteries aged under thermal gradients*, 2021, In Preparation

[1]Equal contribution

Contents

Abstract vii

Acknowledgements ix

Dissemination xi

List of Figures xx

List of Tables xxi

Nomenclature xxiii

1 Introduction 1

1.1 Background . . . 1
1.2 Research Questions . . . 1
1.3 Thesis Structure . . . 2

2 Background 5

2.1 Introduction . . . 5
2.2 Lithium Ion Batteries: Basic Principles and Design . . . 5
2.2.1 Operating Principles . . . 5
2.2.2 Cell Design and Form Factors . . . 7
2.3 Electrochemical Characterisation Techniques . . . 9
2.3.1 General Techniques: Capacity, Pseudo-OCV and OCV Measurements . . . 9
2.3.2 Electrochemical Impedance Spectroscopy . . . 10
2.3.3 Hybrid Pulse Power Characterisation . . . 13
2.4 Cell Degradation: Modes and Mechanisms . . . 14
2.4.1 Overview of Lithium Ion Battery Degradation . . . 14
2.4.2 Degradation: The Consequences . . . 15
2.4.3 Degradation Mechanisms in Lithium Ion Batteries . . . 16
2.4.4 Heterogeneities in Degradation . . . 22
2.5 Diagnostics: Identifying Degradation Processes . . . 23

2.5.1 Incremental Capacity Analysis . . . 23
2.5.2 Differential Voltage Analysis . . . 24
2.5.3 Open Circuit Voltage Analysis . . . 26
2.5.4 Electrochemical Impedance Spectroscopy . . . 27
2.5.5 Other *In-situ* Diagnostic Techniques . . . 28
2.5.6 *Ex-situ* and Post-Mortem Diagnosis . . . 29
2.5.7 Diagnostics Overview . . . 29
2.6 Modelling Lithium Ion Batteries . . . 30
2.6.1 Cell Modelling . . . 30
2.6.2 Degradation Modelling . . . 31
2.7 Conclusion . . . 32

3 Literature Review **35**
3.1 Introduction . . . 35
3.2 Pack Design and Thermal Management . . . 35
3.2.1 Pack Design Overview: Topologies and Battery Management . . . 35
3.2.2 Thermal Management Strategies . . . 36
3.2.3 The Effects of Thermal Management on Performance and Lifetime . . . 39
3.2.4 Interim Summary . . . 41
3.3 Heterogeneities within Lithium Ion Battery Packs . . . 41
3.3.1 Overview of Pack Level Heterogeneities . . . 41
3.3.2 The Effects of Pack Topology . . . 42
3.3.3 The Effects of Interconnection Resistances . . . 47
3.3.4 The Effects of Thermal Conditions . . . 49
3.3.5 The Impact of Cell-Level Parameter Variation . . . 51
3.3.6 The Effects of the Duty Cycle . . . 55
3.3.7 The Effects Heterogeneities on Pack Degradation . . . 56
3.4 Conclusions and Outlook . . . 63
3.4.1 Literature Gaps and Proposed Research . . . 64

4 Experimental Methods and Model Development **67**
4.1 Introduction . . . 67
4.2 Cell Selection . . . 68
4.3 Development of Experimental Equipment . . . 68
4.3.1 Single Cell Testing . . . 68
4.3.2 Design and Development of Pack Test Benches . . . 69
4.3.3 Peltier Element Thermal Control . . . 70
4.3.4 Detail Design of 1S6P Pack Test Bench . . . 71

4.3.5 Detail Design of 1S2P Pack Test Bench . . . 72
4.3.6 Calibration of Pack Test Benches . . . 74
4.4 Diagnostic Model Development . . . 77
4.4.1 Cell Disassembly, Coin Cell Fabrication and p-OCV Measurement . . . 77
4.4.2 Parameterising the OCV Model . . . 78
4.4.3 Simulating Cell Degradation Modes and Effects . . . 80
4.4.4 Quantitative Degradation Mode Fitting . . . 82
4.4.5 Validation of Quantitative Diagnostic Model . . . 84
4.4.6 Diagnostic Model Overview . . . 84
4.5 Equivalent Circuit Modelling . . . 87
4.5.1 Equivalent Circuit Model: Selection and Background . . . 87
4.5.2 Equivalent Circuit Model: Experimental . . . 87
4.5.3 Equivalent Circuit Model: Parameterisation . . . 88
4.5.4 Thermal Model: Selection, Parameterisation and Implementation . . . 90
4.5.5 Model Validation . . . 93
4.6 Conclusion . . . 100

5 The Effects of Heterogeneities on Pack Performance 103
5.1 Introduction . . . 103
5.2 Key Literature . . . 104
5.3 Experimental Methods and Cell Selection . . . 105
5.3.1 Electrical Topology . . . 105
5.3.2 Cell Selection . . . 106
5.3.3 Experimental Methods . . . 109
5.4 The Effects of Thermal Gradients: Experimental Study . . . 111
5.4.1 U-Topology: Homogeneous Temperature Case . . . 111
5.4.2 U-Topology: Heterogeneous Temperature Case . . . 114
5.4.3 Z-Topology: Homogeneous and Heterogeneous Temperature Cases . . . 120
5.5 Interim Discussion . . . 123
5.6 Model Outline and Validation . . . 124
5.7 The Effects of Heterogeneities: Modelling Study . . . 125
5.7.1 The Effects of Thermal Conditions . . . 125
5.7.2 The Effects of Variable Interconnection Resistance . . . 129
5.7.3 The Effects of Variable Branch Resistances . . . 131
5.8 Conclusion . . . 135

6 The Effects of Thermal Heterogeneities on Pack Lifetime 139
6.1 Introduction . . . 139

6.2 Key Literature . . . 140
6.3 Cell Selection and Grouping . . . 142
6.4 Experimental Methods and Data Analysis . . . 145
6.5 Single Cell Reference Lifetime Performance . . . 149
6.6 Capacity Loss in Parallel Cell Strings . . . 154
6.7 Impedance Growth in Parallel Cell Strings . . . 157
6.8 Influence of Thermal Gradients on Heterogeneities . . . 164
6.9 Parallel String Cell Level Diagnostics . . . 174
6.10 Discussion and Proposed Degradation Mechanisms . . . 181
6.11 Conclusion . . . 186

7 Conclusions and Future Work **191**
7.1 Future Work . . . 194

Appendices **215**

A Identification of Missing Data **217**

B Permission to Reproduce Third-Party Works **219**

List of Figures

2.1 Lithium Ion Battery Schematic 6
2.2 Generic HPPC pulse showing measured quantities 14
2.3 Degradation mechanisms in Lithium Ion cells [25] 15
2.4 Cause and effect of degradation mechanisms and associated degradation modes [25] . . 16
2.5 Arrhenius plot for the ageing behaviour of 18650 cells cycled at 1 C in a temperature range of -20 °C to 70 °C [29] 17
2.6 Imaging of particle cracking and pulverisation alongside modelled current densities [45], [46] 19
2.7 ICA signatures from the initial state and at the end of 30 % degradation for each of the four possible variations in loss of active material, loss of lithium inventory, and ohmic resistance increase [74] 25
2.8 Estimation of known amounts of LLI, LAM_{NE} and LAM_{PE} [25] 27

3.1 Examples of cell and pack thermal management strategies [125] 37
3.2 Schematics of various EV battery cooling strategies [127] 38
3.3 Parallel string topologies [154] 43
3.4 SoC variation of individual parallel connected LIBs [155] 44
3.5 Relationship between the number of cells and current heterogeneity [156] 45
3.6 Discharge capacity in parallel strings at difference rates [158] 45
3.7 Studied topologies with varying degrees of string interconnection [161] 46
3.8 Current split and temperature rise in parallel connected LIB strings [141] 47
3.9 Resistance and current variation of a 1S5P pack during a 5 C discharge [139] 48
3.10 Influence of resistance and capacity variation on current distribution [179] 55
3.11 Temperature rise in 12P7S pack under static and dynamic loading [141] 56
3.12 Simulated capacity fade result for a 1S6P pack under a range of thermal gradients [9] 58
3.13 Simulated capacity fade result for a 10S1P pack under a range of thermal conditions [186] 59
3.14 Simulated capacity fade result for a 6S5P pack under a range of thermal gradients [142] 60
3.15 Impedance growth in NMC cells [188] 61
3.16 Time constant and decoupled resistance growth in NMC/NCA cells cycled at intermediate temperatures [93] 62

4.1 Images of single cell test fixtures used 69

4.2 Schematic representation of Peltier surface cooling assembly 70
4.3 Schematic representation of 1S6P surface cooled test bench 71
4.4 Circuit diagram and image of 1S6P test bench 73
4.5 Schematic representation of 1S2P surface cooled test bench 74
4.6 Annotated images of 1S2P pack testing rig 75
4.7 Calibration temperature results for surface cooling fixture 76
4.8 Half cell OCV curves and alignment 78
4.9 Explanatory schematic showing half cell alignment and full cell OCV 79
4.10 Diagnostic modelled OCV response and RSME 81
4.11 Simulated OCV responses under a range of degradation modes 83
4.12 Validation of diagnostic model using synthetic single mode degradation OCV curves . 85
4.13 Validation of diagnostic model using synthetic mixed mode degradation OCV curves . 86
4.14 Parameterisation experimental example and RC circuit model diagram 88
4.15 ECN Simulink implementation 90
4.16 $\frac{\mathrm{d}E}{\mathrm{d}T}$ values 91
4.17 Thermal model schematic implementation 93
4.18 ECN model fit and residuals at 30 °C 94
4.19 ECN validation under a 1 C constant current load at 20 °C 95
4.20 Simulated and experimentally measured cell current for 1S6P pack 97
4.21 Simulated and experimentally measured cell SoC for 1S6P pack 98
4.22 Summary of ECN model validation for a 1S6P pack 99

5.1 Topologies selected for investigation 106
5.2 Cell capacity variation 107
5.3 Cell DC resistance variation 108
5.4 Definition of thermal gradient positive and negative cases 110
5.5 Experimentally measured current and SoC distributions for a U-topology 1S6P pack under homogeneous temperature conditions 112
5.6 Schematic and annotated representation of underlying causes of heterogeneous behaviour in 1S6P parallel cell string at 20 °C homogeneous temperature. 115
5.7 Experimentally measured current and SoC distributions for a U-topology 1S6P pack under heterogeneous temperature conditions 117
5.8 Schematic representation of current distribution during discharge for 1S6P pack under a negative thermal gradient 118
5.9 Experimentally measured current and SoC distributions for a Z-topology 1S6P pack under heterogeneous temperature conditions 122
5.10 Validation of 1S6P model 124
5.11 Contour plots of simulated 1S6P U-topology pack accessible capacity under a range of thermal gradients and mean temperatures 126

5.12 Contour plots of simulated 1S6P U-topology cell accessible capacity under a range of thermal gradients and mean temperatures 128
5.13 Example simulated current and SoC distributions 129
5.14 Contour plots of simulated 1S6P Z-topology pack capacity under a range of thermal gradients and mean temperatures 130
5.15 Circuit diagram for variable R_{IC} simulations 131
5.16 Pack capacity for U-topology with variable $R_{IC,n}$, where $n = \{1, 2, \ldots, 6\}$. In each case $R_{IC,n}$ is varied from 0.1 mΩ to 20 mΩ. All simulations under a 1 C discharge. 131
5.17 Circuit diagram for variable R_S simulations 132
5.18 Pack capacity for U- and Z-topology with variable $R_{S,n}$, where $n = \{1, 2, \ldots, 6\}$. In each case $R_{S,n}$ is varied from 0.1 mΩ to 20 mΩ 132
5.19 Cell accessible capacity for U-topology with variable $R_{S,n}$, where $n = \{1, 2, \ldots, 6\}$. In each case $R_{S,n}$ is varied from 0.1 mΩ to 50 mΩ 133
5.20 Pack accessible capacity for U-topology with variable $R_{S,n}$, where $n = \{1, 2, \ldots, 6\}$. In each case $R_{S,n}$ is varied from 0.1 mΩ to 20 mΩ 134

6.1 Measured capacity and impedance of cell batch 143
6.2 Allocated cell pairs for 1S2P aging experiments 144
6.3 Circuit diagram of 1S2P packs used during aging experiments 145
6.4 Dynamic capacity, static capacity and total current throughput for reference single cells during aging 150
6.5 SoL and EoL EIS spectra for reference cells 152
6.6 Fitted resistances for all reference cells at SoL and EoL 153
6.7 Pack dynamic capacity loss, static capacity loss, current throughput deficit and total current throughput for homogeneous temperature packs 155
6.8 Pack dynamic capacity loss, static capacity loss, current throughput deficit and total current throughput for heterogeneous temperature packs 156
6.9 Reference SoL EIS measurements for Cell 01, including fitted resistances 158
6.10 Growth in measured HPPC resistances, $R_{DC|0.05s}$ and $R_{DC|5.0s}$, for all packs 159
6.11 EIS Spectra at SoL and EoL for all packs, taken at 50 % SoC 161
6.12 Proportional change in fitted resistances R_0, R_{SEI} and R_{CT}, for all packs 162
6.13 Proportional change in fitted resistances R_0, R_{SEI} and R_{CT} against temperature for all cells 163
6.14 Development of $\tau_{Relaxation}$ during voltage relaxation in HPPC measurements 163
6.15 Heatmaps of current distribution within homogeneous temperature packs over lifetime 166
6.16 Peak and mean currents over lifetime for homogeneous temperature packs 167
6.17 Heatmaps of current distribution within heterogeneous temperature packs over lifetime 168
6.18 Peak and mean currents over lifetime for heterogeneous temperature packs 169
6.19 Estimated SoC deficit over lifetime for 1S2P packs 170
6.20 Heatmaps of current throughput deficit per cycle for all packs over lifetime 171

6.21 Schematic representation of homogenisation of current distribution during aging in homogeneous temperature packs 172
6.22 Schematic representation of heterogenisation of current distribution during aging in heterogeneous temperature packs 173
6.23 Example OCV measurements for P20.0/0.0 and P45.0/0.0 at SoL and EoL 174
6.24 Example OCV fits for B1 in P20.0/0.0 and P45.0/0.0 at SoL and EoL 175
6.25 Root mean squared error for OCV fits for all cells. 176
6.26 Fitted degradation modes identified using the OCV model for all cells 177
6.27 EoL SoH and identified degradation modes for all cells with respect to temperature . . 177
6.28 SEM images of cathodes from fresh and cycled cells 180
6.29 Summary of interactions between degradation mechanisms, modes and effects [218] . . 184

List of Tables

2.1 Summary of common cathode properties 6

3.1 LIB thermal conductivities [134] 40
3.2 Comparison between Z and ladder topologies under drive cycle [162] 49

4.1 Properties of Kokam SLPB11543140H5 Cell [193], [194] 68
4.2 Specifications of battery cyclers used in this work 69
4.3 Kokam 5 Ah physical and thermal parameters 92
4.4 ECN capacity prediction and error for rates from 0.04 to 3 C 96
4.5 ECN validation thermal conditions for 1S6P pack 96

5.1 1S6P temperature cases experimentally investigated 109
5.2 Comparison of analytical and experimentally measured initial current distribution for 20-20 case, 1 C discharge. 120
5.3 Percentage error in model capacity predictions. 125

6.1 Cell IDs for full batch and allocation to experiments 145
6.2 Pack aging thermal conditions and identifiers 146
6.3 Single cell aging thermal conditions 148

A.1 Missing cycling cell current data per pack 217

B.1 Summary of copyright permissions. 220

Nomenclature

List of Abbreviations

BEV	Battery Electric Vehicle
BMS	Battery Management System
BoL	Beginning-of-Life
CC	Constant Current
CEI	Cathode Electroyte Interphase
CPE	Constant Phase Element
CV	Constant Voltage
DoD	Depth-of-Discharge
DRT	Distribution of Relaxation Times
DTV	Differential Thermal Voltammetry
DVA	Differential Voltage Analysis
ECN	Equivalent Circuit Model
EIS	Electrochemical Impedance Spectroscopy
EoC	End of Charge
EoD	End of Discharge
EoL	End-of-Life
FEC	Full Equivalent Cycles
HEV	Hybrid Electric Vehicle
HPPC	Hybrid Pulse Power Characterisation
ICA	Incremental Capacity Analysis

ICE	Internal Combustion Engine
IRR	Interconnection Resistance Ratio
KVL	Kirchoff's Current Law
LCO	Lithium Cobalt Oxide
LEAN	Level Evaluation ANalysis
LFP	Lithium Iron Phosphate
LIB	Lithium Ion Battery
LMO	Lithium Manganese Oxide
NCA	Lithium Nickel Cobalt Aluminium Oxide
NMC	Lithium Nickel Manganese Cobalt Oxide
OCV	Open Circuit Voltage
p-OCV	pseudo-Open Circuit Voltage
p-SEI	Positive Solid Electroyte Interphase
PCM	Phase Change Material
PC	Pulse Charge
PD	Pulse Discharge
PID	Proportional Integral Derivative
RUL	Remaining Useful Life
SEI	Solid Electrolyte Interphase
SEM	Scanning Electron Microscopy
SoH	State of Health
$\mathbf{SoH_E}$	State of Health (Energy)
$\mathbf{SoH_P}$	State of Health (Power)
STWE	Short Terminus Warburg Element
TMS	Thermal Management System

List of Symbols

$\boldsymbol{\lambda}$	Losses in each degradation mode	–

$\boldsymbol{\omega}$	Angular frequency	$Rads^{-1}$
$\boldsymbol{\rho}$	Density	kgm^{-3}
$\boldsymbol{\theta}$	Phase angle	Rad
$\boldsymbol{\theta^{MODE}_{ELECTRODE}}$	Stoichiometric drift in each each electrode for each degradation mode	$-$
$\boldsymbol{\tau}$	Time constant	s
$\boldsymbol{A}$	Area	m^2
$\boldsymbol{A^{MODE}}$	Anode peak position after transformation for each degradation mode	Ah
$\boldsymbol{A_{AGE}}$	Anode peak position after aging	Ah
$\boldsymbol{A_{FIN}}$	Anode peak position predicted by optimisation	Ah
$\boldsymbol{C}$	Capacitance	F
$\boldsymbol{C^{MODE}}$	Cathode peak position after transformation for each degradation mode	Ah
$\boldsymbol{C_P}$	Specific heat capacity	$Jkg^{-1}K_{-1}$
$\boldsymbol{C_{AGE}}$	Cathode peak position after aging	Ah
$\boldsymbol{C_{FIN}}$	Cathode peak position predicted by optimisation	Ah
$\boldsymbol{E}$	Energy	Wh
$\boldsymbol{E_a}$	Activation energy	$Jmol^{-1}$
$\boldsymbol{E_m}$	Open-circuit voltage	V
$\boldsymbol{h}$	Convective heat transfer coefficient	$Wm^{-2}K_{-1}$
$\boldsymbol{I}$	Current	A
$\boldsymbol{k}$	Thermal conductivity	$Wm^{-1}K_{-1}$
$\boldsymbol{L}$	Inductance	H
$\boldsymbol{Q}$	Capacity	Ah
$\boldsymbol{Q^{MODE}}$	Cell capacity after transformation for each degradation mode	Ah
$\boldsymbol{Q_{Gen}}$	Total rate of heat generation	W
$\boldsymbol{Q_{Irr}}$	Rate of heat generation due to ohmic heating	W
$\boldsymbol{Q_{Mix}}$	Rate of heat generation due to mixing	W
$\boldsymbol{Q_{Rev}}$	Rate of heat generation due to entropic changes	W
$\boldsymbol{Q_{Side}}$	Rate of heat generation due to side reactions	W

$\boldsymbol{R}$	Resistance	Ω
$\boldsymbol{R}$	Universal gas constant	$Jmol^{-1}K^{-1}$
$\boldsymbol{R_0}$	Ohmic resistance	Ω
$\boldsymbol{R_{CT}}$	Charge transfer resistance	Ω
$\boldsymbol{R_{IC}}$	Interconnection resistance	Ω
$\boldsymbol{R_{SEI}}$	Solid-electrolyte interphase resistance	Ω
$\boldsymbol{R_S}$	Series resistance	Ω
$\boldsymbol{T}$	Temperature	$^\circ C$
$\boldsymbol{t}$	Time	s
$\boldsymbol{V}$	Voltage	V
$\boldsymbol{Z'}$	Real component of complex impedance	Ω
$\boldsymbol{Z''}$	Imaginary component of complex impedance	Ω
$\boldsymbol{Z(\omega)}$	Impedance as a function of angular frequency ω	Ω

Chapter 1

Introduction

1.1 Background

Despite the appearance of the first production electric vehicles (EVs) over a century ago, for most of that period EVs have generally been relegated to niche roles, with internal combustion engine (ICE) vehicles providing superior range and power at lower costs [1]. With the discovery in the 1980s of practical, room-temperature, high voltage cathode materials such as Lithium Cobalt Oxide by Mizushima et al. [2], Lithium Ion Batteries (LIBs) have been seen as a practical technology to advance clean, electrical transportation. LIBs provided a step change in performance compared to previous technologies and over the past decade, cost per kWh has reduced by 87 % to a volume weighted average cost of 156 $/kWh. This dramatic cost reduction and predictions that costs will fall below 100 $/kWh over the next decade, the approximate cost parity point with ICE vehicles, have resulted in a dramatic and accelerating surge in EV adoption [3].

Although state-of-the-art LIBs offer high performance, single cells have a low voltage (2 – 4.2 V range) and relatively small capacity (10s to 100s of Whs). Therefore, it is necessary to connect multiple cells in both series and parallel to form high voltage, large capacity battery packs. For example, in automotive applications demanding multiple kWhs of energy storage or in grid level storage needing even greater storage, hundreds or thousands of cells may be connected in series and parallel to deliver the high capacity and voltages required. As an example, Tesla Model 3 which carries an 50 kWh pack containing 4,416 individual 21700 cylindrical cells, split into 2 23S46P and 2 25S46P modules [4]. Many engineering challenges remain surrounding optimal design of electric powertrains, and issues arise from the high degree of parallelisation seen in commercial battery packs. For example, orientation of the cooling system may lead to hotter cells passing higher peak currents, accelerating degradation, or electrical topology may influence the peak current seen within a parallel string. Therefore, a critical understanding of pack level effects, which are complexly coupled, combined with insight into the influence of these effects on single cell degradation and performance is key to creating improved battery packs in the future.

1.2 Research Questions

Alongside cost reductions due to increased manufacturing volumes and processes, as well as lower-cost battery chemistries, reductions in cost may be achieved via improved system design to improve pack

performance and lifetime, reducing total cost of ownership. Scaling up front the single cell to a full pack introduces additional losses, and typically pack capacity is reduced compared to expected values based on the sum of the capacity of the individual cells in the pack. The causes, effects and coupling between these losses are generally not well quantified or understood, motivating the work presented in this thesis. The underlying aim of this thesis is to link detailed analysis of degradation within individual cells to systems level effects and reveal the coupling between cell level effects and pack level performance loss and aging. In order to achieve this aim, the following research questions are defined which guided the work carried out during the PhD project. The core theme of work presented in this thesis is understanding the coupling between both systems level effects and internal cell processes, for example degradation mechanisms, alongside the coupling between systems level effects.

- What are the principal causes of heterogeneity within a battery pack, and how do they impact performance?
- How do heterogeneities and thermal effects influence the lifetime of a battery pack?
- What are the feedback effects in the coupling between heterogeneities within a battery pack?
- How do the degradation mechanisms and pathways of single cells differ when scaled to a pack?

1.3 Thesis Structure

In order to answer the proposed research questions, the structure of this thesis is outlined as follows:

- Chapter 1 provides context for the project and the research questions this thesis aims to answer.
- Chapter 2 provides a background in the operating principles of Lithium Ion Batteries, including the degradation mechanisms relevant to this work. Additionally, background in fundamental electrochemical characterisation techniques such as electrochemical impedance spectroscopy is provided, alongside a review of common modern diagnostic techniques used to identify degradation modes within cells.
- Chapter 3 contains a detailed and focussed literature review concerning heterogeneous behaviour within parallel connected Lithium Ion Batteries, aiming to summarise the relevant state of the art literature and identify any gaps in said literature.
- Chapter 4 introduces the tools developed during this project to answer the outlined research questions, including experimental test benches, a quantitative diagnostic model and equivalent circuit model used to investigate the effects of various systems-level heterogeneities.
- Chapter 5 presents work carried out to investigate the effects on performance of various heterogeneities, including an experimental study of the effects of thermal gradients on performance of parallel strings. Modelling studies examining the sensitivity of parallel strings to resistance and thermal heterogeneities are also presented.
- Chapter 6 presents an aging study of parallel cell strings under a range of thermal boundary conditions and detailed analysis of the development of heterogeneities, capacity fade, power fade and underlying degradation modes.

- Chapter 7 presents overall conclusions to the thesis and suggested future work.

Chapter 2

Background

2.1 Introduction

In recent years, dramatic acceleration of the use of energy storage devices in a range of applications has occurred, especially driven by the accelerating uptake of electric vehicles and personal electronic devices. The most common energy storage devices used in modern, high performance systems are LIBs, which are a class of electrochemical device designed to store and release energy on demand to power an electrical system. Rechargeable LIBs are secondary batteries and are the focus of this work. Thousands of publications have been written studying many aspects of LIBs since their invention and commercialisation, however Chapters 2 and 3 focus on providing a background to LIB operating principles and aims to provide a comprehensive summary of the state of the art as well as identification of areas requiring continued research. The areas studied in detail are as follows:

- Overview of cell and pack modelling techniques
- Overview of cell and pack level characterisation techniques
- A detailed review of cell and pack level diagnostic techniques
- A detailed review of cell and pack level degradation mechanisms

2.2 Lithium Ion Batteries: Basic Principles and Design

A LIB is an electrochemical device operating using intercalation electrodes to store and release charge, which is carried between the electrodes via an electrolyte containing Lithium ions. Current applications demand ever-higher performance, measured in terms of energy and power density, efficiency and operating lifetime. Meanwhile lower costs and increased levels of safety are also required to allow widespread use of LIB technologies.

2.2.1 Operating Principles

The basic operating principle of a LIB can be explained by considering a 'unit' LIB cell, consisting of 2 porous electrodes (anode and cathode), a separator and an electrolyte, as well as current collectors. A schematic diagram of a LIB is shown in Figure 2.1, representing a typical cell during discharge. Here, lithium is deintercalated from the graphite anode during discharge and intercalated into the cathode,

while the reverse is true during charge. As Li^+ ions cross the porous separator and are inserted into the cathode, an electron flows through the external circuit, powering the external load, or conversely when a negative potential is applied, lithium is intercalated into the anode, charging the cell.

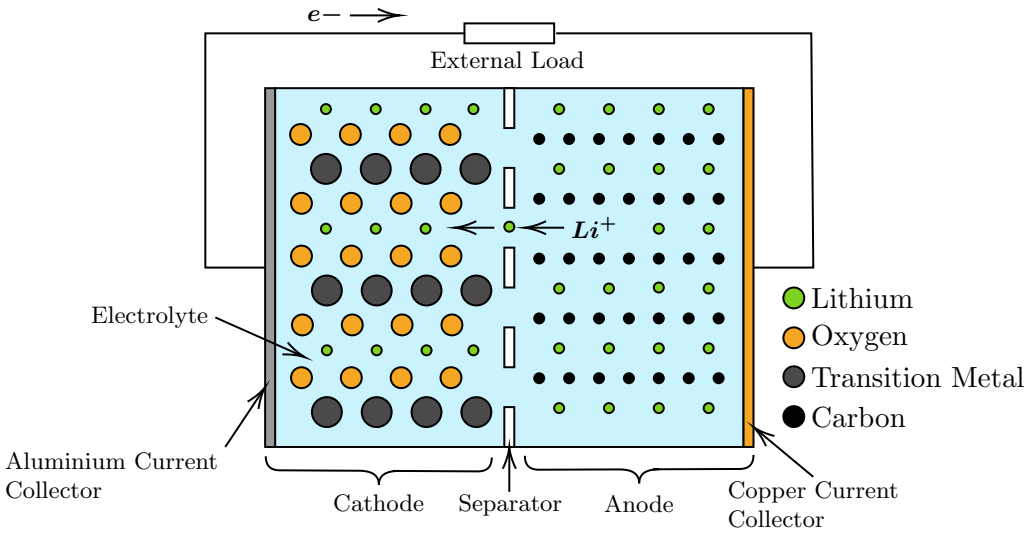


Figure 2.1: Schematic representation of a unit LIB cell, with a graphite anode and layered transition metal oxide cathode

The anode and cathode typically consist of carbonaceous materials and layered transition metal oxides respectively. Natural or synthetic graphite is typically used for the anode while the cathode contains metal oxides such as Lithium Cobalt Oxide ($LiCoO_2$, or LCO), Lithium Iron Phosphate ($LiFePO_4$, or LFP), Lithium Manganese Oxide ($LiMn_2O_4$ or LMO), Lithium Nickel Manganese Cobalt Oxide ($LiNi_x$,Mn_y,Co_z,O_2, or NMC) or Lithium Nickel Cobalt Aluminium Oxide ($LiNi_{0.8}Co_{0.15}Al_{0.05}O_2$, or NCA). Typical capacities of common anode and cathode materials are found in Table 2.1. While still in use, LCO has generally been replaced in many applications (for example automotive powertrains) where high performance, levels of safety and reduced costs are key considerations by more modern cathode materials such as NMC and NCA. These materials contain a reduced fraction of Cobalt by weight, reducing costs. Other Cobalt free cathodes such as LFP and LMO are low cost, however challenges surround achieving competitive capacity and energy densities, particularly in automotive applications where weight is at a high premium. Many other cathode chemistries with potentially higher specific performance are under investigation, however a comprehensive review of these is out of scope for this work.

Table 2.1: Summary of specific energy, capacity and voltage of common cathode materials. Adapted from [5]

Common Name	**Crystalline Structure**	**Compound**	**Specific Capacity [Ah kg^{-1}]**	**Specific Energy [Wh kg^{-1}]**	**Potential vs. Li/Li$^+$ [V]**
LCO	Layered	LCoO2	140	546	3.8
NMC	Layered	$LiNi_{0.33}Mn_{0.33}Co_{0.33}O_2$	180-200	680-760	3.7
NCA	Layered	$LiNi_{0.8}Co_{0.15}Al_{0.05}O_2$	160-170	610-650	3.7
LMO	Spinel	$LiMn_2O_4$	100-120	410-492	4.1
LFP	Olivine	$LiFePO_4$	150-170	518-587	3.4

The anode and cathode both contain an inactive fraction of material to both bind the electrode together and increase the electronic conductivity. To form an electrode, the active and inactive material are

formed into a slurry with a solvent (organic solvents are used for the typically moisture-sensitive cathode) and then coated onto the current collector, which is typically a copper or aluminium foil for the anode and cathode respectively. The separator film, typically consisting of a porous polymer, such as Polypropylene, which separates the anode and cathode and provides electrical isolation of the two electrodes, so charge transfer must occur via the electrolyte. The electrolyte consists of a lithium salt (commonly lithium hexafluorophosphate ($LiPF_6$)) dissolved in an organic solvent (typically a mix of ethylene carbonate and dimethyl carbonate), which provides the charge carrying Li^+ species which are intercalated into the electrodes. The electrolyte will also usually contain additives to either promote stable solid-electrolyte interphase (SEI) formation or extend the stable operating voltage range of the electrolyte, allowing increased energy density.

During operation, the cell can be charged by applying an external potential, oxidising the anode and driving Li^+ ions to the cathode which is reduced. This process is driven by energy delivered from the external circuit. Correspondingly during discharge the anode is reduced and cathode oxidised, and electrons flow through the external circuit, delivering power.

2.2.2 Cell Design and Form Factors

Within a LIB, many layers of electrode and separator are stacked to form the core of the battery, and these elements are packed into a sealed case with electrolyte. LIBs are also produced in various form factors, commonly cylindrical, pouch, prismatic and coin cells. Different form factors will deliver different traits which influence the overall performance of the battery, summarised as follows

- Geometry (e.g. size, shape, tab location, packing efficiency)
- Mechanical (e.g. electrode stresses and compression)
- Thermal (e.g. surface area to volume ratio, thermal mass, thermal conductivity)
- Electrical (e.g. internal current paths)

All the listed factors, as well as many others, will influence the overall electrochemical performance of a LIB. Some influencing factors, for example the thermal performance, do not directly influence the electrochemistry occurring within the cell, but drive the operating conditions within the cell and therefore indirectly influence the cell operation. Overall, it is important to consider all of the above factors during system design and cell selection.

Performance Metrics

The performance of a LIB may be measured against several metrics, depending on the application demand. Typically, a cell is categorised by the cell charge capacity (measured in ampere hours, Ah) and nominal cell voltage (average voltage over a discharge at nominal rate), the product of which gives the cell energy capacity (Wh). However, the true energy capacity of a cell is given by Equation 2.2, while the charge capacity is given by Equation 2.1.

$$Q = \int I \, dt \tag{2.1}$$

$$E = \int I \cdot V dt \tag{2.2}$$

It is noted that while a cell may have a certain theoretical capacity, which is the maximum energy that may be extracted from the cell, the nominal or usable capacity is lower, as usually the cell will not be operating under ideal lossless conditions. Therefore the nominal capacity will usually be measured at a given rate inside the specified operating range of the cell. Another consideration is the rate at which a cell can deliver power to an external load, as a cell may be optimised for either energy or power density which will have a corresponding influence on performance. The standard method for comparing rate capability for cells with differing capacities is to consider cells operating at a given C-rate, which is defined in Equation 2.3.

$$C - rate = \frac{I}{Q_{Nominal}} \tag{2.3}$$

The C-rate allows comparison of cells with different capacities and form factors and is defined such that a discharge at 1 C will occur over a 1-hour period. A high energy cell might be optimised for operation below 0.5 C while a high-power cell might be able to deliver power at 50 C. As the design demands for both cases are very different, high performance in one aspect may detract from performance in other areas. While LIBs are efficient energy storage devices, some energy is lost during a given roundtrip (i.e. a charge and discharge cycle), and the efficiency is typically measured by considering the energy efficiency of a cell, defined by Equation 2.4. Meanwhile the coulombic efficiency may be defined by Equation 2.5, which is equivalent to the ratio between the number of Li^+ ions departing and returning to the cathode in a full cycle. In real systems where $\eta_{\text{Coulombic}} < 100\%$, it is implicit that the deficit in ions departing and returning is a consequence of irreversible chemical or electrochemical side reactions [6].

$$\eta_{Energy} = \frac{E_{Discharge}}{E_{Charge}} \tag{2.4}$$

$$\eta_{Coulombic} = \frac{Q_{Discharge}}{Q_{Charge}} \tag{2.5}$$

A key performance metric for LIBs is the specific energy, relative to either the mass (gravimetric) or volume (volumetric) of the cell. These metrics are defined in Equations 2.6 and 2.7 respectively and are a critical metric when determining relative performance. It is noted that the specific power, defined in a similar manner to the specific energy is also an important metric in some applications which are volume limited.

$$Gravimetric\ Energy\ Density = \frac{E_{Discharge}}{m_{Cell}} \tag{2.6}$$

$$Volumetric\ Energy\ Density = \frac{E_{Discharge}}{V_{Cell}} \tag{2.7}$$

It is noted that the mass of the cell includes that of the inactive fractions, for example the casing, and so form factor will influence the overall energy density. For example, cylindrical or prismatic cells with metal casings may sacrifice some energy density to the mass of the can. Considerations of inactive

fractions is also key at the pack level, where elements such as the thermal management system store no energy but contribute mass to the system, reducing energy density compared to a naked cell.

2.3 Electrochemical Characterisation Techniques

In this section, common electrochemical testing techniques are reviewed, and the underlying theory explained as appropriate. As common characterisation techniques, all the methods reviewed here are applied to characterisation during the experimental studies presented in Chapters 4-6. It is noted that this section is not intended as an exhaustive review of characterisation techniques and is focussed on techniques which are later applied in this work.

2.3.1 General Techniques: Capacity, Pseudo-OCV and OCV Measurements

Cell capacity measures the total electric charge in Ah which can be withdrawn from a fully charged cell at specific operating conditions and therefore, electrochemically, it is a measure of the amount of available intercalation material within the full cell. It is noted that in practical cells, the capacity of each half-cell may be greater, however the possible depth of discharge (DoD) is limited within the voltage limits of the cell. Generally, this can be measured by charging and discharging the cell under controlled conditions, while recording the capacity via Coulomb counting. Typically, cells are charged first under a constant current (CC), until the cell reaches a upper voltage cutoff and then at a constant voltage (CV), commonly with a current cut-off during the CV charge of around 10 % of the CC value [7], [8]. The CV phase is included to fully saturate the active material at the upper voltage limit of the cell. Discharging is most commonly carried out under constant current conditions, until a voltage reaches a lower voltage cut-off, as this approach benefits from repeatable discharge conditions and less current measurement errors, compared to a constant power discharge [7]. Measured cell capacity does however depend on the current rate and the cells temperature during the discharge. At elevated temperatures, improved solid-state diffusion and ion mobility, governed by the Arrhenius rate law described in Equation 2.8, leads to a reduction in the cells internal resistance and thus overpotential. As such, at higher temperatures, more capacity can be extracted before the 2.7 V cut-off voltage is reached [7], [9].

$$\Psi = \Psi_{ref} e^{\frac{E_a^{\Psi}}{R}\left(\frac{1}{T_{ref}} - \frac{1}{T}\right)} \tag{2.8}$$

Where Ψ is the property of interest, Ψ_{ref} is the property of interest measured at T_{ref} (K), E_{a} is the activation energy (Jmol^{-1}) and R is the universal gas constant ($\text{Jmol}^{-1}\text{K}^{-1}$).

Reduction of capacity at increased currents is caused by an increased electrode overpotential, which is related to current via the Butler-Volmer kinetics (Equation 2.9). This assumes that mass transport in the electrolyte is not the rate limiting step, i.e. there is no depletion in reactant concentration in the liquid phase at the particle-electrolyte interface. In a case (for example at high rates) where significant concentration gradients build up in the electrolyte, this description will not be valid, and the effects of solid- and liquid-phase diffusion are significant. The output, j, is the intercalation reaction flux, driven by the charge transfer overpotential.

$$j = i_0 \left(e^{\frac{\alpha_a F}{RT}\eta_a} - e^{-\frac{\alpha_c F}{RT}\eta_c} \right) \tag{2.9}$$

Where η_a and η_a are the anode and cathode overpotentials respectively (electrode potential (E) - equilibrium potential (E_{eq})), α_c and α_c are the cathodic and anodic charge transfer coefficients and F is the Faraday's constant. i_0 denotes the current density for Lithium ion exchange at the solid/liquid interface. As such, the accessible capacity of the cell falls at increased currents, as the resulting increase in the overpotential causes the cut-off voltage to be reached before all the cell capacity can be accessed.

The pseudo-open circuit voltage (p-OCV) refers to an approximated thermodynamic open circuit voltage (OCV) at a given state of charge. The true cell open circuit voltage may be measured by charging or discharging a cell to a range of given states of charge and allowing the cell voltage to relax to a constant value, allowing the fitting of a voltage curve. Alternatively a low rate (<C/10) charge or discharge of the cell may be carried out, approximating this voltage curve as the p-OCV curve. When the rate involved is low, and the cell impedance is also low (on the order of 1-10 mΩ) it can be assumed that this will be a reasonable approximate the true cell OCV curve [10]. In cases where the cell impedance is high, pulse discharge (PD) or pulse charge (PC) methods may be more appropriate to measure OCV, due to increased overpotentials and therefore deviation between p-OCV and true OCV measurements, as extremely low current rates would be required to minimise overpotentials. Additionally, hysteresis is often seen between the charge and discharge OCV curves, leading to subtle differences between charge and discharge behaviour. It has been proposed that this voltage hysteresis is caused by compressive stresses within active material particles impeding lithium intercalation and therefore requiring an extra electrical overpotential to overcome this reaction barrier, leading to voltage hysteresis [11]. Hysteresis has also been shown to be caused by differences in in graphite phase succession during charge and discharge, even at temperatures of over 50 °C [12].

Given the dependence on testing conditions, international testing standards, such as SAE J1798 [13] suggest for capacity tests to be done at various temperatures (commonly -20C, 0 , 25 and 45 °C) and C-rates (for example: 1C, C/2, C/3). A fully charged battery under a 1 C constant current discharge will reach the fully discharged state in 1 hr. An extensive summary of capacity characterisation operating conditions has been carried out by Barai et al. [7]. Analysis of capacity measurements is typically simple as usually no smoothing of the data will be required, allowing results to be measured and used directly.

2.3.2 Electrochemical Impedance Spectroscopy

Measurements and Theory

Electrochemical impedance spectroscopy (EIS) is a common and powerful tool used for analysis of electrochemical systems as it is both able to be applied in-situ and gives the user the ability to decouple processes within a coupled system, such as a LIB. Typically a sinusoidal current or voltage with a known frequency and magnitude is applied to the device under test, with the magnitude small enough that the system remains pseudo-linear. Whether the measurement should be taken in a potentiostatic or galvanostatic mode depends on the system being investigated. The sinusoidal excitation (for a potentiostatic measurement) is defined in Equation 2.10, where V_{DC} is defined as the system equilibrium potential at which the measurement is taken, while Vac is the magnitude of the AC applied voltage.

$$V(t) = V_{DC} + V_{AC} sin(\omega t) \tag{2.10}$$

Therefore the current response of the system will be given by Equation 2.11, where ψ is defined as the phase difference between the AC applied voltage and current response.

$$I(t) = I_{DC} + I_{AC} sin(\omega t + \psi) \tag{2.11}$$

By Ohms law, the impedance response of the system, Z(ω), is defined as the ratio of the applied voltage and current, shown in Equation 2.12.

$$Z(\omega) = \frac{V(\omega)}{I(\omega)} \tag{2.12}$$

The resulting impedance is complex, as shown in Equation 2.13, and both the real and imaginary components may be extracted as shown in Equations 2.14 and 2.15.

$$Z = Z' + iZ'' \tag{2.13}$$

$$Re(Z) = Z' = |Z| cos(\theta) \tag{2.14}$$

$$Im(Z) = Z'' = |Z| sin(\theta) \tag{2.15}$$

Where the phase angle is given by Equation 2.16.

$$\theta = arctan\left(\frac{Z''}{Z'}\right) \tag{2.16}$$

And the modulus by Equation 2.17.

$$|Z| = \sqrt{Z'^2 + Z''^2} \tag{2.17}$$

The output of an impedance measurement are the real and imaginary components of the impedance and the phase angle or phase shift, and is usually represented in the form of a Nyquist plot. In most electrochemical systems, Z is frequency dependant and measurements typically scan over a wide range of frequencies (usually mHz – kHz for LIB systems). Real systems are also usually non-linear and therefore measurements are only typically useful when the applied signal magnitude is sized such that the response is linear or pseudo-linear. This property can be tested by applying the Kramers-Kroniq test [14]–[16]. The Kramers-Kroniq test uses the real component of a transfer function to calculate the imaginary component for a causal, stable time-invariant system (as the frequency tends to 0 and ∞). This allows for the comparison between a model and data, and therefore calculation of residuals during model fitting to assess accuracy. As EIS can be carried out on any electrochemical system, it is useful to extract information about internal processes and kinetics. However, decoupling processes with similar time constants can be challenging so significant consideration of interpretation is required. Additionally, EIS is typically carried out under steady-state conditions and may not capture behaviour

under load in a system. While some researchers have explored using EIS under load in LIBs [17], [18], interpretation of results remains challenging. Often EIS is combined with other techniques to build an overall picture of the system under test.

Equivalent Circuit Fitting

The dynamic impedance response of electrochemical systems can be represented as a sum of equivalent electrical elements, which form a so-called equivalent circuit with the same response characteristics as the real electrochemical system. Ideally the circuit elements should be related to a specific physical property or process of interest, although it should be noted that in general the fitting model has no direct physics based understanding of the system modelled. Thus care is required when selecting the circuit to fit, as improving the model fit may not result in increased overall accuracy. In general, the impedance of n series elements is given by Equation 2.18 while the impedance of n parallel elements is given by Equation 2.19.

$$Z_{TOTAL} = Z_1 + Z_2 + Z_3 + \ldots + Z_n \tag{2.18}$$

$$Z_{TOTAL} = \frac{1}{Z_1} + \frac{1}{Z_2} + \frac{1}{Z_3} + \ldots + \frac{1}{Z_n} \tag{2.19}$$

Where Z_{Total} is the total impedance, and Z_n is the impedance of circuit element n, with $n = \{1, 2, \ldots, n\}$. Within battery systems, three main classes of resistance are of interest – series, charge transfer and diffusion. Series resistance refers to the resistance of the bulk to ion transport as well as electronic resistance while charge transfer resistance is associated with the Faradaic reactions occurring at the electrode/electrolyte interface (i.e. exchange of ions from the electrolyte bulk to the electrode bulk via a redox process). The diffusion resistance is related to mass transport within the system.

Equivalent circuit elements are used to model a system, and some common elements are described and discussed as follows. Pure resistive elements, which might be used for example to represent electronic resistance can be defined by the transfer function shown in Equation 2.20 and have no frequency dependence. This is represented by a single real point on a Nyquist impedance plot.

$$Z_R = R \tag{2.20}$$

A pure capacitive element may be represented as shown in Equation 2.21 and typically is used to represent double layers which form at electrode/electrolyte interfaces within a battery system. This capacitance would be entirely imaginary and negative on a Nyquist plot.

$$Z_C = \frac{1}{i\omega C} \tag{2.21}$$

The inductance of a system, which is generally relevant to the impedance of measurement lines and at high measurement frequencies, can be represented by Equation 2.22, and is purely positive and imaginary on a Nyquist plot

$$Z_L = i\omega L \tag{2.22}$$

However, the basic circuit elements as defined above do not fully represent all behaviour in electrochemical systems, and therefore so-called distributed circuit elements, which consist of a combination of the above elements, may be used to represent real behaviour. The two principal elements for LIB systems are the Constant Phase Element (CPE) and the Warburg element. A CPE is defined by Equation 2.23.

$$Z_{CPE} = \frac{1}{Ti\omega^{\phi}} \tag{2.23}$$

Where T and ϕ are the CPE parameters. A CPE may represent a pure resistor ($\phi = 0$) or capacitor ($\phi = 1$). CPEs are useful to model the impedance response of real double layer charging of rough electrodes, however is not appropriate to apply at high or low frequencies [15].

The Warburg element is used to model one-dimensional diffusion of species within the electrode. In general, for infinite length diffusion, the impedance response induced by diffusion can be modelled by Equation 2.24, where to describe the diffusion of species a, σ_{a} is the Warburg parameter which is a function of the species diffusivity, reaction rate, current density and potential and concentration of species a.

$$Z_{W,\infty} = \frac{1}{\sigma_a\sqrt{(i\omega)}} = \frac{\sigma_a}{\sqrt{\omega}\,(1+i)} \tag{2.24}$$

For battery systems of interest however, the Short Terminus Warburg Element (STWE) or $\mathrm{Z_W}$, which describes diffusion over a distance δ is more appropriate. This is defined per Equation 2.25, where $\mathrm{R_W}$ is the Warburg R parameter, and $\mathrm{T_W}$ is given by Equations 2.25 and 2.26, which relates the diffusivity of species a, $\mathrm{D_a}$, to the diffusion length.

$$Z_W == \frac{R_W tanh\left[(iT_W\omega)^{\psi}\right]}{(iT_W\omega)^{\psi}} \tag{2.25}$$

$$T_W = \frac{\delta^2}{D_a} \tag{2.26}$$

A STWE will behave as a resistor at low frequencies and give a typical 45° response at higher frequencies. For pure diffusion, $\psi = 0.5$, however ψ may be allowed to be free for fitting purposes [14]–[17] Fitting of equivalent circuits is usually carried out using specialist fitting software, for example ZView (Scribner Associates), BT-Lab (Biologic) or NOVA (Metrohm Autolab). In order to accurately fit an equivalent circuit to a system it is required to select an appropriate circuit form and initial values. Initial values are critical as generally the fitting tools use a gradient based solver (for example ZView, used in this work uses a Levenberg-Marquardt algorithm for fitting). General best practice is to begin with the simplest model which describes the system, and to minimise the number of parameters that are adjustable, whilst care should be taken to ensure that the model is relevant to the expected physical processes occurring in the system [14].

2.3.3 Hybrid Pulse Power Characterisation

A common technique for determining the resistance of a cell is the Hybrid Pulse Power Characterisation (HPPC) test, which also may be referred to as PD or PC methods where only charging or discharge

pulses are applied respectively. In order to determine the cell impedance a square wave current pulse (ΔI) is applied to the cell and the voltage response (ΔV) is recorded. It is assumed that over a short pulse the state of charge of the cell will remain quasi-constant and therefore the voltage drop over the period will be purely a function of the current and cell impedance rather than changes to the cell OCV. By Ohms law therefore the cell resistance (R_{Pulse}) can be determined. R_{Pulse} can be considered to include contributions from the ohmic resistance (R_0), the charge transfer resistance (R_{CT}) and the diffusion resistance (R_{Diff}) [7], [19]. Figure 2.2 shows a generic pulse and the quantities required to evaluate R_{DC} via Ohms law.

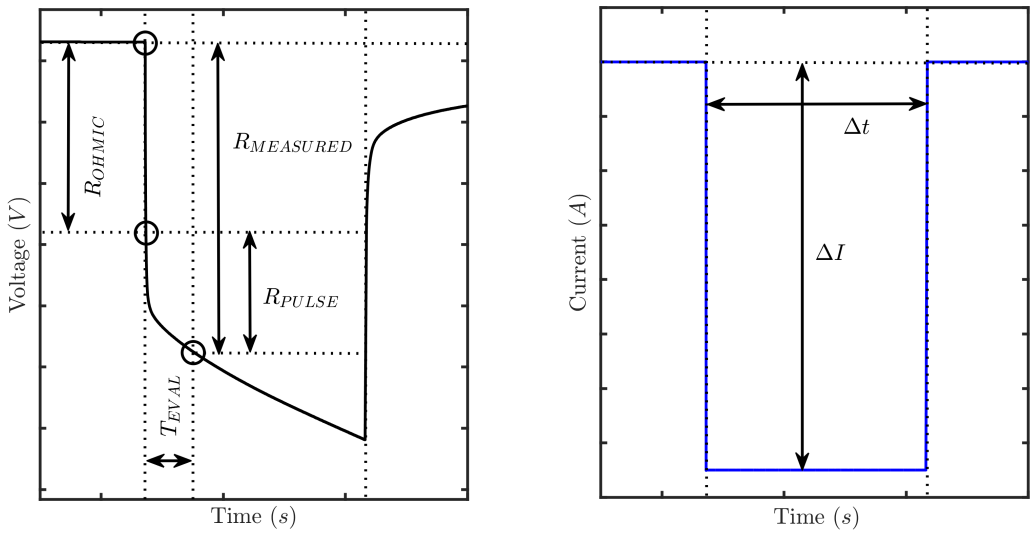


Figure 2.2: Generic HPPC pulse showing measured quantities

The aim of such tests is to characterise the cell under different conditions i.e. in charge and discharge, at different rates and states of charge. Various standard HPPC tests involving a single charge and discharge pulse with a rest period between have been proposed [20]–[22]. For example, the United States Department of Energy recommends 10 s charge and discharge pulses applied with a 50 s rest, applied at 10 % SoC breakpoints with 60 min rests between applied pulse trains. Overall, the HPPC technique is advantageous, as this allows determination of an estimate of cell impedance without use of typically less common and more expensive potentiostat and impedance analysers, which are generally in high demand in a laboratory setting. Additionally, HPPC and PC/PD methods are highly effective for fitting equivalent circuit models, as data is acquired under load as well as during relaxation, which is able to improve the model fitting when compared to EIS parameterisation [23].

2.4 Cell Degradation: Modes and Mechanisms

2.4.1 Overview of Lithium Ion Battery Degradation

Over the service life of a LIB, performance of the battery will degrade due to accumulated damage of the cell. Ageing or degradation of LIBs occurs due to a range of mechanisms including Lithium plating, mechanical fracture and loss of active material, the growth of the solid electrolyte interphase (SEI) layer, electrolyte decomposition, current collector corrosion and others [24]. These degradation mechanisms are illustrated in Figure 2.3. An understanding of why degradation occurs is important in

designing operating regimes to minimise specific effects, increase safety and maximise battery lifetimes. These factors may be influenced by a range of factors including operating conditions, load cycle and depth of discharge (DoD) during cycling, and as such heterogeneities induced by variations within a pack will lead to uneven degradation of cells and therefore accelerated capacity loss, early failure or even safety hazards.

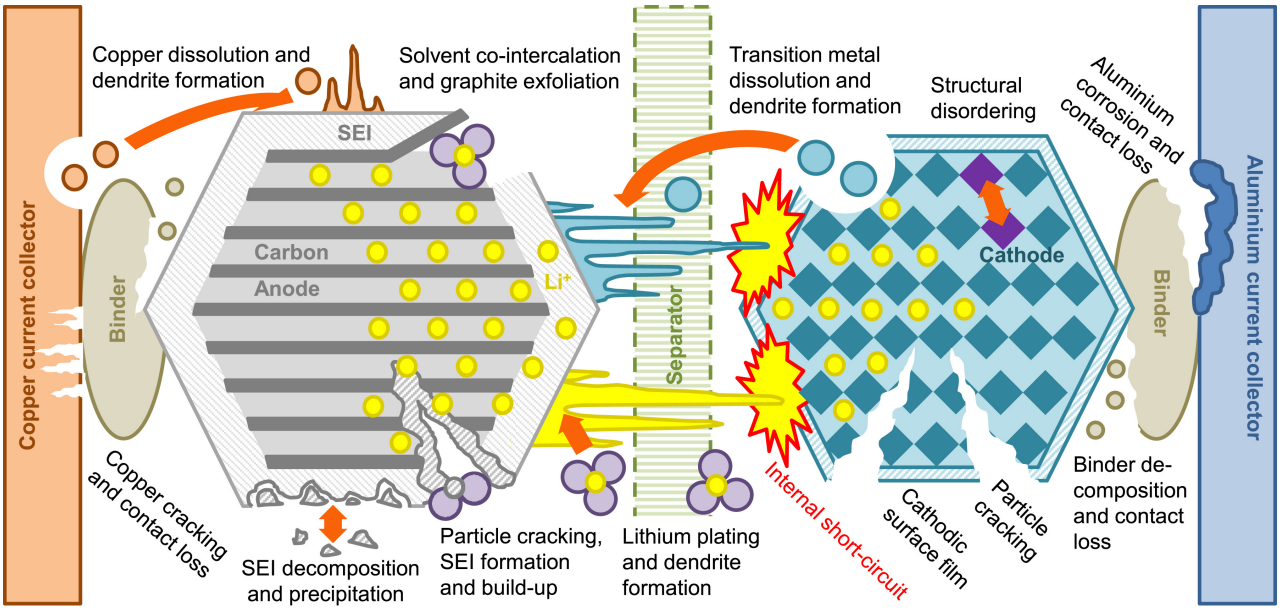


Figure 2.3: Degradation mechanisms in Lithium Ion cells [25]. CC-BY 4.0

2.4.2 Degradation: The Consequences

The principal consequences of degradation, aside from safety concerns, are capacity and power fade. Capacity fade is the fundamental loss of cell capacity, i.e. a decrease in the number of Ah (or coulombs) which can be stored in the electrodes of the cell and is related to the fundamental electrochemistry of the cell. Power fade is related to the increased overpotentials caused by accumulated damage and the consequent resistance increases seen during cell aging and leading to a loss in energy stored (Wh). It is also important to distinguish between causes, mechanisms and modes of degradation within LIBs. Causes of degradation range from temperature and state-of-charge to electrode bending stresses and will cause degradation to occur by a given mechanism, e.g. high temperatures cause accelerated SEI layer growth. This leads to the cell undergoing a certain degradation mode, in this example loss of cyclable lithium or loss of lithium inventory. It is noted that identifying a degradation mode does not necessarily identify the mechanism underlying the mode. As shown in Figure 2.4, multiple mechanistic causes can lead to a single identifiable degradation mode, and often multiple mechanisms will occur simultaneously to a greater or lesser degree. This further complicates attribution of mechanisms to effects without time-consuming and expensive electrode level characterisation.

Overall, understanding of the degradation mechanisms occurring within a cell will lead to improved ability to predict the expected lifetime of a cell, a key challenge in the field. Reliable prognosis of degradation rates and remaining useful life of cells is key to enabling manufacturers to design devices, certify and warranty products and predict safe usage limits.

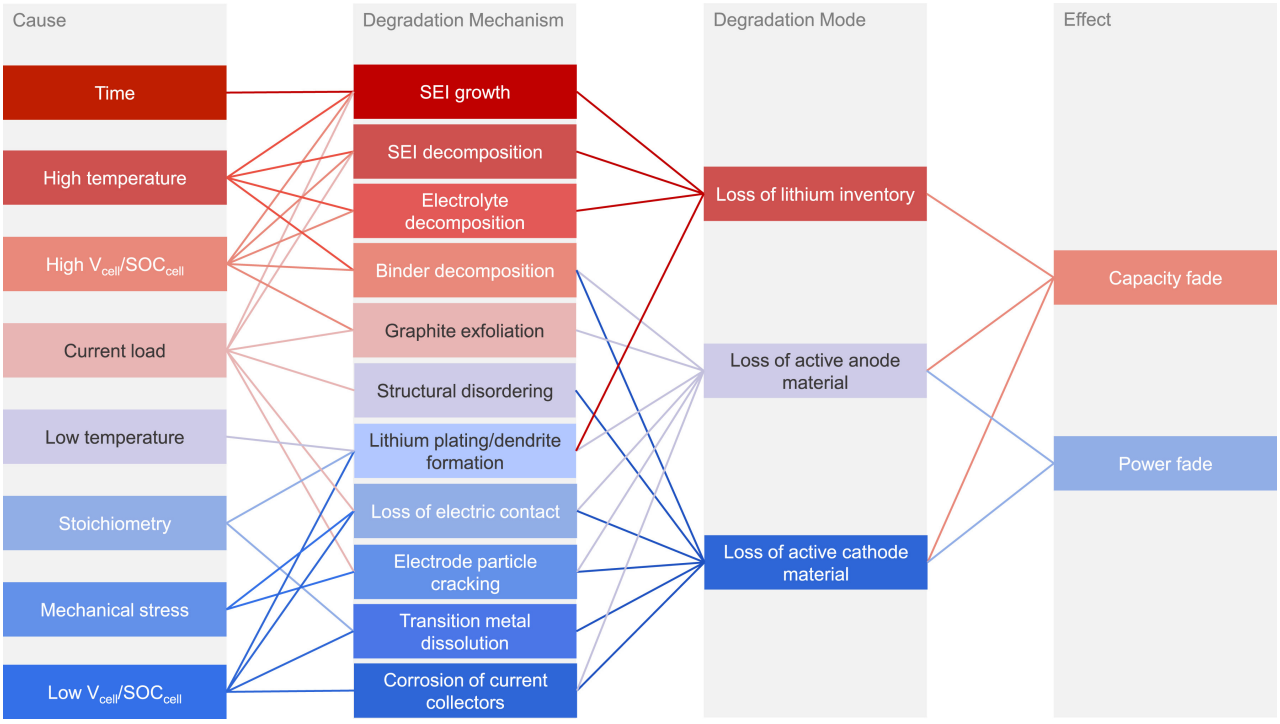


Figure 2.4: Cause and effect of degradation mechanisms and associated degradation modes [25]. CC-BY 4.0

2.4.3 Degradation Mechanisms in Lithium Ion Batteries

A wide range of possible degradation mechanisms and pathways occur within LIBs, and selected relevant mechanisms are summarised below.

Solid Electrolyte Interphase Layer Growth and Decomposition

At the anode, formation of the SEI layer is a key degradation mechanism within LIBs. During cycling the anode potential, may fall below the stability threshold of the electrolyte, leading to unwanted side-reactions. However, stable formation of the SEI determines the safety, power capability, shelf life and cycle life of a battery, and formation of a uniform SEI is critical [26]. On formation of the cell, reactions at the anode surface form the SEI passivation layer which allows stable cation exchange between the electrolyte and anode. Peled et al. [27] showed that the SEI was composed of partial and full reaction products from the reduction of electrolyte solvents while it has also been found that the SEI is formed of reaction products that irreversibly consume cyclable lithium, leading to loss of lithium inventory in the cell [28].

Ideally, the SEI would have full transmissibility of Li^+ cations and zero electronic conductivity, allowing ion exchange while blocking electrical contact between the anode and electrolyte. Additionally, the morphology and composition of the SEI would be uniform and contain principally stable reaction products rather than metastable and poorly passivating reaction products. Mechanically the layer should be compact, elastic and flexible to promote long lifetime of the SEI and cell [28].

As the cell is cycled, the SEI will grow, influenced by multiple factors. Operating conditions (temperature and cell potential) will drive SEI layer growth, as high temperatures and potentials will promote irreversible side reaction pathways that lead to SEI layer formation and growth [30], [31]. Waldmann et al. [29] investigated cycle aging in 18650 NMC-111 cathode cells, measuring the temperature dependence of aging, as shown in Figure 2.5. Above 25 °C post-mortem indicated aging was dominated

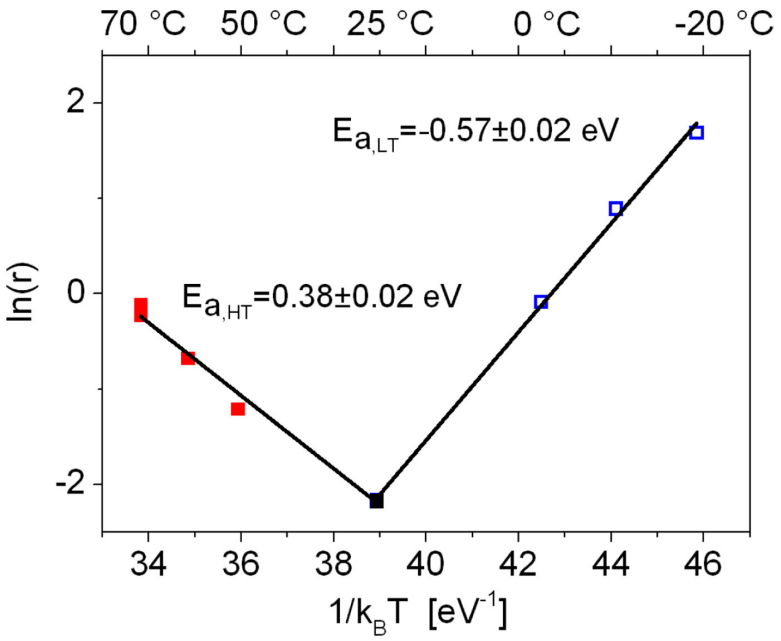


Figure 2.5: Arrhenius plot for the ageing behaviour of 18650 cells cycled at 1 C in a temperature range of -20 °C to 70 °C. The solid lines correspond to linear fits of the data points of the respective temperature ranges below and above 25 °C[29]. © Reproduced with Permission.

by SEI layer growth, showing the positive correlation of SEI growth rate with temperature. The study also highlights the switching of dominant degradation modes under different temperature regimes. After SEI layer formation, the volume change of the anode induced by intercalation/deintercalation will lead to cracks forming in the SEI layer, exposing fresh anode surface which allows further SEI formation. Damage caused to an initially well-formed SEI layer will increase impedance and reduce cell capacity [32].

Formation of 'good' i.e. compact, transmissible, passivating and stable SEI layers may be promoted by the addition of various compounds as additives to the electrolyte. For example, additives such as Vinylene Carbonate (VC) promote the preferential formation of insoluble solids, due to their higher reductive potential than electrolyte solvents, leading to stable and controlled SEI formation, increased coulombic efficiency and reduced self-discharge [33]. Lithium Bis(Oxalato)Borate (LiBOB) has been found to react with major SEI components for form more stable compounds, again promoting the ability for form stable SEI layers [33]. A potential cause of capacity roll-off (rapid capacity loss) is the consumption of stabilising additive leading to increasingly rapid growth of SEI.

Cathode Electrolyte Interface Growth

While the anode SEI layer has attracted much more interest historically, in recent years the Cathode Electrolyte Interphase (CEI) (also referred to as the positive-SEI or p-SEI) layer has been identified as another key component of a long life, safe LIB. Similar to the SEI, the CEI contains both inorganic compounds as well as organic compounds including carbonates and polymers. It has been found that the CEI thickens during cycling and is found to decompose at high potentials vs. Li/Li^+ [34]. While the exact composition and behaviour of the CEI is debated, it is clear that the layer growth is sensitive to various factors including voltage, current and electrolyte composition [35].

Formation of a stable CEI layer may allow the use of higher potential cathodes and therefore increase

the energy density of LIBs. It has been found that the CEI layer has a significant influence on the performance of NMC111 electrodes, which is one of the most common modern cathode materials. Various additives are able to stabilise and reduce the rate of CEI formation, reducing the progressive capacity fade and impedance increase induced by the thickening of the CEI layer [36].

In the case of both the SEI (see Section 2.4.3) and the CEI, formation of a stable layer has been identified as a critical bottleneck in the production of LIBs, due to the time, expense and expertise required to consistently manufacture cells with a well-formed SEI. This is currently achieved by first allowing wetting of the electrodes after electrolyte addition, followed by formation cycling at low rates before a second electrode wetting step. It has been suggested that techniques such as atomic layer deposition may allow the formation of synthetic SEI and CEI layers during manufacturing to reduce time and process costs, or the use of alternative, more stable anode materials such as Lithium Titanate (LTO) or Lithium metal may eliminate the need for SEI formation completely, although many challenges remain in these areas [37].

Structural Disordering

Structural disordering or phase change in cathodes occurs when the the initial structure decomposes in disordered unwanted phases. For a layered NMC cathode this would result into decomposition to spinel and rock salt phases. This effect occurs at the particle surface, leading to passivation of the particle [38]. Jung et al. [38] measured oxygen evolution from NMC cathodes, suggesting that lattice oxygen is released from the cathode during the decomposition from layered to spinel/rock salt phases. Radin et al. [39] suggested that the formation of the disordered spinel and rock salt phases is more favourable in delithiated cathode material, due to collapse of interlayer spacing or stacking-sequence changes when delithiated. Lin et al. [40], using transmission electron microscopy, determined that structural disordering occurs during simultaneous oxygen and Lithium removal from the layered lattice structure, leading to transition metal migration and collapse of the layer structure into disordered phases. Zhao et al. [41] showed that structural changes in NMC particles are unlikely to occur during delithiation, due to the higher potential of the $Co^{3+/4+}$ redox couple than that of the $Ni^{3+/4+}$ redox couple. This implies that if structural disordering is a dominant mechanism of cathode damage, it will be observed to occur principally during discharge of the cell (i.e. during cathode lithiation). Increased cathode charge transfer resistances will be observed after significant cathode phase changes, due to the slowed ion exchange kinetics through the passivated surface and reduction in the availability of electrochemically active sites.

Particle Cracking

During cycling individual active particles in the electrodes of a battery experience significant volumetric changes, due to the volume changes induced by intercalation and deintercalation in the electrodes. The volume change in the electrode is a function of this effect alongside the thickness change induced by thermal expansion of the electrodes during cycling [42]. Cracking of electrode active particles will lead to loss of active material due to the loss of contact between electrode particles and the conductive binder of the electrode, and therefore lead to capacity fade in the cell [24].

For example, it has been shown that due to non-linear changes of the diffusion coefficient in graphite with respect to temperature leads to a strong temperature dependence in the allowable rate before the onset of cracking. Takahashi et al. [43] showed that whilst at 25 °C a 30 C discharge was possible from

a graphite particle without cracking, whilst at -10 °C a 10 C discharge would induce cracking. In the cathode it has been found using scanning transmission electron microscopy that in NMC111 grains intragranular cracks may form during high voltage cycling, which is a limiting factor in extending the allowable operating voltage range [44].

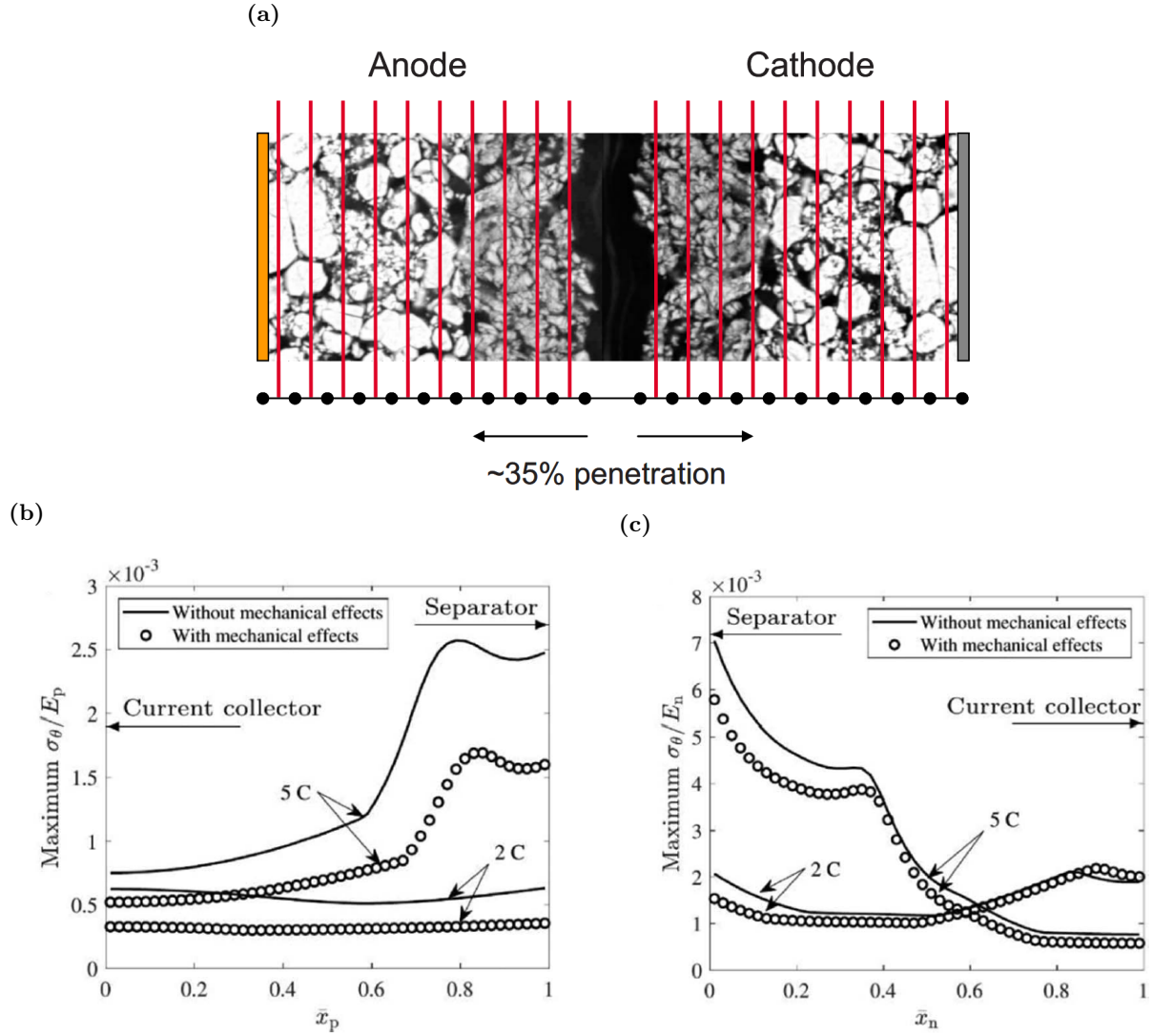


Figure 2.6: a) Depiction of a cell with fractured particles near the separator in both the anode and cathode. The fractured region accounts for roughly 35 % of each electrode [45]. © Reproduced with Permission. b) The distribution of the maximum tangential stress in electrode particles across the cell cross-section under 2 and 5 C discharging in the cathode. c) The distribution of the maximum tangential stress in electrode particles across the cell cross-section under 2 and 5 C discharging in the cathode anode [46]. CC-BY 4.0

Christensen et al. [45] modelled diffusion-induced stress generation in spherical particles, dividing the electrode into fractured and unfractured domains (illustrated in Figure 2.6 for 35 % fractured electrodes). It was found that in electrode materials exhibiting small volume changes during (de)lithiation, solid state diffusion had significant impacts on both voltage and stress responses. Therefore at lower temperatures, where diffusion is slower, particle fracture is more liable to occur. Modelling by Ai et al. [46] has shown that stress induced cracking may be caused by the cyclic stress response within particles during cycling, which may lead to fatigue crack propagation and growth below the material fracture toughness. The magnitude of these stresses increases non-linearly with C-rate, and therefore is of particular concern during fast charging, where pulverisation of electrodes near the cathode-separator

interface has been observed. This effect of local pulverisation at high rates is illustrated in Figures 2.6 b and c for the anode and cathode respectively. Whilst at 2 C, homogeneous maximum tangential stresses are predicted, at 5 C peak stresses in the cathode are increased 5 times in the electrode. These increased stresses are concentrated in particles close to the cathode-separator interface, in the upper 20 % of the electrode. This effect is mirrored in the anode.

Lithium Plating

At low temperatures increased overpotentials at the anode due to increased impedance may lead to the anode potential vs Li/Li^+ falling below the plating threshold during lithiation of the anode during charge. Increasing the cycling rate may also increase the overpotential and therefore the prevalence of lithium plating, which consists of metallic lithium being plated onto the graphite anode rather than intercalating into the anode. Lithium plating may be considered a Faradaic side reaction and while it may be partially reversible will lead to loss of cyclable lithium in the cell [24]. Plating is exacerbated by any factors which reduce the rate of completing intercalation into the anode, for example during operation at low temperatures or when there is insufficient anode material to fully intercalate all cyclable lithium [47]. Work by Waldmann et al. [29] showed the switch in dominant degradation mode from SEI layer growth to lithium plating below 25 °C (Figure 2.5), confirmed by post-mortem analysis and reference electrode measurements.

Although plating may be partially reversible, dendrite formation and growth via plating may ultimately lead to separator puncture, internal short circuit and fire. Even if dendrites do not lead to a short-circuit, if electrical contact is lost then formation is irreversible, leading to loss of cyclable Lithium. As such plating is a key consideration during design of battery operating regimens, as it is critical to avoid plating to maintain long cell life. In the case of dendrite growth it is seen that most small internal short circuits will lead to rapid local heating which 'breaks' the short by melting the dendrite [48]. However, the local temperature rise will promote other temperature dependant degradation mechanisms such as SEI layer growth, electrolyte drying and dissolution of the positive electrode. The plated lithium will also often form at the electrode-separator interface which may form a blocking layer over the anode. As the metallic plated lithium is more reactive than graphite, side reactions between the lithium and the electrolyte such as SEI formation may happen at an accelerated rate in the event of plating [24].

Transition Metal Dissolution

Within layered cathodes such as NMC, transition metal ions contained in the layered structure may be released during aging, referred to as transition metal dissolution. Transition metal dissolution may occur through electrochemical oxidation of oxygen within the layered cathode [49], whilst Nickel at high oxidation states may react when exposed to electrolyte, leading to Ni^{2+} becoming dissolved in the electrolyte and being deposited on the surface of both electrodes [38]. Dissolution of manganese ions is greatly accelerated at high cathode potentials, limiting efforts to increase the energy density of the cathode by extending the operating potential window [50]. It has also been found that the rate of overall transition metal dissolution accelerates dramatically with increased upper cut-off voltage at the cathode, leading to deposition of transition metals on the anode, accelerating SEI layer growth [51]. Side-reactions between the electrolyte and transition metal ions, and consequent deposition of precipitates on the surface of the cathode, may be the cause of CEI layer formation, in a similar

manner to SEI layer formation at the anode surface [52].

Meanwhile, as the electrolyte is typically fluoride containing, acid attack caused by Hydrofluoric acid formed due to residual moisture may also dissolve transition metal ions from the cathode [41]. Loss of cyclable lithium can be accelerated by transition metal deposition on the anode leading to SEI layer decomposition. At the anode, manganese deposition leading to the highest rates of cyclable lithium loss, implying that more modern Nickel rich cathodes may see less detrimental lifetime impacts from transition metal dissolution [53]. Temperature also has a significant impact on the rate of metal dissolution, with a NMC111 cathode loosing 0.9 % of overall transition metal content while stored at 55 °C, degrading the ability of the cathode to store lithium due to structural damage to the cathode structure [54].

Other Mechanisms

The above review of degradation mechanisms is not exhaustive, and many other mechanisms have been shown or are proposed to cause degradation of LIBs. These include but are not limited to Graphite exfoliation, porosity changes, binder decomposition, current collector corrosion and electrolyte decomposition. These mechanisms are summarised in brief here, but are generally out-of-scope within this work.

Graphite exfoliation occurs when layers of graphite are 'exfoliated' or peeled apart. This has been proposed to occur when electrolyte solvent is co-intercalated into the graphite layers, leading to exfoliation and subsequent solvent decomposition. This causes a loss of the ability of the graphite to intercalate lithium and therefore lose capacity [55]. However, addition of stable SEI forming additives has been shown to strongly suppress solvent co-intercalation [55]. Another proposed mechanism is the decomposition of Propylene Carbonate at active sites in the graphite, leading to gas formation, pressure build-up and subsequent exfoliation to the same end result of capacity loss [56]. Gas formation will lead to pressure increasing in a cell and may lead to swelling and in the worst-case cell rupture.

Porosity within a LIB is carefully controlled during design and manufacture to maximise electrolyte wetting of electrodes while maintaining high electrode densities to maintain volumetric energy density. However, SEI layer growth at the anode may block pores, and therefore limit highly ionically conductive pathways into an electrode, increasing path tortuosity. This process may lead to power fade in a cell as deeper areas of the electrode may be blocked to lithiation/delithiation apart from via solid phase diffusion of Li^+ through the electrode [57]. Meanwhile excessive mechanical compression of the polymer separator may lead to deformation and loss of porosity, inhibiting ion transport across the separator [58].

In order to form well coated electrodes that are mechanically stable, a binder is typically required to both stabilise the electrode, provide mechanical strength and adhere the active material to the current collector after slurry coating and drying. The loss of such binders may lead to loss of adherence and mechanical damage to the electrode, and therefore active material loss. Typically, the binder used in LIBs is Polyvinydene Difluoride (PVdF), although many alternatives with increased conductivity have been proposed. PVdF is used due to the high resistance it shows to the electrochemical potentials found in a LIB [59]. It has been shown that in graphite anodes, lithiated anode will react with PVdF to form Lithium Fluoride, contributing to degradation of electrode mechanical properties over time [24]. It has been shown that in LCO-graphite cells that binder degradation was caused by mechanical

cycling of the electrodes induced by cycling, leading to significant (29-42 %) increases in cell internal impedance in coin cell tests [59]. This rise in impedance is caused by the loss of contact between the binder and active material particles, and potentially the current collector. It is also possible that areas of the electrode may fully detach in the event of significant binder decomposition, leading to capacity loss.

Current collector corrosion may occur due to reactions between electrolyte components or at the anode if the anode potential becomes too high vs Li/Li^+. Corrosion of the current collectors may lead to loss of electronic and mechanical contact between electrode particles and the current collector and therefore impedance increase and power fade [24]. Both aluminium and copper forming the current collectors are vulnerable to corrosion. In aluminium pitting corrosion may occur at high potentials whilst overdischarge may lead to cracking in copper. These corrosion mechanisms have been shown to be specific to the conditions seen within batteries i.e. presence of electrochemical potentials and organic electrolytes [60].

The electrolyte within the LIB is critical to continued operation, and usually consists of a mixture of a Lithium salt and aprotic solvent, e.g. $LiPF_6$ and Ethylene Carbonate. However at high temperatures it has been shown that decomposition occurs due to the irreversible reactions that may occur between the salt and solvent above 60 °C [61]. Additionally, the electrolyte is unstable relative to the anode in a carbon anode system, and therefore the electrolyte will decompose on SEI formation, consuming lithium and leading to loss of lithium inventory and therefore cell capacity. These side reactions consuming electrolyte will also lower the ionic conductivity of the electrolyte and lead to sluggish kinetics in the cell, increasing overpotentials and decreasing available power.

2.4.4 Heterogeneities in Degradation

After manufacture, there is naturally a degree of variation between individual cells, due to unavoidable variations in manufacturing, and cells may be graded or 'binned' based on formation tests. However, there will be some variation in key battery parameters such as impedance, capacity and OCV at the beginning on life. Due to the differences seen at the beginning of life, it is expected that cells undergoing aging will deviate from one another. This is a key challenge in prognostic prediction of cell life, leading to issues with cell or device warranty, safety and certification.

Considering start-of-life cells, Rumpf et al. [62] investigated 15 parameters in 1100 commercial LFP cells and identified small differences between using a combination of charge/discharge tests and EIS. The differences in capacity and impedance was found to be small but significant; 0.28 % and 0.72 % respectively. While this is a unique dataset in the literature, it still addressed beginning of life cells, and it is expected that even under identical loading conditions, cells will deviate in parameters over the life of the cell [63]. Harris et al. [64] found that after 600 cycles, the capacities of 24 commercial LCO cells dropped to between 45 % and 85 % of their initial value, a dramatic range of capacity loss. However, these cells were cycled at 10 C, likely exacerbating the deviations seen.

Dubarry et al. [65] investigated the path dependence of EV batteries used in grid operations. 52 NCA-graphite 18650 cells were aged under 20 different aging conditions, under both cycling and calendar aging regimens. Using incremental capacity analysis to assess the degradation modes occurring, it was found that cells exhibited path dependence with differing proportions of loss of lithium inventory and active material depending on aging regimen. The same group also demonstrated significant

path dependence in cells cycled under a range of rates and temperatures, with the aging regime depending significantly on the SOC range during cycling, temperature and rate [66]. On the other hand, considering calendar aging, it has been found that cells aged under a storage conditions ranging from 43-65 °C and 40-95 % SoC did not exhibit statistically significant path dependence. However these tests were limited in duration to 180 days of storage and did not involve combine cell cycling, and it is likely that combined calendar and cycle aging will exhibit be path dependant [67].

2.5 Diagnostics: Identifying Degradation Processes

Identification of the state-of-health of a cell as well as the degradation mechanisms occurring within the cell is challenging, as few if any practical *in-situ* methods for directly measurement of key internal parameters of a cell exist. To the scientist or engineer at the full-cell level, limited information is available or can be measured, where typically only the cell terminal voltage, applied current, cell temperature and time are known. While other measurements such as geometric changes or mass changes might be measured, generally the information available is limited and key parameters such as internal concentrations or electrode potentials cannot be practically measured. Therefore, most diagnosis of cell behaviour during service must be done using *in-situ* methods which do not involve disassembly of the cell but instead infer behaviour from in service measurements, although these may be required to be taken under specific controlled conditions. *Ex-situ* techniques may be used but are principally reserved for end-of-life (post-mortem) analysis, or specific characterisations.

2.5.1 Incremental Capacity Analysis

Incremental capacity analysis (ICA) has been used for over 15 years to probe the degradation modes occurring within LIBs [68]–[72]. Using ICA, it is possible to distinguish different degradation modes occurring within the cell, when half-cell data is available, and thus verify hypothesis about internal cell processes. In order to generate an ICA spectra, constant current charge or discharge data, usually at a relatively low C-rate, is used. The voltage and capacity are differentiated with respect to time and the ratio taken to give $\mathrm{d}Q/\mathrm{d}V$, as shown in Equation 2.27.

$$\frac{\mathrm{d}t}{\mathrm{d}V} \cdot \frac{\mathrm{d}Q}{\mathrm{d}t} = \frac{\mathrm{d}Q}{\mathrm{d}V} \tag{2.27}$$

By plotting $\mathrm{d}Q/\mathrm{d}V$ against capacity or more typically voltage, several characteristic peaks are present, which imply that the voltage is changing slowly relative to the amount of charge passed at that stage. The height of the peak represents the amount of charge that must be passed to cause a given voltage change in the cell. This implies that each peak represents a phase equilibria in one of the electrodes, where only the lithium concentration in the electrode is changing, and the active material is thermodynamically stable i.e. there is a phase equilibria occuring at that point.

As the lithium concentration in the material changes the electrode will become thermodynamically unstable and a phase transition will occur. The new material phase formed will have an altered OCV, and therefore a rapid potential change will occur, which are represented as peaks in the ICA curve. Therefore during charge or discharge multiple peaks will appear, corresponding to phase changes in the cathode and staging in the anode (if graphite is used). Peaks may not be 'sharp' as an electrode will not be homogeneously charged or discharged during operation, due to heterogeneities in internal

current distribution. Therefore, different areas of an electrode will have different SoCs and thus lithium concentrations, leading to increasingly lower peak intensities in the resultant diagnostic spectra. This effect is likely to increase with greater internal heterogeneity in electrode SoH. As an example of how this effect may arise in practice, Finegan et al. [73] used high speed X-ray diffraction to analyse graphite electrodes during high rate charge and discharge. By tracking Lithium concentration, highly heterogeneous temporal and spatial distributions of electrode SoC were identified at rates as low as 2 C. Phase co-existence was observed as the lithiation front progressed deeper into the electrode, highlighting the limitations of ICA at high rate for tracking anode features.

Over the lifetime of a cell the peak intensity and position will change, both in absolute terms and relative to one another. Tracking features of interest may be used to allow identification of internal degradation modes, either through inspection of diagnostic spectra or fitting to a simple cell model. In practice ICA results may be calculated from any set of voltage and current charge or discharge data. However, it is preferable to use low rate data as this will minimise the influence of both internal heterogeneities in the cell as well as overpotentials induced by the cell resistance, which may distort the results. As an example of ICA analysis, Dubarry et al. [74] use a mechanistic model to simulate the effect of differing degrees of degradation modes on the ICA signatures from 0 - 30 % degradation in each mode, shown in Figure2.7. In each case, different changes to the ICA signature are observed with the peaks (labelled 1-5 in Figure 2.7) representing graphite staging phenomena, and each degradation mode presents unique peak translations allowing identification of the dominant mode. In this case the analysis presented was parameterised for an LFP cell but is easily applied to other cathode chemistries.

Analysis of data for calculating the ICA spectra from a test may be challenging, as due to the discrete nature of the experimental test data, smoothing will need to be applied to the data before differentiation. As there is no standardised smoothing or analysis approach, it is often difficult or impossible to compare results in the literature. Typically researchers have applied data smoothing techniques such as moving average filters, Savtisky-Golay filters [75] or Support Vector Regression [76], [77]. However, these techniques rely on researchers selecting adjustable input parameters which may have a dramatic impact on the fitted curves, especially relating to the locations and heights of peaks, meaning overfitting of data is a concern. Feng et al. [78] proposed the Level Evaluation ANalysis (LEAN) method to combat these issues. The LEAN method operates instead by counting and binning results to generate a response curve. .

2.5.2 Differential Voltage Analysis

An alternative method to the ICA technique is Differential Voltage Analysis (DVA), proposed by among others Bloom et al. [79]. In structure the technique is similar to ICA, only the derivative of voltage with respect to capacity is considered as shown in Equation 2.28.

$$\frac{\mathrm{d}V}{\mathrm{d}t} \cdot \frac{\mathrm{d}t}{\mathrm{d}Q} = \frac{\mathrm{d}V}{\mathrm{d}Q} \tag{2.28}$$

Once plotted a $\mathrm{d}V/\mathrm{d}Q$ analysis will lead to similar spectra being plotted for graphical analysis as the ICA technique. However, while peaks in the ICA spectra represent phase equilibria, when using DVA peaks will represent phase transitions, i.e. points at which material changes are occurring in the cell electrodes. As with ICA, use of half-cell information to identify the initial electrode alignment and

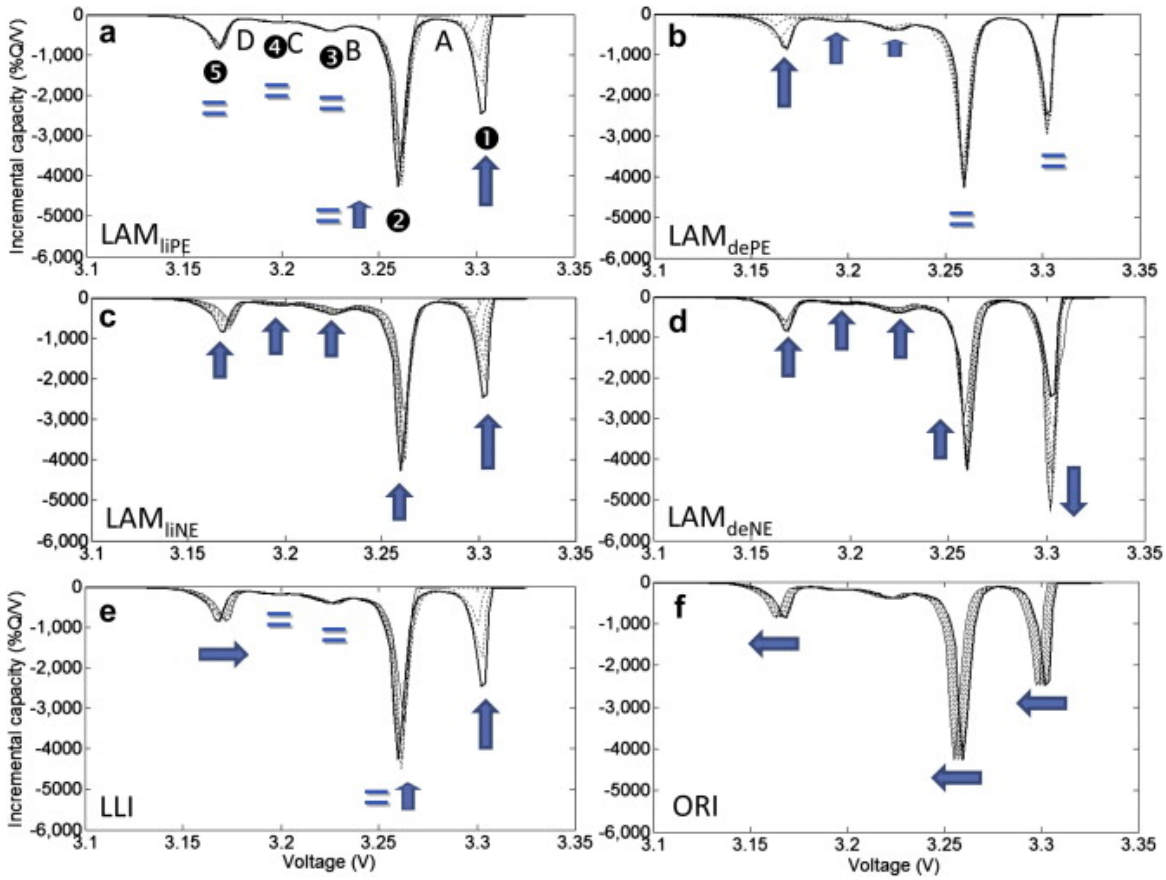


Figure 2.7: ICA signatures from the initial state (thick solid line) and at the end of 30 % degradation (thin solid line) with 5 % increment (dotted lines) for (a-d) each of the four possible variations in loss of active material, (e) loss of lithium inventory, and (f) a 100 % ohmic resistance increase at C/25 [74]. © Reproduced with Permission.

anode excess capacity is required, but once this initial fitting has been carried out it is possible to identify the limiting electrode and degradation modes from independent full cell information [79].

Bloom et al. [80] demonstrated the use of DVA to identify anode degradation modes in NCA-graphite cells, finding that initial capacity loss was caused by anode active material loss, most likely caused by physical damage, while subsequent capacity loss was caused by side reactions between the anode and electrolyte, leading to loss of cyclable lithium. Extending this analysis to NMC-graphite cells, Bloom et al. [81] found that similarly in NCA-graphite cells, it was possible to identify the mode of anode degradation as well as stoichiometric drift between the two electrodes, implying changing anode potentials at the same full cell voltage over the lifetime of a cell, due to the removal of regions of the anode due to side reactions. Taking the same approach, Dahn et al. [82] created a free tool to carry out DVA analysis and predict cell behaviour after degradation while also allowing users to accurately predict anode and cathode voltages without the presence of a reference electrode.

More recently, Ando et al. [83] applied the DVA technique to blended NMC532 and LMO cathode cells, and successfully used DVA to diagnose different degradation modes occurring in cells with the same apparent capacity loss under different aging conditions. By cycling 18 cells at 3 different temperatures under 2 DoD ranges, they were able to show that while the capacity retention was almost identical in both circumstances, in the case of full DoD range cycling cathode degradation became significant, whereas at the same number of full equivalent cycles at 30 % DoD no cathode degradation

was identified at any of the temperatures identified, demonstrating the value of DVA as a tool to diagnose aging modes in cells with nominally similar capacity losses. DVA has also been shown to be effective in diagnosis of lithium plating, and able to identify reversibility in lithium stripping from the anode via identification of voltage plateaus [84]. In terms of data analysis similar challenges to those present during ICA (Discussed in Section 2.5.1) relating to initial alignment of half-cell curves as well as data smoothing and fitting remain. While both ICA and DVA analysis have great potential as a quantitative tools to diagnose cell degradation, in much of the published literature, analysis of these diagnostics is primarily qualitative, and most available fitting tools are limited to qualitative simulation of degradation rather than quantitative fitting [70], [82].

2.5.3 Open Circuit Voltage Analysis

A final type of diagnostic approach uses the cell OCV to identify individual electrode parameters, and therefore quantify degradation. At beginning of life, a LIB will have specific electrode capacities and stoichiometry. Combined with the individual electrode OCV curves gives rise to the full cell OCV, by Equation 2.29.

$$E_{Cell}^{OC} = E_{Cathode}^{OC} - E_{Anode}^{OC} \tag{2.29}$$

The specific half cell voltages, $E_{Cathode}^{OC}$ and E_{Anode}^{OC} are a function of the thermodynamic properties of each electrode. Over the full cell voltage window, the cell OCV is therefore a function of the maximum and minimum lithiation states of each half cell, which combined give the full cell OCV response. During degradation, as the capacity and alignment of each electrode changes, the cell OCV response will change. By fitting an OCV model at to measurements during cell life, it is possible to infer the degradation modes occurring within a LIB. Whilst physical OCV models existed previously [74], [85], [86], the approach of fitting a parametric OCV model and using this class of model to identify degradation modes was pioneered by Birkl et al. [87], with further work providing the first direct experimental validation of an OCV model [25]. Based on additive terms, each representing phase transitions in the electrodes, it is possible to fit this model to OCV data of both half and full cells [87]. If the half cell voltage curve is fitted at beginning of life, it is subsequently possible to use the model to fit to aged cell OCV data, and by reparameterising the model identify degradation modes occurring within the cell based on the OCV response [25].

Figure 2.8 a-f shows validation results from Birkl et al. [25], who used synthetically generated full cell OCV curves to validate the model fitting approach. As shown, the parametric OCV model is capable of identifying accurately degradation for all identifiable modes. It is important to note that whilst loss of both lithiated and delithiated electrode material is possible, it is not possible to distinguish between loss of lithiated active material, and loss of delithiated active material combined with pure loss of Lithium inventory based solely on full cell measurements. Further validation of the OCV diagnostic model using half cells with a known amount of removed active material or mismatched electrode SoCs demonstrates that when fitting to experimental data the model is able to identify the dominant degradation mode in all cases, with typical relative errors of <20 %. It is noted however that identification of anode degradation is in general more challenging, due to the generally flat nature of the graphite OCV curve. This means that in general the identification of $\mathrm{LAM_{NE}}$ is less accurate than identification of $\mathrm{LAM_{PE}}$ and LLI using this class of model.

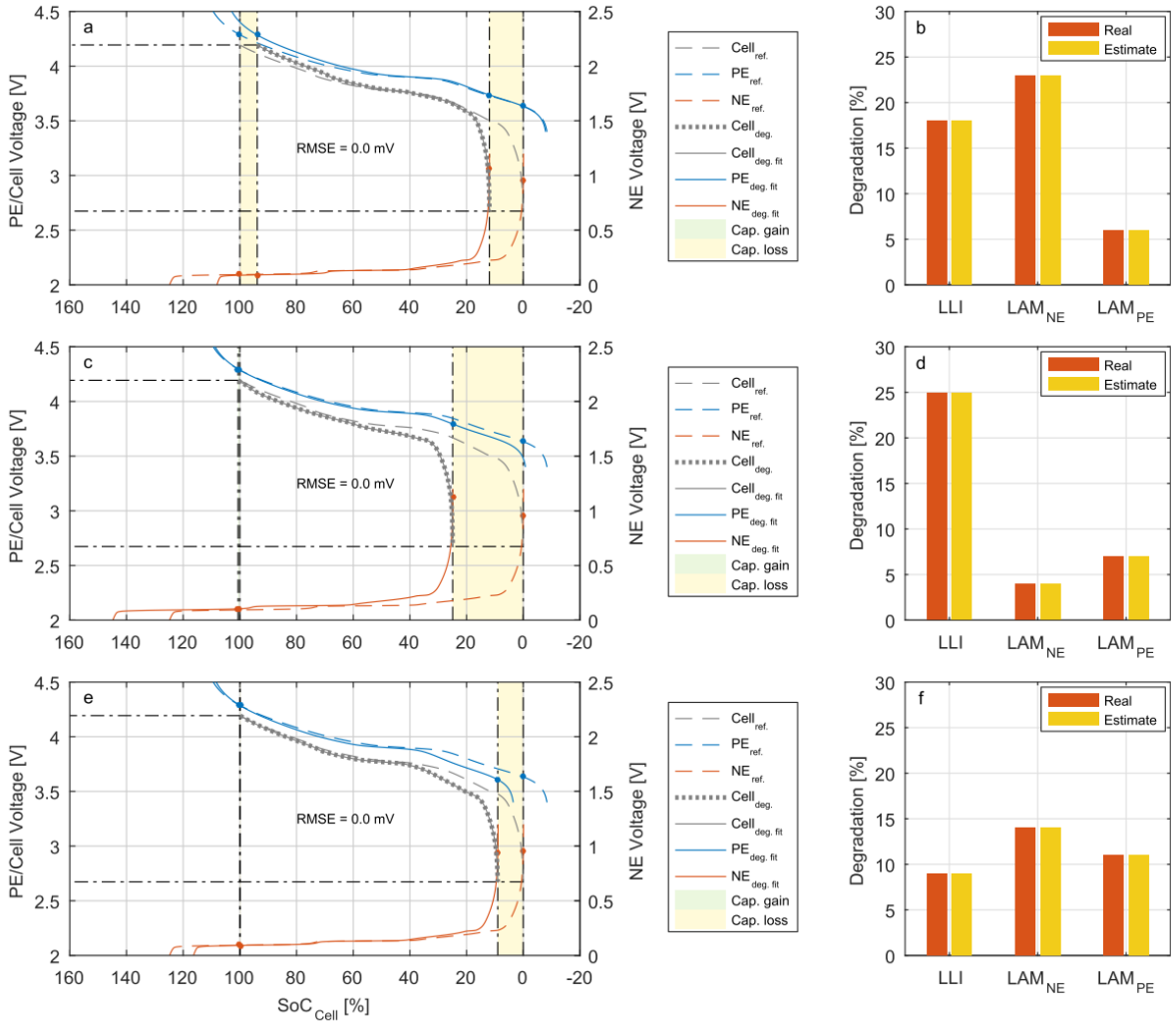


Figure 2.8: Estimation of known amounts of LLI, LAM_{NE} and LAM_{PE}. a) and b) Scenario I: 12 % (pure) LLI, 23 % $LAM_{NE,De}$, 6 % $LAM_{PE,Li}$. c) and d) Scenario II: 21 % (pure) LLI, 4 % $LAM_{NE,Li}$, 7 % $LAM_{PE,De}$. e) and f) Scenario III: 9 % (pure) LLI, 14 % $LAM_{NE,De}$, 11 % $LAM_{PE,De}$. [25]. CC-BY 4.0

This model has the advantages of a simple parameterisation process, high model accuracy and simple experimental measurements and analysis (once half cell voltage curves are known). As such parametric OCV models have been applied as benchmarks for new diagnostic techniques [88] whilst significant work has focused on accelerating [89] or reducing [90] computational overheads. Further details of OCV model diagnostics can be found in Section 4.4.

2.5.4 Electrochemical Impedance Spectroscopy

Electrochemical impedance spectroscopy (EIS) has already been discussed as a general electrochemical measurement technique in Section 2.3.2, however in this section the specific application of EIS to diagnosing LIB degradation mechanisms will be evaluated. 3 keys challenges have been identified as limiting adoption of EIS as a commercial degradation diagnostic tool; Separation of electrode impedance responses, design of suitable equivalent circuits and development of low cost methods and equipment to allow widespread application of EIS in-service [91].

However, the battery research community commonly uses EIS as a diagnosis tool, in applications ranging from during materials development to analysis of commercial cells cycled under service conditions.

Using EIS to assess the relative contributions of the electrodes to power and capacity fade, Zhang and Wang [92] used cells instrumented with Lithium metal reference electrodes to assess the relative contributions during degradation. It was found that the resistance increase, in this case, was dominated by growth of R_{CEI} for NCA cells, with less significant increases in anode resistances. However the effect of cycling temperature on overall impedance growth was not assessed. Analysis by Zhu et al. [93] has indicated that for NMC cathodes, the total charge transfer resistance is dominated by the cathode R_{CT} as opposed to R_{SEI}, which is also shown to increase significantly faster than the anode R_{CT}, with increases inversely proportional to temperature. This indicates that power fade in NMC-cathode cells is dominated by growth in R_{CT}, especially at lower temperatures. Pastor-Fernandez et al. [94] carried out a comparison of the use of EIS and DVA to identify degradation modes. EIS was used to track LLI based on the change in R_{CT} and R_{SEI}, assuming that changes to high frequency impedance is principally caused by SEI formation leading to consequent increased R_{CT}. LAM was tracked using changes to $R_{Warburg}$, which is a function of the effective diffusion path length. Tracking of LAM assumed that diffusion processes are related to morphological changes in the electrodes, and therefore an increase in $R_{Warburg}$ implies LAM has occured. Tracking of LLI and LAM via ICA analysis was achieved using techniques proposed by Dubarry et al. [74]. Overall it was found that both techniques were complementary in identification of LLI and LAM processes, and predictions were shown to be correlated at a 95 % confidence level. As an example of potential applications of EIS to diagnosis of cell SOH, Zhang et al. [95] used Gaussian process machine learning to process over 20,000 EIS spectra from commercial LIBs at a wide range of SOH, temperature and SOC values. They found that using a black-box model it was possible to accurately predict remaining useful life of cells, with potential applications in battery management systems.

2.5.5 Other *In-situ* Diagnostic Techniques

Many other diagnostic techniques have been proposed and tested and are at various stages of development for *in-situ* applications and are discussed here. Differential Thermal Voltammetry (DTV) has been proposed as an alternative, low cost method for diagnosis of aging mechanisms within LIBs. The technique involves assessing the differential temperature-differential voltage ($\mathrm{d}T/\mathrm{d}V$) spectra of a cell. It has been shown that DTV is able to identify aged cells within while retaining the low-cost approach, requiring only a single temperature measurement per cell which is often already available in many systems. Functionally DTV uses changes in entropic heat generation during phase transition to identify the voltage of phase transitions within electrodes during galvanostatic charge/discharge, and can therefore be applied in a similar way to ICA/DVA [96]–[98].

High Precision Coulometry (HPC) has been proposed, principally by the Dahn group at Dalhousie University, as an alternative approach to diagnosis, using high-precision charging equipment to accurately measure coulombic efficiency of cells, a task which many commercial battery cyclers are unable to achieve to a high degree of accuracy due to insufficiently precise coulomb counting [99]. Stevens et al. [100] used the HPC method to show that the failure modes in 2 different pouch cells would be different due to changes in cathode chemistry, while the degradation modes occurring can be inferred using HPC measurements and careful analysis of differential voltage. It has also been shown that lithium plating is effectively detected by measuring the CE of the cell, where an onset of decreasing coulombic efficiency implies plating is occurring in the cell [101]. HPC has also shown promise in assisting the development of improved formation procedures, which have previously been identified as

a key production bottleneck for LIBs [102].

2.5.6 *Ex-situ* and Post-Mortem Diagnosis

While *in-situ* diagnostic techniques are commonly used, *ex-situ* diagnosis of mechanisms and modes of degradation are key for development and validation of cell level diagnostics. This may be carried out either during life, or as a pre- or post-mortem to either identify cell parameters or validate diagnostic models. The simplest post-mortem technique available to the battery community is a cell teardown, where some limited evidence of different degradation modes may be found, for example in the case of plating where characteristic deposits on the anode caused by plating may occur [84].

Coin cell measurements are used to assess the performance of half cells, i.e. anode and cathode materials cycled against a Lithium metal reference electrode. This allows the validation of models and the data is often a pre-requisite for use of full cell diagnostics, for example ICA measurements, where half-cell data is required to model full cell degradation modes [68]. For example, Howey et al. [25] used harvested electrodes of different areas to mimic the loss of active material from cells, and validate an OCV-based ICA model for cell degradation.

During pre- and post-mortem analysis, 2-D and 3-D imaging may be used to achieve a range of goals. Identification of key parameters such as particle size and porosity may be achieved using 2-D imaging techniques such as Scanning Electron Microscopy (SEM), while parameters such as electrode tortuosity may be identified using 3-D imaging techniques such as X-Ray Computed Tomography (XCT) measurements. Applications of post-mortem techniques are limited to research and development applications due to time taken and cost, however the information provided may be impossible to otherwise obtain. For example, Carter et al. [103] used multi-length scale XCT measurements to identify mechanisms within cells ranging from nano-scale features of the cell such as the SEI or dendritic deposition, to macro, cell scale effects such as copper dissolution and subsequent current collector damage. While not discussed in detail here, at the materials scale many other chemical analysis techniques may be applied and used to inform understanding of battery materials during degradation, and diagnose mechanisms leading to loss of performance.

2.5.7 Diagnostics Overview

Considering the diagnostics reviewed in this section, a critical analysis of the current state-of-the-art is required. Recent reviews [7], [104]–[106] have identified a wide range of challenges that remain in the analysis and application of cell level diagnostics. Challenges remain in BMS implementation, remaining useful life (RUL) prediction and suitability of diagnostics for onboard implementation at reasonable cost. In particular Lipu et al. [104] highlight the need for improved certainty and increased robustness in on-board RUL and SOH estimation to improve safety, increase reliability and improve warranty conditions for automotive batteries. Barai et al. [7] highlight that differential diagnostic techniques are highly advantageous, as they provide comparable information to post-mortem disassembly for identification of degradation modes within cells, and allow qualitative analysis of cell degradation, and over the past decade these techniques have become essential to aging studies. While challenges remain in accurate automation of such methods, their many advantages, such as low computational cost, simple onboard implementation with minimal extra sensing or complex protocols alongside their relatively simple nature ensures their continuing development and relevance.

In this section several of the most common and promising *in-situ* diagnostic tools for use when studying LIB degradation has been carried out. Tools such as OCV, ICA and DVA diagnostics are becoming more commonly used in research and are promising for the quantitative assessment of degradation modes occurring within cells. However, challenges remain with quantitative assessment of the contribution of different degradation modes to overall cell degradation, with these tools often used in a more qualitative manner. Therefore, developing robust fitting tools to quantitatively identify degradation modes is identified as a significant research challenge. Other tools such as DTV or HPC are promising, however more development of these tools is required before widespread adoption is possible. Using EIS as a diagnostic tool for identification of degradation processes, particularly in power fade, has been shown to be effective. However, in order to accurately assess the contribution of different electrodes to overall degradation, instrumented cells are required, which is challenging to accomplish. Nevertheless, when combined with other diagnostic tools such as OCV models, EIS is an effective tool for providing insights into degradation processes occurring within a LIB.

2.6 Modelling Lithium Ion Batteries

Modelling of LIBs is a complex topic, and this review focusses primarily on systems level modelling techniques i.e. equivalent circuit network (ECN) models. Broadly, cell, pack and degradation models are considered separately.

2.6.1 Cell Modelling

P2D models are generally derived from the work of Doyle, Fuller and Newman [107] who used porous electrode and concentrated solution theories. This class of modelling produces a comprehensive and versatile simulation framework which allows simulation and prediction of cell behaviour over a wide range of operating conditions and allows for physical insights into internal cell processes to be assessed. On the other hand, the computational requirements are high and detailed parameterisation experiments are needed, requiring access to specialist and costly equipment. While the computational requirements can be significantly reduced by reducing model order, many physical parameters describing the physical structure of the LIB are required, such as chemical compositions, material conductivities and diffusion coefficients for all electrochemically active elements. Parameterisation of P2D models is therefore highly time and cost intensive, and requires extremely specialist equipment and knowledge [108]. This class of model is typically constructed of a set of partial differential equations grounded in fundamental physical chemistry. Simulated length scales may vary from atomistic to full cell domains, with multiple length scales able to provide inputs across scales. Typically charge and mass conservation in the solid and electrolyte are modelled alongside lithium flux between the solid and liquid phase [107], [109]. One approach to simplification of the P2D model is to simplify each electrode domain into a single spherical particle (the so-called Single Particle Model (SPM)). By assuming that radial diffusion is the slowest occurring process, and therefore neglecting other elements of diffusion, it is possible to reduce the computational cost of the model [110], [111]. However, SPM models neglect Li-ion distribution in the electrolyte, limiting applicability to low rates. Consequently, application of SPM models to scenarios such as BEV fast charging may be limited, although enhanced SPM models have been proposed which account for concentration gradients [112], [113]. As a consequence, for both on-board and pack modelling applications, P2D modes are prohibitively complex and computationally intensive and the remainder of this review focusses on equivalent circuit modelling

which is more applicable in this work.

As an alternative to P2D models, ECN models are widely used in the engineering community for battery modelling due to their simplicity, ease of parameterisation and low computational cost. An ECN consists of a network of resistors, capacitors and voltage sources, parameterised to empirically replicate the behaviour of a battery. Unlike when fitting EIS data, the equivalent circuit elements are generally only indirectly linked to physical cell processes, although authors such as Merla et al. [114] have developed 'physics-informed' ECN models, applying principles from P2D modelling to ECN models. This has the potential advantage of retaining the simple parameterisation methodology of ECN models while allowing inferences to be made about internal physical processes. While making predictions outside of the parameterisation data is rarely possible, within the scope of the training data ECNs are typically robust. Parameterisation can be achieved simply using standard techniques, most commonly PC or PD methods (although EIS measurements may also be used). During parameterisation lookup tables of individual circuit element parameters with respect to temperature and LIB SoC are obtained. Simulations are possible using the ECN model, commonly in graphical programming environments such as MATLAB/Simulink or Dymola.

For onboard implementation Plett et al. [115]–[117] introduced a non-linear enhanced self-correcting model to adaptively estimate LIB SoC using extended Kalman filtering (EKFs), considering current direction, OCV hysteresis and voltage relaxation behaviour alongside temperature and ohmic losses to improve predictions during dynamic load cycles. By applying it is possible to estimate accurately SoC and other model states, providing a dynamic estimate of the state of available power from a cell [117]. Using EKFs it is possible to simultaneously estimate both model states and parameters, with obvious advantages for on-board BMS applications. Excepting the EKF fitting approach, parameterisation of ECN models is assessed in more detail in Chapter 4.

Considering the types of ECN available for use, Nejad et al. [118] systematically reviewed 10 common variant ECN modelling frameworks, including the Plett model, Randles model, adapted Randles model and n-RC models (n = 1, 2) with and without hysteresis. Each model was assessed to find their relative accuracy, comparing the implementation of each model to the same set of parameterisation data. Parameters and states were estimated using a dual-EKF framework. It was found that after testing against a NEDC drive cycle, n-RC pair models were optimal, with 2RC pair models most accurate, with an overall error in voltage prediction of < 2.5 mV over a temperature range of 5-45 °C.

Applications of ECN models are wide-ranging, and apart from use in on-board applications their simple parameterisation and solving lends ECNs to investigation of phenomena such as internal cell thermal gradients under different thermal management regimes. For example, Zhao et al. [119] used a discretised 3-RC pair ECN model to predict internal SoC, temperature and current distributions. Using the distributed model, it was found tab cooling led to improved cell performance while reducing heterogeneities in internal current and temperature distributions.

2.6.2 Degradation Modelling

Degradation modelling within LIBs may be considered a related but separate topic to cell response modelling, as degradation models operate somewhat independently to a cell model, usually by updating a subset of parameters. A distinction may also be made between physics-based degradation models and empirical or semi-empirical models as detailed below:

- **Empirical Models:** This class of models rely on large datasets to parameterise degradation. Typically, a range of stress factors are identified and cell-level experiments are carried out to identify empirical relationships between stress factors.
- **Semi-Empirical Models:** Semi-empirical degradation models bridge the gap between empirical and physics-based degradation modes, using physics-informed relationships, with stress factors fitted to experimental data.
- **Physics-Based Models:** Physics-based degradation models are built using fundamental physics to predict the rate of degradation processes rather than empirical relationships.

Physics based degradation models are considered out-of-scope for this work, due to their difficulties in parameterisation. Therefore, the remainder of this review is focussed on empirical and semi-empirical models, which are generally used in combination with ECN models to simulate high cycle numbers for cells. Typically, these models are parameterised for a specific use-case with dedicated parameterisation data, requiring large experimental campaigns to validate which is both time and cost intensive. As an example, Cordoba-Arenas et al. [120] derived an empirical model for degradation in HEVs, considering SoC range, current and temperature as stress factors, predicting both power- and capacity fade proportions over lifetime. Meanwhile, Wang et al. [121] concluded that for LFP cells, SoC range did not significantly influence degradation at low C-rates, simply focussing on time (equivalent to charge passed during cycle aging) and temperature as aging stress factors, highlighting the application-specific nature of empirical aging models. Several authors have noted that capacity loss in general tends to follow an empirical relationship with the square root of charge throughput, [120], [121]. This has been attributed to the relationship of capacity fade to irreversible capacity loss through SEI layer growth, consuming cyclable lithium, as SEI layer growth is typically a diffusion-controlled process [122]. An example of a semi-empirical model is presented by Schimpe et al. [123], who aimed to disassociate aging stress factors into multiple, physically justified mechanisms over different temperature ranges. In this case, cycle aging rates are split into high- and low-temperature stress factors, as well as cycling at high SoC values. Using this approach, it was possible to quantify aging due to low temperature capacity loss cause by possible plating and high temperature aging likely caused by SEI layer growth independently, and aging stress factors were parameterised against temperature.

2.7 Conclusion

In this chapter the theory underlying LIB operation, characterisation and degradation has been reviewed, providing the essential context for the subsequent targeted literature review found in Chapter 3, and the underpinning understanding for the work presented in Chapters 4-6. Additionally, common diagnostic techniques applied to LIBs have been reviewed, identifying ICA/DVA as the most well-developed and promising techniques for bulk identification of internal degradation modes within cells, although challenges remain with quantitative identification of degradation modes as opposed to qualitative assessment. Therefore, in future work, these methods are identified as ideal for analysis of long-term cell and pack cycling data. Considering cell level modelling, ECN models are identified as the optimum choice for pack-level modelling, given their ease of parameterisation, low complexity and low computational costs.

Chapter 3

Literature Review

3.1 Introduction

In this chapter, specific literature relevant to this work is presented and reviewed, aiming to cover the state-of-the-art in thermal management of LIB packs and the effects of heterogeneities on both the instantaneous performance and lifetime of LIB packs. In particular, the effects of thermal gradients and the links between thermal management and heterogeneous performance and aging are explored in detail. The overall aims of this literature review were to answer the following:

- What mean temperatures and magnitude of thermal gradients are commonly found in battery packs during normal operation?
- What effects do heterogeneous temperatures have on pack-level performance and aging?
- What effects to heterogeneous resistances have on pack level performance and aging?
- What effect does pack topology have on overall performance?

3.2 Pack Design and Thermal Management

3.2.1 Pack Design Overview: Topologies and Battery Management

In order to meet the demanding weight, volume and performance requirements for electrification of vehicles, large battery packs are required, as single cells typically have relatively small capacities (<100 Ah) with a low nominal voltage (typically circa 3.8 V). Therefore, large battery packs consisting of up to hundreds of cells are needed to meet the application demands, Parallelisation of cells increases capacity while serial connections increase the pack voltage, reducing losses and allowing common electrical voltages to be used. Increasing the pack voltage is noted as important, as it allows the use of lower cross-sectional area cables, which is an important practical consideration, while also allowing the use of off-the-shelf electrical components designed to operate in the 200-450 V range. EV packs typically operate at approximately 380 V nominal, leading to approximately 96 cells being connected in series. As an example of a modern EV architecture, the Tesla Model S contains an 85 kWh pack in a 96S74P configuration for a total of 7104 individual 3.4 Ah cylindrical cells used. A pack is usually divided into distinct, interchangeable modules, in this case 16 6S74P configuration modules, for simplification of manufacturing, assembly and maintenance of the pack

Another key component of the battery pack is the battery management system (BMS), which has dramatically increased in complexity and processing power in recent years. Although detailed consideration of the BMS is out-of-scope for this work, some assessment of the role of the BMS is included for completeness. The role of the BMS is to both control the pack while delivering demanded power to the drivetrain or charging while maintaining safe operation of the pack. In order to achieve these goals, the BMS will typically monitor pack, module and in some cases cell voltages as well as pack currents and strategically selected temperatures. Using this sensor information, the BMS will be able to intervene during operation, for example by derating the pack to ensure temperatures are maintained within set, safe limits. The BMS may also contain onboard battery models which allow the BMS to predict variables such as SoC and State of Health (Power) (SoH_P) during operation, as in-service estimation of the true SoC or SoH_P of a battery is non-trivial without access to costly high accuracy test equipment.

3.2.2 Thermal Management Strategies

Considering issues of thermal management within LIBs, in 2019 Wu et al. [124] identified at least 15 reviews focussing on thermal management issues within LIBs, dating back to 2004. However, despite significant attention from researchers, significant issues in thermal management is still identified as a critical issue within electrification, especially within the high performance and large packs required by EVs. As shown in Figure 3.1, multiple strategies for cooling cells are available to designers, with the surface of the cell through which heat is rejected being a basic consideration. The choice of cooling methodology is also important, with selection of appropriate cooling systems being critical to adequate performance while minimising costs [125]. A schematic of available strategies, highlighting advantages and disadvantages is shown in Figure 3.1. One issue identified by Hales et al. [126] is the lack of standardised metrics for thermal performance of LIBs, leading to cell manufacturers optimising for cell specific energy density at the cost of thermal performance, which leads to on-paper high performance cells being sub-optimal for use in real systems, and so the Cell Cooling Coefficient (CCC) metric is proposed to standardise measurement of heat rejection rate through different cell surfaces.

To the pack designer, 3 broad classes of thermal management system (TMS) are available; air cooling, liquid cooling or phase change cooling. Air cooling may be either natural or forced air cooling, where air is used as a medium to reject heat to the environment from the cell. Liquid cooling systems typically pass a liquid past the cell, and heat is then rejected via a radiator to the environment. Liquid cooling systems may be direct contact (cell immersed in liquid) or indirect contact (liquid passed through a cold plate or cooling via a heat pipe), with many variations of both strategies. Phase change systems utilise the latent heat of the cooling material during melting, typically enclosing the cell in a block of material which maintains a desired temperature during melting [124]. Specifically considering TMS for EVs, Kim et al. [127] identified a range of thermal management options as shown in Figure 3.2.

Considering air-based thermal management systems, significant optimisation has been carried out on forced air systems, investigating the effects of cell arrangement, flow rate and flow paths on thermal management performance, as summarised by Wu et al. [124]. For example, Tong et al. [128] carried out a parametric study of forced air cooling of cylindrical LIBs, considering the effects of flow rate, cell layout and airflow reversal. Without mitigation it was found that the peak temperature rise was 11 °C, with a maximum thermal gradient of 5 °C, although it is noted that this study did not consider

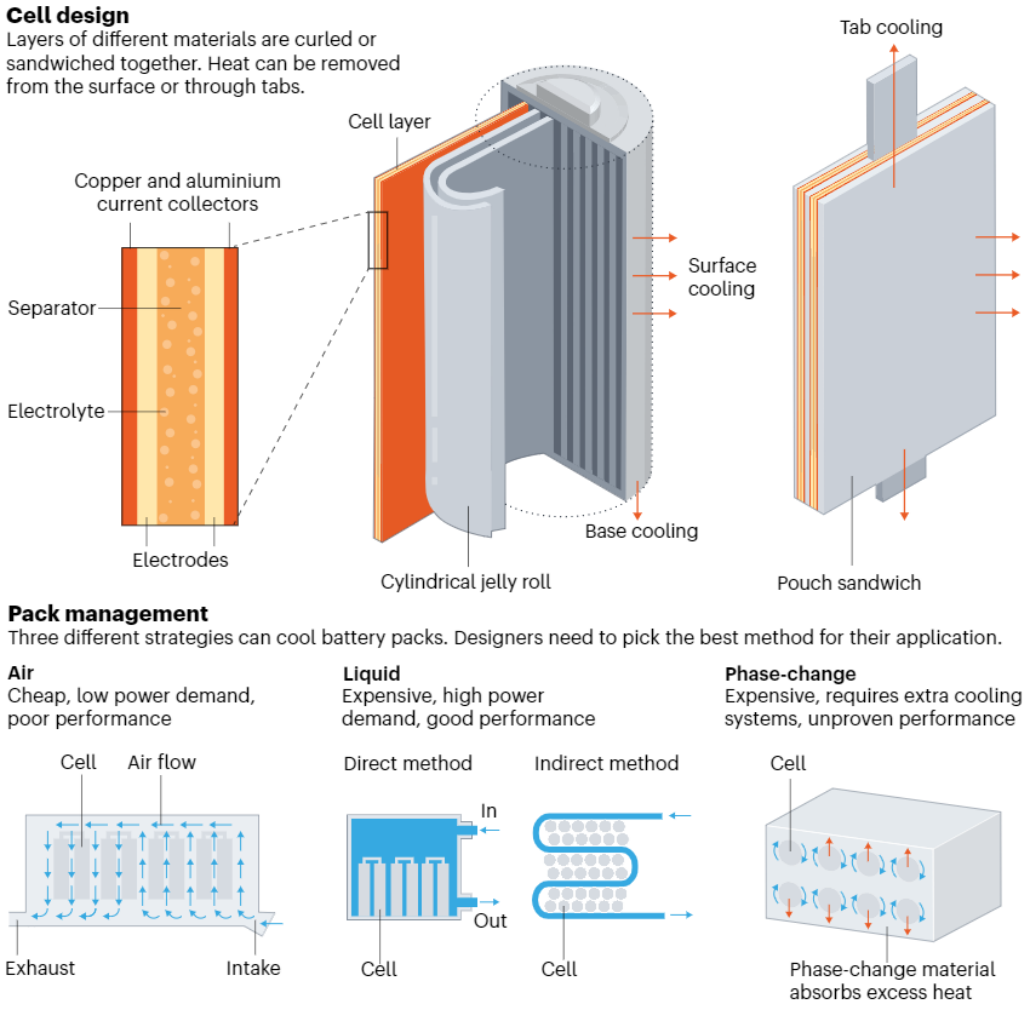


Figure 3.1: Examples of cell and pack thermal management strategies, highlighting positives and negatives in each case [125]. © Reproduced with Permission

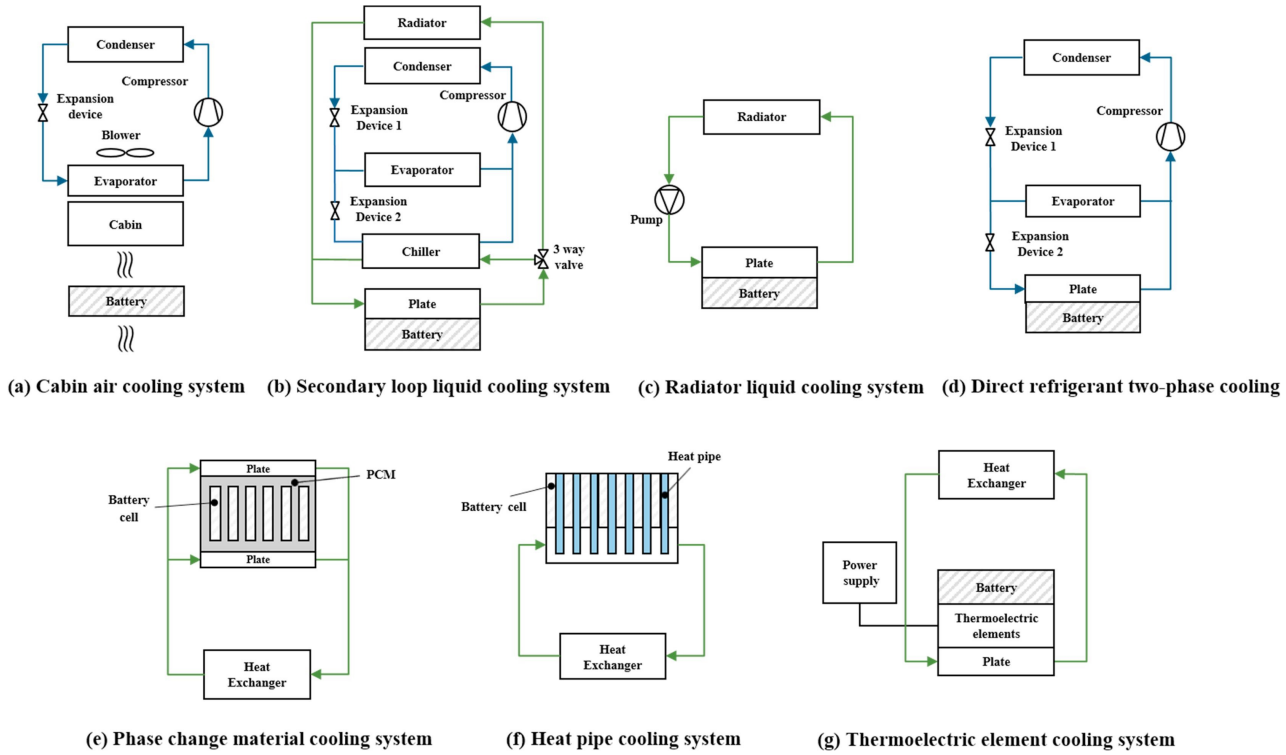


Figure 3.2: Schematics of various EV battery cooling strategies [127]. © Reproduced with Permission

the effects of rate, with a moderate rate of 1 C simulated. Additionally, only a single charge/discharge cycle was simulated, and therefore it is possible that the equilibrium peak temperature/thermal gradient would be greater in continuous use, for example in a HEV application. It was found that thermal gradients may be reduced by also increasing flow rate, staggering columns of cells or periodically reversing the air flow (effectively periodically moving to a counter-flow heat exchange arrangement). In an optimal configuration the latter strategy was able to effectively halve the simulated thermal gradient. This effect highlights the need to carefully consider interactions between thermal management and electrical topology during design of packs.

In comparison, liquid cooling systems offer higher cooling powers and overall performance when compared to air cooling systems, however at increased costs and weights. In particular, liquids typically have a significantly higher specific heat capacity when compared to gaseous coolants, leading to increased cooling performance. Within a liquid cooling system, the overall arrangement of the system, the selected fluid, thermal contacts and ambient temperature are all considerations effecting performance, among many others. With sufficient optimisation, liquid cooling systems have been found to be effective in high performance applications such as EVs, and as of 2020 are commonly found in mass-market EVs such as the Tesla Model 3 and General Motors Volt [124]. Despite potentially improved performance when compared to air-cooling systems, recent numerical simulations of a 144 cell pack, using large format pouch cells, by Chung et al. [129] under a range of realistic liquid cooling schemes, predicted mean temperature rises of 12.5-20.5 °C, with induced thermal gradients of between 9.5 and 13.0 °C, depending on thermal management strategy during a simulated 2 C fast charge. However, through optimisation of the cooling strategy it was possible to reduce this thermal gradient to 4.5 °C.

Meanwhile Rao et al .[130] simulated the effects of indirect liquid cooling using conformal aluminium contact plates combined with cylindrical cells. Thermal gradients of between 3.4 and 7.2 °C were

identified and are found to be highly dependent on the thermal mass of the contact plate and coolant flow rate. However, this study simulated a small, 6 cell pack, highlighting the likely large thermal gradients that may occur within large multi-cell modules or packs. Xia et al. [131], conducting a review of TMS strategies, highlighted the inconsistency of performance between different TMS configurations, which may result in significantly different boundary conditions and therefore performance. The topology of the thermal management system at the module level is also identified as a key consideration, although the interaction between electrical and thermal management topology is less well studied. Despite some limitations, liquid cooling systems have become industry standard for EVs, due to their high cooling powers, compactness and the relatively homogeneous temperature distributions achievable with optimisation. However, it is in general difficult to generalise the magnitude of thermal gradients in packs, as thermal boundary conditions, control strategies and operating conditions are highly variable.

Other cooling methodologies have been proposed. In particular phase change material (PCM) cooling has attracted significant attention in recent years, where the latent heat of a material melting at approximately the desired operating temperature is used to maintain a cell at that operating temperature. The PCM material is then able to absorb or release energy as it is melted or freezes during operation. Typical materials are paraffin waxes, although a wide variety of materials have been investigated for use. While PCMs may be effective in cooling battery systems, several challenges remain. While, as passive systems, PCM thermal management is reliable, many proposed materials exhibit low thermal conductivities and significant work has aimed at improving this property using additives, fillers or fins. Additionally while a PCM may provide adequate cooling, there is an effective limit on cooling imposed by the amount of PCM present, as once the phase transition is complete there is limited remaining ability to remove heat [124], [127]. However, due to the increased mass of PCM systems compared to liquid or air cooling systems, they considered out-of-scope for this work.

3.2.3 The Effects of Thermal Management on Performance and Lifetime

Due to the layered nature of an LIBs internal structure, heat rejection rates will be significantly different depending on the surface through which heat is rejected, with in-plane (of cell layers) heat transfer coefficients typically being significantly higher than those seen through-plane. For example the thermal conductivity of the current collectors are found to be 398 and 238 $Wm^{-1}K^{-1}$ for the aluminium and copper current collectors. This compares unfavourably to 1.58 and 1.04 $Wm^{-1}K^{-1}$ for anode and cathode of a NMC-graphite cell [119], [132], [133]. It should be noted that these values are sensitive to the exact chemistry used and actual hear transfer will be influenced by cell internal geometry. In a comprehensive review of in- and through-plane conductivity, Wei et al. [134] performed computational fluid dynamic simulations of both cylindrical and prismatic cells with a range of cathode chemistries under convective cooling. The results are summarised in Table 3.1 for k_x/k_a (in-plane) and k_z/k_r (through-plane). In all cases in-plane thermal conductivity ranges from 10-50 times greater than through-plane, highlighting the potential for through-plane thermal gradients to form within LIBs, especially at high rates.

Due to this order of magnitude difference in thermal conductivity, researchers have found this difference in thermal conductivity will allow significant thermal gradients to build up within cells. Zhao et al. [119] compared the effects of tab and surface cooling (i.e. heat rejection via cell tabs which are connected directly to the plane of cell electrodes, versus heat rejection through the major cell

Table 3.1: Thermal conductivity bounds for different types of Lithium Ion Batteries. Adapted from [134]

Cathode Chemistry	**k_x,y, k_a [$Wm^{-1}K^{-1}$]**	**k_z, k_r [$Wm^{-1}K^{-1}$]**
$LiFePO_4$	10.09-45.06	0.66-1.04
$LiCoO_2$	10.30-45.65	0.75-1.47
$LiMn_2O_4$	10.09-45.06	0.66-1.04
$LiNi_{0.33}Mn_{0.33}Co_{0.33}O_2$	10.37-45.83	0.77-1.55

surfaces which occurs principally through-plane). Using a distributed 3-RC pair ECN model, it was shown that the surface cooled case showed significantly increased internal heterogeneity, indicating that thermal management design choices have a significant impact on cell performance. Under a tab cooling regimen, for tabs held at 20 °C, a 1.8 °C internal thermal gradient was predicted, compared to a 9 °C increase for a surface cooling scenario with the same boundary temperature. It is noted that the heat flux and cooling power will not be the same in both cases due to the different heat transfer coefficients and contact areas modelled. Li et al. [135] examined the temporal and spatial distribution of temperatures within large-format pouch cells by embedding thermocouples within the cell, and compared the temperature rise to the cell surface temperature. During a 1.5 C discharge, in-plane thermal gradients of up to 12.5 °C were found, with minimal differences in internal and surface cell temperatures. Therefore, the degree of in-plane thermal gradient induced even under moderate discharge conditions is highlighted, which has significantly implications for heterogeneous degradation of large-format cells through thermally accelerated degradation mechanisms. While the differences in surface and internal temperature was found to remain below 1.1 °C for a 7 mm thick pouch cell, the likelihood of large internal thermal gradients in cylindrical or prismatic cells is highlighted. Modelling of large-format cells by Kim et al. [136] predicted temperature rises under convective cooling of 3.0 and 17.5 °C at 1 and 5 C charge respectively, with corresponding thermal gradients of 1.5 and 11.5 °C respectively. The maximum temperature rise was found to be concentrated close to the tabs of the cell, due to the increased Joule heating induced by local current concentrations. Considering thermal gradients within cylindrical cells, Forgez et al. [137] used embedded thermocouples within 26650 LFP cells and measured thermal gradients of 10 °C under a 20 A cycling pulse load, highlighting the significant radial thermal gradients which may occur within cylindrical cells under demanding loading conditions. While not considering the effects of tab design on temperature, Zhao et al. [138] found that increasing the number of tabs in a spirally wound electrode from 2 to 4 increased the energy density of a cell from 52 to 89 % of that predicted by coin cell measurements for the electrode. Significant differences were noted between co-located and counter-located tabs (at the same side vs opposite sides) of the cell stack, which has strong parallels to the effects of parallel string topology on performance, which is explored in further detail in 3.3.2.

Considering the effects of thermal management strategy on cell lifetime, Hunt et al. [133] compared cells cycled using a 6 C discharge and 2 C charge under both tab and surface cooling, where thermal boundaries were controlled using Peltier elements, with a control test of a convective cooling strategy. It was found that while reference performance tests (capacity at C/20) exhibited similar results for all 3 strategies, at high rates surface cooling led to a 9.2 % loss in capacity, comparing unfavourably to the 1.2 % capacity loss seen in the tab cooled scenario. It is proposed that this deviation is caused by internal thermal gradients leading to heterogeneous internal impedances in the surface cooled case, leading to loss in capacity when cycled at high rates, a hypothesis which is supported by further work

from Zhao et al. [119]. Additionally, it is thought that heterogeneous internal conditions will lead to heterogeneous aging, meaning voltage cut-offs will be reached earlier under load, causing a reduction in effectively accessible capacity of the cell.

3.2.4 Interim Summary

In this section multiple strategies for thermally managing battery packs have been assessed. Whilst in general it is found that liquid cooling strategies are effective in EV applications, various modelling studies provide contradictory results for the magnitude of thermal gradients induced under air- and liquid cooling. It is clear that the degree of thermal gradient formation under these strategies is highly dependent on the specific design and parameters of the TMS. Nevertheless it can, in general, be concluded that liquid cooling will be generally preferred for maintaining the optimal pack temperature range of 15-35 °C [129], [131]. It is noted that the interactions between cooling system design and pack electrical topology is a relatively understudied area with potential for further research. This is commonly neglected in modelling studies aimed at optimising pack TMS systems. While the effects of thermal gradients within cells are out-of-scope of this work, due to the focus on thermal gradients within packs, it is interesting to note the effects induced by cell internal electrical topology and spatial location. Significant internal thermal gradient build-up within cells during operation, and it is therefore likely that strong parallels may be drawn between the effects of thermal gradients at the cell and pack level.

3.3 Heterogeneities within Lithium Ion Battery Packs

3.3.1 Overview of Pack Level Heterogeneities

Within parallel cell strings a range of heterogeneities have been identified as causing variation within these cell strings. A coupling exists between cell impedance, load current, cell state of charge (SoC) and temperature, as identified by Hosseinzadeh et al [139]. Load currents will be distributed within the parallel connected cells due to the finite value of the interconnect resistance as well as cell-to-cell variability, as a perfect system with zero interconnect resistance and no cell heterogeneities would experience identical conditions for each cell. Offer et al. [140] developed an LIB pack consisting of 508 4.8 Ah lithium polymer batteries and found that interconnects have significant pack level performance implications due to the interconnection overpotential inducing higher currents in some cells of the same parallel string. The critical factor determining the effects of interconnect resistance is the ratio of interconnect resistance to cell resistance [139]. Wu et al. reported this ratio as around 0.02 [141] while Bruen and Marco [10] report a value of approximately 0.125. It is noted that measuring the Interconnection Resistance Ratio (IRR) is dependent on the cell SoC and temperature, as cell impedance is a strong function of both factors, and therefore a pack with a low IRR value at low temperature may exhibit significantly higher value at elevated temperatures. In particular, cell impedance may vary by an order of magnitude between low and high temperatures. Other root causes of heterogeneity identified include uneven thermal effects, variations in coulombic efficiency and different self-discharge rates [142]–[144].

In nearly all pack level modelling work involving LIBs, authors have assumed that all cells have the same performance with limited works also considering the effect of thermal gradients. Yet, it is well known that there is a performance distribution between cells that exist due to small variations in

the manufacturing in the cells which can lead to uneven heat generation. The result is that some cells have higher/lower capacities and impedances, with this distribution varying depending on many factors such as the manufacturing quality, age and other factors. Yang et al. [145] used a thermal-electrochemical model to investigate the impact that temperature has on unbalanced discharging and aging of parallel connected LIBs. They show that cells at higher temperature provide more current until approximately 75 % of the depth of discharge which coincides with the voltage drop-off of the discharge profile. At this point, the current distribution switches due to increases in cell impedance. It was found that that for parallel-connected battery packs, the rate of capacity loss increases linearly with temperature difference, and the rate accelerates with increasing operating temperature. Gogoana et al. [146] showed that 2 parallel connected cells with a 20 % difference in internal resistance can result in a 40 % reduction in cycle life when compared to cells with matched internal resistances. This pack level non-uniform behaviour becomes even more critical as hybrid systems using different chemistries are investigated [147]. Brand et. al. [148] found, on disassembly of BEV modules, that capacity and impedance parameters differed less in aged modules. They postulated this to be due to self-balancing of parameters during aging in parallel strings, a finding which was contradicted by Baumann et al. [149], who identified significant aging induced heterogeneities in capacity and internal resistances due to thermal and current heterogeneities.

Meanwhile Campestrini et al. [150] investigated aging in 2 112 cell 8S14P modules, and found that despite residual variations in capacity and cell impedance at start of life, no significant differences in pack-level aging rates were observed compared to naked cell cycling. Liu et al. [9] simulated aging of 1S6P parallel cell strings under a range of thermal gradients and predicted that aging rates of the strings were significantly sensitive to both the magnitude and direction of the applied thermal gradients. Fleckenstein et al. [151] identified significant SoC inhomogeneities in LFP cells connected in parallel, due to their relatively flat OCV curve, predicting that as a consequence aging rates would increase, due to the SoC, temperature and current distributions. Cavalihero et al. [152] induced thermal gradients in parallel connected cell strings, and found that degradation rates increased by 7 % under non-uniform thermal conditions compared to a baseline pack. Clearly, the effects of heterogeneities on cell parameter development are complex and coupled, and this literature review aims to explore in detail the influences of various parameters on overall parameter development and aging. However, disagreement exists in the literature as to the effect of initial cell-to-cell variation on overall lifetime, and further investigation of these effects is warranted.

3.3.2 The Effects of Pack Topology

Electrical topology, referring to the arrangement of electrical components in a circuit, is highly relevant to battery pack design and performance of parallel cell connections. This is due to the balancing of currents within parallel circuits with unequal branch resistances, where any induced current distribution cannot be directly controlled in service and is typically unmonitored. While a battery is an electrochemical device which is complex and not simply described by single circuit elements, the configuration or electrical topology of the system is a key design consideration within an LIB pack. Multiple authors have investigated the effects of changing the layout of battery packs, and key results are critically analysed here. A key consideration is the interconnection resistances, which in real packs will be finite as cells must be connected, and studies concerning these effects will also be reviewed here. As an initial example of effects within single LIBs, Osswald et al. [153] modified 26650 cells

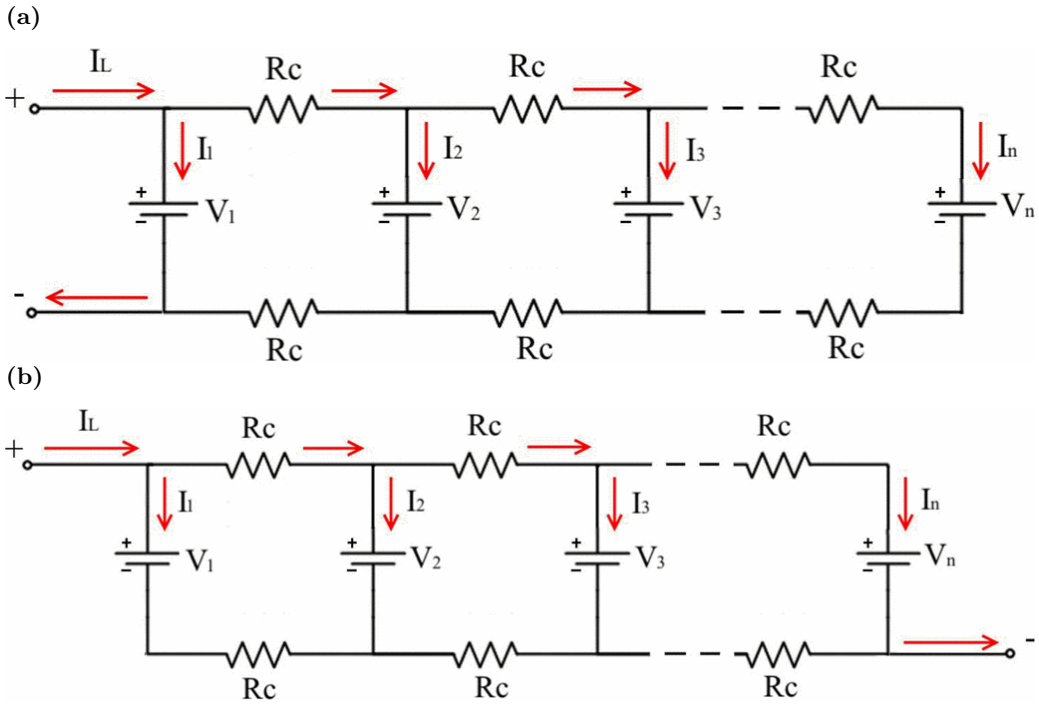


Figure 3.3: a) Cis-configuration Li-ion cell string b) Trans-configuration Li-ion cell string [154]. © IEEE, Reproduced with Permission.

such that the 4 tabs from the jellyroll could be connected to an external load in any configuration desired. It was found that the tab connection pattern had an influence on the cell internal current distribution, highlighting the effect of system topology on current distribution.

Considering the specific topology of parallel cell strings, LeBel et al. [154] investigate two different topology classes within battery packs, which have been classed as either 'cis' and 'trans' configurations, shown in Figure 3.3, based on the position of the string tabs. It was shown that the 'cis' configuration showed a higher degree of current heterogeneity than the 'trans' configuration, as well as slower SoC rebalancing after discharge, while heterogeneous current distributions lead to different current throughputs cell-to-cell. This effect may be attributed to the increased differences in total branch impedance in the 'cis' case between the branches close to the pack terminals and those furthest away due to the increasing contribution from the interconnections. In comparison in the 'trans' case, branch impedances are approximately equal and therefore the current and SoC distributions are decreased. Wu et al. [141] mathematically showed that for a 'trans' configuration battery pack if the interconnect and contact resistance is finite then there must be a difference in the currents supplied by each cell (analysis which could be extended simply for a 'cis' pack).

Meanwhile, Lv et al. [155] assessed the performance of a 1S4P pack with a range of 3 pack topologies, a 'cis' case, partially symmetric and fully symmetric (it is noted that the symmetric case may be treated as a pair of 'cis' cases, i.e. if cells behave homogeneously the system may be considered as 2 1S2P packs). As shown in Figure 3.4, it was found that in the 'cis' and partially symmetric cases, the SoC deviation between the cells increased by nearly 3 times compared to the symmetric case, reaching similar conclusions to LeBel et al. [154] that this effect is induced by topologically induced variations in branch impedance. This highlights the importance of balancing branch impedances at the pack design stage as the electrical topology is selected. Extending this analysis, it was concluded

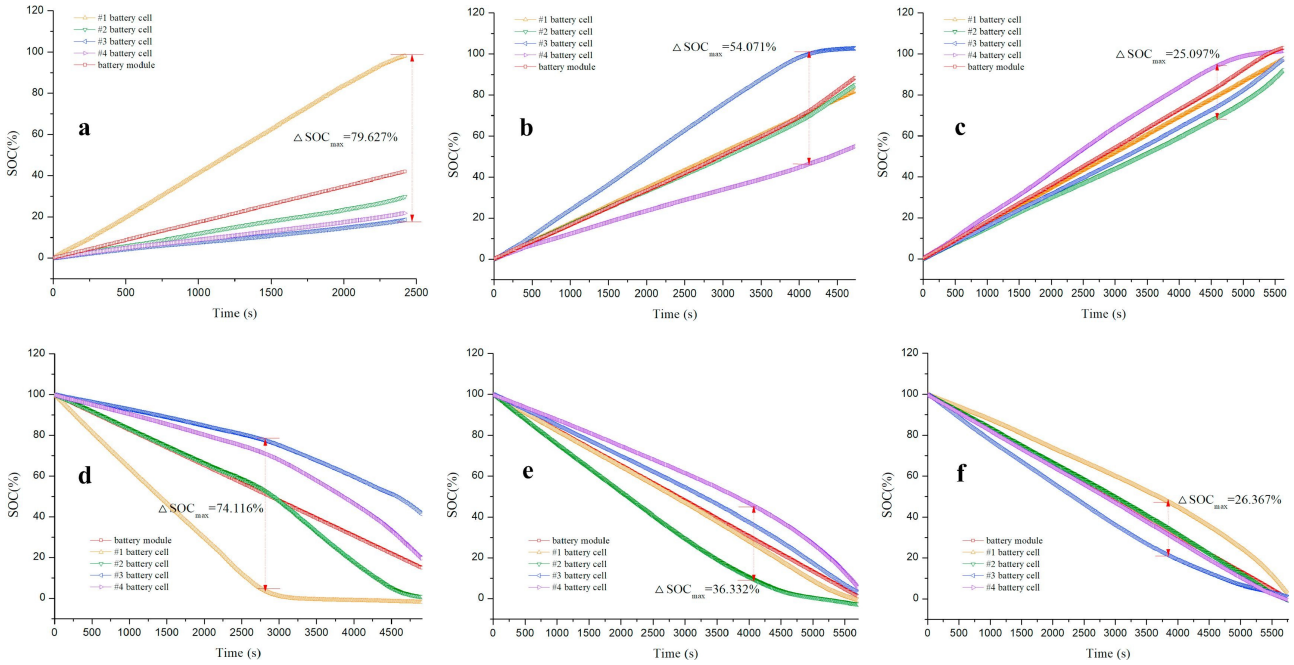


Figure 3.4: SoC variation of individual cells and parallel battery module with a 0.625 C current rate: (a), (d) battery terminals connected with # 1 battery cell; (b), (e) battery terminals connected with # 2 battery cell; (c), (f) same circuit impedance of each parallel branch [155]. © Reproduced with Permission.

that the closer the string terminals are to the marginal cell, the greater the induced heterogeneities and therefore losses induced by self-equalisation of the pack. Diao et al. [156] investigated balancing and management of increasingly parallel connected cell strings, and the current deviation maximum was found to increase monotonically with the increasing numbers of cells connected in parallel, as shown in Figure 3.5. Neupert et al. [157] have suggested that selecting a 'trans' pack topology is effective at reducing, although not eliminating, current variation between cells, though this is noted to have reduced effects with increasing parallelisation. However, for an equal number of cells connected in parallel it is expected that the 'trans' configuration will show smaller degrees of heterogeneity

Zhang et al. [158] also investigated the effects of increasing parallelisation on battery cell strings. Using a combined experimental 1S5P system and an EEC model derived from Bruen and Marco [10], they found that cells furthest from the terminals initially exhibited the smallest currents and this shifted during the discharge, which is termed the 'surge wave phenomena'. Heterogeneities in current are identified as well as SoC deviation during discharge. As the C-rate increases, the energy loss from the pack compared to the theoretical capacity dramatically increases, from 9.3 % at 0.5 C to 21.4 % at 1 C, shown in Figure 3.6. An approximately linear relationship between rate and inaccessible capacity was identified. It was found that the cells furthest from the terminals contribute most significantly to this energy loss due to the limits to the possible depth of discharge in these cells. This leads to an overall underutilisation of the battery pack, potentially limiting performance during service, and indicates that such effects should be considered during design and specification. The underlying causes of these performance deficits can be attributed again to the variations exhibited in branch impedance leading to under utilisation of cells far from the string terminals.

Extending this work to analyse the effects of topology on lifetime, Grun et al. [159] used an equivalent circuit model to investigate the effects of topology on current distributions, finding that using a 'cis' topology increased peak currents (identified at the end of discharge during rebalancing) by 60

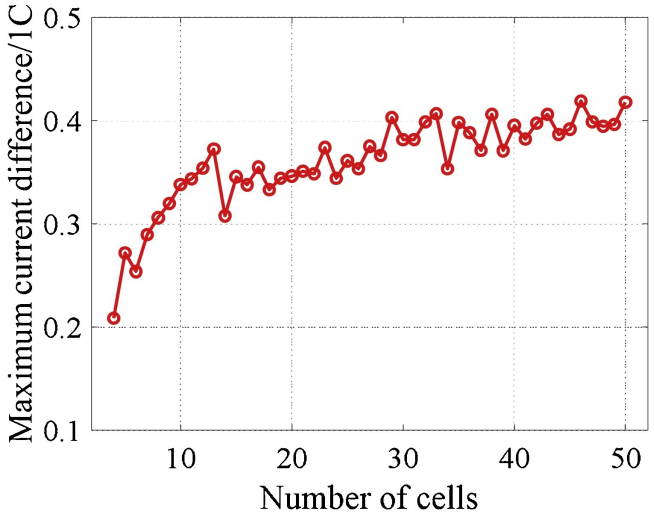


Figure 3.5: Relationship between the number of cells and maximum discharge current discrepancy [156]. © Reproduced with Permission.

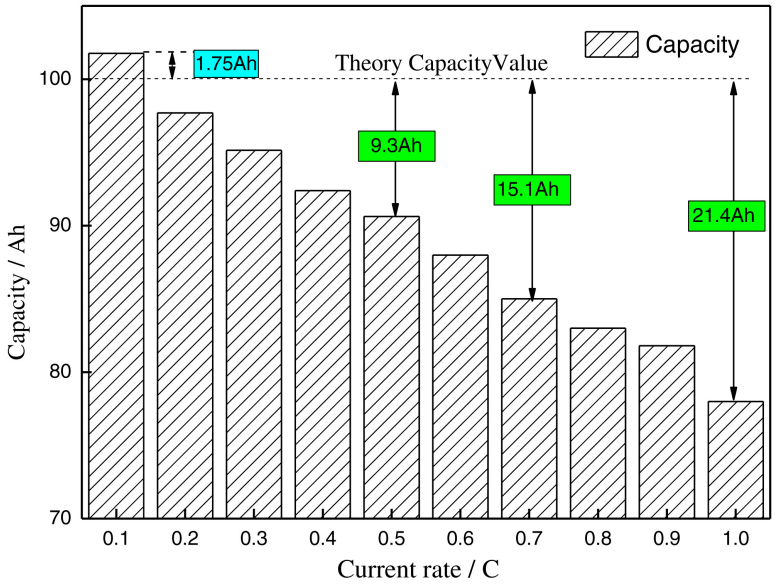


Figure 3.6: Comparison among the discharge capacities with various current rate [158]. © Reproduced with Permission.

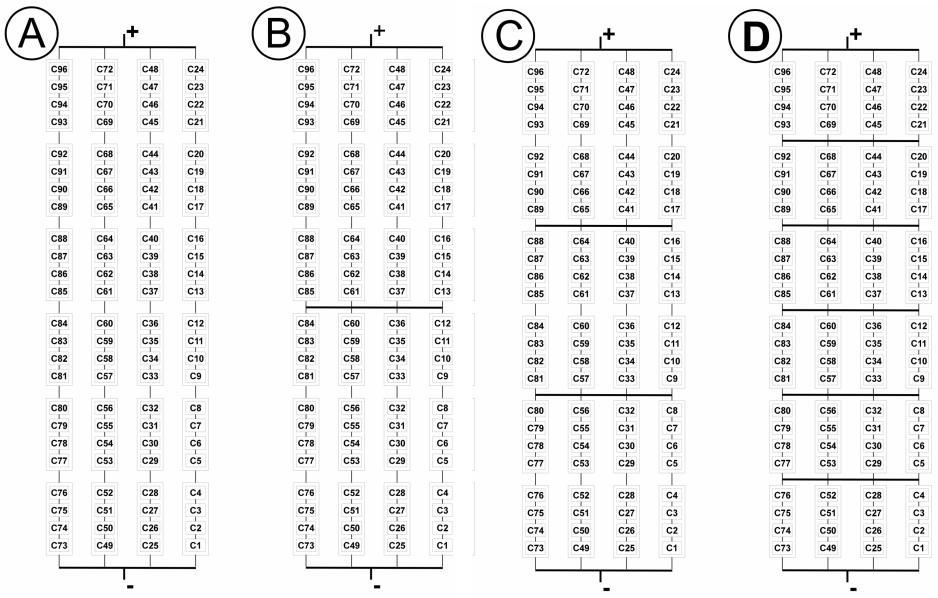


Figure 3.7: Studied topologies A-D with varying degrees of string interconnection [161]. © IEEE, Reproduced with Permission.

%. Using a current throughput degradation model as proposed by Sauer and Wenzel [160] to make lifetime predictions for equivalent 'cis' and 'trans' configuration systems, it was found that increasing the number of cells from 4 to 8 decreased the lifetime by 73 %. However, the degradation model used was fairly rudimentary as it was only parameterised at a single temperature and rate. While the capacity loss model is parameterised for temperature, the proposed model is unlikely to be robust outside of a limited window of operation. In all cases, increasing interconnection resistances led to accelerated aging, with increased effects identified in 'cis' packs, for example a 2.6 times increase in interconnection resistance leading to an 8 % reduction in cycling capacity predicted for a 1S4P LFP pack. It is noted that the predicted deviations in cell currents lifetime are significantly greater for LFP cells than LCO, attributed to the relatively flat OCV curve allowing greater build-up of SoC heterogeneities by minimising the rebalancing effect of decreasing cell OCVs in initially highly loaded cells. This in turn leads to greater current throughput deviation and deviation in aging rates, leading to an overall acceleration in capacity loss.

At the full pack/module level, Baronti et al. [161] investigate the properties of mixed parallel and series connected modules, using a first order ECN model, investigating a range of interconnection schemes shown in Figure 3.7. The individual cell parameters are varied based on a gaussian distribution of capacity with standard deviations of 2.5, 5 and 10 % to simulate the variability in cells seen due to manufacturing and aging heterogeneities (discussed in detail in Section 3.3.7). 200 simulations are carried out for each topology, and topology D is shown statistically to provide a greater capacity than topology A. Topology A was found to demonstrate a greater sensitivity to the mismatch in cell capacity between each string . This difference may be explained by considering the effects of inserting a low capacity cell in series into a branch of topologies A and D. In the case of topology A, a low capacity cell will be limiting to the total capacity that can be safely extracted from a single branch, whilst in case D, the fully interconnected nature of the pack will allow for the low capacity cell to be bypassed. Utilising a fully interconnected topology, similar to D, Offer et al. [140]investigated a highly interconnected 12P7S pack, and found that in highly topologically interconnected packs, faults in cell

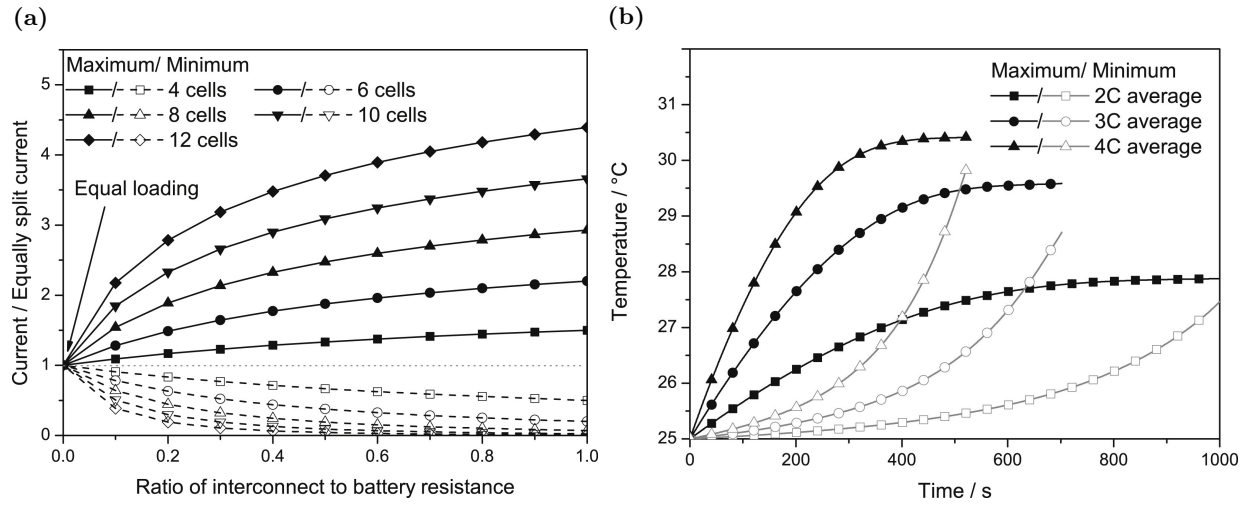


Figure 3.8: a) Ratio between predicted current and equivalent equal split current for cells closest and furthest from the load points for different ratios of interconnect resistance to battery impedance and cells in a single parallel strip. b) Maximum and minimum temperature of a 8P1S pack under an equivalent 2 to 4 C loading, starting from 60 % SOC [141]. © Reproduced with Permission.

connections may lead to extreme current deviations of over 200 % between cells, leading to potential safety concerns. Therefore, whilst increasing interconnectivity is attractive from the perspective of balancing cell level loads, increasing the interconnectivity of a pack may lead to greater difficulties in practice alongside increasing the impacts of fault conditions on overall safety. Miyatake et al. [147] also investigated the effects of both increasingly series- and parallel-connected modules in a xSyP system, and found that in series packs the capacity was limited primarily by the lowest capacity cell in string. Meanwhile cross-coupling, to increase parallelisation, increased current heterogeneity. This validates the conclusions made by Baronti et al. [161] regarding the cause of capacity loss in topologies investigated with varying degrees of string interconnectivity.

In conclusion, the topology of a pack is a base consideration when assessing the heterogeneity of packs, with different topological arrangements having a significant impact. While considering the topology of the parallel cell string is a fundamental consideration, the electrical properties of the circuit, specifically parasitic resistances such as the interconnect resistance must also be considered.

3.3.3 The Effects of Interconnection Resistances

As previously identified, the interconnection resistances between parallel connected cells, due to the electrical connections or busbars, will have a singificant influence on heterogeneous current distributions in parallel connected LIBs. In a parallel configuration, the ratio of the cell impedance to the interconnection resistance, the IRR, as defined in Equation 3.1 is a key driver of heterogeneities and will also be assessed here.

$$IRR = \frac{R_{Interconnect}}{R_{DC,\ Cell}} \tag{3.1}$$

To model the influence of the IRR on current heterogeneities Wu et al. [141] used a P2D model to explore the effect of variation on a parallel cell string. The ratio of current to nominal current is then explored for a range of cell numbers and IRR ratios. It was shown that increasing the resistance ratio, and the number of connected cells increased current heterogeneity dramatically, as shown in Figure

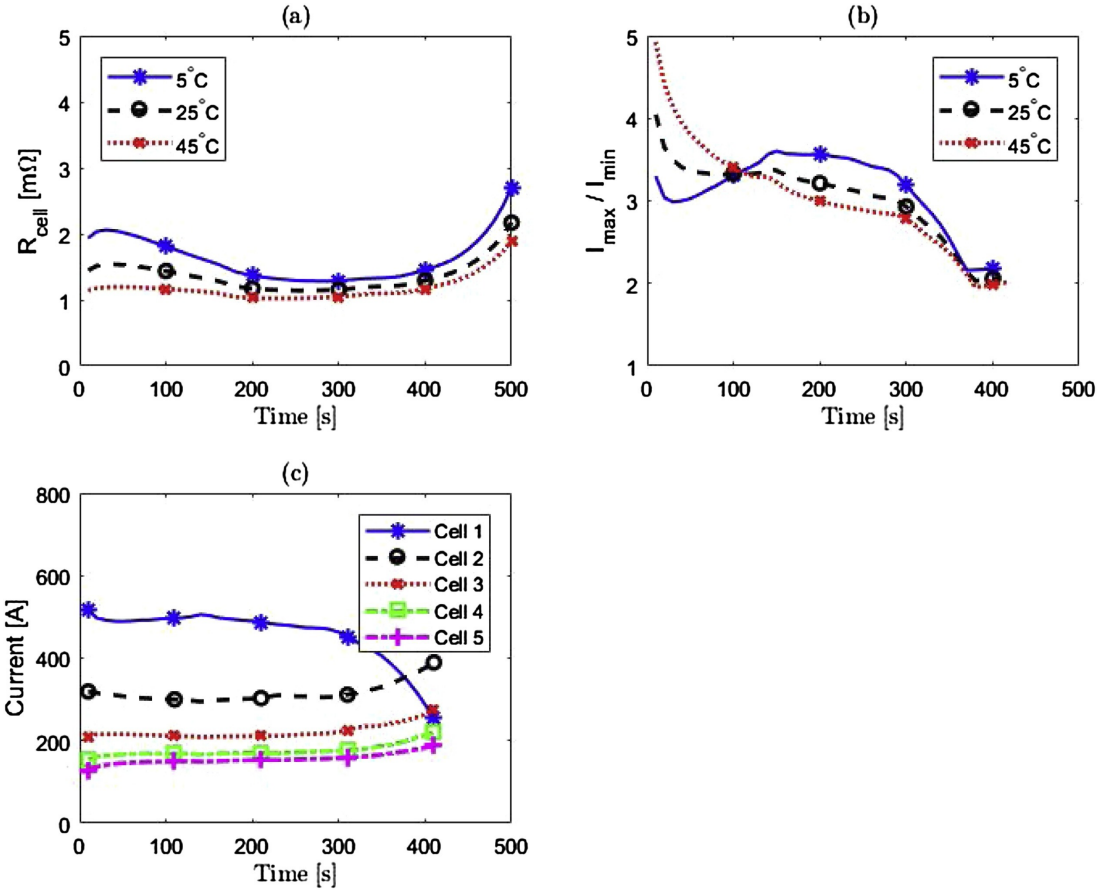


Figure 3.9: a) The resistance of cell 1 in a 1S5P battery pack. b) The maximum to minimum current ratio within the battery pack, during 5 C discharge at 5, 25 and 45 °C, R_{IC}=0.133 mΩ. (c) Current variation of the cells during 5C discharge at 25 °C, R_{IC}=0.1mΩ. [139]. © Reproduced with Permission.

3.8 a, leading to extremely uneven heat generation, as shown in Figure 3.8 b for an 1S8P pack. Peak thermal gradients are induced mid-discharge, with thermal gradients and temperature rises increasing from 2.5 to 5.5 °C and 2.0 to 4.5 °C respectively as the applied current rate is increased from 2 to 4 C. This is due to the unequal heat generation induced by the unequal cell currents leading to increased localised heat generation in cells seeing high peak currents at different stages of the string discharge. Hosseinzadeh et al. [139] investigated the current distribution between large, 60 Ah pouch cells using a coupled P2D and ESS model. It was shown that varying the IRR and the number of cells in the system has a significant impact on pack thermal performance and accessible capacity and it was found that in a worst case, with a resistance ratio of 0.1 at 5 C, the temperature difference between hottest and coldest cells was almost 50 °C, and the pack capacity was reduced by 40 %. Increasing the number of cells in parallel from 3 to 5 also increased the temperature difference and decreased available capacity, although less dramatically. The reduction in accessible capacity may be attributed to the unequal current rates leading to accelerated depletion in SoC of the highly loaded cells in the string, leading to overall cut-off of the pack discharge early and leaving a significant fraction of capacity inaccessible in the remainder of the pack.

Extending this work, Hosseinzadeh et al. [162] investigated the aforementioned 'cis' and 'trans' configurations, referred to as a 'Z' and 'ladder' configuration. Simulating a range of case studies, including IRR values of 0.01 to 0.1, it was found that for the same topology, induced peak thermal gradients increased by a factor of 5 and 6.5 respectively, due to the increasingly dominant effect of the IRR on

Table 3.2: A comparison between Z shape and ladder shape configuration for different interconnection resistances, under Artemis Rural Road drive cycle from 96 % to 4 % SoC with a nominal applied cell current of 20 A [162]. © Reproduced with Permission.

IRR	**Configuration**	**ΔV [V]**	**I_{Max} [A]**	**I_{Min} [A]**	**$I_{Balancing}$ [A]**	**ΔT_{Peak} [°C]**
0.01	Z	0.18	25.4	16.8	-0.5-0.8	3.0
0.01	Ladder	0.66	40.7	10.7	-2.4-4.6	9.8
0.05	Z	0.72	41.2	9.4	-3.2-5.4	10.3
0.05	Ladder	1.56	86.8	2.0	-4.6-27.3	37.0
0.10	Z	1.00	54.7	5.2	-5.2-15.6	17.0
0.01	Ladder	1.60	118.5	0.5	-5.3-32.0	65.4

current distribution. The results of these case studies are summarised in Table 3.2. This in turn leads to high peak currents and aggressive discharge of certain cells in the packs, leading to high peak heating. This effect is significantly greater in the 'ladder' configuration, due to the increasing imbalance between branch resistances induced when all interconnection resistances are varied homogeneously. It was found that the degree of heterogeneity was 2-2.5 times more sensitive to increasing the number of parallel cells in the ladder configuration. Considering the impacts of heterogeneous temperatures on safe operation, a significantly greater range of safe operation was identified for the Z configuration. For the ladder configuration with above 10 cells in parallel, IRR values of greater than 2-4 % are predicted to lead to thermal gradients of sufficient magnitudes to constitute a significant safety hazard. In comparison for the Z configuration, safety hazards are only identified with IRR values of >9 % over 14 cells connected.

Further validating these results, Liu et al. [9], using a SPM model, found that increasing the IRR of a single cell in 1S6P pack by 4 times led to a decrease in accessible capacity in all cases. However, the placement of the high IRR cell had a significant impact on the degree of heterogeneity in the 'cis' topology investigated, and while if the high IRR cell is the furthest from the pack terminals there is a minimal improvement in current heterogeneity, placing the cell close to the tabs led to a halving in mean standard deviation of current. Investigating the impacts of varied IRR on pack lifetime, Grun et al. [159] used a current throughput model to predict effects of IRR variation on lifetime. It was found that increasing the interconnect impedance by 250 % leads to a 20 % increased capacity loss rate compared to the base case for interconnect resistance. Overall, a significant portion of the literature identified the IRR as a key driver of heterogeneous current build-up and given that many cell degradation processes may be current activated, it is reasonable to conclude this effect will have an impact on overall lifetime. However, a comprehensive overview of the effects of IRR on aging rates is currently not found in the literature, and experimental validation datasets are lacking. This highlights the need to both experimentally validate these predictions and reiterates the need to understand the convergent/divergent aging behaviour within parallel strings, as it has already been identified that heterogeneous cell parameters will have significant effects on parallel string current distributions.

3.3.4 The Effects of Thermal Conditions

As identified in Section 3.2, thermal effects within battery packs have a significant impact on performance and lifetime while also proving to provide a significant engineering challenge during design and manufacture of large, highly parallel battery packs. Non-uniform temperature distributions in

particular are thought to be highly detrimental to the lifetime of LIB packs, with researchers developing bespoke equipment to investigate thermal effects within parallel cell strings [163], [164]. As the internal structure of a single LIB may be considered to be a distributed set of smaller cells, first thermal effects within a cell can be considered. Troxler et al. [165] investigated the effects of thermal gradients within a single cells by approximating R_{CT} as a function of distance based on a linear temperature distribution. Under thermal gradients, the cell was found to not perform as it would under a uniform temperature equal to the theoretical average temperature of the imposed gradient, but as a cell at a higher average temperature. The larger the gradient, the larger the deviation from the behaviour of a cell with a constant average temperature. Zhao et al. [119] considered internal thermal gradients within an LIB cell, using a distributed ECN model, a system which is analogous to a parallel connected string of LIBs, and found that significant thermal gradients were induced internally, with thermal boundary conditions significantly influencing the temperature distribution, current distribution and SoC deviation, with tab cooling providing more uniform performance due to the increasingly homogeneous internal temperatures.

Extending analysis to multicell systems, Klein and Park. [163] investigated heterogeneities within two groups of LFP and NMC parallel connected 18650 modules, in a 1S5P symmetric configuration, which was designed apply a bulk thermal gradient to the pack, although individual cell temperatures were not controlled. A range of mean temperatures and thermal gradients were tested at 20, 50, and 80 % SOC, using C/5, C/2, 1 C, and 2 C 10 s constant-current pulses to evaluate heterogeneities. It was found that the total normalised current difference was highest when the cell impedance was more temperature sensitive, tending to occur at lower states of charge. At 20 % SOC, with a T_{Avg} of 15 °C and a ΔT of 20 °C, and at C/5 the hottest cell in the NMC pack carried an 80 % higher current than the mean cell current. In comparison, the hottest cell in the LFP pack under the same conditions carried only a 40 % greater current. This indicates that under pulse conditions, LFP cells have a lower sensitivity to temperature heterogeneity due to their flatter OCV response. This leads to smaller differences in individual cell OCVs within the pack caused by SoC heterogeneities occurring due to the heterogeneous currents. Considering the current distribution, it was found that as T_{Avg} lower and/or the C rate increased, the current became less dynamic due to increased overpotentials.

Yang et al. [166] investigated 1S2P and 2S1P packs discharged under constant power conditions in both series and parallel configurations, and at a range of thermal gradients and average temperatures. They found that the differences in terminal voltages of two series cells increase as the temperature difference increases when the ambient temperature of the two cells remains at the same average value, with thermal gradients further increasing the deviations in terminal voltage. For the 1S2P case, increasing the temperature gradients between the cell increased the current heterogeneity, with high currents applied to the high temperature cell, due to the reduced cell impedance at high temperatures. As the temperature gradient increases, the difference in accessible energy increased linearly by 123.5 $mWhK^{-1}$ for the average temperature of 10 °C and 43.8 $mWhK^{-1}$ at 30 °C. The rate of increase is higher at lower temperatures due to the increasing rate of change of apparent cell impedance at lower temperatures, and the proportionally greater influence of the cell impedance on the total branch impedance at low temperatures. These differences were 5–10 times higher than that of the series connected cells at the same temperature gradient, which makes the temperature uniformity requirements within parallel battery packs higher than that within series battery packs.

In a similar approach, Huang et al. [167] used a P2D model, coupled with a 3D thermal model of the battery pack, considering natural convection to the environment, modelling a 4S6P pack to study thermal effects. Thermal gradients were found to form due to the upwards flow of hot air and the vertical orientation of the pack, which led to a temperature rise of 17 °C at 2 C. It was noted that the temperature heterogeneity was more dependent on operating conditions than ambient temperature. However, after cycling, the heterogeneity in discharge capacity is double that compared to a single discharge at a high ambient temperature. When significant temperature deviations exist in the battery pack, cells with lower temperature have higher impedance and vice versa. In turn, higher currents pass through the high temperature cells, which despite having a lower impedance will concentrate Joule heating into these cells, leading to a positive reinforcement of the thermal gradient. It was also noted that the deviations in discharge capacity among the parallel-connected cells is increased with increasing thermal gradient, again due to the high apparent impedances in the low temperature branches blocking access to a significant fraction of the available capacity.

Thermal effects may both be difficult to diagnose in service due to limited temperature sensing while also having an impact on diagnostic results. As such both Merla et al. [97] and Liu et al. [9] considered the effects of thermal gradients on ICA results from parallel strings under applied thermal gradients, and showed that the ICA response when highly heterogeneous currents are seen will be significantly shifted, both increasing the difficulty of diagnosis but potentially allowing identification of thermal gradients from discharge based diagnostics.

Considering the effects of thermal gradients on series cell strings, Zilberman et al. [168] investigated a 5S1P series pack, under an applied thermal gradient, controlling temperature using Peltier elements. Applying thermal gradients to the, significant temperature-induced variations in end-of-charge and end-of-discharge voltages between the cells were observed. With applied thermal gradients, low temperature cells reached cut-off voltages earlier due to increased overpotentials. Despite the small (5 °C) thermal gradient applied, significant uneven aging was found. This indicates that despite series connected cells nominally being exposed to identical currents and current throughput, significant differences in degradation rates may be occur, with 2.5 times greater capacity loss in the low temperature (25 °C) cell than the high temperature (30 °C) cell.

Yang et al. [145] considered the effects of thermal gradients on current distribution within parallel strings at different mean temperatures. They found that cells at higher temperatures experience a higher current below approximately 75 % depth of discharge before the current drops in those cells, and that this effect is increased in magnitude at lower temperatures, indicating that the mean temperature at which a thermal gradient is applied to a pack is also an important consideration, due to non-linearities in cell impedance response with respect to temperature.

3.3.5 The Impact of Cell-Level Parameter Variation

Apart from the topological and thermal effects considered in Sections 3.3.2 and 3.3.4, the inherent parameter variation seen in LIBs has been examined as a cause of heterogeneity within LIB packs. While LIBs are often considered to have identical performance, particularly when modelling battery packs, there are typically significant differences in key battery parameters induced by variations in manufacturing and over the life of the cell. This parameter variation may in turn have an impact on pack level performance. Investigating cell level variations, Rumpf et al. [62] investigated the cell

parameter distribution for 1100 commercial 26650 LFP cells, determining capacity, DC resistance and impedance at fixed states of charge. They found small variations in parameters, with capacity varying by small (<0.5 %) amounts. In comparison, the AC impedance and DC resistance parameters varied by a greater degree, although variations were still relatively small. While the variations in parameters are small, in particular the variations in cell impedance may have significant impacts at the pack level. Schuster et al. [71] investigated the parameter variation in 484 new and 1908 used (in EV service) cells, measuring capacity and impedance of the cells. It was found that, in agreement with Rumpf et al. [62], cells initially exhibited normally distributed parameters, however after aging it was found that parameters fitted a skewed Weibull distribution, alongside an increasing spread caused by heterogeneous aging. Researchers have explored how the variations principally in cell capacity and impedance will lead to differences in pack performance and lifetime, and this will be examined in this section. As early as 2006, Wu et al. [169] investigated parallel-connected LIB cells, simulating current distributions for parallel strings with cells of different capacities. It was found that even under constant current conditions, the simulated current distributions are not constant but change with time and voltage, and that variations were more significant close to pack voltage limits, while noting that the current through each cell was neither constant nor proportional to the ratio of the cell capacities.

Investigating the effects of including pre-aged cells within a parallel cell string, Gong et al. [170] harvested cells with 2 years use in a series pack of an EV and created 27 packs using various combinations of 2, 3 and 4 cells. They noted increases in heterogeneity of current and SoC distribution when packs including degraded cells are included. Increasing the number of cells in the test pack was found to decrease current variation, and it was also concluded that the currents are approximately in ratio with the cell capacity for most of the discharge although this effect broke down at lower states of charge. Similarly, Pastor-Fernandez et al. [171] investigated a 1S4P pack where the cells had been previously aged for 0, 50, 100, 150 cycles respectively, leading to an initial difference in the SoH of each cell. The cells are then connected in parallel and cycled to 500 cycles, which is defined as the end of life condition, and each individual cell is characterised at every 50 cycles. It was found that the SoH_P (defined as the resistance change relative to Beginning-of-Life (BoL) and End-of-Life (EoL) conditions) decreases faster than the SoH_E (defined as the capacity change relative to BoL and EoL conditions), however it was also found that the SoH metrics, which divergent at the start of pack life tended to converge during pack cycling, due to the self-balancing nature of the cell loads leading to greater charge throughput and therefore accelerated degradation in the less-degraded cells. However, in this study the aged cells were introduced into the pack in a pre-degraded state, which limits the insights into how such a difference in SoH between cells could arise in a pack with initially relatively well-matched cell parameters. While the maximum initial difference in impedance and capacity were 30 and 8 % initially, significantly tighter (1-2 %) distributions of initial parameters have been identified in other large-scale studies of cell parameter distributions [62]. Manufacturers may screen and group cells before assembly to match capacity and impedance, further reducing initial variations. Additionally, cumulative differences in charge throughput are highlighted during cycling of the pack. Fang et al. [172] characterised 138 cells and cycled a subset for either 50 or 100 cycles to increase the already present parameter inconsistency. These cells were paired and combined into 1S2P modules for cycling at a range of temperatures. Parameter inconsistency decreases while larger parameter inconsistencies at the start of life leads to more rapid aging. Overall, it is clear that increased parameter variation leads to increased rates of degradation and divergence in SoH between cells, however the use of pre-

aged cells does not directly inform behaviour in real packs, where cells will begin life with significantly less parameter variation as previously identified.

Brand et al. [173] investigated pairs of parallel connected 18650 cells using a high accuracy and low impedance system design for a symmetric pair of parallel cells. A combination of hall effect sensors and shunt resistors were used to minimise the influence of sensing on the current distribution. A simplified EEC model (single resistor and linearized OCV) was presented to illustrate the influence of different parameters on current distribution under variations of capacity and resistance. Based on current pulse testing and simulations they conclude that in a scenario where resistance is variable, initially cell currents will be divergent based on the current divider ratio and subsequently will begin to equalise, which has also been observed and mathematically shown by Wu et al. [141]. In a variable capacity scenario, a difference in SoC builds up and over time the currents will diverge based on the capacity ratio. It was concluded that as resistance variation is more significant for commercial cells this will be a more significant effect.

Fill et al. [174] made assumptions allowing the derivation of an analytical solution for parallel connected cells using a simplified ECN (source and resistor) model for a cell and linearised OCV curves. They found that at higher SoCs the model gave similar results to more complex ECN models and only generated large errors at low SoCs, indicating that simplified models may provide adequate accuracy for general modelling and analysis of heterogeneities within parallel strings. Varying the cell resistance and capacity based on a distributed gaussian function to investigate the effects of parameter variation on peak cell currents via Monte Carlo simulations. It was found that by increasing the number of cells in a parallel string the peak cell currents and SoC imbalances increased. Correspondingly it was found that system time constants and SoC imbalance decreased with decreasing product of cell resistance and capacity, a finding which has been supported by Chang et al. [175]. Chang et al. [175] also suggest that while there is a correlation between SoC deviations and deviation in cell time constants, this does not scale with number of parallel cells, and it is suggested that matching cell time constants may be effective in reducing heterogeneity. Extending this approach, Fill et al [176] used the same approach to investigate the effects of cell level parameter variation on series connected modules. The methodology used was able to obtain an analytical solution to the current distribution for any system of nSmP cells. This solution showed an almost logarithmic increase of the maximum cell currents and SoC differences within the parallel-connected cells with respect to the number of parallel- and series-connected cells, and a linear correlation to the standard deviation of cell resistance and capacity distributions. Meanwhile a decreasing square root dependence was identified between maximum string current and cell-to-cell OCV difference with the number of parallel- and serial-connected cells.

Devie et al. [177] used a simplified ECN to investigate balancing currents in parallel cells strings where the SoC and thus voltage is not the same. They were able to accurately predict the cell balancing currents and therefore the OCV after a balancing event and use these simulations to assess the impacts of either a short or open circuit failure on a parallel cell string, and it was found that balancing currents may be used as an indicator or diagnostic of cell failure within large, highly parallelised systems.

Several authors have also investigated the effects of the variation in system parameters such as convective heat transfer coefficients on pack level heterogeneities, typically using models to simulate variation in such parameters. For example, Li et al. [178] use a first order ECN model to investigate the properties of parallel connected cell systems, which was linked to a lumped thermal model of the 1S2P systems

under investigation. 4 cases for cell pairs (1S2P configurations) were investigated with either varied cell impedances, heat transfer coefficients or cell-to-cell contact thermal resistances. It was found that out of the wide range of scenarios simulated, thermal isolation combined with differing heat transfer coefficients generated the greatest deviation in cell temperatures, while thermal isolation between cells, resistance variations and invariant heat transfer coefficients led to similar temperatures rises, but the greatest current variations. Hosseinzadeh et al. [139] investigated the current distribution between large, 60 Ah pouch cells, and found that variable heat transfer rates, unequal interconnect resistances and variable ambient temperature had a significant influence on observed cell currents. Increasing the interconnect resistance ratio was found to logarithmically increase the electrical load imbalance, which was shown to lead to dramatic thermal gradient formation (48 °C at IRR = 0.10 under a 5 C load). Even with more moderate IRR values, significant thermal gradients were induced. Varying the ambient temperature had a significant impact on the current distribution, with lower temperatures leading to relatively lower current distributions. This is caused by the lower apparent cell impedance at high temperatures, due to improved reaction kinetics, leading to increased apparent IRR values compared to low temperatures, and consequently higher magnitude current distributions. As high-power cells are likely to exhibit lower absolute impedances than high energy cells, these effects are of more concern in high-power battery packs, such as those used in HEVs. With lower absolute impedance values, for a given busbar design the IRR will be increased. Therefore, consideration in design should be taken when specifying the acceptable impedance values of the busbars and therefore interconnections in parallel connected cell strings.

Hofmann et al. [179] use a state space formulation of a 3RC EEC model to simulate an arbitrarily sized parallel pack. This model was validated for a high power and a high energy cylindrical cell, while a virtual cell with a linearized OCV and an impedance model consisting of an ohmic resistance, a variable ZARC (i.e. a parallel resistor and CPE elements) impedance and a Warburg element was used for parameter variability studies. For validation the high energy and high-power cells were connected in parallel and various load profiles were applied, using sinusoidal pulses from 1000 Hz to 1/1000 Hz. Using parameter variations found in the literature a range of parameters were varied based on realistic values, and a 2P string was investigated. The parameters varied were all ECN parameters, the overall capacity and the OCV. It was found that non-linearities in the OCV curve prevent a constant difference in SoC from forming. It was found that with high energy cells the series resistance has a greater influence on current and SoC distribution whereas for a high-power cell the relative capacity is more significant, as shown in Figure 3.10.

In order to extend their analysis of the effects of cell parameter variation, Rumpf et al. [180] used the cell variability values experimentally found in their previous work [62] to investigate the effects of cell parameter variation in parallel connected cell strings. Using a Newman-type cell model linked to a 0D thermal model and 0D electrical circuit model, they aimed to provide general conclusions about multicell systems and so focussed on a 1S2P topology to illustrate general behaviour. A range of scenarios with variable topologies and varied capacity, resistance and temperature between cells were investigated, with parameter variation mimicking those experimentally determined. It was highlighted that for parallel strings symmetric topological design of cell modules from a resistance perspective is critical and minimisation of thermal gradients, resistance and capacity variations is important for minimisation of peak currents. Additionally, it was shown that for an asymmetric module, correct cell matching may decrease the peak currents seen in the case where cells with higher capacity or

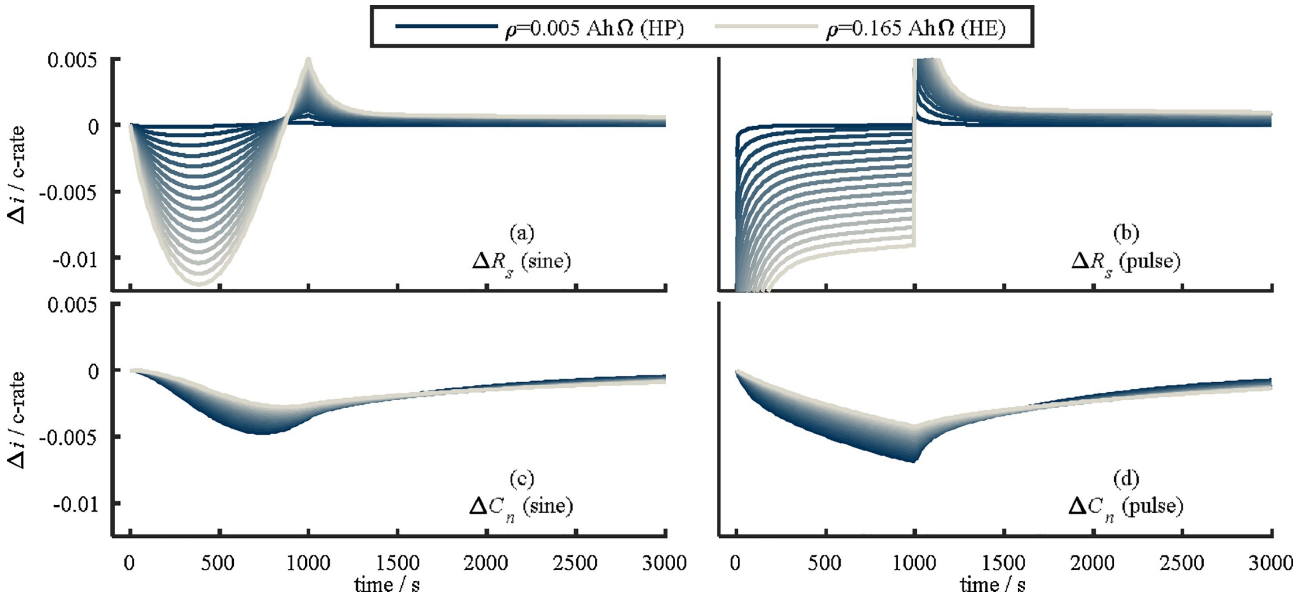


Figure 3.10: Resistance coefficient variation (ρ 0.005 . . 0.165 AhΩ) and its influence on the current distribution at capacity (ΔCn = -1 %) and impedance (ΔR = 7.6 %) [179]. © Reproduced with Permission.

impedance are placed closer to the module tabs.

In order to reduce lifetime variations seen within packs, several authors have proposed cell grouping methodologies to reduce or minimise cell-to-cell heterogeneities. For example, work by An et al. [181] indicated that simple ECN models (0th order) were adequate to group cells based on manufacturer parameter data. It is noted that while aging metrics are key to include during cell grouping, such metrics must be practically obtainable, and the cell self-discharge rate (or steady state OCV change) are a practical metric. This proposed methodology is statistically investigated in work from the same authors [182], where analysis of multiple 1S2P packs during cycling found that only changes in self-discharge rate were statistically significant in leading to lifetime reductions, although it is noted that the sample size used was still relatively small (9 packs).

3.3.6 The Effects of the Duty Cycle

While topology, thermal conditions and cell parameters have been shown to be key drivers of heterogeneity within LIBs, the duty cycle the pack or cell is exposed to will also have a significant impact, both driving formation of heterogeneities and potentially accelerating degradation. To investigate these effects, Bruen and Marco [10] use a state space ECN to analyse a 4 cell parallel cell string. Two principal applications were considered, those being a HEV and BEV drive cycle. In a HEV application is was found that the peak current was 14.4 % above nominal while the current throughput was increased by 6.7 % between cells. In comparison under a BEV drive cycle the peak current was 159.2 % above nominal, however the current throughput range was only 3 %. While perhaps unexpected, this effect is caused by the greater SoC range and more homogeneous load giving greater opportunities for differences in cell OCVs and SoCs to build-up, in turn leading to greater deviations in cell impedance and higher peak current values. Wu et al. [141] used a P2D model was used to explore the effect of variation on a parallel cell string, and the effect of sinusoidal loads on a 12P7S battery pack is explored. It was found that dynamic loads (10A at 1Hz for a 100A load) dramatically increased the peak temperature of the pack, and it was concluded that the effects of interconnection resistance are

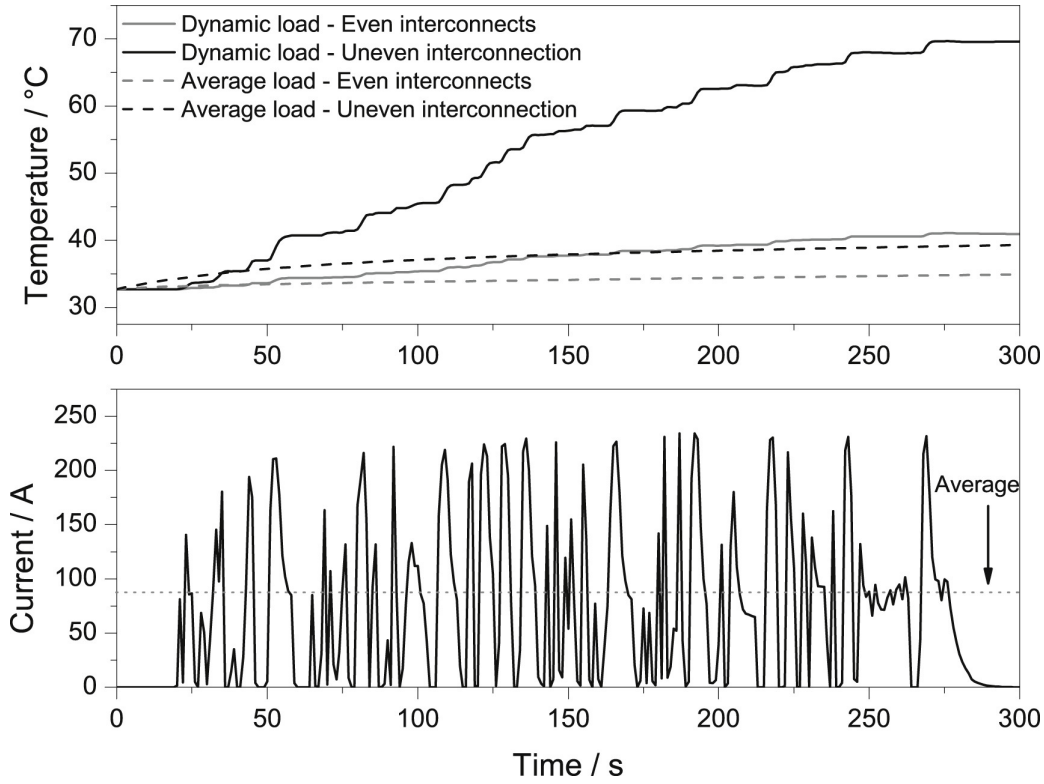


Figure 3.11: Simulated temperature of the hottest cell in a 12P7S battery pack under static and dynamic loads with equal and unequal interconnect resistances [141]. © Reproduced with Permission.

more significant in confined SoC windows, for example in HEVs. Considering the effects of realistic load cycles and uneven interconnect resistances, as shown in Figure 3.11, it was shown that when simulating the highly parallelised 12S7P pack first presented by Offer et al. [140] that interconnection resistance faults are predicted lead to temperature rises to unsafe levels. In this case, modelling the pack as a system with equal interconnection resistances would imply safe operation under the given duty cycle, however combining the duty cycle with uneven interconnections leads to 4.7 times increase in the maximum cell temperature. This effect may be attributed to uneven branch resistances leading to concentrated Joule heating.

Considering the effects of load profile on highly parallelised packs, Bruen et al. [183] investigated the current distributions in a 1S70P system, using a 3rd order ECN model. A 200 % difference in peak current during a dynamic driving profile is seen in a 70 cell parallel pack, which while unmonitored by the BMS may allow some cell currents to greatly exceed their intended operating current, or be aged more quickly due to increased charge throughput and ohmic heat generation, shortening the overall lifespan of the pack.

3.3.7 The Effects Heterogeneities on Pack Degradation

Many authors have considered the origins of heterogeneity within LIB packs, as discussed in Section 3.3, and several effects such as the pack topology, cell parameter variation and operating conditions (thermal conditions and duty cycle) have significant effects. However, a more limited selection of literature is available analysing the effects of such variation on pack lifetime rather than instantaneous performance. While it is clear from a fundamental understanding of LIB degradation that heterogeneity will lead to reduced overall lifetime performance, the direct causes and effects of heterogeneity on

degradation is less well explored. As an example of the effects of heterogeneous degradation Schuster et al. [71] found increased spread in cell capacity and resistance in 1908 cells aged in-service in EVs, and identified that while in this particular design there was no significant positional effects (i.e. caused by high temperatures or currents in specific module positions), the intrinsic variation caused by cell and pack manufacturing tolerances leads to increasing parameter variation during service.

Gogoana et al. [146] investigate current distributions induced by internal resistance mismatches between individual cells in a pack, using 2.2 Ah cylindrical LFP 18650 cells. 72 cells were tested, and the internal resistance was measured at 50 % SoC by applying a 17 C current pulse for 15 s. A maximum difference of 25 % was found between R_{DC} of the most and least resistive cells tested. 6 1S2P packs were then created and tested. The packs had a symmetric arrangement. Mismatches in R_{DC} were generated in pack construction, with 2 packs each at approximately 0, 10 and 20 % mismatch. The packs were cycled, and degradation modelled as basic SEI growth, assuming a constantly proportional relationship between the resistance of the two cells. It was concluded that towards the end of discharge, cells in a mismatched pack may experience abnormally high currents, and if the cells are not specified to take currents this high then this may lead to issues and accelerated degradation of the system. The proposed degradation model suggests that maximum charging current experienced by a cell has a strong influence on the degradation rate and therefore current balancing in parallel strings is critical to maintain pack lifetime. However, limited further validation of the aging model is presented whilst the effects of current-activated aging mechanisms are not considered. Under high peak currents, aging mechanisms such as particle cracking are expected to become increasingly significant and these effects are not captured. Westenhover et al. [184] experimentally investigated 1S30P packs, cycled at 6 C and 15 C. It was found that for the high-power cells used at 6 C, well below the cell operating limits, the imbalance of currents was insufficient to cause serious deviation in aging, however this was not the case at 15 C where especially at full depth of discharge, where significant deviation between cells was seen. The increasingly heterogeneous aging with C rate may be attributed to increasing current-activated degradation of the cells under test, due to the extreme peak currents. The increasing deviations during high DoD cycling was likely due to increasing cell impedances at low SoC values. This leads to greater peak currents in the high DoD cases during the pack SoC rebalancing phase close to the end of discharge (EoD). However, no further exploration of this effect was presented.

Considering the effects of thermal gradients on uneven aging within parallel cell strings, Cavalheiro et al. [152] investigated induced thermal gradients within 1S5P stack of cells under convective cooling, and compared the degradation rate to a single cell under the same nominal cycling procedure. Highly non-uniform degradation occurred in the string, and that the parallel string degraded significantly faster (7 % greater capacity loss at 2215 cycles) than the baseline pack, which was attributed to the higher mean cycling temperatures of the central cells in the pack. It was found that the stack cell temperature during discharge increased by 400 % more than in the baseline single cell, and the temperature distribution became more heterogeneous with time. Again considering the effects of thermal gradients on aging, Shi et al. [185] investigated the effects of imbalanced currents on large format LFP cells in a 1S2P configuration, comparing a homogeneous and heterogeneous case. It was found that in the heterogeneous case (30°C thermal gradient), the degradation rate was more than double that of the homogeneous case. Over 1000 cycles, both the initial deviation in currents was higher for the heterogeneous pack, and this difference also increased with cycle number. It was therefore concluded that imbalanced currents directly affect the rates of capacity loss during cycling of

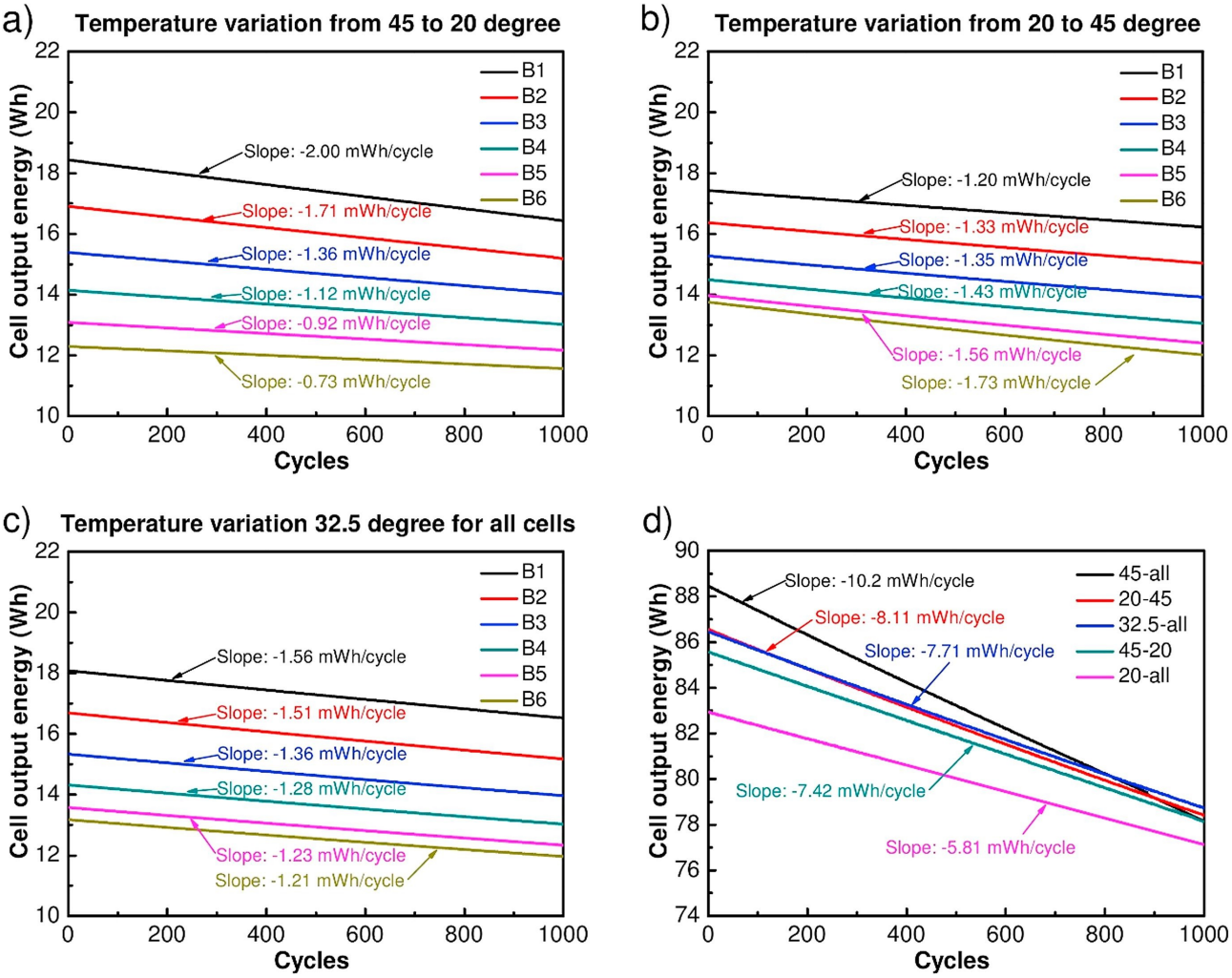


Figure 3.12: Simulated discharge energy loss for battery packs with thermal gradients under 1 C constant current cycling. a) 45 to 20 °C decreasing by 5 °C for cells B1 to B6. b) 20 to 45 °C increasing by 5 °C for cells B1 to B6. c) 32.5 °C for all cells. d) pack output energy during cycling and degradation rates [9]. © Reproduced with Permission

parallel strings, and therefore supressing branch current variation rapid capacity fade may be avoided.

Liu et al. [9] used a model based approach to investigate the effects of a range of thermal gradient conditions on a 1S6P pack, and found that both the degradation rate and accessible capacity were highly linked to the applied thermal gradient, with thermal gradients in all cases decreasing accessible capacity. However, it was also identified that the direction of the thermal gradient relative to the position of the tabs had a significant impact on the predicted degradation rate (calculated using an SEI growth based degradation model), with a predicted 66 % increase in the degradation rate when comparing a 25 °C thermal gradient applied with the coldest cell at the terminal side of the pack to the reverse case, as shown in Figure 3.12. A significant limitation of this study is identified as the attribution of all degradation to SEI layer growth, whilst it is expected that differences in peak current will lead to deviation in the degree of degradation induced by other mechanisms such as particle cracking.

Considering the effect of thermal gradients on series connected cells, Chiu et al. [186] used an SPM to investigate the effects of thermal gradients on series connected cells. A SEI growth-based degradation model is included. After experimental validation on a reduced size (2S1P) system, the principle

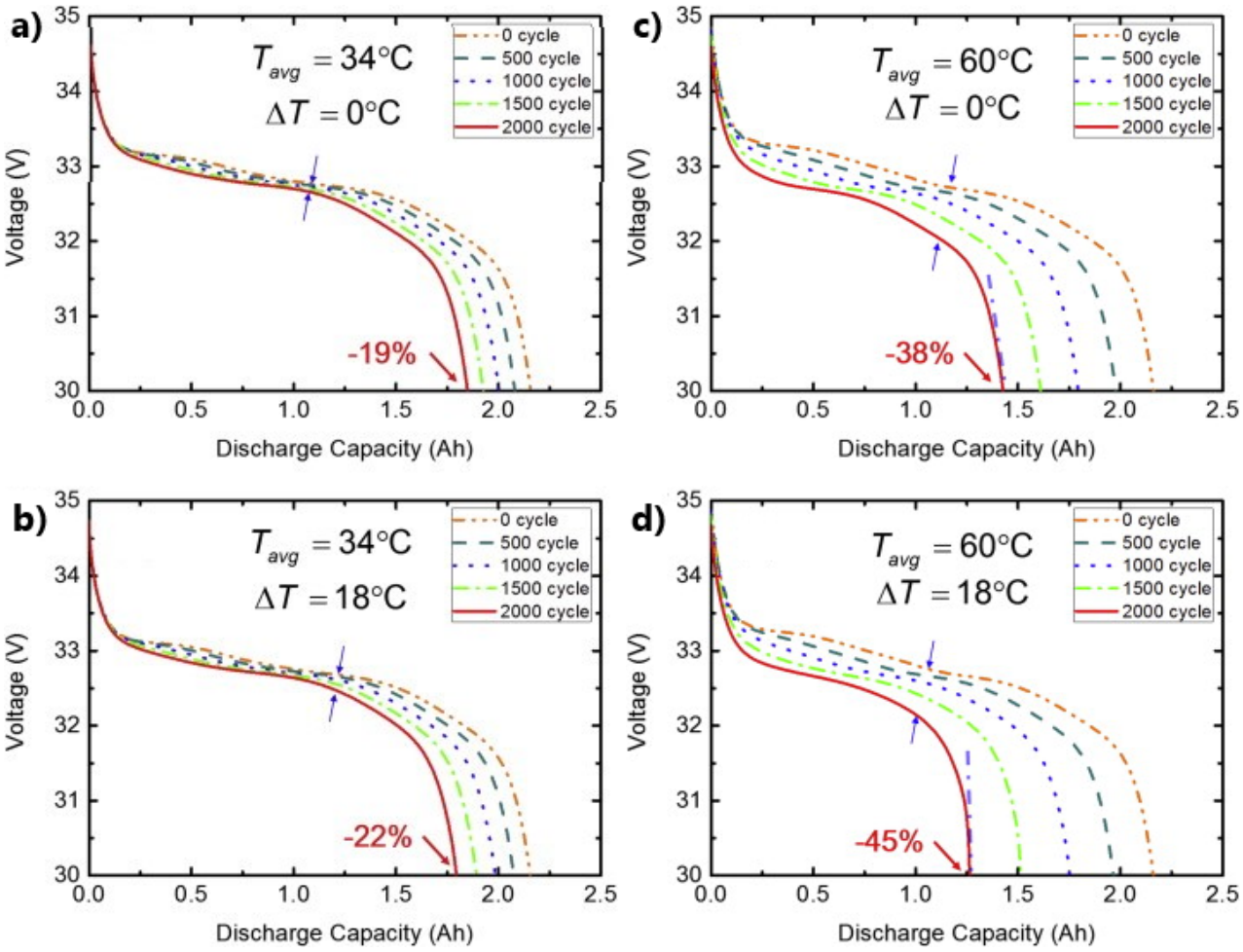


Figure 3.13: Simulated capacity fade result of ten cells connected in series with a) T_{Avg} = 34 °C and ΔT = 0 °C. b) T_{Avg} = 34 °C and ΔT = 18. c) T_{Avg} = 60 °C and ΔT = 0 °C. d) T_{Avg} = 60 °C and ΔT = 18. [186]. © Reproduced with Permission.

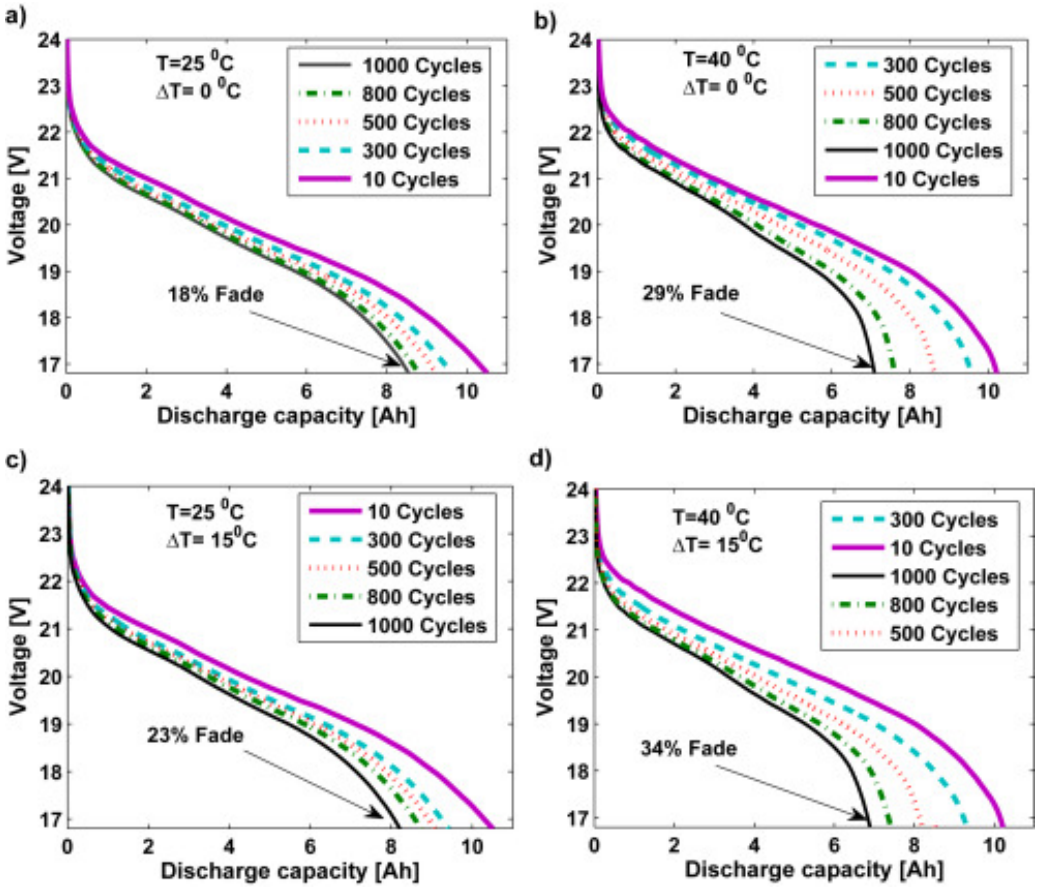


Figure 3.14: Simulated capacity fade result for a 6S5P pack under different thermal conditions. a) Discharge curves at T_{Avg} = 25 °C and ΔT = 0 °C. b) Discharge curves at T_{Avg} = 40 °C and ΔT = 40 °C. c) Discharge curves at T_{Avg} = 25 °C and ΔT = 0 °C. d) Discharge curves at T_{Avg} = 40 °C and ΔT = 40 °C [142]. © Reproduced with Permission

topology modelled was a 10S1P pack, under 2 different average temperatures and 3 thermal gradients in each case. It was found that a thermal gradient of 18 °C decreased available capacity by only 3 % to 22 % from 19 % at an average temperature of 34 °C compared to with no thermal gradient (Figure 3.13 a and b). However, at an average temperature of 60 °C these values increased to 45 % and 38 % respectively (Figure 3.13 c and d), both increasing the rate of degradation and increasing the spread caused by the applied thermal gradient at 2000 cycles. In the second case the pack capacity is limited by the performance of the hottest cell in the series string, which had undergone significant aging. Ganesan et al. [142] experimentally cycled 6S5P packs under a range of mean temperatures and thermal gradients, and found that application of a thermal gradient in all cases increased the rate of capacity fade. The greatest increase in the capacity fade rate, by up to 30 %, was observed when a 15 °C thermal gradient is applied to the pack at a mean temperature of 25 °C. This increase was reduced to a 17 % for the same thermal gradient at a mean temperature of 40 °C. Figure 3.14 shows the modelled capacity loss in 4 test cases.

The underlying cause of this effect is again identified as the non-linear impedance behaviour of LIBs, with greater relative changes induced at low temperatures. This in turn leads to greater SoC deficits in low temperature cells in parallel strings. It was also indicated that for the NCA cathode chemistry studied, degradation of the cathode had a significant contribution to the overall rate of capacity loss, highlighting the importance of consideration of cathode degradation in parallel strings. This is of

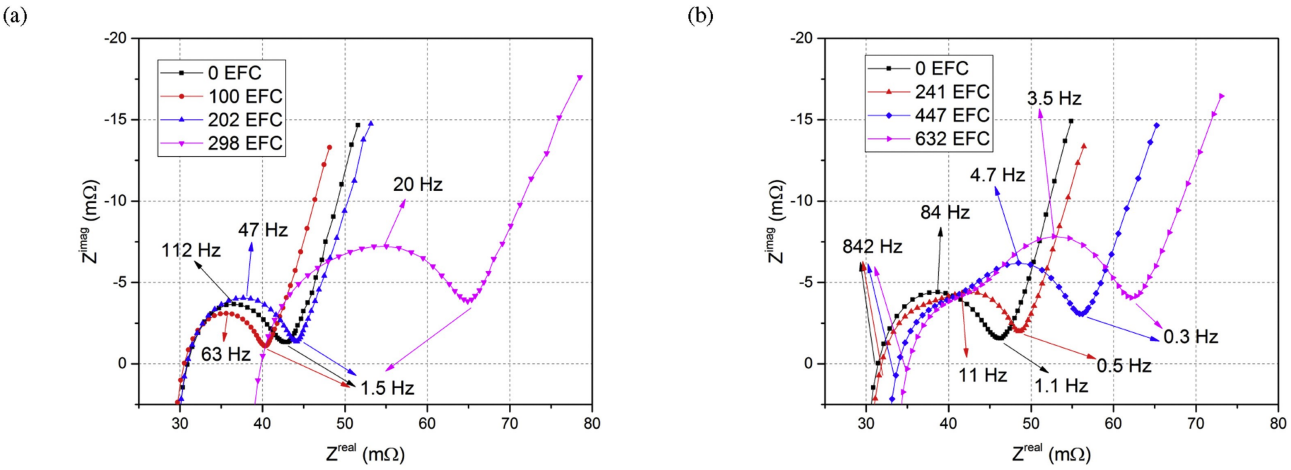


Figure 3.15: a) EIS spectra for cell at 20 °C (50 % DoD, 1 C charge and 2 C discharge) at four different FEC. b) EIS spectra for cell at 45 °C (50 % DoD, 1 C charge and 2 C discharge) at four different FEC. For the cell cycled at 20 °C, the spectrum does not change much but instead after a few hundred FEC is horizontally shifted towards higher impedance. The spectrum at 45 °C does not shift but instead it enlarges gradually and two electrode processes become distinct as the cell ages with a shift towards low frequencies [188]. © Reproduced with Permission

particular interest in packs designed for high rate loading, as heterogeneities in current may lead to extreme peak currents at top and bottom of charge, leading to accelerated particle fracture. However, whilst the model used was validated at start of life, no aging experiments were carried out to validate the model at the pack level, whilst the degradation model used simulated only SEI and CEI growth as degradation modes, a potential limitation given that highly heterogeneous currents may for example exacerbate particle fracture.

Further considering the effects of temperature on impedance growth in NMC cells (the cell chemistry selected for use in this work), several authors investigating the impedance growth of NMC cells have noted greater growth in charge transfer impedances at intermediate temperatures (10-45 °C), while lower growth is seen at elevated temperature. Investigating the contribution of each electrode to overall cell impedance by harvesting electrodes and constructing coin cells, Jalkanen et al. [187] identified the NMC cathode as the dominant contribution to the medium frequency charge transfer resistance of the cell. This impedance contribution was particularly dominant at room temperature (assumed 20-25 °C) and 45 °C. Meanwhile, Maheshwari et al. [188] found a greater growth in the low frequency semicircle (in this case attributed as R_{SEI}) at 20 °C than 45 °C, shown in Figure 3.15 a and b respectively. As can be seen, similar magnitudes of growth are seen after 50 % less Full Equivalent Cycles in the 20 °C case. Significant growth in both R_S and the low frequency semicircle are noted in the 45 °C case, likely attributable to accelerated SEI growth at the anode with elevated temperature.

Buchberger et al. [51] also identified this trend in NMC-111 cathodes, investigated in coin cells with a graphite anode. Minimal impedance growth at high temperature (60 °C) was identified compared to SoL, although cell capacity was reduced by 42 %. This trend is reversed at 25 °C, with a capacity loss of less than 4 % but an approximate doubling in R_{CT}, indicating more significant impedance growth at interim temperatures, and above the temperatures typically associated with lithium plating at the anode. Therefore, it is reasonable to conclude for NMC-graphite cells, growth in R_{CT} is inversely proportional to temperature. Zhu et al. [93] used distribution of relaxation times (DRT) analysis to further decouple the impedance response of blended NMC/NCA cathode 18650 cells after cycle

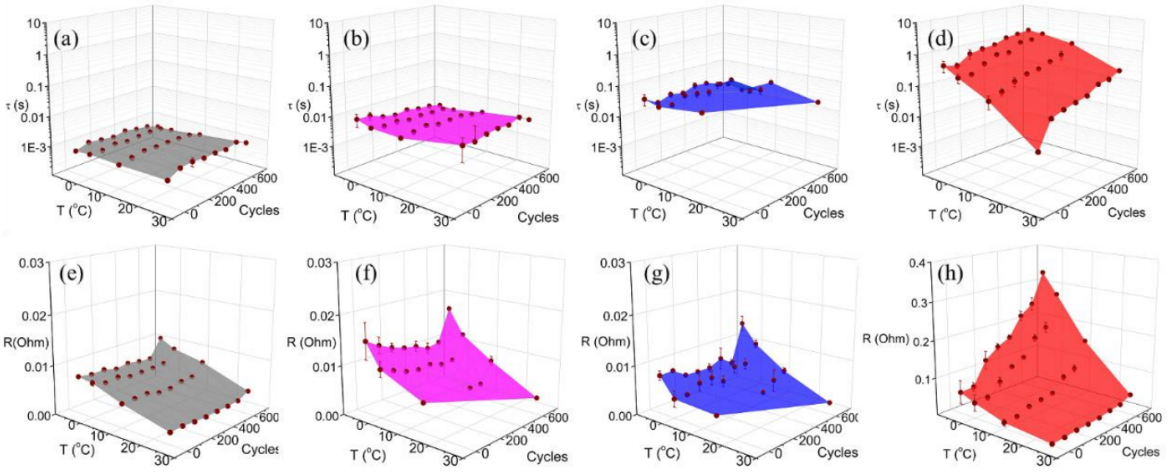


Figure 3.16: Observed central time constant τ and resistance R for the four processes against temperature and cycling numbers at 50 % SoC. (a) (e) for the contact process, (b) (f) for the process of passive films, (c) (g) for the charge transfer process of the anode, (d) (h) for the charge transfer process of the cathode [93]. © Reproduced with Permission

aging at -5 to 25 °C. After decoupling and comparison to half-cell measurements, it was noted that the contribution to the charge transfer from the cathode was dominant. Using DRT analysis it was possible to decouple the contributions of the different electrodes to overall cell impedance over life. As can be seen in Figure 3.16 g and h, the contribution of anode charge transfer impedance was relatively stable over the 600 cycles at all temperatures, while the cathode charge transfer impedance was both two orders of magnitude greater and significantly more sensitive to temperature. The growth rate of the cathode R_{CT} is dramatic below 10 °C, although the growth relative to the other impedance contribution at intermediate temperatures is significant.

Considering the mechanistic origins of power fade within NMC cathodes, single particle cycling of NMC-111 by Tsai et al. [189] indicated that electrochemically induced fracture occurs in NMC-111. Changes in charge transfer resistance against SoC are attributed to changes in the cathode electrolyte interface, potentially via reversible changes in the CEI composition or particle surface structure. Charbonneau et al. [190] observed increases in NMC-111 cathode R_{CT} which were attributed to damage to the surface layer of particles, caused by either transition metal dissolution or oxygen depletion in the surface layer (structural disordering). Meanwhile increasing the maximum charge voltage during cycling significantly reduced in Li^+ diffusion coefficient observed. Linking to the increased rates of R_{CT} increase at low temperatures, these mechanisms are accelerated at cathode potentials above 4.2 V versus Li/Li^+. Therefore, a potential mechanism for accelerated R_{CT} growth at low temperatures is increased maximum cathode voltages during charge, due to increased overpotentials caused by the slower kinetics at low temperature.

In conclusion these results are highly significant in their implications for NMC cathode cells, as high impedance growth is seen at the interim temperatures deemed ideal for battery pack operation. In parallel strings this may lead to a blocking effect on low temperature cells, increasing heterogeneities when thermal gradients are present.

Finally, Baumann et al. [149] investigated the parameters varying within battery packs and their influences on aging. Citing Brand et al. [191] they note that dispersion in capacity and resistance

is higher in fresh cells than aged cells which have been connected within a parallel cell string as do Pastor Fernandez et al. [171], due to differentials in charge throughput between cells of lower and higher impedance. A set of 164 fresh and 192 aged (in an in-service EV) cells were investigated. Cells were characterised using impedance, capacity measurement and HPPC for both batches. 2 modules from the aged batch were then further aged via cycling. They found that the aged cells had a strongly increased parameter spread, and continued aging increased this spread further. While there was no correlation between capacity and resistance for the fresh batch of cells, a negative correlation was observed in the aged cells, suggesting that cells connected in parallel do not in fact adjust their SoH balance with life due to self-balancing. Additionally, the SoH_P showed no trend in terms of convergence.

3.4 Conclusions and Outlook

Creating large packs, in some cases consisting of thousands of cells in parallel and series, leads to challenges at the battery pack level. Moving from single cells to packs however leads to loss in available capacity, energy and power compared to the expected values based on the number of cells within the pack. Additionally, a shorter lifetime of a pack compared to individual cells is often seen. These effects are caused by variability between cells due to manufacturing differences between cells [62], thermal gradients in large packs, heterogeneous current distributions and state of charge imbalances between cells. Hypothetically by optimising pack designs to account for these effects it is possible to improve the achieved performance and lifetime of packs.

Specifically, within parallel cell strings there is no control of the current seen by each cell, only of the string total applied current. Consequently, significant variations in cell current may be seen during a charge or discharge event. These variations in cell current are ultimately driven by the overpotential of each cell relative to the string terminals, which in turn is affected by the cell impedance and interconnect/branch resistances in the string. The cell resistance in turn is a function of cell state of charge, state of health and temperature, and as a consequence balancing branch resistances and cell impedances is critical in parallel connected LIBs. However, the initial variation in current will lead to variations in temperature [140] and SoC deviation [155], and may lead to accelerated aging (i.e. state of health loss) in certain cells, although in general the principal degradation mode considered has been SEI layer growth, with the impacts of other degradation modes neglected [9], [146], [186]. Therefore, there is a complex interaction between different factors affecting heterogeneous behaviour in parallel cell strings which warrants detailed investigation of both the relative importance of involved factors and system sensitivity to changes.

A range of studies in the literature demonstrate the potential impacts of differences in thermal gradient, resistance ratio and pack topology on the current distribution within a battery pack. Klein and Park found that for a 1S5P cell string with a 20 °C thermal gradient, an 80 % increase in current was seen in the hottest cell [163]. In comparison Hosseinzadeh et al. [139] showed that with a high interconnect to cell impedance ratio of 0.1, a thermal gradient of 50 °C could be induced with a capacity reduction of 40 % at 5 C. Meanwhile LeBel et al. [154] demonstrated that the selected topology of the pack plays a key role in determining the degree of current heterogeneity. Principally, studies have focussed on assessing the impacts of cell-level variability in capacity and impedance, simulating expected manufacturing differences between cells [180]. However, the interaction between topology

and thermal conditions remains a relatively understudied area, warranting further investigation due to the complex interactions between thermal management, electrical topology and cell performance.

Alongside these considerations, the duty cycle applied to a pack will impact the magnitude of these heterogeneous effects. Most studies focus on constant current duty cycles over full DoD [10], [171], [173], [185], however this is not in general a realistic use scenario as a battery pack will typically see constant power or variable power duty cycles over smaller DoDs in service use. Seldom have either realistic electric vehicle power profiles [10], [146] or dynamic loads [141] been tested. Wu et al. [141] investigated the effects of additional sinusoidal components of a constant current load which was found to dramatically increase temperature rises induced by uneven interconnection resistances in a 12P7S pack, increasing the predicted peak temperature by 35 °C.

Considering in brief the current literature concerning overall effects at the string level, some disagreement exists between authors over the effects of heterogeneities on overall lifetime, with some stating that SoH and aging rates are convergent between parallel connected cells [185], while others find these parameters tend to diverge [9], [148], [149], [171]. It is therefore reasonable to conclude that both types of behaviour are possible, as a function of pack design and operating conditions. This is a key research gap, as heterogeneous aging poses greater challenges during pack design, and therefore a detailed consideration of the operating conditions leading to each type of behaviour is timely and necessary.

Concerning the effects of heterogeneities on aging rate, there is also disagreement in the literature. Several authors have identified no significant impact on aging rate in parallel connected cells with different parameters or operating induced heterogeneities [150], [152], while others note increases in aging rate [9], [142], [146], [151], [186]. Therefore, further investigation of this phenomena is also of importance. It is also notable that many of the models used to investigate pack aging account only for SEI [9], [186] or SEI/CEI growth [142]. This is a limitation as highly heterogeneous currents may promote other aging modes such as particle fracture, and therefore improved modelling is required to identify the effects of heterogeneities in promoting other degradation modes. Meanwhile in experimental studies, limited analysis of the promoted degradation modes using in-situ diagnostics has been carried out, which would be beneficial to understanding of how heterogeneous operating conditions promote certain degradation modes.

Given that within NMC cathode cells the mid-frequency R_{CT} is dominated by the cathode [187], cathode degradation is highly relevant to aging of parallel connected packs, as power fade due to impedance rise may lead to increasingly unbalanced branch resistances. Given that for NMC cells R_{CT} growth has been shown to be inversely proportional to temperature [51], [93], [188], over the lifetime of a pack increasingly heterogeneous currents may be seen despite accelerated degradation of higher temperature cells. However, this effect has not been explored previously in the literature at the pack level. Therefore, an investigation of impedance growth within parallel connected NMC-cathode LIBs is warranted, given the increasingly common use of NMC cells within large battery packs, particularly in the automotive industry.

3.4.1 Literature Gaps and Proposed Research

To conclude the literature review, several key gaps were identified as clear avenues for further investigation in this work as follows:

- The relative effects of topology, capacity and resistance variations and temperature on degree of heterogeneity warrants further investigation.
- The effects of impedance growth of NMC cells on heterogeneities in parallel cell strings at interim (20-45 °C) temperatures warrants further investigation.
- While the interaction between the thermal management system and pack electrical topology is often neglected, further investigation of these effects is necessary.
- The development of thermally controlled test benches to allow accurate experimental measurements to be obtained from parallel cell systems under a range of thermal conditions.
- Exploring the relationship between operating conditions, in-service current, SoC and temperature distributions with cell parameter development and aging rates is necessary.
- Detailed exploration of the underlying degradation modes and physical mechanisms induced in packs is rarely found in the literature, warranting further investigation.

Considering the aims of this work laid out in Chapter 1, and the conclusion of the literature review, it was possible to formulate the overarching research questions of this work into the specific studies presented in Chapters 4-6.

Chapter 4

Experimental Methods and Model Development

The work presented in this chapter is entirely the authors own except where otherwise acknowledged here. The 1S6P pack thermal control test bench was developed as part of a Master's project by Patryk Gawlinski (PG), supervised by Max Naylor Marlow (MNM) and Dr Yatish Patel. PG carried out the detail design of the test bench, which was built and calibrated by MNM and PG. The Peltier control system was based on that developed by Hales et al. [126], who kindly provided basic designs and software. The 1S2P test bench used Peltier control power boards designed by Oisin Shaw and Gavin White, and the PC control software was kindly provided by Ryan Prosser (RP). All other systems were developed and built by MNM. The OCV diagnostic model is derived from work by Birkl et al. [25], [87], as implemented with kind assistance from RP.

4.1 Introduction

This chapter provides background and details of the equipment developed to carry out experiments to achieve the aims of this project. This includes background, detailed design considerations and performance validation of the test rigs used. Additionally, details of the derivation, parameterisation of the two principal models uses in this project are presented. The OCV diagnostic model is presented alongside the cell ECN model, with details of the parameterisation and validation of both models discussed in this chapter.

4.2 Cell Selection

The cells selected for study in this work, was a pouch cell manufactured by Dow Kokam, with a nominal capacity of 5 Ah; the SLPB11543140H5 cell. This is a high-power pouch cell which contains a cathode consisting of blended NMC and LCO (estimated approximately 80/20 % mix respectively, shown via EDX analysis of disassembled cell cathodes), and a graphite anode [192]. The typical datasheet characteristics, as supplied, of the SLPB11543140H5 (hereby referred to as the 'Kokam 5 Ah' are detailed in Table 4.1. The Kokam 5 Ah cell was selected for this work as it is a highly repeatable and consistent cell, therefore allowing robust hypothesis testing and consistent performance between cells, which is of particular importance within parallel cell strings.

Table 4.1: Properties of Kokam SLPB11543140H5 Cell [193], [194]

Cell Identifier	SPLB11543140H5
Anode Chemistry	Graphite
Cathode Chemistry	NMC/LCO
Nominal Capacity	5 Ah
Nominal Energy	18.5 Wh
Maximum Continuous Discharge Rate	30 C
Maximum Pulse Discharge Rate	50 C
Maximum Continuous Charge Rate	2 C
Upper Voltage Limit	4.2 V
Lower Voltage Limit	2.7 V
Nominal AC Impedance	3 mΩ
Operating Temperature Range	-20 °C - 60 °C
Weight (Nominal)	132 g
Width (Nominal)	43.0 mm
Length (Nominal)	142.5 mm
Thickness (Nominal)	11.7 mm
Volume (Nominal)	0.0178 m^3
Gravimetric Energy Density (Nominal)	140 Wh/kg
Volumetric Energy Density (Nominal)	1040 Wh/L

4.3 Development of Experimental Equipment

In this section, the development of the principal test rigs used in this work is discussed, and where appropriate the validation of the equipment is presented.

4.3.1 Single Cell Testing

Single cells were tested using custom test fixtures, of which two models were used. A standard fixture was used for testing that did not require regular changing of the cells (shown in Figure 4.1 a), while a quick-release test fixture was designed and used for experiments where cells would be regularly switched (shown in Figure 4.1 b). In both cases brass contact blocks were used to make the intermediate connection between the cell tabs and the cycler cables.

In all cases the brass contact blocks were cleaned before connections were made, firstly using an abrasive (P400 Wet/Dry Glass Paper or Medium Grit 3M Scotchbrite Abrasive Pads) and then by cleaning sequentially with Acetone and Isopropanol. Cell tabs were typically cleaned using Acetone

(a) (b)

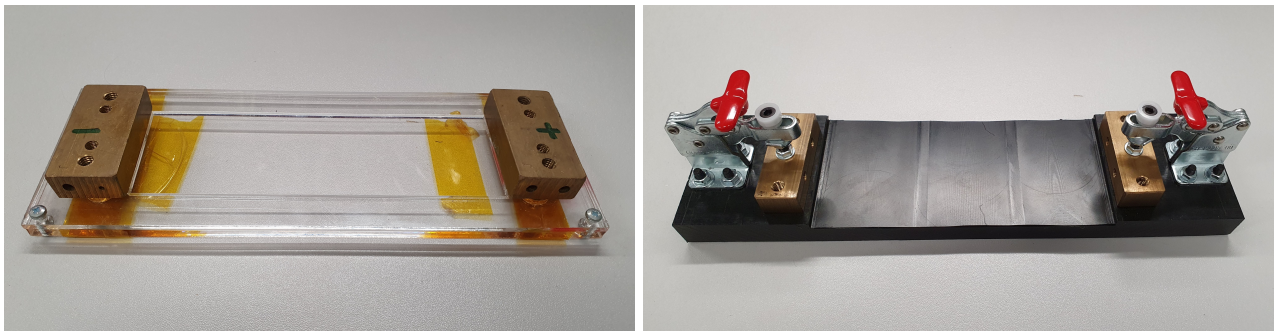


Figure 4.1: Images of single cell test fixtures used. a) Standard fixture. b) Quick-change fixture.

Table 4.2: Specifications of battery cyclers used in this work for pack level testing. FSR denotes Full Scale Range

Cycler	**BaSyTec XCTS Mk I**	**Maccor 4300**
Channel Current [I]	50	50
Channel Voltage [V]	0-4.5	0-5
Current Ranges	25 A, 50 A	500 mA, 5 A, 50 A
Current Resolution [mA]	2	5 mA
Voltage Resolution [mV]	0.1	1 mV
Current Precision	50 mA +0.1% up to 25A 100 mA +0.1% up to 50A	±0.025% of FSR
Voltage Precision	2.5 mV	±0.02% of FSR
Min. Pulse Length [ms]	10	

and Isopropanol sequentially. Where it was critical to ensure that contact resistance between the cell tabs and the brass contact blocks was minimised, for example during EIS or HPPC measurements, the contact resistance was measured using a Keithley 2182A Bench Digital Multimeter, which can measure up to 1 μV in DC mode. For contact resistance measurements, a current of 1 A was applied to the cell using the attached cycler or potentiostat, and the voltage drop between the contact block and the cell tab measured and recorded allowing direct calculation of the contact resistance. Given the applied current and voltage resolution, this implies a resolution in the measurement of 1 $\mu\Omega$, below the expected order of magnitude of the contact resistance which is 50-500 $\mu\Omega$.

Testing of single cells is typically carried out in a 4-electrode mode where the working and counter electrodes of the cycler are attached to the cathode and anode tabs of the cell respectively. The voltage sense and reference (positive and negative sense electrodes) are attached at separate points to the brass contact blocks in order to minimise the influence of the contact resistance between the battery cycler terminals and brass contact blocks on the measured voltage response of the cell.

4.3.2 Design and Development of Pack Test Benches

Battery packs typically operate at higher voltages than single cells, however the packs investigated in this work were parallel cell strings and therefore operate in the same voltage ranges as single cells. Therefore, it was possible to use battery cyclers typically designed for use with single cells to carry out pack testing as the voltage ranges were appropriate. The detailed specifications of the battery cyclers used to carry out pack level testing can be found in Table 4.2.

The main aim of this work was to investigate the effects of various heterogeneities on the performance and lifetime of battery packs, specifically in parallel cell strings where there are often unmonitored heterogeneities in conditions between individual cells. Therefore, specifically designed pack test benches were required to both a) control external conditions and b) monitor behaviour of each cell. Principally this means controlling the cell temperatures individually to allow application of a desired thermal gradient and monitoring the current distribution within the pack. Two versions of the pack test bench were produced: firstly a single test bench designed for model validation and to explore thermal effects on instantaneous performance within 1S6P parallel cell strings (similar to the system previously investigated by Liu et al. [9]). Secondly, a test bench capable of simultaneously testing 6 1S2P packs was developed, to allow investigation of the impact of thermal heterogeneities on pack lifetime, which has been identified as a significant research gap. In both cases, Peltier element surface cooling via a large aluminium heating/cooling plate was selected as the optimal method to control cell temperature. As many elements of the pack test benches, particularly the Peltier element control and thermal management system, are common between the test benches, they are discussed together.

4.3.3 Peltier Element Thermal Control

In order to apply a desired thermal gradient to the cells within the packs, by controlling the thermal boundary conditions, it was required to directly control the surface temperature of the cells. This was accomplished using Peltier elements to either cool or heat an aluminium heat distribution plate which was in direct contact with each broad face (top and bottom) of the cell. The use of heat distribution plates of high thermal conductivity ensures that a homogenous temperature is applied to the cell surface, and similar designs (of which a schematic cross-sectional diagram and CAD image are shown in Figure 4.2 a and b) were used for both the 1S6P and 1S2P test benches. In both cases, the upper cooling plates were removable to allow insertion of cells as required, using 4 M4 screws. In all cases, the screws were torqued to 0.75 Nm to ensure consistency of the thermal contact between the cell and heating plate. While either thermal paste or thermal interface material would have improved the thermal contact between the plates and cell surfaces, this was not used to simplify the setup procedure of the test benches.

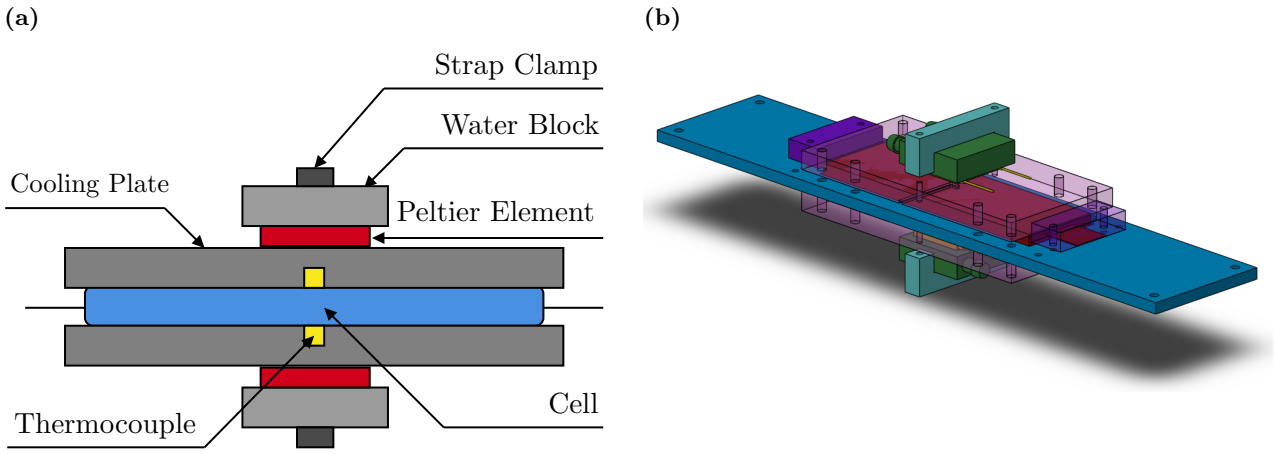


Figure 4.2: Schematic representation of Peltier surface cooling assembly. a) Cross-sectional schematic of assembly. b) 3-D CAD representation of surface cooling assembly

Peltier elements have been previously used by researchers in the Imperial College Electrochemical Science and Engineering group to produce a variety of thermally controlled test benches to probe

performance of LIBs under a range of thermal conditions [126], [133], [165]. Two versions of the Peltier control system were used in this work. Firstly for the 1S6P test bench 3 control systems each capable of controlling 4 independent Peltier elements, derived from work by Hales et al. [126], was reproduced and used without significant modification. Secondly, for the 1S2P test benches, a lower cost and more compact system was developed and is described here. As the Peltier elements operate at a relatively low efficiency, and in the case of cooling, the cell will heat on the reverse side, a method for rejecting this waste heat was required. To accomplish this, a water-cooling circuit was used in both test benches, with a chiller providing cool (15 °C) deionised water to the aluminium water blocks which were attached via a thermal interface compound to the elements.

For the 1S2P test bench, power was supplied via a custom H-bridge motor controller designed and built for control of Peltier elements. In order to control the temperature of the system a Proportional Integral Derivative (PID) control scheme was implemented and programmed in a custom applet in C#. The PID coefficients were tuned using the Zeigler-Nicols method to estimate parameters for a no-overshoot controller. The temperature at the centre of each heat distribution plate was measured using a single K-Type thermocouple, situated at the centre of the cooling plate, using PicoLog TC-08 data logger. The applet received temperature data from the TC-08 and calculated the required heating or cooling power based on a setpoint in the software, which was then sent via a serial connection to an Arduino Mega 2560 in the control box. This microcontroller in turn provides an enable signal, direction and pulse width modulated power signal to each slave motor controller board. This system could maintain a controlled setpoint temperature to within ± 0.10 °C at the temperature measurement point over the required operating range (20.0 – 45.0 °C) with applied C-rates of up to 3 C.

4.3.4 Detail Design of 1S6P Pack Test Bench

With the Peltier control system developed, the remainder of the 1S6P test bench could be designed and produced. A schematic layout of the system is shown in Figure 4.3. In the system, a chiller (Hailea HC-100) was used to provide coolant water to each Peltier cooling block. Data logging was achieved using PicoLog TC-08 dataloggers to record heating plate temperatures via a single K-type thermocouple bonded to the outer surface of the cooling plate, while current sense resistor voltage values were recorded using a single PicoLog ADC-24 datalogger, measuring differential voltage in the ± 39 mV range over each current sense resistor.

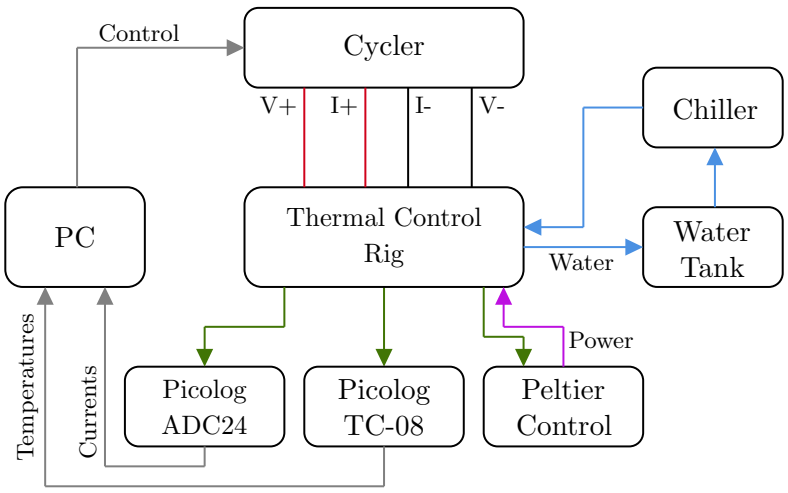


Figure 4.3: Schematic representation of 1S6P surface cooled test bench

In order to connect the cells needed in parallel, custom busbars were designed and produced. In this case, a PCB was designed to allow simple design and production. The custom PCB was designed to allow insertion of a single current sense resistor in each parallel branch and a fixed interconnection resistance between each branch. For both, any 4026 package size resistor could be used. All current sense resistors were soldered into the negative busbar, and gold-plated copper shorts (0 Ω resistors) were inserted on the positive busbar to bridge the current sense resistor positions. The circuit diagram of the 1S6P test bench as completed is shown in Figure 4.4 a, while Figure 4.4 b shows an image of the completed test bench. Cells were attached to the PCB using 15 mm thick Acrylic contact blocks bolted through the PCB to the baseplate of the test bench, which were torqued to 0.75 Nm in all cases. It was found that the measured contact resistance was < 100 $\mu\Omega$ in all cases. On each setup, the contact resistance was measured using a Keithley 2182A Bench Digital Multimeter to ensure consistency of contact resistance. The total magnitude of the contact resistance was 5 times smaller than the current sense resistor and given the cell impedance of 2.5-6.0 mΩ over the temperature range investigated did not lead to significant changes in the interconnection resistance ratio when maintained within the acceptable range defined.

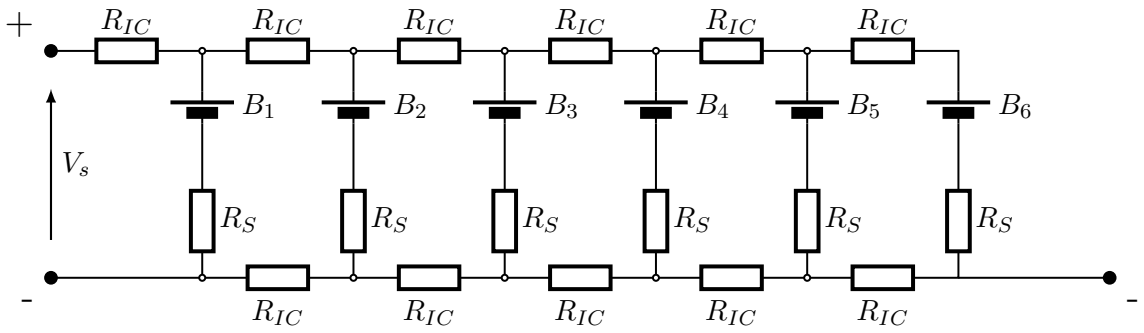
4.3.5 Detail Design of 1S2P Pack Test Bench

In order to carry out multiple degradation experiments simultaneously, a simplified version of the 1S6P test bench was developed for testing 6 1S2P parallel cell strings. In this case, the design of the cell thermal control system was retained, however new PCBs were designed. In this case, as it was essential to be able to rapidly change the cells as it was intended to characterise cells from the packs individually during degradation, and therefore the bolted contact blocks were replaced with toggle clamp retained contact blocks, and the PCB was soft-gold plated to reduce contact resistances. However, this change slightly increased contact resistances, typically to 200-250 $\mu\Omega$ and so in all cases contact resistance was measured using a Keithley 2182A Bench Digital Multimeter to ensure consistency of contact resistance between runs and cells within the pack.

A schematic layout of the 1S2P pack test bench is shown in Figure 4.5. In this configuration, currents and temperatures are logged using TC-08 dataloggers. PID control is implemented in an applet running on the PC, which reads the temperatures and then serially communicates the desired control point to the Peltier Controller, with an Arduino Mega 2600 handling onboard control. Figure 4.6 a shows an image of the overall configuration of the pack test bench, configured to test 6 1S2P packs. As can be seen, the test bench was built in a rack cage, with the battery cycler (BaSyTec 50 A XCTS G1), PC and custom Peltier controllers at the top, and the water chiller at the bottom of the rack. The individual pack test fixtures were distributed between on three full depth pull out shelves, with two fixtures per level, as shown in Figure 4.6 b. Each shelf contained both the test fixtures and PicoLog TC-08 dataloggers used for current and temperature sensing and was designed to be self-contained. The levels were separated by 1 mm Mild Steel sheeting to provide isolation in the event of cell failure and fire.

In the 1S2P test bench, cooling water was provided by a CW-5200 Chiller with an internal pump. The coolant, deionised water, was distributed to each level of the rack via quick disconnect fittings to allow rapid maintenance and switchover of cells. The pipework was designed to ensure a similar length flow path through each individual pack test fixture, to ensure sufficiently low temperature coolant was available for heat rejection from each Peltier element. A spill tray was attached below each level to

(a)



(b)

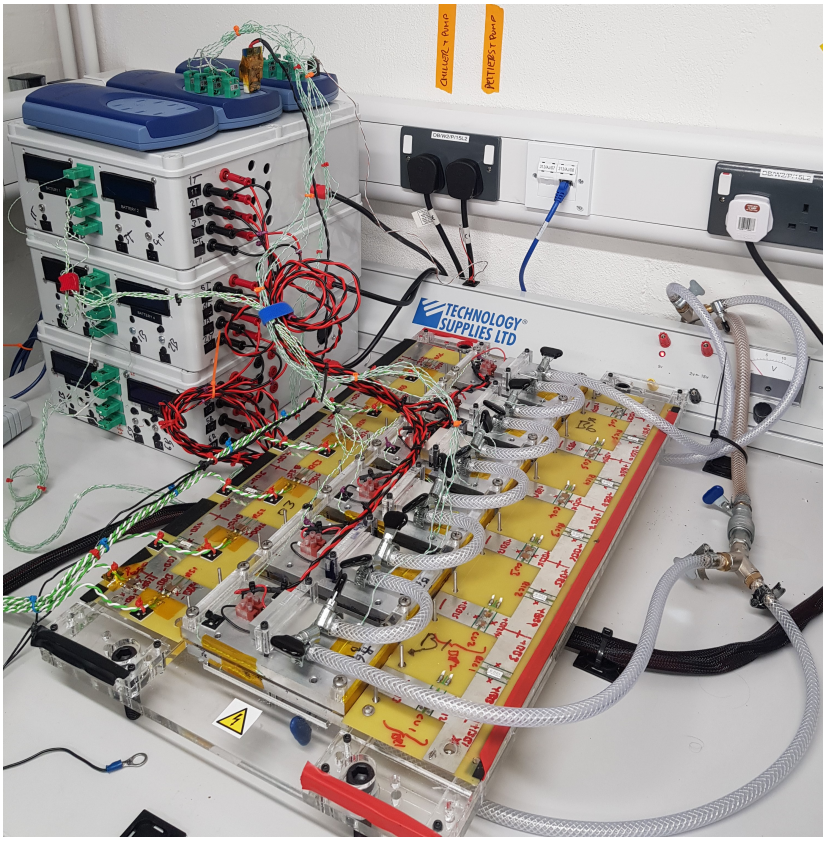


Figure 4.4: Circuit diagram and image of 1S6P test bench. a) Circuit diagram of test bench, showing the reconfigurable nature of the circuit between a 'U' and 'Z' topology. b) Image of full test bench setup, including Peltier controllers

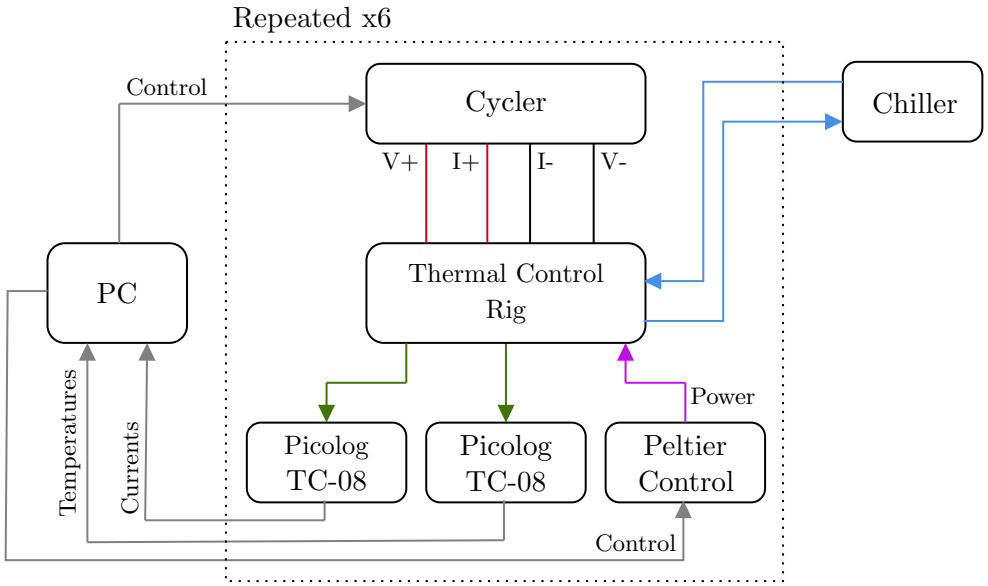


Figure 4.5: Schematic representation of 1S2P surface cooled test bench

ensure any coolant leaks would be collected and returned to the sump at the bottom of the test bench.

4.3.6 Calibration of Pack Test Benches

Both test benches required calibration of resistances and sensing in order to ensure accurate measurement of currents, and to ensure consistency between modelling and experimental results. Current sensing within the parallel cell strings was accomplished using current shunt resistors to measure the individual string currents, as well as the total applied current to the pack. Current sense resistors with a nominal value of 1 mΩ and 2 mΩ were used (Bourns CSS4J-4026R-1L00F and CSS4J-4026R-2L00F respectively) with a nominal 1 % accuracy. These current sense resistors were in part selected due to their 4-wire configuration allowing for increased measurement accuracy alongside their low temperature coefficient of 75 ppm/°C, which ensures that resistive heating of the current sense resistors does not lead to drift in current measurements.

In both cases, once assembled, the resistances of the busbar boards and current sense (or shunt) resistors were measured using a potentiostat (Biologic VMP-3) to apply a current over the current sense resistors, and the voltage drop over the current sense resistors was measured using the sense cables attached. A linear voltage sweep between the working and counter electrodes, slewing at a rate of 2500 mV/s between 0 and 10 mV (selected to give a peak current of approximately 10 A, the maximum allowable current that could be applied with the VMP-3). The true resistance of the current sense resistors was calculated by fitting a straight line to the current response, meaning that the gradient of the line gave the resistance of the cell, by Ohms law. For calibration of various resistances throughout the busbar the same approach was used, measuring the response between marked points on the busbars.

Once calibrated, the voltage drop across each current sense resistor was recorded in the 1S2P test bench using a PicoLog TC-08 data logger, which has a 20-bit analogue-to-digital converter, therefore giving a voltage resolution of 67 nV in the ± 70 mV range. In the 1S6P test bench, a PicoLog ADC-24 datalogger was used, with a 24-bit analogue-to-digital converter, giving a voltage resolution of 2.3 nV in the ± 39 mV range. Given the current sense resistor values and expected operating currents this is

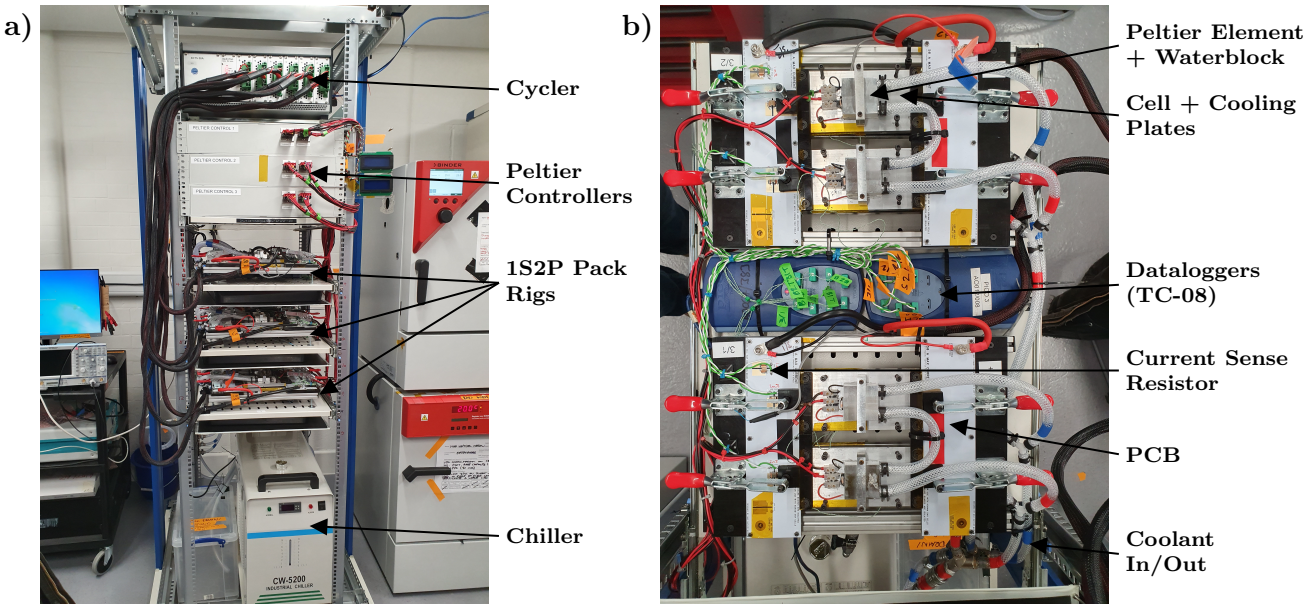


Figure 4.6: Annotated images of 1S2P pack testing rig. a) Full system. b) Layout of 2 pack fixtures on a rack shelf

an adequate resolution to ensure accurate recording of cell currents.

In order to ensure that the cell surface temperature was controlled to the desired setpoint, a calibration cooling plate was manufactured with 4 additional thermocouple slots milled into the surface. K-type thermocouples were embedded into this plate using thermal epoxy, at locations shown in Figure 4.7 a, and the plate was setup in one of the 1S2P pack test fixtures. A cell was introduced and cycled at 2 C to test the uniformity of cell surface temperature with a heat-generating cell introduced. After the setpoint was set to 20 °C and allowed to settle, a 600 s discharge followed by a 600 s charge was applied. The setpoint was then moved to 45 °C and the process repeated.

Figure 4.7 b shows the temperature at each measured location and the applied current. It is expected that the outer measurement points will be at a slightly lower temperature, as the Peltier element is both situated centrally, leading to some convective temperature loss towards the edges of the plate. Additionally and the control sensor used is T_M, which will also lead to somewhat lower temperatures further from the plate midpoint. As can be seen in Figure 4.7 c, the heating plate performed well, with a maximum difference between measurements (typically between $T_{R,O}/T_{L,O}$ and T_M) of 0.82 °C at a setpoint of 20 °C, and a maximum difference of 1.26 °C at a setpoint of 45 °C. The plate was also moved over the entire temperature range used in Chapters 5 and 6 (20-45 °C) and rested at each setpoint for 600 s to evaluate the system settling time (Figure 4.7 d). The maximum difference was again found to occur at a setpoint of 45 °C, due to the increased temperature difference between the plate and ambient air leading to increased convective losses. The maximum temperature difference in this case (Figure 4.7 e) was found to be 1.27 °C. As the magnitude of thermal gradients under investigation was an order of magnitude greater than the maximum temperature differences measured, including under typical cycling loads, the surface cooling test fixtures were deemed sufficiently accurate for use. While some overshoot in the PID control was also seen, this was not deemed an issue as all planned measurements were at steady-state temperatures.

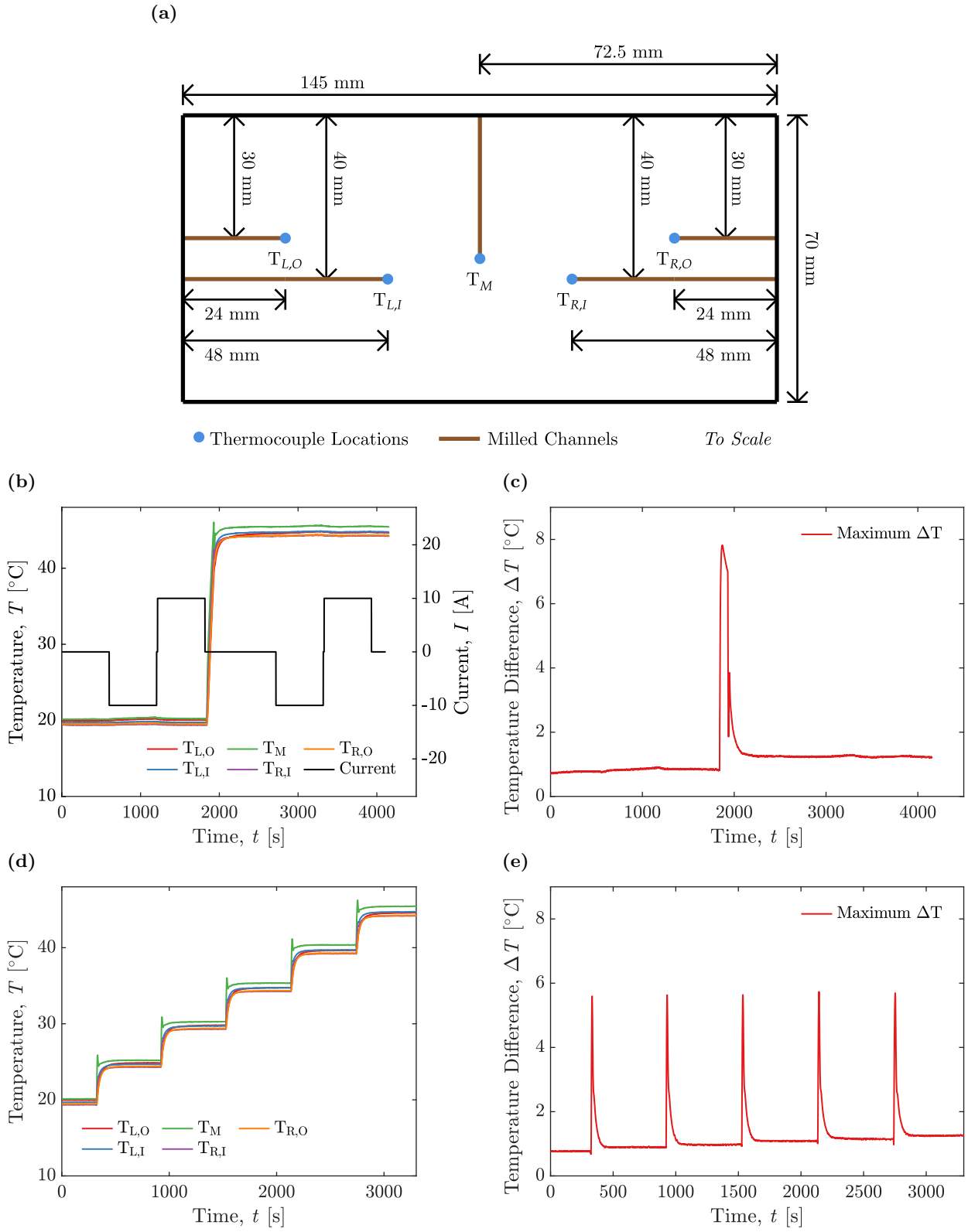


Figure 4.7: Calibration temperature results for surface cooling fixture. a) Schematic showning the location of the additional thermocouples used during calibration. b) Calibration temperature under 2 C load, charge and discharge. Initial setpoint = 20 °C. setpoint moved to 45 °C at t = 1800 s. c) Calibration temperature residual under 2 C load. e) Calibration temperatures under no load, with temperature setpoint steps of 5 °C. e) Calibration temperature residual under no load.

4.4 Diagnostic Model Development

In order to use the cell OCV response as a quantitative as well as qualitative diagnostic tool, it was necessary to fit a model for the initial behaviour of the cell, which then allows predictions to be made about OCV behaviour over the lifetime of cells, and for quantitative measurements of cell degradation modes to be obtained. In order to achieve this goal, it was necessary to fabricate half cells to obtain reference measurements of the half-cell voltage response, estimate the initial loading ratio and anode/cathode offsets and fit the model. This allowed for both the prediction of the qualitative changes in cell OCV response over the life of the cell alongside quantitative fitting of the model to identify the proportion of combined degradation modes occurring in an aged cell. Dubarry et al. [74] highlighted the complementary nature of ICA and DVA analysis, as whilst capacity quantification is clearer using DVA, using ICA it is simpler to decipher degradation modes. However in this work an OCV model was selected for use, derived from work by Birkl et al. [25], [87].

4.4.1 Cell Disassembly, Coin Cell Fabrication and p-OCV Measurement

To obtain an accurate fit to the OCV curves from full cell measurements, reference half cell curves were required to identify the individual voltage response of each electrode. Therefore, a fresh 5 Ah Kokam cell was discharged to 2.7 V and disassembled in an Argon-filled glovebox to provide sample electrodes for coin cell fabrication. The cell was opened using a ceramic scalpel to cut the pouch, and after opening, the cathode and anode were gently separated and the cell tabs cut. The cell stack was unwound as required to provide electrodes to be harvested into coin cells. In the Kokam cell, all but the outer layers were coated on both sides, and therefore it was necessary to remove the electrode material coating one side of both anode and cathode sheets. This was achieved by wetting with 1-Methyl-2-Pyrrolidinone (NMP, Sigma-Aldrich), and gently wiping the electrode to dislodge the active material. Once single sided electrodes were obtained, circular discs of 16 mm diameter were punched out and rinsed using 1 M dimethyl carbonate (DMC, Sigma-Aldrich), before vacuum drying at 45 °C for a minimum of 1 hr to remove any remaining DMC. The as-prepared electrodes were assembled into CR2032 form-factor coin cells with lithium anodes (0.45mm thickness, 15.6 mm diameter), a polypropylene separator (Celgard 2400, 25 μm) and filled with 100 μL of 1.0 M $LiPF_6$ in a 1:1 mix of ethylene carbonate/DMC (Sigma-Aldrich). The cells were then crimped and allowed to rest overnight before testing, in order to ensure that electrodes were fully wetted. 8 sample coin cells from both the anode and cathode were prepared to ensure consistency in 2 separate batches.

Once half-cells were been fabricated, the p-OCV response of each half cell was measured using a 10 mA LAND Battery Cycler. In each case, the cells were cycled under a constant current load at C/40, with the current magnitude selected based on the estimated capacity of the anode and cathode, calculated based on the area of the harvested electrodes divided by the approximate total area of anode and cathode in the cell (in this case 0.05 mA). The anode was cycled between 0.01 and 1.5 V, while the cathode was cycled between 4.3 and 3.0 V. Cycling was carried out at room temperature, which was 23 °C ± 2 °C. Reference measurements from a separate fresh Kokam 5 Ah cell, from the same batch, were carried out by discharging the cell at C/20 (0.25 A) using a BaSyTec XCTS G1 Battery Cycler. The cell was initially charged at 1 C to 4.2 V using a CC-CV protocol with a cutoff current of C/100 (0.05 A), which was followed by a 1 hr rest period and subsequent C/20 discharge. All measurements on the full cell were carried out in an incubator (Binder KB53) set to 20 °C. The reference voltage measurements against SoC are shown in Figure 4.8.

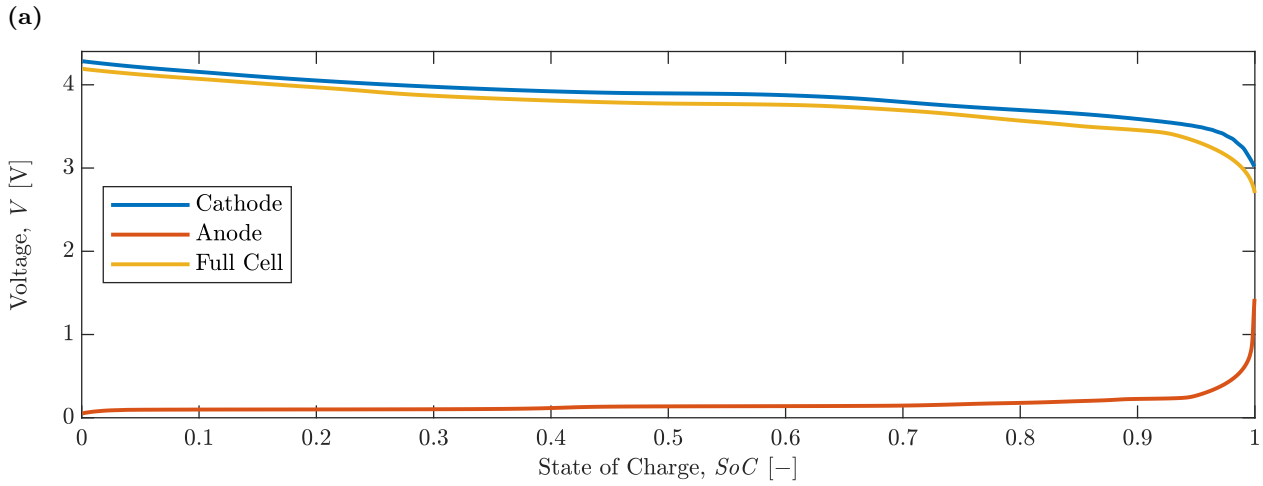


Figure 4.8: Anode, cathode and reference full cell OCV curves, measured at C/40 (half cell) and C/20 (full cell).

4.4.2 Parameterising the OCV Model

As can be seen in Figure 4.8 a, voltage plateaus exist in the OCV response of each electrode, which occur during phase transitions in the cathode [38] or staging in the graphite anode [195] during lithiation or delithiation. Typically, in commercial LIBs, the anode capacity is higher than the cathode capacity, due to the differential loading ratio of the electrodes, while the overall capacity of both electrodes is typically higher than can be accessed safely in a full cell due to both the electrolyte stability window and the need to suppress lithium plating in the anode. Additionally, there is typically an offset found between the SoC of each electrode. In order to identify the capacity and offset of each electrode, an OCV model based approach, derived from work by Birkl et al. was selected [25], [87] due to its simplicity and ease of parameterisation.

Broadly the OCV model functions by adjusting the half cell measured p-OCV responses to minimise the error between the measured cell OCV response and the simulated OCV response based on a given alignment of half cell OCV curves. This allows identification of electrode capacities and offsets for a given cell SoH, and therefore by comparing the identified cell parameters at SoL and EoL it is possible to identify the degradation modes occuring within the cell. This approach differs from that taken by Birkl et al. [25] in that the measured half cell curve is used directly, rather than via fitting a parametric function to the half cell curves as described in [87]. This approach is not appropriate for on-board applications, due to the increased computational effort and memory required, however for offline diagnostics this is adequate. A downside of this approach is it does not allow adjustment of the half cell OCV curves based on degradation specific to certain electrode phases, although in Birkl et al.'s work it is assumed that the relative shape of each half cell OCV curve also does not change.

For a LIB, each cell SoC value corresponds to a given lithiation fraction (denoted z) for both the anode and cathode. As the degree of lithiation in a given electrode increases, the voltage of the electrode decreases. However, the cell voltage range is fixed in order to ensure stable and safe operation, and therefore each electrode may not be fully lithiated or delithiated when the cell is either fully charged or discharged. By adjusting the lithiation limits the shape of the simulated full cell OCV curve may be adjusted while the capacity of the simulated full cell remains constant. The relationship between z, the anode and cathode OCV and full cell OCV are shown in Figure 4.9.

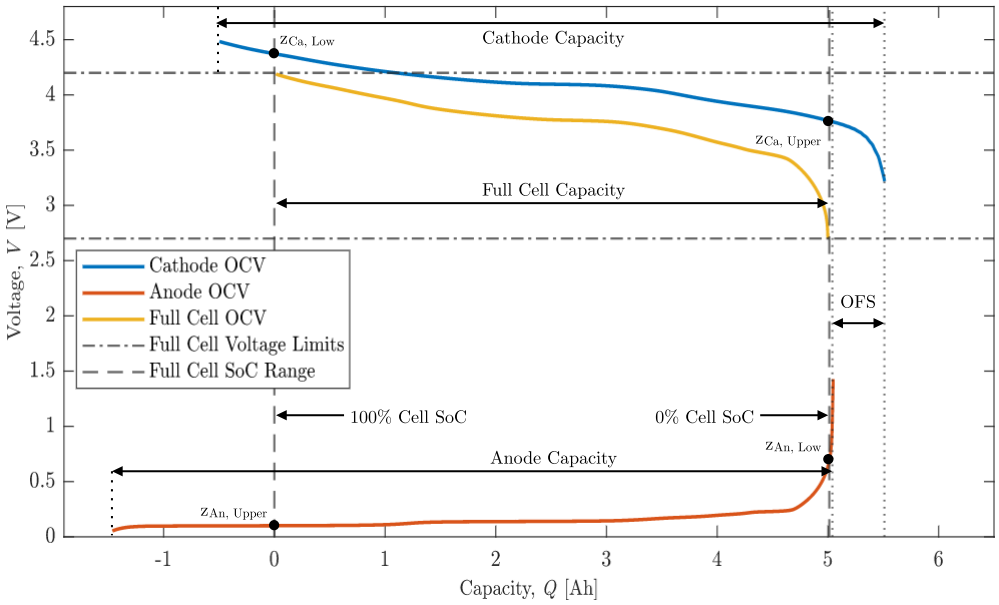


Figure 4.9: Explanatory schematic showing half cell alignment and full cell OCV. The maximum and minimum lithiation state of each half cell at 0 and 100 % full cell SoC, z is marked. Note that half cell voltage curves are adjusted for clarity and are not presented to scale in this figure.

As shown in Figure 4.9, over the full cell SoC range when the cell is fully charged (100 % SoC) the cathode is delithiated to the maximum extent possible within the defined cell operating voltage range. Meanwhile the anode is again lithiated to the maximum extent possible within the given voltage range. It is not desirable to either fully delithiate the cathode, in order to maintain stability of the cathode, or to fully lithiate the anode, to avoid the anode potential becoming negative and inducing lithium plating. Therefore, typically excess capacity is available at SoL in both the anode and cathode. At SoL for a given anode and cathode half cell OCV response, the lithiation fraction for the cathode over the full cell voltage window ranges from $z_{Ca,Low}$ at 100 % full cell SoC to $z_{Ca,Upper}$ at 0 % full cell SoC. The corresponding values for the anode are $z_{An,Upper}$ at 100 % full cell SoC to $z_{An,Low}$ at 0 % full cell SoC.

Formally the model can be divided into two sections. Firstly and critically, the OCV fitting process is described as follows. Based on two half cell voltages, the full cell predicted voltage is given by Equation 4.1. The quantitative degradation mode fitting is described in 4.4.4.

$$V_{Full}\left(SoC\right) = V_{Cathode}\left(z|_{SoC}\right) - \ V_{Anode}\left(z|_{SoC}\right) \tag{4.1}$$

Where $V_{Full}(SoC)$ is the full cell voltage as a function of full cell SoC, $V_{Cathode}\left(z|_{SoC}\right)$ is the cathode voltage as a function of the cathode lithiation fraction at a given full cell SoC and $V_{Anode}\left(z|_{SoC}\right)$ is the anode voltage as a function of the anode lithiation fraction at a given full cell SoC. The vector of half cell lithiation fractions is defined by Equation 4.2.

$$z = [z_{Ca,\ Low},\ z_{An,\ Upper},\ z_{Ca,\ Upper},\ z_{An,\ Low}] \tag{4.2}$$

Subsequently the model parameters are estimated by minimising the objective function defined in Equation 4.3.

$$\arg_z \min \text{RSME} = \sqrt{\frac{\sum_i^n (\hat{V}_{Full,\ i}(z) - V_{Full,\ i})^2}{n}} \tag{4.3}$$

Where $\hat{V}_{Full,\ i}(z)$ is the simulated cell OCV at measurement point i for a given value of z, $V_{Full,\ i}$ is the measured cell OCV at measurement point i, and n is the number of measurements. The error between the simulated and measured OCV is minimised in MATLAB 2021a, using the '*lsqcurvefit*' function and trust-region-reflective minimisation algorithm. After minimisation, the vector z is evaluated to extract the individual electrode capacities and offset, using Equations 4.4 - 4.6.

$$C_{An} = \frac{C_{Cell}}{z_{An,Upper} - z_{An,Low}} \tag{4.4}$$

$$C_{Ca} = \frac{C_{Cell}}{z_{Ca,Upper} - z_{Ca,Low}} \tag{4.5}$$

$$OFS = (1 - z_{Ca,Upper}) \cdot C_{Ca} - z_{An,Low} \cdot C_{An} \tag{4.6}$$

Where C_{An}, C_{Ca} and OFS define the anode capacity, cathode capacity and offset respectively. These parameters define the cell capacity and stoichiometry at a given SoH value. C_{Cell} is defined as the cell capacity during p-OCV measurements obtained.

Based on this approach for the reference cell at SoL, the initial loading ratio was estimated based on the ratio of adjusted capacity between the anode and cathode half cells and was found to be approximately 1.146 (the cathode capacity ratio was 1.1057 while the anode capacity ratio was 1.267), which matches values of 1.1-1.3 found in the literature [196], [197]. It is expected that the anode capacity will be in excess when the cell is fully charged, in order to suppress lithium plating.

After error minimisation for the reference cell was completed the predicted OCV response of the cell could be calculated and compared to the measured cell OCV response. Predicted and measured cell OCV responses can be seen in Figure 4.10 a, whilst the voltage residual error is shown in Figure 4.10 b. While the overall RSME was 21.69 mV, for the bulk of the SoC range predicted the error was found to be below 5 mV, with a large contribution to the error at low SoCs, i.e. below 10 % SoC. This was not viewed as a significant issue as the bulk of phase transitions and staging occur at higher SoCs, and so this error does not affect overall fitting. To avoid biasing the fit towards low SoC values, the final 10 % SoC of the discharge is discarded from the calculation of the RSME, an approach derived from Birkl et al. [25]. This fit ultimately resulted in an RSME of 7.63 mV in the OCV fit at SOL.

4.4.3 Simulating Cell Degradation Modes and Effects

Using the half-cell OCVs obtained from the harvested coin cells, the fitted OCV model may be operated in 'forwards' mode i.e. predicting the changes to the full cell OCV response for given changes to the anode and cathode lithiation fractions at EoC and EoD, and the offset. Active material may be lost either lithiated or delithiated state, so 5 possible degradation modes are available: $\text{LAM}_{\text{Ca, Delithiated}}$, $\text{LAM}_{\text{Ca, Lithiated}}$, $\text{LAM}_{\text{An, Delithiated}}$, $\text{LAM}_{\text{An, Lithiated}}$ and LLI. It is critical to note that whilst in 'forwards' mode, it is possible to simulate loss of lithiated or delithiated active material, it is not possible

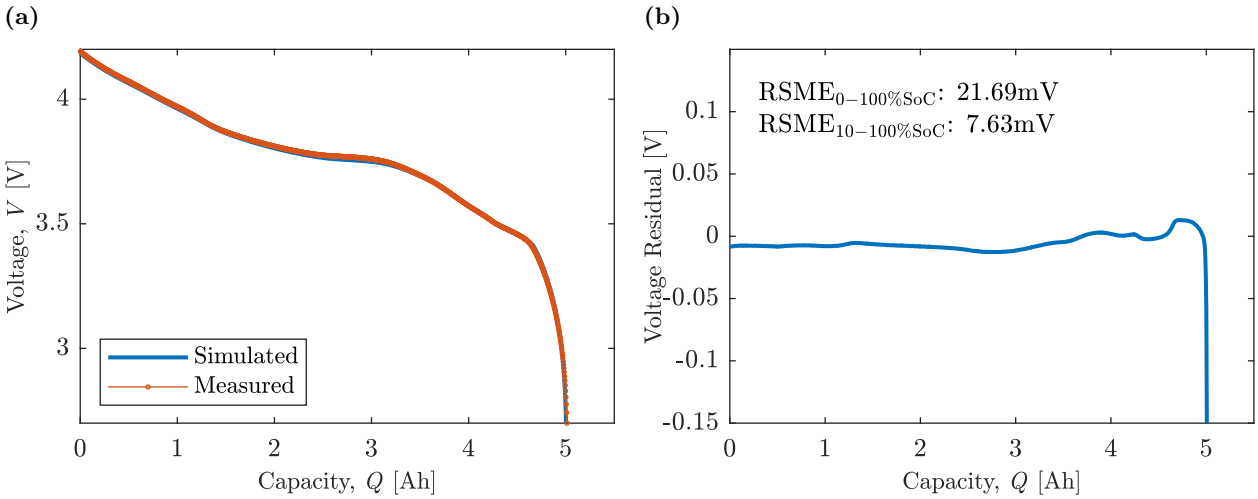


Figure 4.10: a) Simulated OCV curve and measured p-OCV at C/20. b) Simulated OCV voltage residual and RSME. RSME calculated both over full SoC range and from 10-100 % SoC to avoid bias.

when diagnosing degradation to make this distinction. This is because when fitting to experimental data. Using these simulated translations of the full cell OCV response, it is possible to comment qualitatively on the implications of changes in experimentally derived OCV results. As an example, the changes to the simulated full cell OCV curve are shown in Figure 4.11, with simulation results for each mode up to 20 % degradation are shown:

- **Loss of Delithiated Anode** – Loss of Delithiated anode material leads to a scaling of the anode half-cell OCV curve, with the EoD position ($z_{An,\ Low}$) fixed (Figure 4.11 a). Due to the excess anode capacity in the cell, this leads to negligible changes in the simulated OCV response until there is no longer any excess anode, and minimal changes to the full cell capacity. This is due to the fact that the initial cell stoichiometry identifies an approximately 26 % excess capacity in the anode at EoC. Some small changes to the full cell OCV response are identified, with an increased voltage at the anode voltage plateaus at 1.75 and 4.75 Ah, sharpening these plateaus.

- **Loss of Lithiated Anode** – Loss of lithiated anode material leads to a scaling of the anode half-cell curve with the EoC ($z_{An,\ Upper}$) position fixed (Figure 4.11 b). Qualitatively this leads to a shift to lower capacity values of the anode voltage plateau initially occurring at 4.75 Ah and a significant reduction in overall cell capacity. The voltage at the anode voltage plateaus at 1.75 and 4.75 Ah decreases, reducing the prominence of these plateaus,

- **Loss of Delithiated Cathode** - Loss of delithiated cathode material leads to a scaling of the cathode half-cell curve with the EoD ($z_{Ca,\ Low}$) position fixed (Figure 4.11 c). Loss of delithiated cathode leads to an overall reduction in cell voltage and a leftwards shift of all cathode voltage plateaus. It is noted that at 10 % simulated degradation, the changes to the cell OCV response is minimal, although in simulations of higher levels of degradation the movement was more significant. This is due to the 10 % excess cathode capacity at EoD leading to minimal changes of up to 10 % loss of delithiated cathode, and implies that limited loss of delithiated cathode will lead to minimal overall capacity loss until this excess capacity is lost.

- **Loss of Lithiated Cathode** - Loss of lithiated cathode material leads to a scaling of the

cathode half-cell curve with the EoC ($z_{Ca,\ Upper}$) position fixed (Figure 4.11 d). This leads to a movement to lower capacities of the all cathode voltage plateaus and a reduction in overall cell voltage. Unlike in the case of loss of delithiated cathode, a reduction in overall cell capacity is immediately seen, due to the additional LLI occuring

- **Loss of Lithium Inventory** – Loss of lithium inventory is caused by the loss of cyclable lithium due to consumption in irreversible side reactions during SEI formation or being trapped in active material which is lost. LLI leads to a leftwards translation with respect to full cell capacity of the anode half-cell curve (Figure 4.11 e). This leads to a reduction in the capacity at which anode plateaus occur and an increase in the capacity at which cathode plateaus occur, due to the shifting cell stoichiometry.

In conclusion, using the initial fitting of the model, it is possible to build a set of qualitative distinctions between different degradation modes and their effects on the full cell OCV response, allowing qualitative descriptions of internal cell degradation modes to be made.

4.4.4 Quantitative Degradation Mode Fitting

While understanding the qualitative effects of different degradation modes is helpful, it is of overall limited use, especially when attempting to identify degradation modes when multiple modes are occurring. For example, a cell which is cycled at high temperature and high rate may see loss of active material due to particle fracture in the electrodes, while also undergoing loss of lithium inventory due to high temperatures promoting irreversible side reactions. As such, a quantitative model is needed to assess such contributions to overall cell degradation. Birkl et al. [25] previously extended the parametric OCV model derived in their previous work [87] to identify degradation modes occurring within cells, by fitting to the cell OCV response. The quantitative diagnostic model described here is a derivation of this work.

The approach taken in this work is outlined as follows. By using the parametric OCV model introduced in Section 4.4.2, it is possible to identify the half cell capacities and cell stoichiometry at any given SoH value for a cell. This assumes that both the cell OCV curve shape does not change beyond translation and scaling, and that p-OCV measurements remain an accurate approximation of the true cell OCV at all measured points. The OCV model is used to identify cell parameters at both SoL and EoL, and subsequently the degree of degradation in each identifiable degradation mode ($\mathrm{LAM_{Ca}}$, $\mathrm{LAM_{An}}$ and LLI) may be estimated using Equations 4.7 - 4.9 respectively.

$$LAM_{Ca} = 1 - \frac{C_{Ca,\ EoL}}{C_{Ca,\ SoL}} \tag{4.7}$$

$$LAM_{An} = 1 - \frac{C_{An,\ EoL}}{C_{An,\ SoL}} \tag{4.8}$$

$$LLI = C_{Ca,\ SoL} \cdot \mathrm{LAM_{Ca}} + OFS_{EoL} - OFS_{SoL} \tag{4.9}$$

Where $C_{Ca,\ BoL}$ and $C_{Ca,\ EoL}$ are the cathode capacity at SoL and EoL respectively, $C_{An,BoL}$ and $C_{An,EoL}$ are the anode capacity at SoL and EoL respectively and OFS_{BoL} and OFS_{EoL} are the

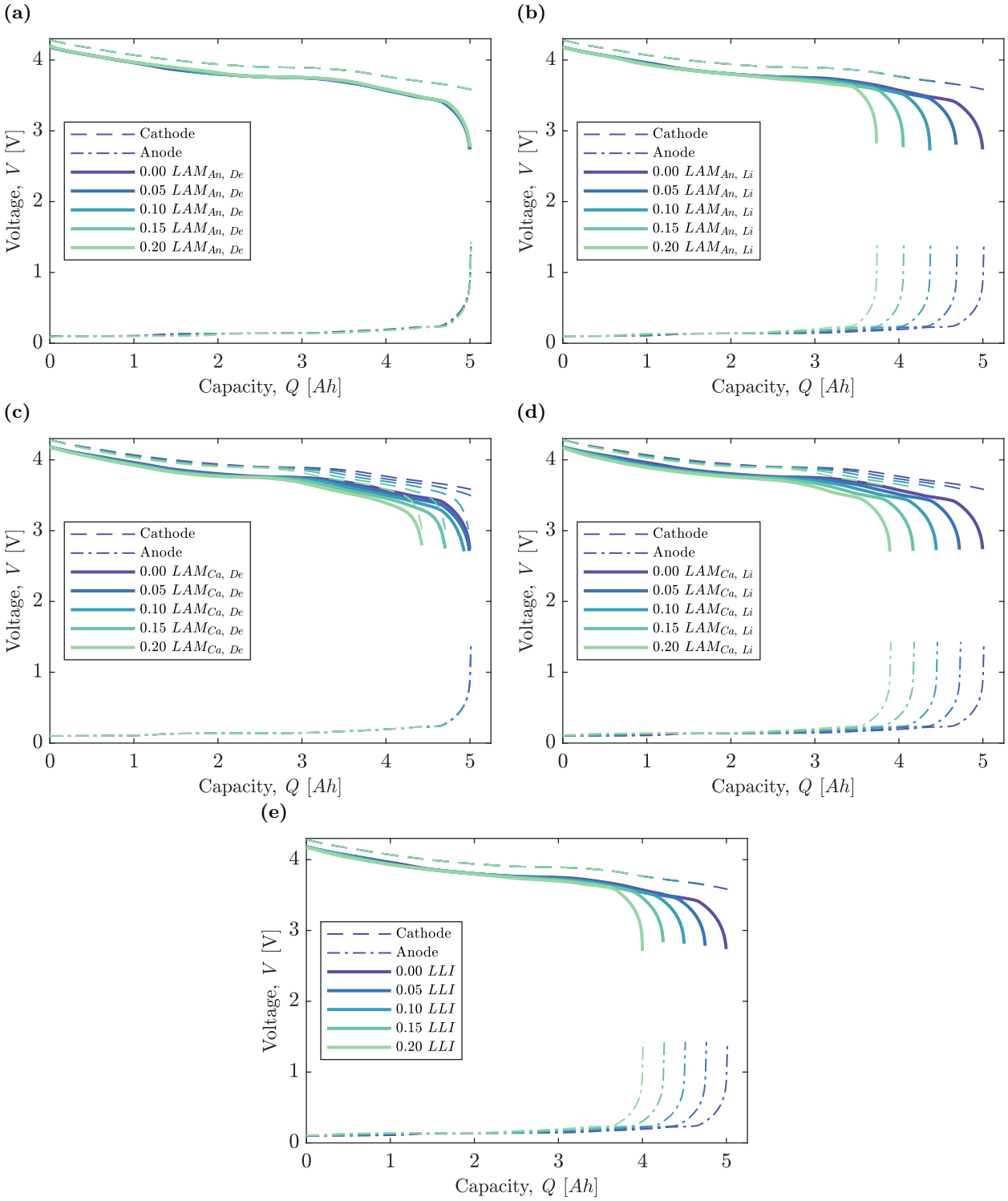


Figure 4.11: Simulated OCV responses for the the following cases; a) OCV response for 0 - 20 % $LAM_{An,\ Delithiated}$. b) OCV response for 0 - 20 % $LAM_{An,\ Lithiated}$. c) OCV response for 0 - 20 % $LAM_{Ca,\ Delithiated}$. d) OCV response for 0 - 20 % $LAM_{Ca,\ Lithiated}$. e) OCV response for 0 - 20 % LLI

stoichiometric offset at SoL and EoL respectively. It is important to note that whilst there are 5 possible degradation modes within the cell i.e. $LAM_{Ca,\ Delithiated}$, $LAM_{Ca,\ Lithiated}$, $LAM_{An,\ Delithiated}$, $LAM_{An,\ Lithiated}$ and LLI, the model is unable to distiguish between loss of lithiated and delithiated active material, as the change to the cell OCV curve from an equal contribution of LLI and $LAM_{An/Ca,\ Delithiated}$ will lead to an identical change to the cell OCV response as an equal amount of $LAM_{An/Ca,\ Lithiated}$. As such whilst it is possible to simulate (as presented in Section 4.4.3) the differing changes to the cell OCV curve caused by loss of lithiated or delithiated electrode material using the parametric model operating in forward mode, it is not possible to identify if lithiated or delithiated active material is lost from measured cell OCV data. As such only total *LAM* for each electrode is considered in this analysis.

4.4.5 Validation of Quantitative Diagnostic Model

In order to validate the quantitative diagnostic model, synthetic voltage curves were generated for the Kokam 5 Ah cell under 5 and 10 % loss in each of the 5 degradation modes singly, and for 1, 4 and 10 % of all modes (referred to as 'mixed-mode'). Using identical processes to those used for fitting experimental data the diagnostic fitting model was used to estimate the degree of each degradation mode occurring. Figure 4.12 a-e summarises the predicted loss in each mode for the 5 and 10 % synthetic single mode losses. For each single degradation mode, the fitting tool is able to accurately identify the dominant degradation mode occurring. In all cases excepting $LAM_{An,\ Delithiated}$ (Figure 4.12 c, with a 3.3 % under prediction of $LAM_{An,\ Delithiated}$), the model is able to diagnose the amount of degradation occuring with <2.5 % absolute error, whilst the diagnosed LAM_{Ca} is accurate to <0.25 % in all cases. Performance in identification of LAM_{An} and LLI is worse, as generally the anode voltage curve is flat. This means the fitting algorithm is biased towards identification of changes to the cathode voltage curve rather than the anode, as a change in lithiation state of the cathode will generally lead to a greater change in full cell voltage. However, in all cases the model is able to correctly identify the dominant degradation mode, and performs sufficiently accurately in identification of the amount of each mode.

Figure 4.13 a-c summarises the predicted loss in each mode for the 1, 4 and 10 % synthetic mixed mode scenarios. In this case again the model is able to correctly identify that both all degradation modes are occurring, and reasonably accurately predict the amount of each mode occurring. The absolute error is <3.5 % in all cases, with typical relative errors in prediction of <10 %. As in practice it is likely that a LIB will undergo multiple simultaneous degradation mechanisms, leading to occurrence of multiple degradation modes, validation in a mixed mode scenario is critical, and indicates that the model performs adequately in quantification of degradation.

4.4.6 Diagnostic Model Overview

To summarise, the models and tools introduced in this section, firstly a model for simulating the effects of 5 identified degradation modes on the OCV curve for the Kokam 5 Ah cell is presented and validated, using half-cell OCV curves to construct the full cell response. The model parameterisation was possible using the OCV model fitting approach pioneered by Birkl et al. [87]. Using this model to fit to experimental data for a full cell, the excess anode and cathode capacity alongside the loading ratio and offsets may be estimated. Secondly, a quantitative diagnostic fitting methodology is presented and validated. The diagnostic tool presented is able to both correctly and accurately identify the

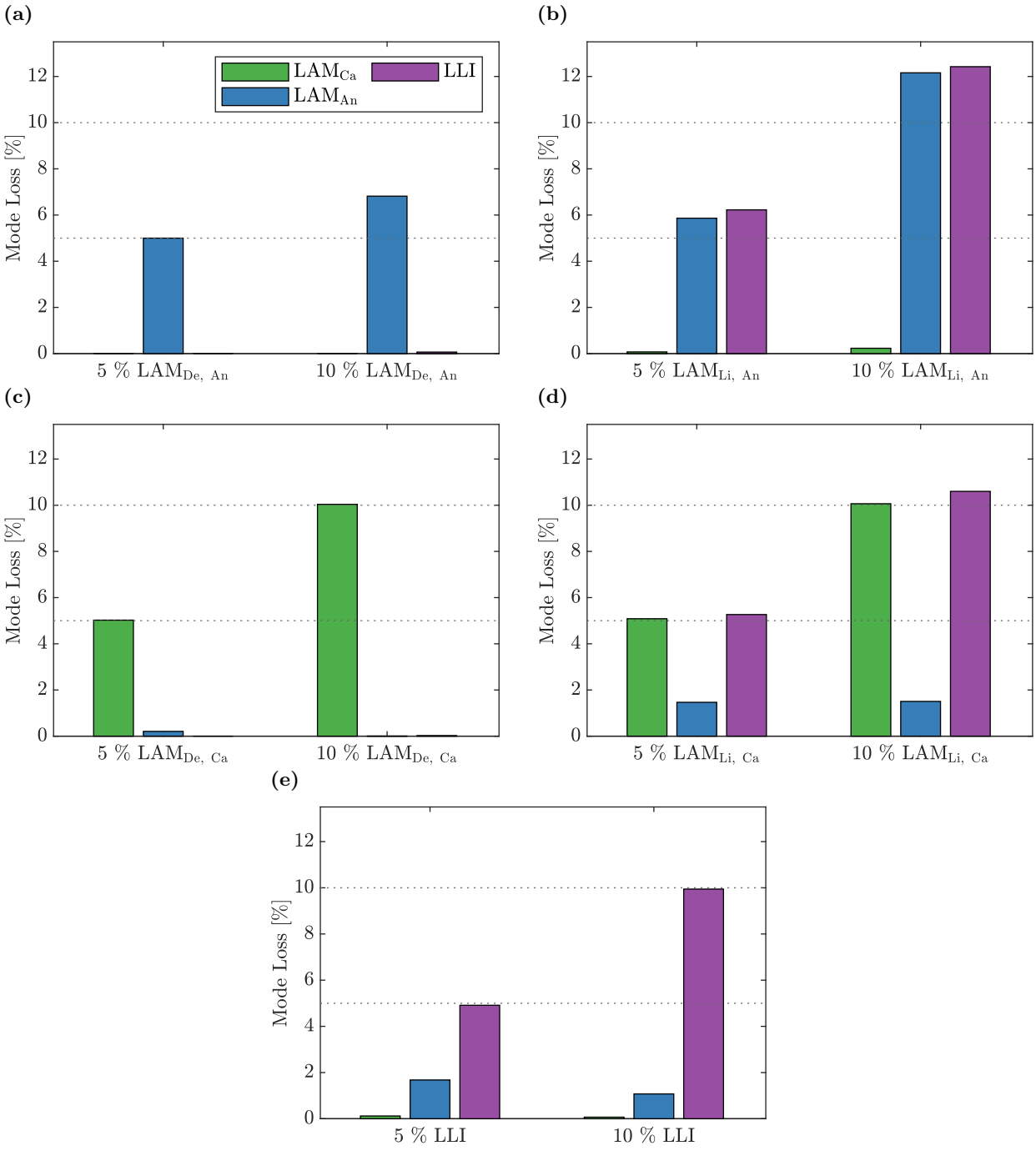


Figure 4.12: Validation of diagnostic model using synthetic single mode degradation OCV curves; a) Identified degradation modes with 5 and 10 % simulated LAM$_{An,\ Delithiated}$. b) Identified degradation modes with 5 and 10 % simulated LAM$_{An,\ Lithiated}$. c) Identified degradation modes with 5 and 10 % simulated LAM$_{Ca,\ Delithiated}$. d) Identified degradation modes with 5 and 10 % simulated LAM$_{Ca,\ Lithiated}$. e) Identified degradation modes with 5 and 10 % simulated LLI. In all cases horizontal lines indicate 5 and 10 % mode loss.

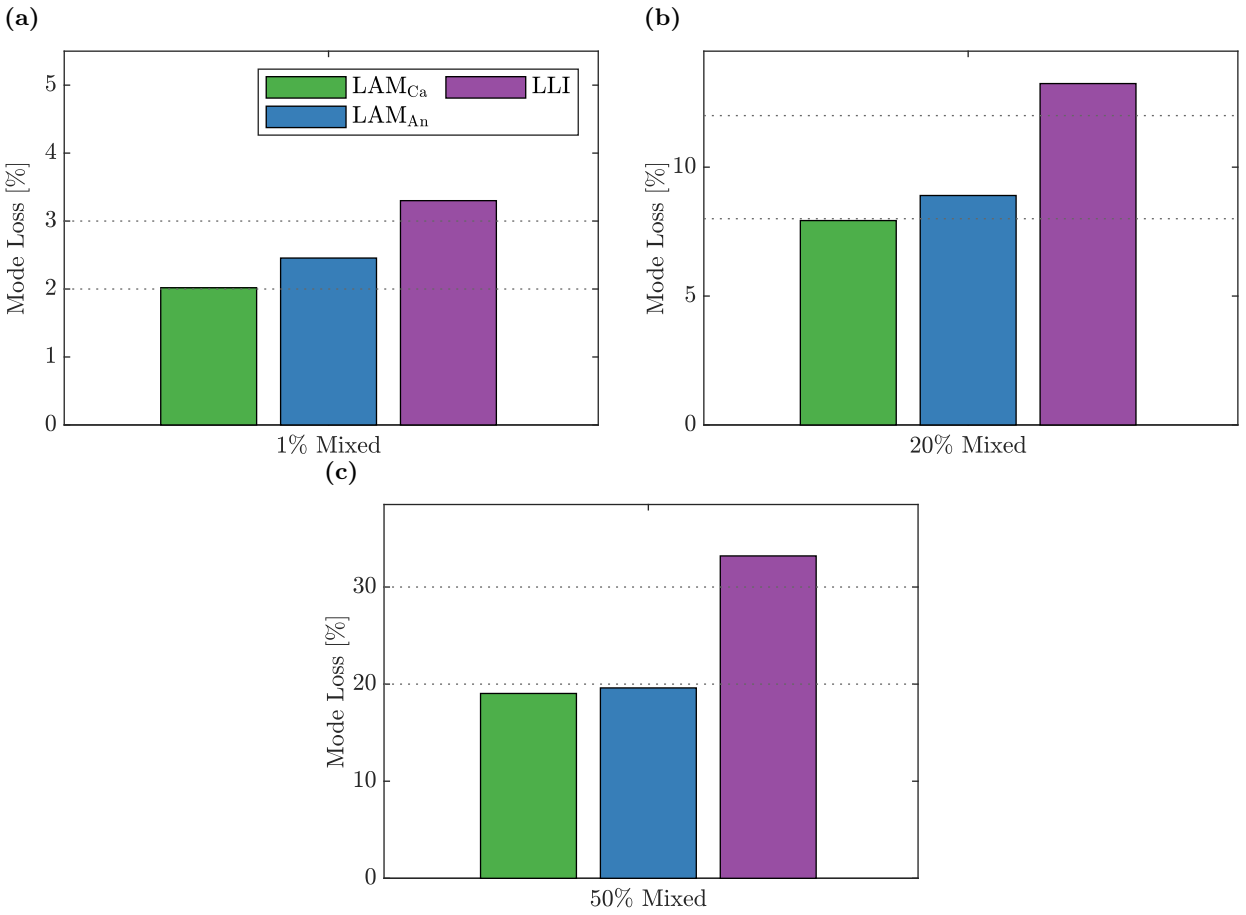


Figure 4.13: Validation of diagnostic model using synthetic mixed mode degradation OCV curves; a) Identified degradation modes with 1 % degradation in each mode (2 % total LAM_{An} and LAM_{Ca}, 3 % LLI). b) Identified degradation modes with 4 % degradation in each mode (8 % total LAM_{An} and LAM_{Ca}, 12 % LLI). c) Identified degradation modes with 10 % degradation in each mode (20 % total LAM_{An} and LAM_{Ca}, 30 % LLI). Horizontal lines indicate the actual total mode losses in each case.

dominant degradation mode from single-mode synthetic OCV curves. The diagnostic tool has also been shown to be able to accurately identify mixed-mode degradation, excepting some inaccuracy in identification of $LAM_{An,\ Delithiated}$. Using these tools it is possible to carry out a detailed analysis of the degradation modes occurring within parallel cell strings, presented in Chapter 6.

4.5 Equivalent Circuit Modelling

As identified in Section 2.6, equivalent circuit models are a useful tool to explore LIB behaviour and have lower parameterisation costs than physics-based models. As a consequence, while ECN models do not provide physical insights into cell behaviour (although some physics-informed ECN models have been proposed [114]), they remain useful for exploring pack level effects and for online use. In this work, an ECN model was selected as appropriate for investigating pack level effects, where an ECN is able to capture the pack behaviour caused by variations in cell temperature, interconnection resistance and overall cell impedance. Other authors commonly explored using ECN models for simulation of pack level effects, typically using 1-RC pair models due to their simplicity and stability in large pack simulations [177], [183], [198]–[201], although higher order RC pair models have also been used [202].

4.5.1 Equivalent Circuit Model: Selection and Background

The form of the model selected was chosen with the ultimate aim of modelling pack behaviour considered. Therefore, the model was selected to allow accurate predictions to be made at the pack level with variations in cell impedance, capacity and temperature as well as changes to the external circuit (interconnection resistance and topology) as parameters for investigation. As such a 1RC pair ECN model was selected as a compromise between accuracy of predictions at the single cell level and stable predictions at the pack level.

The electrical circuit model of the selected 1RC pair model is shown in Figure 4.14 b, consisting of a voltage source, E_m, a series resistance R_0 and a parallel RC branch. In this case, E_m models the cell OCV, R_0 the cell series resistance and the RC pair models the cell dynamic behaviour. It is noted that higher order, i.e. multiple RC pair models are better able to capture the multiple time constant dynamics present in a LIB, however the simpler 1RC model has advantages in terms of stability in multicell systems when predicting cell currents. It was found using higher order models (3RC), when behaviour of a multi-cell, surface cooled pack the higher order models were unable to stably predict the cell current response and as such a simple model was deemed more effective in predicting behaviour. As all the model parameters are known to vary with both temperature and SoC in LIBs, these parameters can be implemented as a 2-D lookup table in the model, allowing all parameters to vary as a function of both.

4.5.2 Equivalent Circuit Model: Experimental

In order to parameterise the model, 4 fresh Kokam 5 Ah cells were selected from a single batch and placed in jigs in a forced air convection incubator (Binder KB23). The pulse discharging experiments were carried out using a BaSyTec XCTS G1 battery cycler. Each cell was charged using a CC-CV protocol at 1 C (5 A) to 4.2 V with a current cutoff of C/100 (0.05 A) and then allowed to rest for 2 hrs. Subsequently 2 C (selected to emulate the expected typical cell operating conditions) current pulses applied with a 1 % SoC passed cutoff (based on the nominal cell capacity) for the initial 10 high

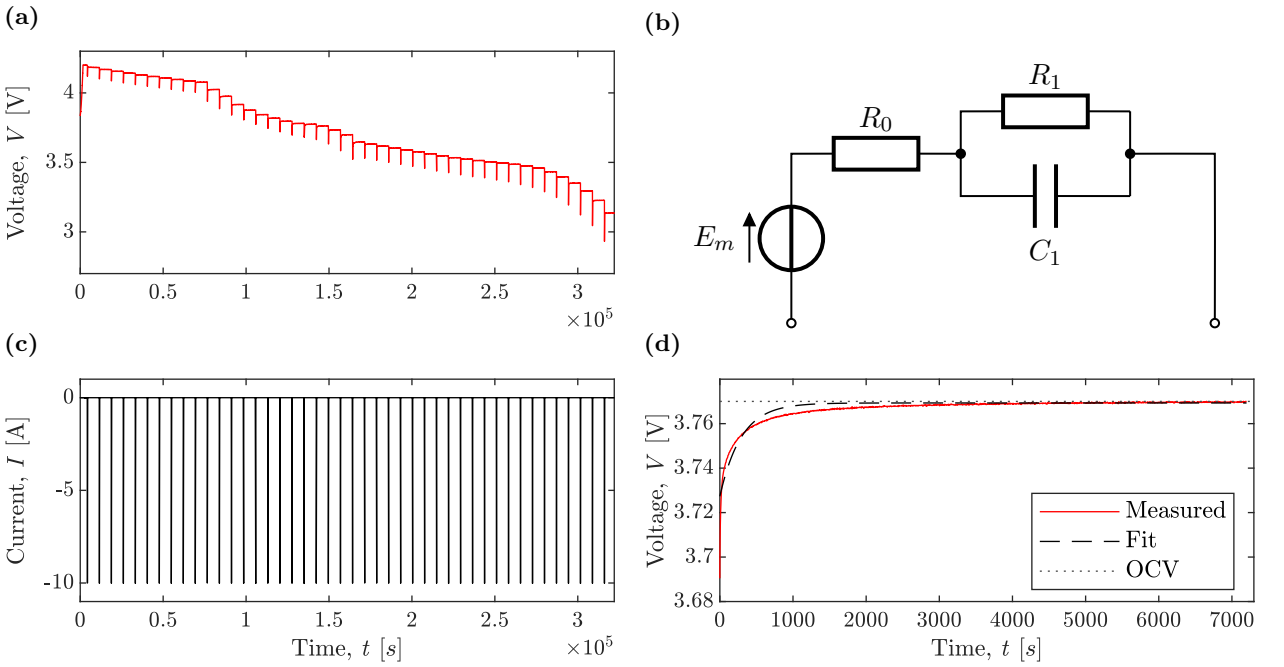


Figure 4.14: a) Example cell voltage response during parameterisation at 20 °C, with 2 C applied current pulses. b) 1-RC pair ECN model used. c) Applied 2 C current pulses during parameterisation. d) Example voltage relaxation and model fit after parameterisation.

SOC pulses, followed by 13 pulses with a 5 % SoC passed cutoff, and finally followed by 1% SoC cutoff pulses until the cell voltage decreased to below 2.7 V. The decrease in the SoC breakpoint magnitude at start and end of discharge was to ensure parameter accuracy in the most dynamic portions of the overall cell voltage response. Figure 4.14 a shows a typical cell voltage response at 20 °C, while Figure 4.14 c shows the applied current profile during the test. This resulted in a total of 40-45 pulses per cell, depending on the overall cell capacity deviation from nominal and test temperature. A 2 hr rest period was allowed between application of each current pulse, to allow the cell to equilibrate to OCV between pulses, and the procedure was repeated at 5 temperatures to provide parameterisation data over a wide temperature range (10 – 50 °C in 10 °C increments).

4.5.3 Equivalent Circuit Model: Parameterisation

Typically, ECN models may be parameterised using either pulse discharge measurements or using EIS. In this work, pulsing methods were used as it allowed parameterisation without use of high cost EIS equipment. An additional challenge with parameterisation using EIS is that measurements are generally taken under no-load, and as the cell polarisation resistance is current dependant, EIS measurements may underestimate the cell resistance. The cell parameters may then be estimated based on the voltage relaxation after the application of current pulses. This approach allows the overall time constants of cell relaxation to be identified and fitted, and resistances to be extracted. More complex approaches have been used, for example by Jackey et al. [23] to fit to the under-load portions of the voltage response between SoC breakpoints. However, in fitting a 1-RC model it is accepted that grouping all cell processes into a single time constant will lead to errors in prediction and therefore a simple approach to parameter identification was selected. All data analysis and fitting was carried out in MATLAB 2020a, using the non-linear least squares fitting tools provided in the Curve Fitting Toolbox. In order to estimate the necessary parameters, i.e. RC time constant, R_0 and

initial voltage in the RC pair, cell terminal voltage during relaxation is approximated by Equation 4.10.

$$V = E_m - V_1 \cdot e^{\frac{-t}{\tau_1}} \tag{4.10}$$

Where V is the cell terminal voltage, E_m is the cell OCV, V_1 is the initial voltage in the RC pair and τ_1 is the RC pair time constant. As the fitting was carried out using a gradient based algorithm, it is key to obtain good initial parameter guesses to avoid minimisation to local minima. As such, the initial guess values for the RC voltage, V_1 and RC time constant, τ_1 were estimated as shown in Equations 4.11 - 4.13.

$$V_{\tau_1} = \Delta V(1 - \frac{1}{e}) \tag{4.11}$$

$$V_1 = V_{\tau_1} - V_{start} \tag{4.12}$$

$$\tau_1 \ = t|_{V=V_{\tau_1}} \tag{4.13}$$

Where V_{τ_1} is the voltage after one time constant has passed (i.e. after the cell voltage has recovered by approximately 63.2 % of the difference between the voltage at the start of relaxation and OCV), V_{Start} is the voltage at the start of the relaxation, ΔV is the overall voltage change between the start and end of the relaxation and t is the time after 1 time constant has passed. After minimisation, the RC pair values R_1 and C_1 could be estimated as shown in Equations 4.14 and 4.15.

$$R_1 = \frac{V_1}{1 - e^{\frac{\Delta t}{\tau_1}}} \cdot \frac{1}{\Delta I} \tag{4.14}$$

$$C_1 = \frac{R_1}{\tau_1} \tag{4.15}$$

Where Δt is the pulse duration in seconds. An example cell voltage response, estimated OCV and applied current for the pulsing portion of the experiment can be found in Figure 4.14 d. It can be seen that the 1RC model does not fully capture the dynamics of the voltage relaxation, however given the high level of simplification of the model, the fits were in general deemed sufficiently accurate. It is noted that the aims of the model were to accurately predict current and capacity distributions within parallel connected cell strings, rather than predict cell voltage behaviour per-se, for which reason a simple model was selected. Therefore, the overall accuracy of the model was deemed acceptable. Once the RC parameters were obtained, the parameters were smoothed using a Savitzky-Golay filter to eliminate expected noise and resampled to account for differences in the location of the SoC breakpoints between different runs due to differences in absolute cell capacity with respect to temperature, thus forming an aligned 2-D lookup table. In order to improve the fit at low SoCs, the OCV was estimated by fitting to a reference p-OCV discharge for the same cell, taken at C/25 and at the same temperature breakpoints as the pulse measurements. It is noted that more complex fitting procedures for higher order models have been proposed, such as the piecewise 'layered' method proposed by Jackey et al. [23] which has the advantage of using multiple state of charge breakpoints and the underload portion of each pulse to improve parameter estimation. However, it was judged that more complex optimisation of parameters would not significantly improve the model fit, as single time constant dynamics are accepted to be

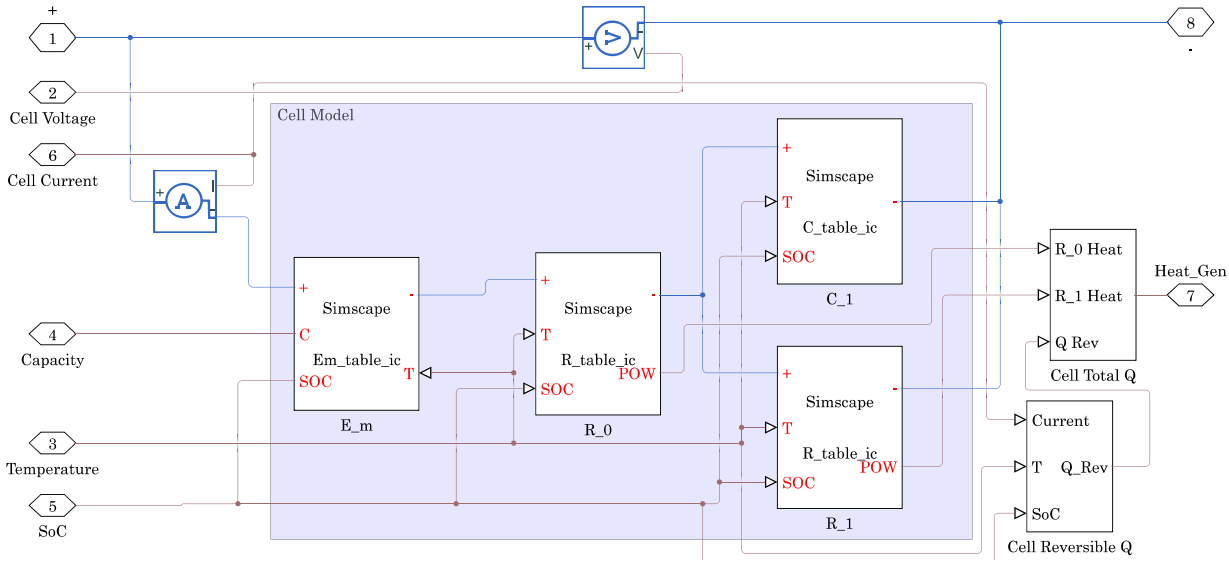


Figure 4.15: ECN Simulink implementation

insufficient to fully describe LIB dynamic behaviour. Finally, after parameterisation, the equivalent circuit model was implemented in MATLAB 2020a and Simulink 10.2, using the Simscape toolbox to implement the electrical network. The model as implemented is shown in Figure 4.15.

4.5.4 Thermal Model: Selection, Parameterisation and Implementation

The cell thermal model was adapted from prior work from Zhao et al. [119], which extensively and accurately thermally parameterised the Kokam 5 Ah cell. Their parameterisation approach, results and adaptation are discussed in this section. In the prior work, Zhao et al. [119] used a 2D heat transfer model, with the cell divided into multiple nodes both in- and through-plane. In this work, it was decided to use a simpler lumped thermal model, effectively modelling the cell as a single lumped node. The temperature distribution within the cell is therefore modelled as a transient lumped heat conduction problem.

Within the cell, the heat generation may be split into 4 separate elements – the irreversible Joule (resistive) heating due to the cell impedance (Q_{Irr}), reversible heating due to entropic changes during lithiation or delithiation (Q_{Rev}), heat generation due to mixing (Q_{Mix}) and heat generation induced by aging side reactions (Q_{Side}) [203]. Therefore, the total heat generation in a cell is given by Equation 4.16.

$$Q_{Gen,Total} = Q_{Irr} + Q_{Rev} + Q_{Mix} + Q_{Side} \tag{4.16}$$

For the purposes of this study, using high power cells with thin electrodes at rates well below their specified maximum, it may be assumed that the heat generation due to mixing is negligible as concentration gradients will be insufficient to generate significant heating, limiting the mixing heat generation [137]. The heat generation due to side reactions may also be neglected, as it is assumed that aging side reactions are slow and therefore generate minimal heat compared to the reversible and irreversible heating [204]. The irreversible heating may be calculated using the resistance values for each circuit node (R_0 and R_1), alongside the applied current (I). The reversible heat generation may be calculated

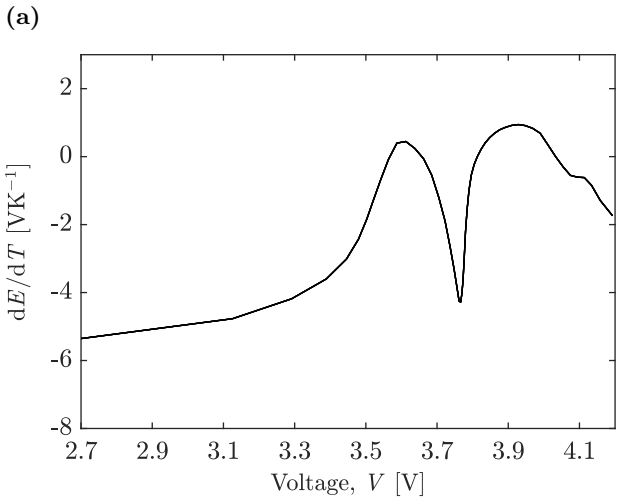


Figure 4.16: a) $\frac{\mathrm{d}E}{\mathrm{d}T}$ values used during modelling, from Zhao et al. [119].

using a lookup table for $\frac{\mathrm{d}E}{\mathrm{d}T}|_{SoC}$, alongside the temperature (T) and applied current. Therefore the total heat generation, $Q_{Gen,\ Total}$ can be found by Equation 4.17. It is noted for highly transient loads, the contribution from R_1 may not be fully realised due to the associated resistance time constant, and so Equation 4.17 is only strictly valid for a constant current load.

$$Q_{Gen,Total} = I \cdot T\frac{\mathrm{d}E}{\mathrm{d}T}|_{SoC} + R_0 \cdot I^2 + R_1 \cdot I^2 \tag{4.17}$$

Where R_0 is the cell series resistance and R_1 is the resistance of the RC pair. Zhao et al. [119] previously measured $\frac{\mathrm{d}E}{\mathrm{d}T}|_{SoC}$ for the Kokam 5 Ah cell, and so the same values are used in this work. In order to parameterise the entropic heat generation, the cell OCV changes at equilibrium as a function of temperature were measured over a range of SoC breakpoints. Zhang et al. [205], previously described this methodology, where the cell is discharged to specific SoC values, allowed to equilibrate and the cell temperature is subsequently varied. The cell voltage change is recorded, allowing $\frac{\mathrm{d}E}{\mathrm{d}T}$ to be estimated. These values may then be used to generate a lookup table of values for the reversible heat generation of the cell. The values of $\frac{\mathrm{d}E}{\mathrm{d}T}|_{SoC}$ measured by Zhao et al. [119] can be found in Figure 4.16 a, after interpolation to align with the SoC breakpoints used for the 1RC ECN lookup table.

Cell physical parameters were used as measured for the Kokam 5 Ah cell by Hunt et al. [133], while thermal parameters for cell internal components are taken Taheri et al. [132], who thermally parameterised a cell of similar NMC chemistry, identifying thermal conductivities and specific heat capacities. These thermal model parameters used can be found in Table 4.3. In order to model the cell as a single lumped thermal model, mass averaged thermal properties were calculated for the cell, based on work from Pesaran [206]. This gave a lumped thermal conductivity of 152.5 $\mathrm{Wm^{-1}K^{-1}}$, and a specific heat capacity of $\mathrm{Jkg^{-1}K^{-1}}$. As the cell has a high aspect ratio, is assumed to loose heat only via the top and bottom surfaces, with heat generated at the centre of the cell, the cell may be considered symmetrical and therefore only half of the cell is considered in the model. The model assumes that no heat is lost through convection through the sides of the cell, or via conduction through the tabs.

Thermal boundary conditions were selected to replicate specific experiments carried out, both for

Table 4.3: Cell physical and thermal parameters used in modelling. Physical parameters were determined by Hunt et al. [133] while thermal parameters were measured by Taheri et al. [132].

Component	Thermal Conductivity [$Wm^{-1}K^{-1}$]	Thickness [μm]	Specific Heat Capacity [$Jkg^{-1}K^{-1}$]	No. Layers
Cu Current Collector	398	21	385	50
Al Current Collector	238	21	903	51
Separator	0.34	24	1978	104
Anode	1.58	38	1437	100
Cathode	1.04	29	1270	100
Cell Case	238	160	903	2

validation and modelling various scenarios. Broadly the thermal boundary conditions used can be split into two modes replicating two principal cooling scenarios – forced convection to ambient (replicating experiments carried out in a thermal chamber with forced circulation) and constant temperature (replicating experiments carried out in surface cooling rigs). It is assumed in both cases that the majority of heat loss from the cell occurs through-plane, via the large top and bottom surfaces of the cell. It is noted that this assumption is likely less accurate when the cell is under convective cooling. However, the primary aim of this model was to simulate surface cooled cells, where this assumption will have a smaller impact on accuracy. In the case of convective boundary conditions, the convective heat transfer coefficient for the Kokam 5 Ah cell under force convection was previously estimated as 10 W/m^2K using transient heat transfer experiments by Zhao et al. [119]. This value was used where appropriate.

The lumped cell thermal ECN, as implemented, can be found in Figure 4.17 a. In the lumped thermal model, the cell heat generation is assumed to occur at the centre of the cell, with conduction transferring heat to the cell surface. The convective boundary condition thermal ECN can be found in Figure 4.17 b. For the surface cooled cases investigated, the convective heat transfer to the ambient air was replaced by a conductive heat transfer element, as shown in Figure 4.17 c.

The underlying equations solved by the lumped thermal model outlined in Figure 4.17 may be summarised as follows in Equations 4.18-4.20 for the cell lumped model (Figure 4.17 a), the convective boundary condition model (Figure 4.17 b) and the conductive boundary condition model (Figure 4.17 c) respectively.

$$Q_{Gen} - Q_{Out} = 0 \tag{4.18}$$

$$Q_{Out} - Q_{Convection} = 0 \tag{4.19}$$

$$Q_{Out} - Q_{Conduction} = 0 \tag{4.20}$$

Where Q_{Gen} is the cell heat generation at a given timestep, Q_{Out} denotes the heat transfer through the cell. $Q_{Convection}$ denotes the convective heat loss from the cell, whilst $Q_{Conduction}$ denotes the

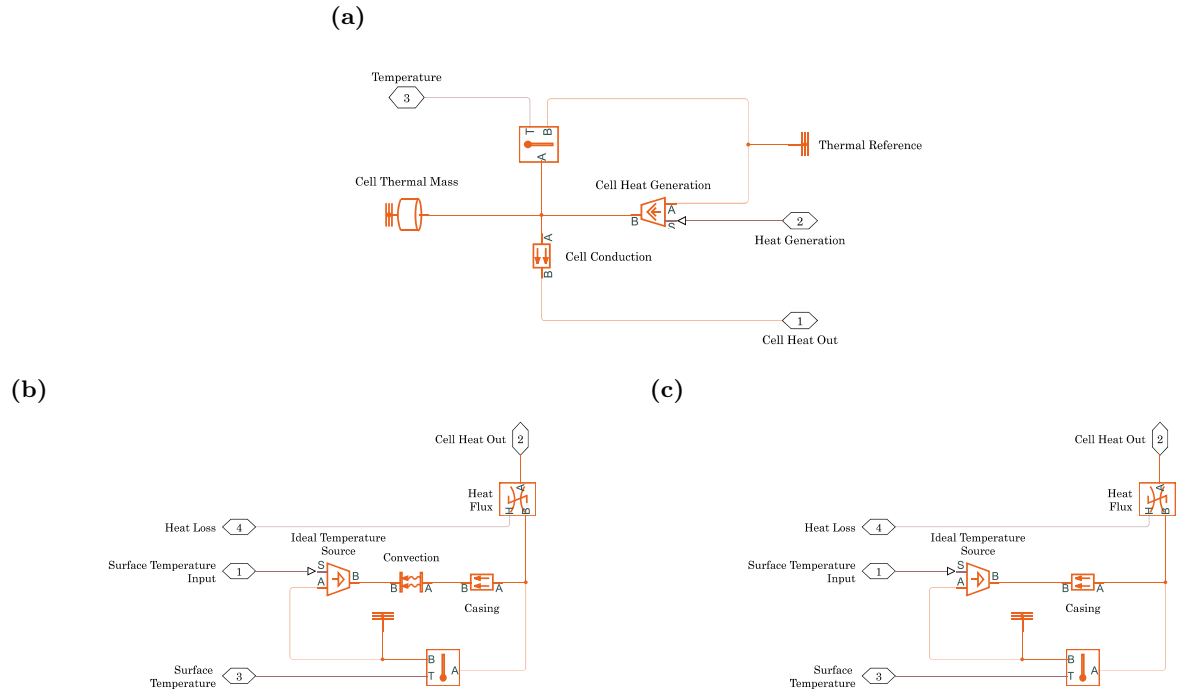


Figure 4.17: a) Cell thermal model. b) Convective thermal model. c) Conductive thermal model.

conductive heat loss from the cell.

4.5.5 Model Validation

Initially to validate the model, the fitted parameters were validated by comparing the cell voltage response to the input current profile used in the parameterisation experiments, and the residual voltage error between the measured and simulated voltages are assessed (an example is shown in Figure 4.18 for a cell at 30 °C). The input current profile is shown in Figure 4.18 a, and as shown in Figure 4.18 b, there was generally a good agreement between the simulated and measured cell voltage response, with the voltage residual values (shown in Figure 4.18 c for fitting at 30 °C) for the temperature breakpoints from 10 – 50 °C being 25.44, 16.44, 6.60, 9.78 and -5.06 mV respectively. The maximum errors occurred at the beginning of the under load portions of the validation experiment, and at low SoC values (typically the final 5 % SoC). These errors occur where the model accuracy is limited by the highly non-linear cell voltage response, the increased error in cell SoC estimation and the limited number of pulses at low cell voltages, due to the need to remain within safe voltage limits. It is noted that in order to improve the model fit, a charging pulsing experiment could be carried out to avoid these limitations at low SoC. The residual error was highest at 10 °C, likely due to increased contributions to the overall cell impedance from diffusion processes, the contribution of which are not fully captured in the single RC pair model.

Next, the model was validated for two cases – a single convectively cooled cell and a surface cooled 1S6P parallel cell string configuration under a range of applied thermal gradients. The acquisition of the 1S6P data is discussed in greater detail in Chapter 5, however as the objective of the model was ultimately to predict current splits within parallel cell strings, and the associated cell SoC and current throughput, validation against that case was critical.

In the case of a constant current load on a single cell, the model was in good agreement with ex-

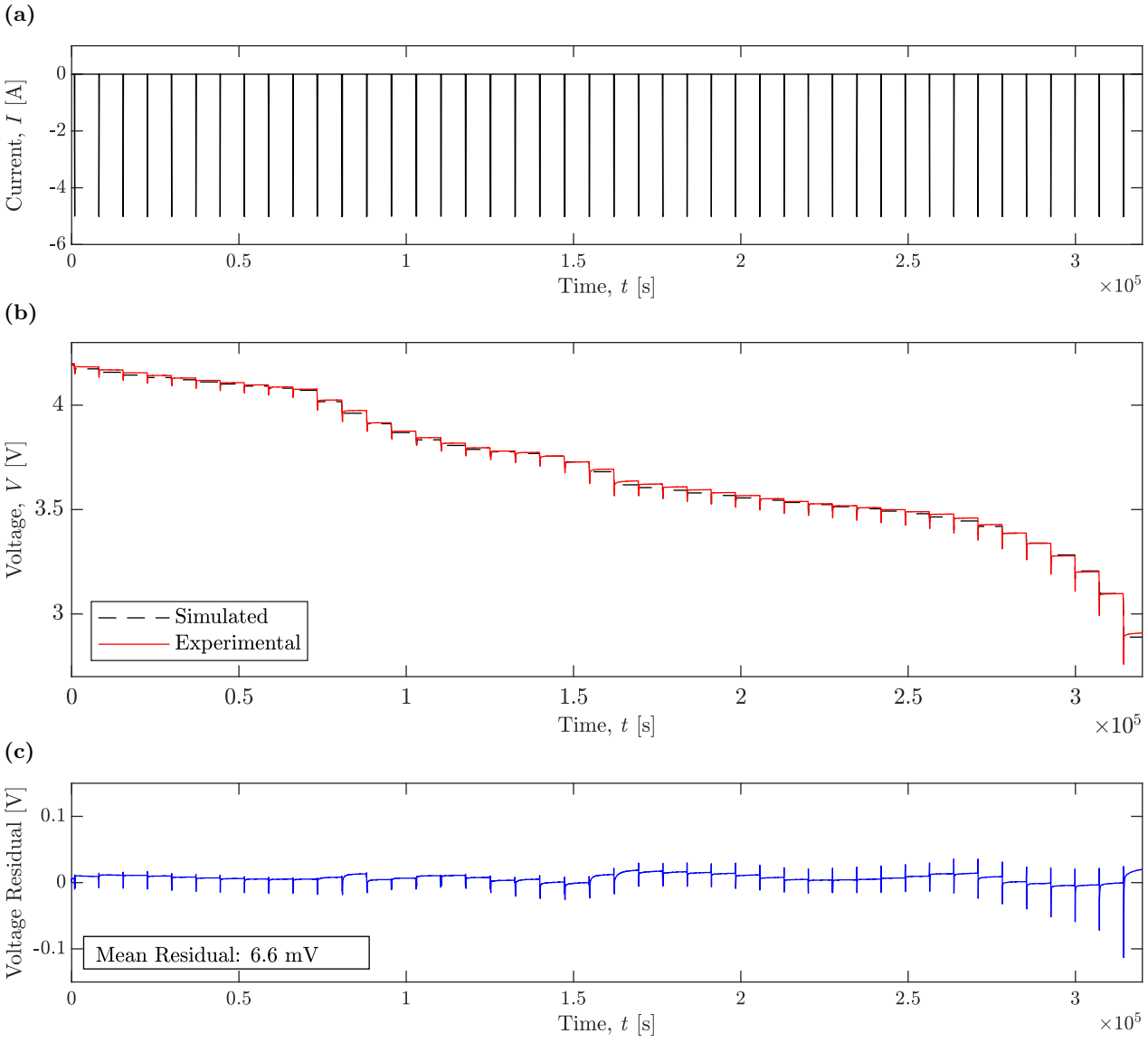


Figure 4.18: ECN model fit and residuals at 30 °C. a) Input current profile with 1 C pulses. b) Simulated and experimentally measured cell voltage response. c) Voltage residuals over fit.

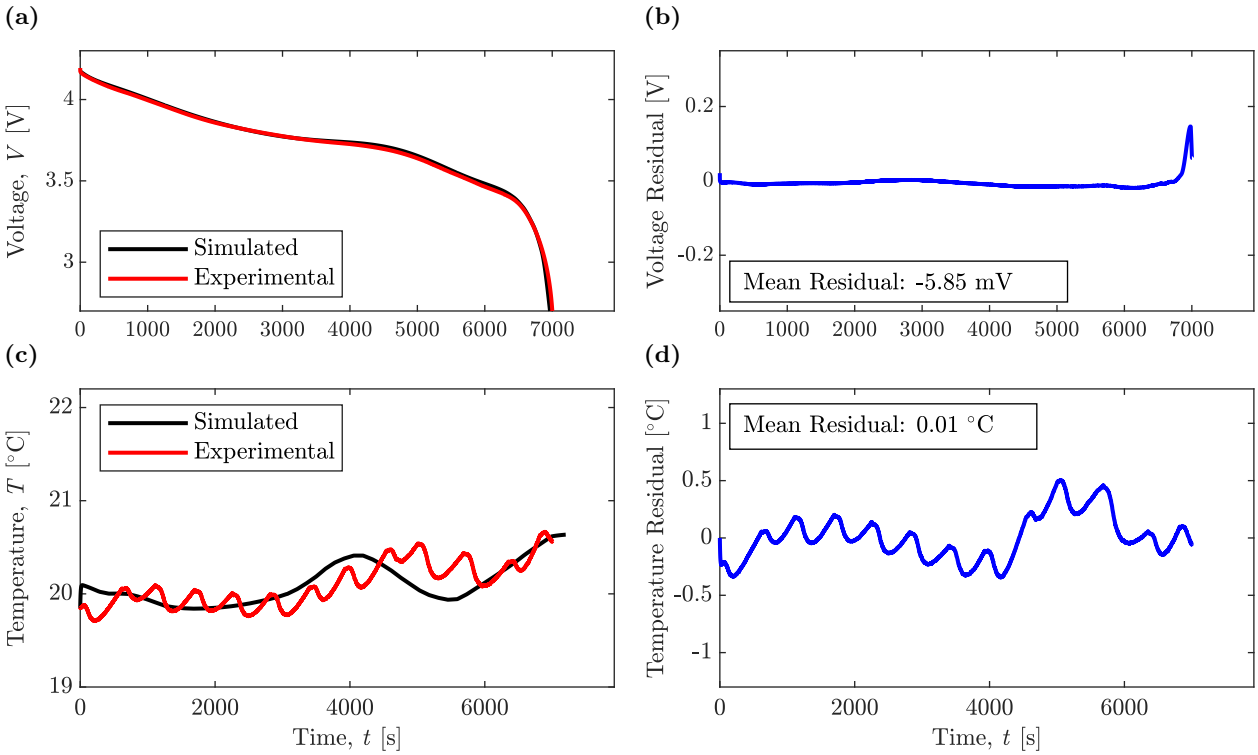


Figure 4.19: ECN validation under a 0.5 C constant current load at 20 °C. a) Simulated and experimentally measured cell voltage response. b) Voltage resiudal. c) Simulated and experimentally measured cell temperature (experimentally measured at cell surface midpoint. d) Temperature residual.

perimental data. The validation data was acquired by discharging a cell at a range of rates under convective cooling in an incubator (Binder KB23) set to 20 °C. For each rate the cell was charged using a CC-CV protocol at 1 C to 4.2 V, with a current cutoff of C/100 (50 mA). The cell was then allowed to rest for 1 hour before a discharge at the set rate, terminating at 2.7 V. This process was repeated for 6 rates: 3, 2, 1, 0.5, 0.1 and 0.04 C. In order to validate the model, simulations under the same conditions were carried out, and the error in temperature, voltage and predicted capacity evaluated. An example of the fit to experimental data under a 0.5 C discharge, and residual errors, can be seen in Figure 4.19. Figure 4.19 a and b show the voltage fit and residuals respectively, and the predicted cell voltages were in good agreement with the measured cell response, with residuals below ± 20 mV in all cases excluding the 3 C case, where the maximum mean voltage residual -42.6 mV was obtained. This was due to overprediction of the cell OCV at low SoCs, likely due to errors in SoC estimation during parameterisation and underprediction of the cell impedance in that SoC range. This second effect is a limitation of the 1 RC model, which only has single time constant dynamics and therefore is unable to incorporate longer time constant diffusion impedances, which increase in magnitude at low SoCs.

Considering the accuracy of the model under constant current loads with convective boundary conditions predictions, the model errors are shown in Table 4.4. The voltage RSME was found to be small below 0.5 C, with increasing errors above 1 C. This is likely due to the model not capturing the true internal cell temperature, due to the lumped nature of the model. However, the aim of the model is to capture dynamics of a pack under surface cooling, where smaller thermal gradients can be expected when compared to a cell under forced convection cooling. Therefore the model was deemed sufficiently accurate to simulate this scenario, and further validation against experimentally measured data for a

Table 4.4: ECN capacity prediction and error for rates from 0.04 to 3 C

Rate [C]	3	2	1	0.5	0.1	0.04
Voltage RSME [V]	0.0396	0.0285	0.0186	0.0101	0.005	0.007
Temperature RSME [°C]	1.0941	0.7535	0.4861	0.2059	0.1225	0.1966
Error [%]	2.77	1.64	0.19	-0.49	-1.15	-1.05

Table 4.5: ECN validation thermal conditions for 1S6P pack

	Cell 1 [°C]	**Cell 2** [°C]	**Cell 3** [°C]	**Cell 4** [°C]	**Cell 5** [°C]	**Cell 6** [°C]
Case 1	20.0	20.0	20.0	20.0	20.0	20.0
Case 2	20.0	25.0	30.0	35.0	40.0	45.0
Case 3	45.0	40.0	35.0	30.0	25.0	20.0
Case 4	45.0	45.0	45.0	45.0	45.0	45.0
Case 5	32.5	32.5	32.5	32.5	32.5	32.5

surface cooled 1S6P pack indicated that the model was able to accurately capture pack dynamics. The maximum error in capacity prediction was found to be 2.77 % at 3 C, where the model overpredicted the cell capacity. This is attributed to the impedance effect previously discussed, which lead to an error in cell voltage prediction at low SoC and therefore in the point at which the cell reaches the lower voltage limit and EoD, alongside the aforementioned inability of the model to capture cell internal thermal gradients.

The predicted cell temperatures were found to be in reasonable agreement with the measured values, and an example of the cell temperature predictions and residuals for the 1 C case can be seen in Figure 4.19 c and d. The greatest mean residual was -0.37 °C during a 3 C discharge, giving a mean error of approximately 5 % when compared to the overall temperature rise of 7 °C in this case. In other cases, the error in temperature fit was smaller than in the 3 C case, although the error as a proportion of the absolute temperature rise remained constant. The oscillations measured temperature which can be seen in Figure 4.19 c and d are a result of the thermal chamber temperature control regime oscillating about the setpoint of 20 °C. Below 1 C, whilst the model predicts a greater amount of reversible heating than irreversible, the overall heat generation is minimal. However, distinctive reversible heating is also identified in the experimental temperature data obtained below 1 C.

The final validation case considered was the prediction of cell currents and cell-wise current throughput in a 1S6P surface cooled pack, the most critical validation step given the objectives of the cell model and the intended use, which was to explore the current distribution, accessible capacity and energy and heterogeneous effects within parallel cell strings. The acquisition of the validation data and rig design is discussed in detail in Chapter 5. 5 cases were selected to validate the model in the 1S6P case, as laid out in Table 4.5, which shows the set cell surface temperature in each case, numbered 1 to 5. This included 3 cases of homogeneous temperature, cases 1, 4 and 5, and 2 with a 25.0 °C thermal gradient applied in both directions to the pack.

Firstly, errors in current prediction are shown in Figure 4.20 a-f for case 5 as an example, the homogeneous 32.5 °C case. The current dynamics in the pack are in good agreement between the simulated and experimentally measured validation case. This trend was repeated over all 5 validation cases, with accurate prediction of current dynamics in each case. While the position in time (which may

be equated with depth of discharge in the constant current case as used in this validation) of the current peaks and troughs is accurately predicted, the magnitude of the current peaks is generally less accurately predicted. This is attributed to the lumped nature of the model, whereas in reality there will be internal current distributions and thermal gradients in each cell which are not modelled in the lumped cell model. These unmodelled heterogeneities will in turn lead to changes in cell impedance and therefore changes in the experimentally measured current versus the modelled case. Figure 4.21 a-f shows the predicted cell SoC for case 4, and there is good agreement between the predicted and measured cell SoCs. As the cell SoC is a function of the current throughput through the cell, the error in SoC prediction is directly related to the error in current prediction and occurs for the same reasons.

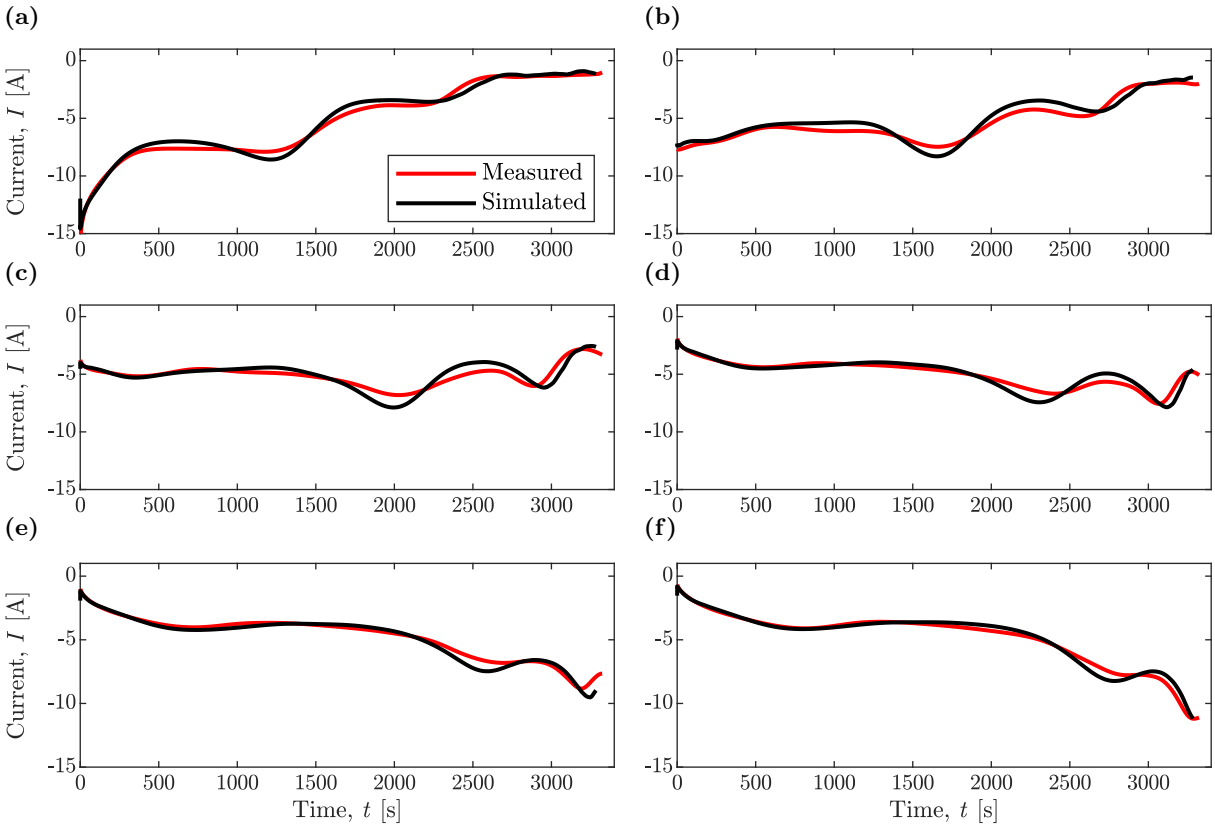


Figure 4.20: Simulated and experimentally measured cell currents for 1S6P pack with all cells held at 32.5 °C. a) Cell 1. b) Cell 2. c) Cell 3. d) Cell 4. e) Cell 5. f) Cell 6

The residual errors and RSME values for current and SoC predictions are summarised for all 5 validation cases in Figure 4.22. Figure 4.22 a shows an example current residual error for case 5, while Figure 4.22 b shows the current RSME for each cell and validation case. In all examples, the RSME in current is below 0.55 A. The residual current error, is variable, with maximum error at start of discharge. However apart from in prediction of the initial current split, residual current errors are generally $<\pm$ 1 A. Figure 4.22 c and d show the SoC residual for case 5 and SoC RSME for all cases respectively. The error in SoC increases towards the end of discharge, which is expected due to the unmodelled longer time constant processes within the cell. Nevertheless, the RSME is maintained below 0.0277 (2.77 %) in for all cells and cases, while the SoC RSME is below 2 % in most cases.

In summary, a 1RC pair cell model was parameterised over a temperature range of 10-50 °C, and the model validated against; the input parameterisation current profile, a range of constant current discharges and finally against a 1S6P parallel cell string under a range of thermal conditions. In all

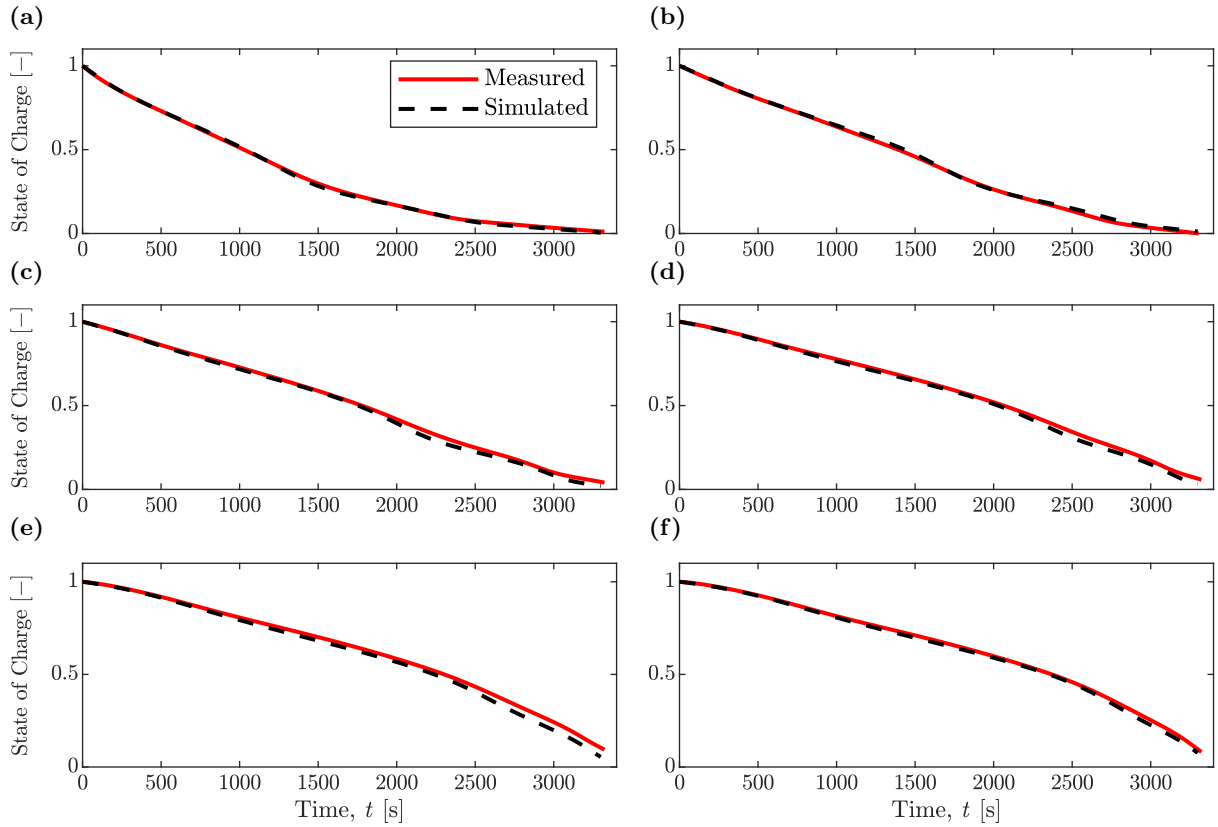


Figure 4.21: Simulated and experimentally measured cell SoC for 1S6P pack with all cells held at 32.5 °C. a) Cell 1. b) Cell 2. c) Cell 3. d) Cell 4. e) Cell 5. f) Cell 6

cases, the model performed acceptably, most significantly in the 1S6P case where the aim to use the model to predict lifetime current throughput and degradation was critical. In general, the current RSME was maintained below 0.6 A, while the SoC error in all cases was maintained below 2.6 % SoC. As such, accurate prediction of cell currents and therefore cell SoC values is key, and the model was capable of predicting such values to an acceptably high degree of accuracy.

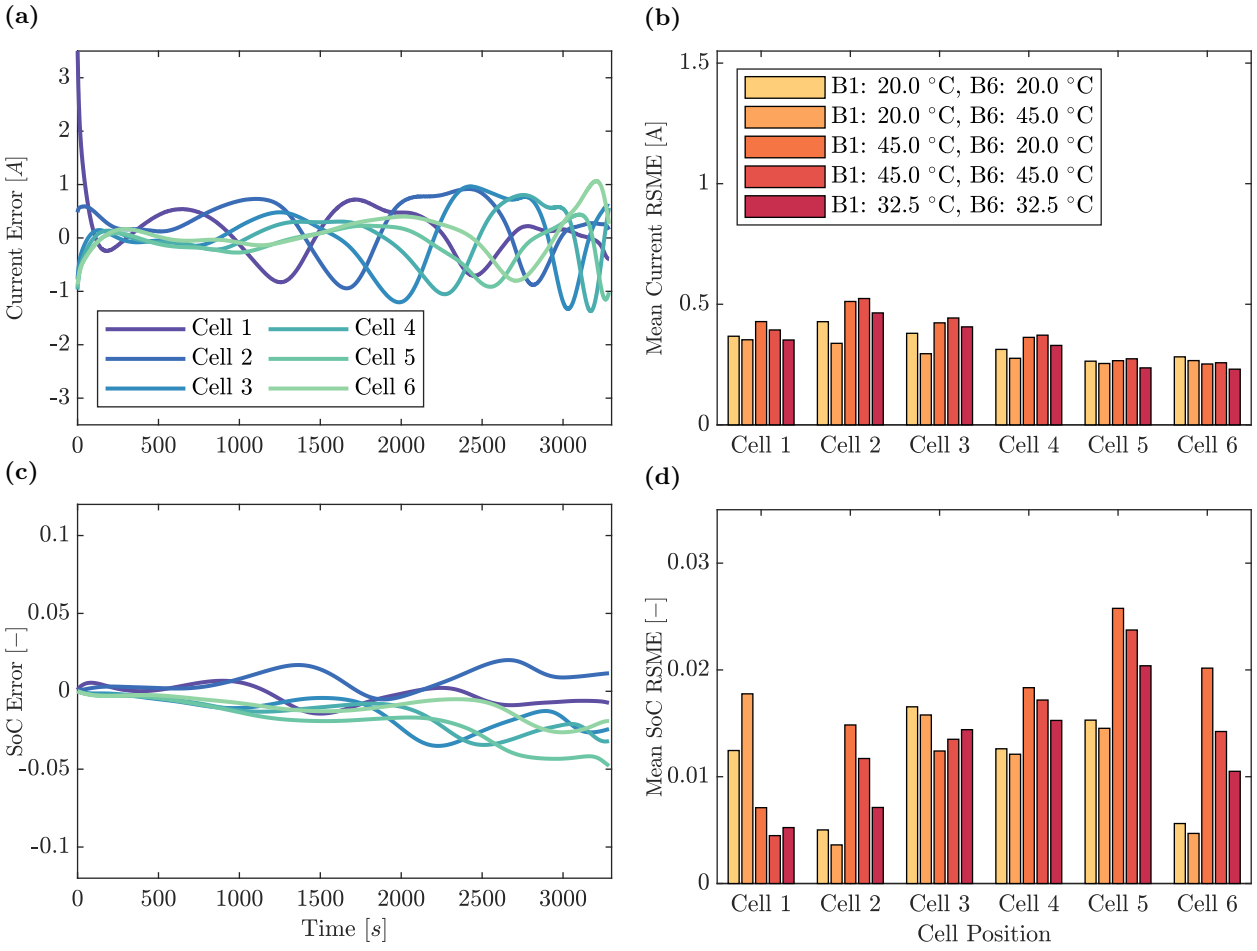


Figure 4.22: Summary of model validation to 1S6P test cases. a) Current residuals for all cells for test case 1 (all cells held at 20.0 °C). b) Mean current RSME for all cells in all 5 test cases. c) SoC residuals for all cells for test case 1 (all cells held at 20.0 °C). d) Mean SoC RSME for all cells in all 5 test cases.

4.6 Conclusion

In this chapter, the tools developed to investigate heterogeneities and aging of parallel connected LIB packs are presented. Firstly, thermally controlled test benches were developed to allow 1S2P and 1S6P parallel strings to be tested and aged under surface temperature-controlled conditions. A single 1S6P test bench was fabricated and used to carry out the experimental investigations presented in Chapter 5, whilst 6 1S2P test benches were fabricated to carry out the long-term aging experiments presented in Chapter 6.

Secondly, a quantitative diagnostic model has been implemented based on the voltage and capacity differential peaks, which evaluate the extent and mode of degradation, i.e. LLI and LAM in the anode and cathode. The model parameterisation includes association of the full cell OCV and anode and cathode half cell OCV responses and identification of the excess anode/cathode at EoC and EoD. This requires only 5 parameters and is less resource-demanding than physical models. Synthetic OCV responses with known extent and modes of degradation were used to validate the model. In this approach, the dominant degradation mode is identified with an error of less than $\pm$ 20 % in synthetic mixed-mode degradation, excepting in the case of simulated loss of delithiated anode. In Chapter 6 the model is further applied to investigate aging within parallel connected packs.

Finally, a 1RC pair ECN model was parameterised, with the objective of simulating the current distribution within parallel strings accurately and computationally inexpensively, allowing the investigation of a wide range of pack topologies and conditions. This was achieved, with the model achieving a mean residual current error of $<$6 % in all cases except at low temperature. However, the model was able to accurately capture the dynamics of the current splitting effect in all cases and was therefore deemed sufficiently accurate for further investigation of current heterogeneities, presented in Chapter 5. Additionally, the mean RSME in current was maintained below 2.77 % in all cases, again deemed sufficiently accurate to allow a detailed investigation of SoC deficit buildup.

Chapter 5

The Effects of Heterogeneities on Pack Performance

The work presented in this chapter is entirely the authors own apart from where otherwise acknowledged here. Part of the work, as described in Section 5.4 was carried out as part of a Master's Project by Patryk Gawlinski (PG), supervised by Max Naylor Marlow (MNM) and Dr Yatish Patel. PG was the principal contributor to detailed rig design and derivation of mathematical expressions for current splitting in parallel cell strings. PG and MNM contributed equally to data acquisition, test rig development and implementation and data analysis. All subsequent modelling and analysis was carried out in full by MNM, using the ECN model derived in Chapter 4

5.1 Introduction

The work presented in this chapter aims to answer the questions raised in Chapter 3 regarding the effects of thermal gradients on the performance of parallel cell strings, namely on instantaneous pack performance and degree of heterogeneity. Through both experimental and modelling investigation of a 1S6P pack with highly controlled thermal boundary conditions, the underlying effects dictating pack performance may be understood in detail. The test setups and equipment both developed and used have previously been described in detail in Section 4.3. As previously identified in Chapter 3, several research gaps exist concerning the effect of thermal gradients within parallel cell strings on the instantaneous performance and particularly the impacts on lifetime. In this chapter, the effects of variable thermal conditions, topology and resistance variations on instantaneous performance are investigated, using a model 1S6P system. Therefore, the aims of the work presented in this chapter aims to develop underpinning understanding of the following effects:

- The impacts of mean temperature and thermal gradients on pack instantaneous performance.
- The impacts of increased cell and interconnection resistance on pack instantaneous performance.
- The dominant causes and effects of heterogeneous current and SoC distributions within parallel cell strings.

5.2 Key Literature

Several key papers have aimed to address the effects of variations within parallel strings on instantaneous performance, however few have considered in detail how thermal effects will influence instantaneous performance and the magnitude of the impact of different heterogeneities. Considering the effects of topology, LeBel et al. [154] investigated the effects of two topologies, an asymmetric case with terminals on the same side of the pack and a symmetric case with terminals on opposite sides of the pack. Uneven currents within the 2 configurations were identified, however the magnitude of imbalance was found to be significantly greater in the asymmetric case, due to the imbalance of branch resistances in the pack. This effect has also been investigated by Wu et al. [141], who derived an analytical expression for current distribution, and showed that even in the case of equal busbar resistances and cell SoC and impedance, a differential current will still be present in the pack. This implies that cells will experience different conditions over lifetime and potentially age differentially even when great care is taken to ensure cells are consistent and all parasitic resistances are minimised and equalised. It is noted that the ultimate cause of current splitting is the different overpotentials in each branch, which are a function of the cell resistance, OCV and instantaneous current. These differences in overpotential are driven principally by two coupled factors, firstly the changing cell impedance and secondly the instantaneous current. Additionally, in cells where the SoC has decreased faster than other cells in a parallel string, the increased cell impedance will reduce currents compared to higher SoC cells, due to Kirchoff's Current Law (KCL).

Considering the effects of increased or uneven interconnection resistances and cell impedances, Wu et al. [141] also investigated the effects of increasing both the IRR and number of parallel connected cells. It was shown that increasing the IRR from 0 to 0.2 leads to approximately a 10 % increase in maximum cell current for 1S4P configuration, but a 300 % increase for a 1S12P configuration. This work only considered effects in symmetrical topologies, and it is expected that asymmetric topologies will experience greater variations in peak current, and a higher sensitivity to interconnection resistance. Hosseinzadeh et al. [139] investigated unbalanced currents within an asymmetric 1S5P pack, identifying significant current deviations at high discharge rates. By varying the IRR, it was found that increased interconnection resistances near the terminals of the string led to the greatest impacts on peak current, with diminishing peak currents the further from the terminals the high interconnection resistance was placed. However, the effect of increased interconnection resistances on capacity was not assessed, although it can be expected that higher peak currents imply a greater mean current, and therefore accelerated SoC depletion for the specific cell. Accelerating the rate of SoC depletion in the cells close to the pack terminals is likely to lead to reduced overall capacity, due to the pack lower voltage limits being reached earlier, with the remaining cells in the pack still retaining a higher SoC (i.e. inaccessible capacity) and leading to a loss in pack performance.

Considering the effects of thermal gradients on the performance of parallel cell strings, Yang et al. [145] used a physics based thermo-electrochemical model to simulate the effects of thermal gradients on a 1S2P string, although of unspecified topology. It was found that introducing thermal gradients to the 1S2P string increased the deviation in current throughput between the cells approximately linearly, with a 12 °C thermal gradient leading to a 7.5 % deficit with a cold cell ambient temperature of 25 °C, and a 40 % deficit between the cells with a cold cell temperature of 5 °C. This implies that parallel strings are more affected by thermal gradients at lower temperatures, due to the non-linear

impedance-temperature relationship. It was also found that increasing the thermal gradient led to increased accessible capacity, with a more significant effect at 5 °C. On the other hand, in this study the mean temperature of the 1S2P cell string was increased with application of thermal gradients, and therefore it is expected that the accessible capacity will increase due to reduced cell impedances. Meanwhile, Fill et al. [164] used a thermally controlled test bench to investigate the effects of induced thermal gradients on parallel connected cells in an asymmetric topology. It was found that significant current distributions and therefore SoC distributions could be induced, and that these distributions were significantly affected by the thermal conditions of the cells under test, with varying the thermal coupling, isolation and thermal gradient direction leading to significant changes in current and SoC profile for a 1S2P string. Finally, Klein and Park [163] comprehensively investigated the effects of thermal gradients on a symmetrical 1S5P pack, and found that increased thermal gradients led to dramatic changes in peak currents, with a 400 % increase in deviation with a 20 °C thermal gradient applied when compared to a 5 °C thermal gradient. The SoC deficit at EoD was identified as leading to a reduction in accessible capacity, with increasing SoC deficits at higher rates. Increasing the applied thermal gradient was found to increase the SoC deficit and therefore reduce capacity, while increasing the mean temperature was found to decrease the magnitude of this effect, with a 400 % reduction in the SoC deficit when comparing a 20 °C thermal gradient applied at 15 °C and 35 °C mean temperature.

Considering the effects of heterogeneities in a comprehensive manner, Liu et al. [9] investigated a 1S6P asymmetric pack, using a physics-based thermo-electrochemical model. It was found that in the case of a high (400 % increased) cell impedance, placing the cell close to the terminals equalised the current distribution (although accessible capacity was reduced), while placing it away from the terminals led to an approximately 6 % reduction in accessible capacity at 1.5 C. It was found that increasing the mean temperature led to increased accessible capacity due to lower overpotentials, and an uneven effect of thermal gradients at the same mean cell temperature was identified. Increasing the cell temperatures moving away from the terminals led to increased accessible energy while the converse led to decreasing accessible energy when compared to the same system at a constant and equal mean temperature.

Due to the high number of variable factors involved, such as interconnection resistances, contact resistances, cell impedance magnitude, pack topology, applied rate and thermal boundary conditions, generalisation of design rules surrounding parallel cell strings remains challenging. In particular, understanding the coupling between variables is critical and is therefore aimed to be addressed in this Chapter.

5.3 Experimental Methods and Cell Selection

5.3.1 Electrical Topology

In this chapter, two principal topologies are investigated, which encompass the majority of parallel string configurations. These topologies are outlined in Figure 5.1 a and b for the investigated 1S6P string showing a ‘U’ and ‘Z’ topology respectively. The U topology describes when the positive and negative tabs of the string are located electrically on the same side of the pack (Figure 5.1 a), while the Z topology describes the case of the tabs being diagonally opposed (Figure 5.1 b). These topologies have been identified as the ‘cis’ or ‘ladder’ and ‘trans’ or ‘Z’ cases respectively in the literature [154],

[162], and may be considered as an asymmetric and symmetric case respectively.

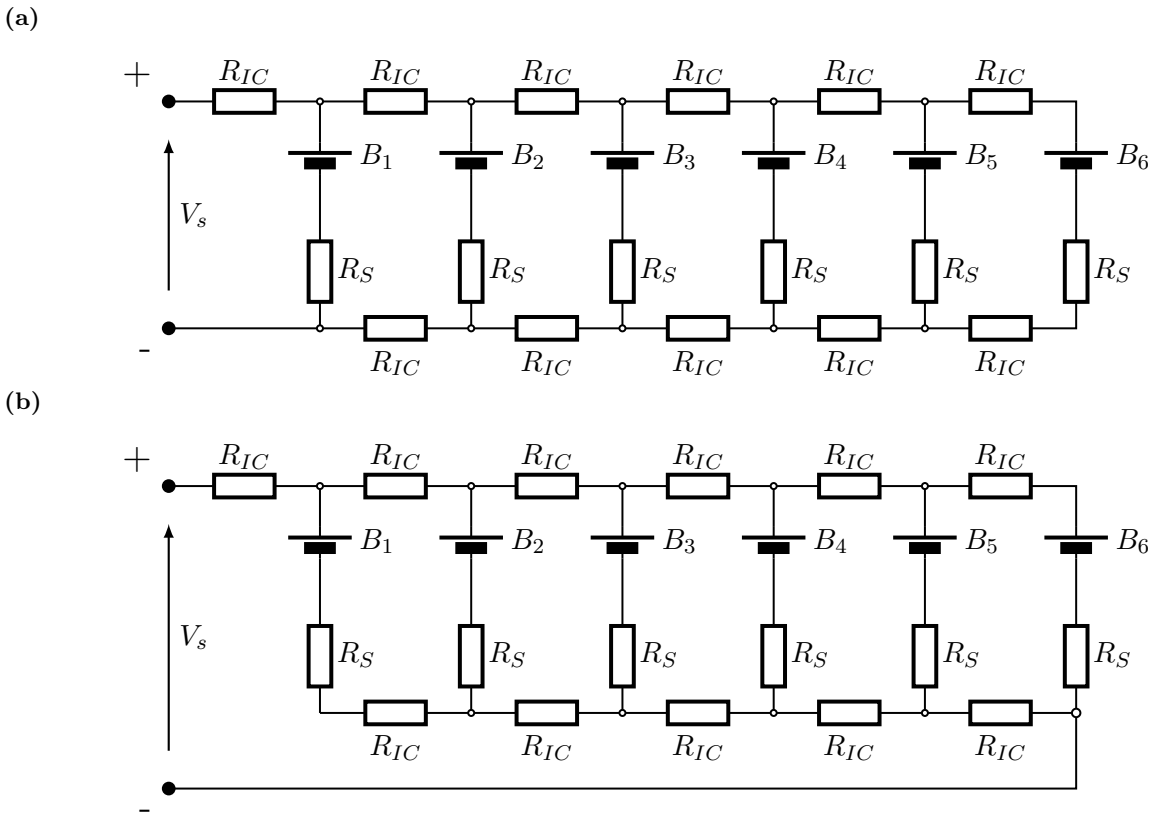


Figure 5.1: Topologies selected for investigation. a) 1S6P 'U' topology. b) 1S6P 'Z' topology.

Within the identified string topologies, several resistors can be seen. These encompass both the busbar or interconnection resistances, R_{IC}, and the current sense resistors, R_S, which was required to experimentally measure current flow in each parallel branch of the system. V_S defines the string terminal voltage.

5.3.2 Cell Selection

The first consideration during development of the experimental campaign was to ensure that the cells selected to explore the effects of thermal gradients on overall performance were uniform. Therefore, reference capacity and pulse resistance of 6 fresh Kokam 5 Ah cells was measured to ensure sufficient uniformity of the cells, to avoid the influence of cell-to-cell capacity and impedance variations affecting the string current response. In order to measure the reference capacity of the selected cells, a p-OCV test at 20.0 °C was carried out. The cells were attached to a simple jig and placed in a cooling incubator (Binder KB23) set to the desired temperature. All cell testing was carried out using a Biologic BCS-15 battery cycler. The cells, with a nominal capacity of 5 Ah, were then allowed to equilibrate for 60 mins before being charged using a CC-CV scheme with a rate of 1 C and a cutoff of 0.01 C (50 mA). The cells were then allowed to further equilibrate for 60 mins before discharging at 0.05 C to 2.7 V. This process was repeated for 4 additional rates; 0.2 C, 0.5 C, 1 C and 2 C to provide information about the rate capability of the cells. Subsequently, the cell pulse resistance was measured using a pulse discharge scheme, again with the temperature controlled using a cooling incubator (Binder KB 23). The cells were again CC-CV charged to 4.2 V, with identical charging parameters to the reference capacity measurements, before being allowed to rest for 180 mins. The cells were then discharged at

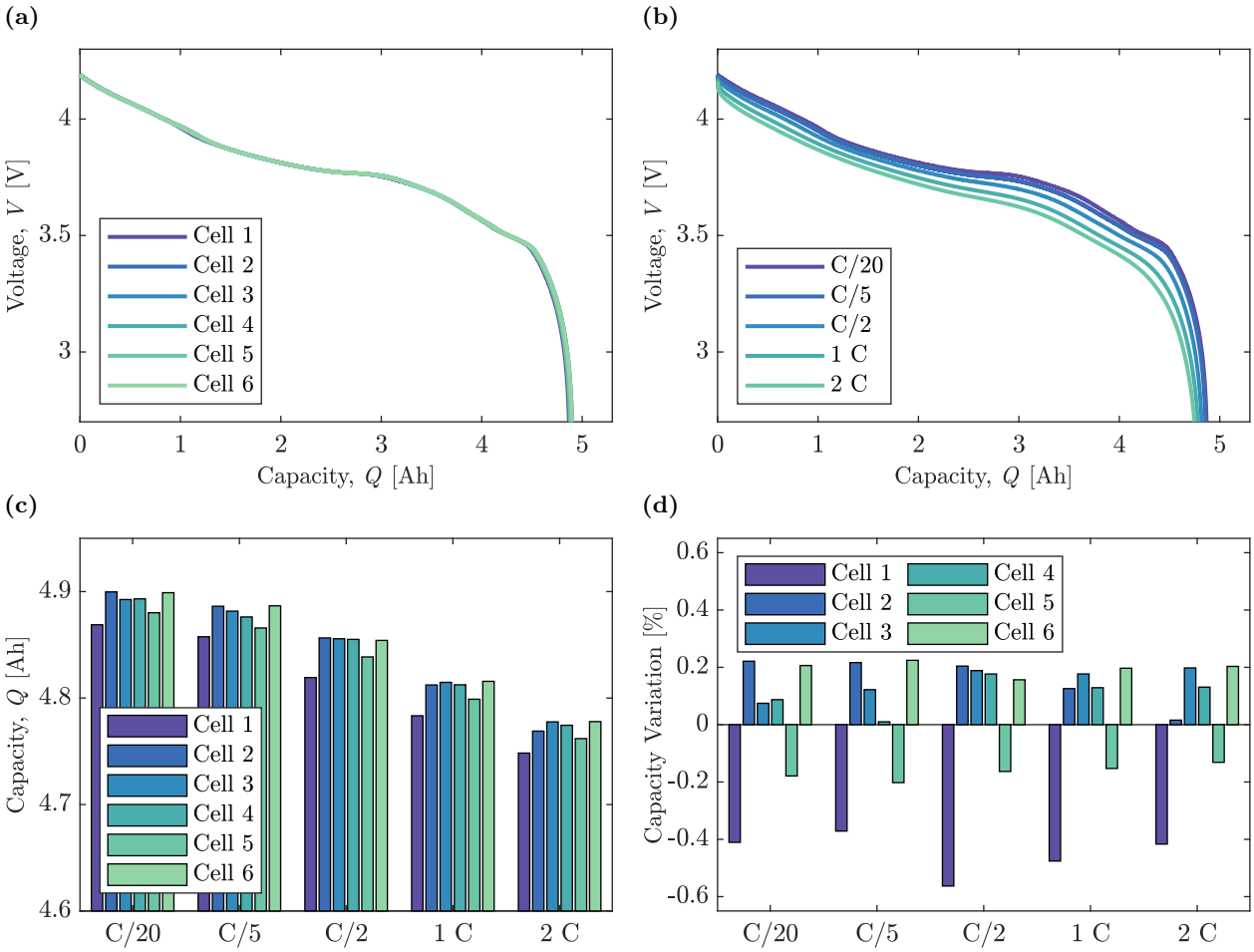


Figure 5.2: Cell capacity variation at a range of rates for all 6 cells used in 1S6P pack. a) Cell OCV curves measured at C/20. b) Cell 1 voltage response from C/20 - 2 C. c) All cell measured capacity from C/20 - 2 C. d) All cell capacity variation from mean from C/20 - 2 C.

1 C, with termination after 5 % nominal SoC (i.e. 250 mAh charge passed), before being allowed to equilibrate for 180 mins. This process was repeated until the cell voltage reached the lower voltage limit (2.7 V), and the cell was subsequently charged to resting potential (3.85 V) using a CC-CV charge. The pulse measurement was repeated at both 20 and 40 °C.

Figure 5.2 a shows the results for the reference capacity voltage curve for all cells selected, showing both the p-OCV response and cell capacity was similar in all cases. An example of the cell voltage response under the range of applied rates, for Cell 1, is shown in Figure 5.2 b. These results indicate that the selected cells are highly rate capable over the range selected, with minimal capacity loss. The cells were consistent in capacity over all rates, as shown by Figure 5.2 c and d, which demonstrate both the consistency of capacity over all rates, although it is noted that the measured capacity of cell 1 was a somewhat lower than that of the other cells at all rates, by approximately 40 mAh. Figure 5.2 d shows the percentage difference in capacity at each rate, referenced against the mean capacity of the cells tested (4.88 Ah measured at C/20), and it was found that the maximum capacity spread was 0.7 % at C/2, with the capacity spread being approximately 0.6 % at all other rates. This was deemed an acceptable level of capacity spread for this work.

Figure 5.3 a and b show the calculated $R_{DC|10s}$ for all cells at 20 and 40 °C respectively. The cell resistance is consistent between the cells at all temperatures, and behaves as expected, with a signif-

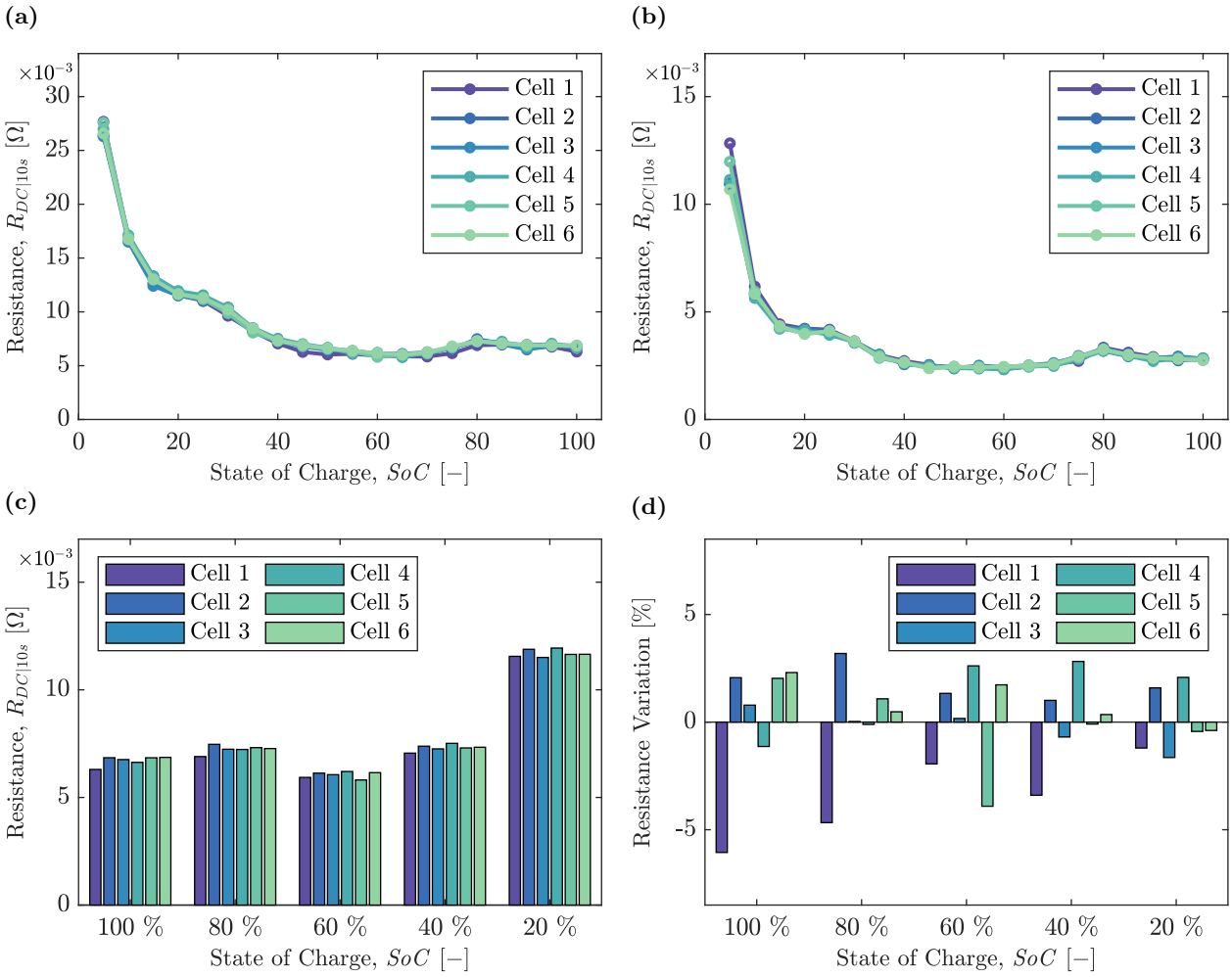


Figure 5.3: Cell $R_{DC|10s}$ variation for all 6 cells used in 1S6P pack. a) Cell $R_{DC|10s}$ measured at 20 °C. b) Cell $R_{DC|10s}$ measured at 40 °C. c) All cell $R_{DC|10s}$ magnitude at at 100, 80, 60, 40 and 20 % SoC, measured at 20 °C. d) All cell $R_{DC|10s}$ variation from mean at at 100, 80, 60, 40 and 20 % SoC, measured at 20 °C.

Table 5.1: 1S6P temperature cases experimentally investigated

	Name	Cell 1 [°C]	Cell 2 [°C]	Cell 3 [°C]	Cell 4 [°C]	Cell 5 [°C]	Cell 6 [°C]
Case 1	**20-20**	20.0	20.0	20.0	20.0	20.0	20.0
Case 2	**20-45**	20.0	25.0	30.0	35.0	40.0	45.0
Case 3	**45-20**	45.0	40.0	35.0	30.0	25.0	20.0
Case 4	**45-45**	45.0	45.0	45.0	45.0	45.0	45.0
Case 5	**32.5-32.5**	32.5	32.5	32.5	32.5	32.5	32.5
Case 6	**26.5-39**	26.5	29.0	31.5	34.0	36.5	39.0
Case 7	**39-26.5**	39.0	36.5	34.0	31.5	29.0	26.5
Case 8	**20-45-20**	20.0	32.5	45.0	45.0	32.5	20.0
Case 9	**45-20-45**	45.0	32.5	20.0	20.0	32.5	45.0

icant increase below 40 % SoC in each case, eventually increasing by a factor of 400 % in the 20 °C case at 5 % SoC, and 250 % in the 40 °C case. This increasing overall impedance is caused by the growing influence of the charge transfer resistance. In NMC cells, the charge transfer resistance has been shown to be dominated by the cathode. At low full cell SoC values the cathode is increasingly lithiated, making further intercalation of Lithium ions less favourable. The converse is the case for the anode at high full cell SoCs. Previous studies have noted that the increase in cathode resistance at low full cell SoCs is greater than the increase in anode resistance at high full cell SoCs [207], [208]. Figure 5.3 c shows the $R_{DC|10s}$ values for all cells at 5 selected SoC breakpoints at 20 °C. There is no significant variation in the measured values. The percentage difference from the mean value of all the tested cells is shown in Figure 5.3 d for each cell, with a maximum variation of 8 % between cells 1 and 6 at 100 % SoC. In general, the DC resistance measurements indicate the cells are relatively consistent, and was again deemed acceptable for this work.

5.3.3 Experimental Methods

As previously described in Section 4.3, a custom Peltier element-controlled surface cooling test rig was used to replicate thermal gradients within the pack. A range of thermal gradients were considered to replicate a number of possible scenarios within the pack, for both investigated topologies. The scenarios were selected to investigate extremes of thermal gradients which could be found in parallel strings, and to validate the ECN model used (as described in Section 4.5). The selected thermal conditions are summarised in Table 5.1. 3 homogeneous temperature cases were considered, with all cells at 20.0, 32.5 and 45.0 °C, along with 6 cases with applied thermal gradients.

For the applied thermal gradient cases, a 'positive' and 'negative' thermal gradient convention is used, as shown in Figure 5.4. As can be seen, apart from the 'pyramidal' cases, the temperature conditions can be divided into homogeneous temperature cases and cases with linear applied thermal gradients. The 'positive' convention implies that the cells within the string are becoming hotter the further they are electrically positioned from the string terminals, while the converse is true for the 'negative' case, with cells becoming colder the further they are positioned from the string terminals. Two magnitudes of thermal gradient, 12.5 and 25.0 °C were selected, and were applied to the U-topology pack in both directions (i.e. away and towards the tabs), as well as two 'pyramid' thermal gradients, replicating cases where the string is cooled either only at the core or only on the outside cells. In the Z-topology, cases 3 and 7 are expected to provide identical results to cases 2 and 6 respectively, as the

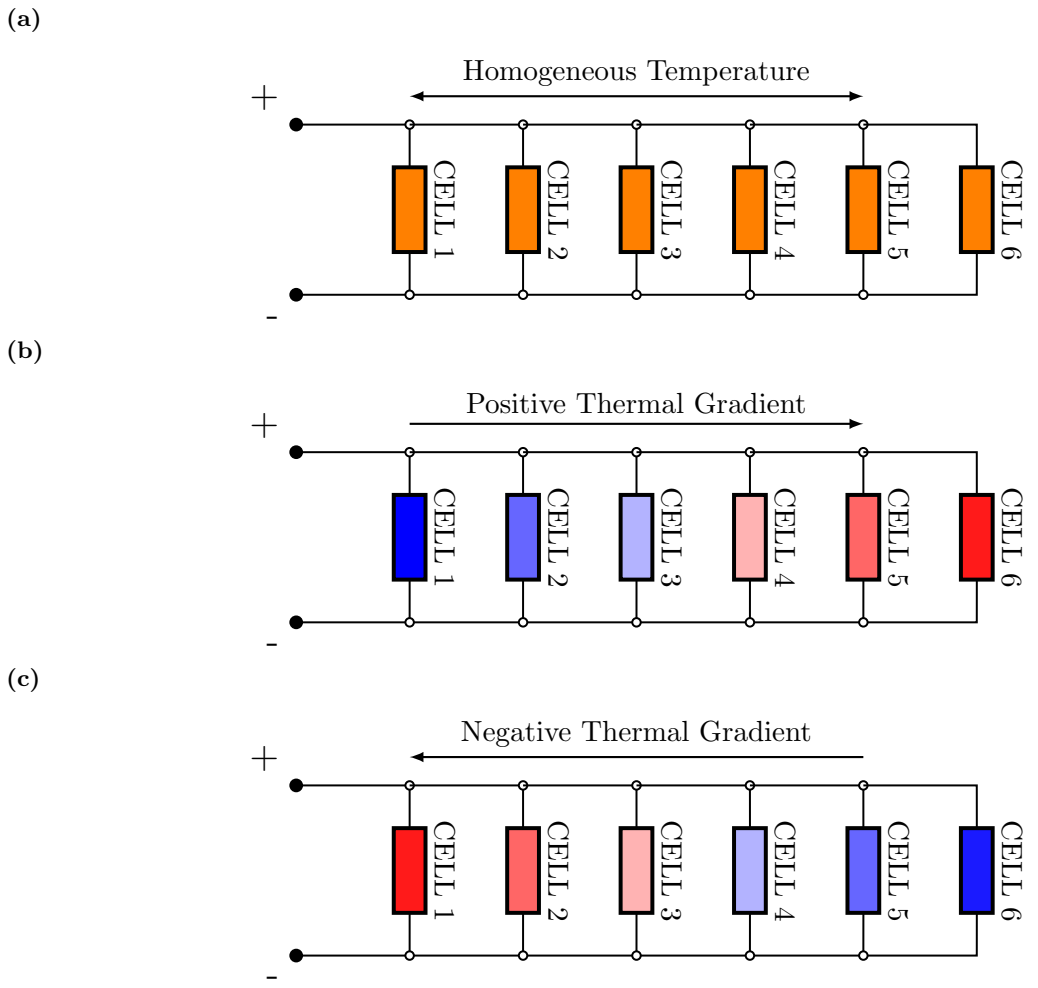


Figure 5.4: Definition of thermal gradient positive and negative cases. a) Homogeneous temperature case. b) Positive thermal gradient case. c) Negative thermal gradient case.

symmetry of the pack in that case will lead to identical results, assuming that there are no differences in cell performance or interconnection resistances. However, these cases were included to verify this assumption.

The interconnection and current sense resistances, R_{IC} and R_S were selected and set to 1 mΩ. R_S was selected as the smallest practical current sense resistor possible while retaining accuracy with the shunt voltage sensors, while R_{IC} was selected to give an interconnection resistance ratio of approximately 12.5 %, which was selected based on reported values in the literature to provide a high but realistic value [209], [210]. The current sense resistor voltage drop was recorded independently using a Pico Technologies PicoLog TC-08, logging in $\pm$ 39 mV mode with a logging rate of 1 Hz, using a 18-bit effective analogue-to-digital converter to achieve a voltage resolution of 0.27 μV.

With the operating conditions selected, the pack was assembled, and each temperature case was investigated by setting the pack temperature using the Peltier surface cooling plates. A typical run was carried out by applying the desired temperature conditions and allowing the pack to thermally equilibrate for 60 mins. The pack (nominal capacity 30 Ah) was then charged from storage potential (3.85 V) to 4.2 V using a CC-CV charging scheme with a rate of 1 C and a cutoff current of 0.01 C (300 mA). The pack was then allowed to further equilibrate for 60 mins before a CC discharge at 1 C was carried out, with a lower voltage cutoff of 2.7 V. The pack was subsequently charge using

a CC-CV scheme with a rate of 1 C and a current cutoff of 0.02 C to resting potential of 3.85 V. All testing of the 1S6P parallel cell strings was carried out using a 50 A Maccor Series 4000 battery cycler.

5.4 The Effects of Thermal Gradients: Experimental Study

5.4.1 U-Topology: Homogeneous Temperature Case

In this section, the experimental results for the U-topology 1S6P pack configuration are presented and discussed in detail to identify the causes of the current splitting effects within the parallel string. Figure 5.5 shows the current and SoC split per cell for the homogeneous temperature cases, 20-20, 32.5-32.5 and 45-45. Selecting the first example, the 20-20 case, where the current and SoC distributions are shown in Figure 5.5 a and b respectively, the complex current distribution can be explained. Over the full discharge, 3 principal sections can be seen. Initially, at the start of discharge (Q = 0 Ah) the cell currents are split, as predicted by the analytical expression for the current distribution derived later in this Section. The current in Cell 1 in this case is initially at the highest value seen over the entire cycle, with an initial value of approximately 12.5 A, 2.5 times higher than the nominal applied current of 1 C, and almost an order of magnitude higher than the initial current in Cell 6. This initial distribution of currents may be predicted analytically as the SoCs and internal temperatures of the cells are initially equilibrated and equal. As the cell impedance and OCV are a function of both the temperature and SoC, this implies that the only variable factor driving the current distribution at start of discharge is the branch parasitic resistance (the sum of the interconnect and current sense impedances), which in a U-configuration increases further from the string terminals as there are more resistive elements in each path. The initial cell current can be seen to decrease geometrically moving away from the cell terminals, due to the fact that as the magnitude of the current sense and interconnect resistances is equal, the path resistance between branches 1 and 2 is 200 %. However, the increase between branches 2 and 3 is 150 %, and this trend continues the further the branch is from the terminals.

As the state of charge of the cells close to the terminals decreases, the cell OCV decreases and the cell overpotential increases. This increase in overpotential is due to the cell overpotential being a function of the cell impedance, which has been shown to increase with decreasing SoC. As the node potentials must be equal, the current through the branches further from the terminals must increase in order to equalise these potentials. Over time this effect leads to a reversal in the branch with the peak current (beginning at Q = 12.5 Ah), where the SoC of Cell 1 is depleted to the extent that it is no longer exposed to the largest current. This point corresponds to Cell 1 SoC equalling approximately 25 %, below which the cell DC resistance increases non-linearly (as shown in Figure 5.5 a and b), further decreasing the cell current. As the discharge continues, this effect is seen sequentially in all branches moving away from the terminals, until the magnitude of the measured currents has reversed when compared to their initial state.

Figure 5.5 c and e shows the current distribution for the 32.5-32.5 and 45-45 cases respectively, while Figure 5.5 d and f shows the SoC distribution for same cases. Increasing the temperature of the packs in the homogeneous cases leads to increasingly unbalanced current and SoC distributions. This is attributed to the decreasing cell impedance with increasing temperature, which leads to a decreased contribution of the cell overpotential to the total branch overpotential. Consequently, the parasitic resistances in the branches have a greater influence on the current distribution at high temperature.

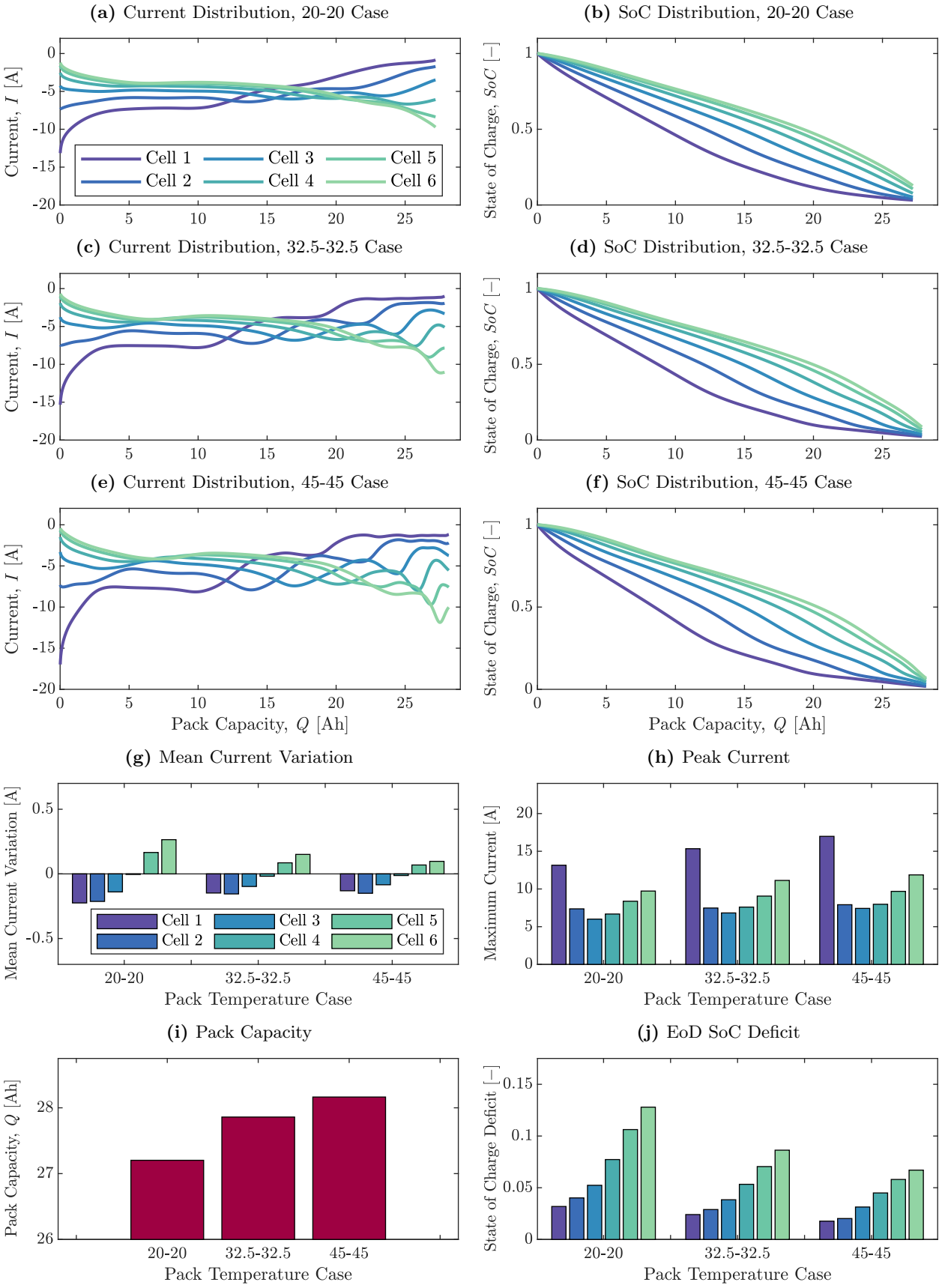


Figure 5.5: Experimentally measured current and SoC distributions for a U-topology 1S6P pack under homogeneous temperature conditions. All measurements taken during a 1 C discharge. a) Current distribution for 20-20 case. b) SoC distribution for 20-20 case. c) Current distribution for 32.5-32.5 case. d) SoC distribution for 32.5-32.5 case. e) Current distribution for 45-45 case. f) SoC distribution for 45-45 case. g) Mean current variation for all homogeneous temperature cases. h) Peak current for all homogeneous temperature cases. i) Pack capacity all homogeneous temperature cases. j) EoD SoC deficit for all homogeneous temperature cases.

As the cell temperature increases, cell impedance drops and therefore the IRR is increased for a constant interconnection resistance. As all parasitic resistance values are identical in all cases there is therefore a greater distribution of currents and SoCs at higher temperatures. The effect of increasing the mean string temperature can be seen in Figure 5.5 g and h, which shows the mean current deviation from nominal and maximum applied current for each cell. The mean variation is decreased as the mean temperature increases (Figure 5.5 g), due to the reduced overall branch resistance at higher temperatures. However, increasing the mean temperature also increases magnitude of the maximum applied current by 30 % at the start of discharge, from 2.6 to 3.4 C.

Another effect of note is the inaccessible capacity in each case, as the final SoC of each cell is not zero (Figure 5.5 i and j), which shows the overall pack capacity and cellwise EoD cell SOC (referenced against the cell reference capacity) respectively. This reduction in overall capacity, shown in Figure 5.5 i, is due to the inaccessible capacity of each cell within the string. This is a consequence of the lower cutoff voltage being measured at the string terminals. In the U-topology case, Cell 1 is closest to the terminals and is the overall most depleted cell, which means the cell OCV is lowest. The lower voltage cutoff is reached when the OCV of Cell 1 minus the branch 1 overpotentials equals the cutoff voltage, leaving inaccessible energy in both Cell 1 (due to the overpotentials present) and the other cells. The amount of inaccessible capacity decreases with increasing mean temperature, due to the lower cell resistances, which allows the cells further time to homogenise towards the EoD before the lower cutoff voltage is reached. In the cases investigated, there is a 3.3 % reduction in pack capacity when comparing the 20-20 to the 45-45 case. The reason for this reduction in capacity is further illustrated in Figure 5.5 j, which shows the EoD cellwise SoC deficit. In the 20-20 case there is a significant distribution of cell EoD SoC. By increasing the pack temperature, both the EoD SoC of Cell 1 is decreased and the deficit between Cells 1 and 6 is reduced significantly, from approximately 10 % in the 20-20 case to approximately 5 % in the 45-45 case.

To explain these effects in more detail, Figure 5.6 shows both a schematic representation of the factors leading to current distributions, and annotated plots identifying the causes of the current distributions. Figure 5.6 a shows a schematic representation of the current split, while Figure 5.6 b and c show the experimentally measured current and SoC distribution in the 20 °C homogeneous temperature case (20-20). To estimate the total branch resistance (Figure 5.6 c), all measured parasitic resistances are summed with the cell impedance, which is interpolated from the PD measurements of cell $R_{DC|10s}$ (see Section 5.3.2), using a '*pchip*' spline interpolation. The interpolation was evaluated at each measured cell SoC value to predict the instantaneous branch resistance during the full discharge. Figure 5.6 e shows the estimated cell OCV, interpolated from the PD measurements of cell pseudo-OCV (Section 5.3.2). Crossover points between when the highest loaded cell switches are marked in Figure 5.6 b-e as points 1-6.

Firstly considering the current distribution (Figure 5.6 b), during discharge phase 0-1, Cell 1 in branch 1 initially experiences the highest current. There is an initial reduction in current up to 3 Ah discharge capacity preceding stable current distribution up to point 1 (12 Ah discharge capacity). Initially the branch resistance in branch 1 is approximately 2 mΩ lower than branch 2, and approximately 10 mΩ lower than branch 6 (Figure 5.6 d). As such, the initial peak current is passed through branch 1. Over the phase 0-1, some equalisation of currents occurs due to the cell OCV changes at SoD (Figure 5.6 e).

At point 1, crossover occurs between Cells 1 and 2, with Cell 2 now the highest loaded cell in the string. At this stage, the branch resistance of branch 1 increases rapidly (Figure 5.6 d), due to the onset of non-linear impedance changes in Cell 1 below approximately 40 % SoC. Progressively from points 1-5 the branch with lowest total resistance is shifted further from the terminals. This decreases the SoC of the initially heavily loaded cells further and the total resistance in the corresponding branches increases. In phase 0-1, where despite the branch resistances being relatively constant up to approximately 10 Ah, the current through branches 1 and 2 is seen to decrease, as the OCV of Cells 1 and 2 is decreasing more rapidly than the remaining cells in the pack. This is caused by the initially larger currents in these branches leading to more rapid SoC change in these cells, and consequently a more rapid drop in cell OCV.

However, in phase 5-6 it can be seen that the maximum cell current is found in branch 6, however the branch 6 total impedance is higher than that of other branches for the initial portion of this region. This serves to illustrate again the coupled role of overpotentials in dictating the current distribution. As cell SoCs deviate, the estimated cell OCV deviates. By KVL, the terminal voltage is given by Equation 5.1.

$$V_T = V_{OCV,n} - R_{Cell,n} \cdot I_{Cell,n} - \sum_{1}^{k} R_{P,k} \cdot I_k \tag{5.1}$$

Where V_T is the terminal voltage, $V_{OCV,n}$ is the cell voltage, $R_{Cell,n}$ is the DC resistance and $I_{Cell,n}$ is the cell current where $n = \{1, \ldots, 6\}$. $R_{P,k}$ is the magnitude of each parasitic resistance (interconnection, busbar and contact resistances) and $I_{B,k}$ is the current in each parasitic resistor, for parasitic resistances numbered $k = \{1, \ldots, k\}$. It is important to note that the total current passing through each interconnection resistor is not equal to the corresponding cell current (i.e. $\mathrm{I_{R_{IC,1}}} \neq \mathrm{I_{R_{B,1}}}$). For example, the interconnects closest to the pack terminals will pass the full applied pack current, increasing the potential drop across the resistor compared.

By Equation 5.1, for a given pack terminal voltage, if $V_{OCV,n}$ drops, the cell current must also drop, an effect which can be clearly observed at the beginning of phase 0-1 where the branch resistance is stable yet rebalancing of currents occurs. This is also illustrated in phase 5-6, where cell 6 is experiencing the maximum current. Despite the branch resistance of branch 6 being higher than that of branches 3-5, Cell 6 begins to be most heavily loaded at point 5, due to the higher OCV value of cell 6 offsetting the increased branch resistance. This example overall serves to demonstrate the complex interactions between OCV, overpotentials and total branch resistances on dictating the current distribution. These effects are also coupled, as the overpotential due to the interconnections is a function of the total current passing through the specific interconnection considered.

5.4.2 U-Topology: Heterogeneous Temperature Case

After considering the effect of changing the temperature homogeneously within a parallel cell string, the effect of applying a linear thermal gradient to a parallel string is explored. Figure 5.7 shows the effect of linear thermal gradients on the current distribution in the 20-45 and 45-20 cases, which are defined as a +25 °C and -25 °C thermal gradient respectively, as detailed in Section 5.3.3. In both cases the mean temperature is constant at 32.5 °C. Considering the 20-45 case, it can be seen in Figure 5.7 a that the applied thermal gradient leads to a reduction in the current splitting effect when

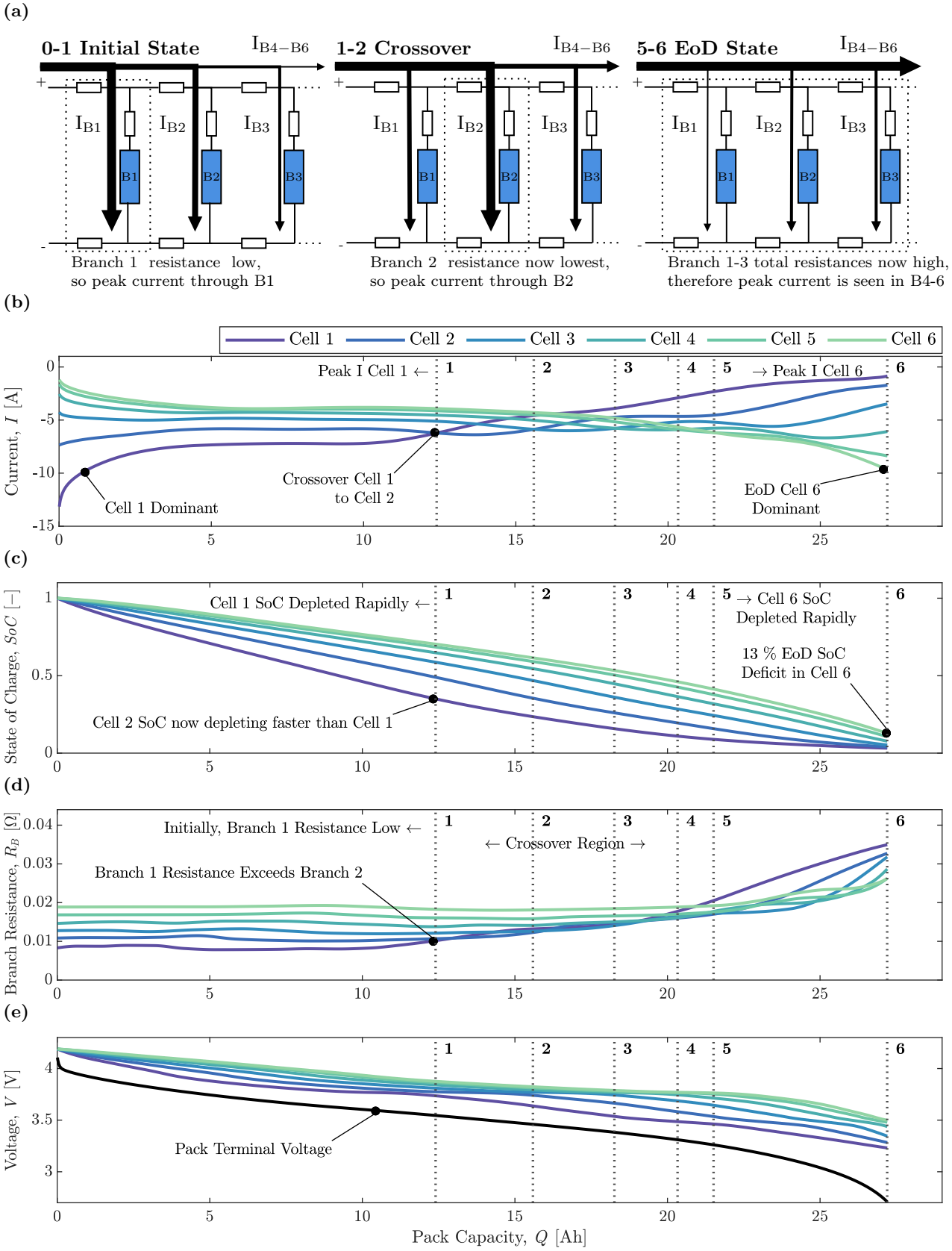


Figure 5.6: Schematic and annotated representation of underlying causes of heterogeneous behaviour in 1S6P parallel cell string at 20 °C homogeneous temperature. a) Schematic representation of current split. b) Annotated current distribution. c) Annotated SoC distribution. d) Estimated branch resistance distribution. e) Estimated cell OCV distribution. Pack terminal voltage is denoted in black

compared to the homogeneous 32.5 °C case (Figure 5.7 c and d). In this case, Cells 1-3 are cooled, and Cells 4-6 are heated relative to the mean temperature of the pack, and so the branch resistances are more even than in the homogeneous case. Due to the more even current split, the SoC distribution shown in Figure 5.7 b, is more even when compared to the 32.5-32.5 case. Additionally, there is a significant reduction in the SoC deficit between Cells 1 and 6 at the end of discharge, as shown in Figure 5.7 h, implying the operating depth of discharge is more equal in this positive thermal gradient case.

During the rebalancing phase during discharge, each cell will sequentially provide the maximum current through the pack, as the SoC of the cell prior is depleted. Below approximately 40 % SoC, significant non-linear increases in cell impedance occurs.Therefore once the SoC of the cell experiencing the maximum current falls below 40 % SoC, rebalancing of pack currents occurs. By EoD, despite lower cell impedance in the hotter cells, the combined effect of branch resistances and cell OCV deviation drives the peak current through branch 6 . In the positive thermal gradient case, the reverse effect occurs, where the thermal gradient serves to equalise branch resistances, reducing the current and SoC heterogeneity. Overall in the positive thermal gradient case the discharge is more homogeneous, allowing fuller extraction of pack capacity.

Conversely, Figure 5.7 c and d show the current and SoC distribution respectively for the 45-20 case, with a negative 25 °C thermal gradient applied. In this case, this leads to an increasing magnitude of branch resistance moving away from the string terminals, which correspondingly leads to a greater magnitude of current and SoC distribution and a greater end of discharge SoC deficit between Cells 1 and 6. This is as a consequence of the increased branch resistance increasing difficulty of accessing the energy in Cell 6 due to the higher cell impedance at low temperature. This correspondingly leads to a decrease in the overall string accessible energy of 1.13 % when compared to the reference 32.5-32.5 case. Figure 5.7 g demonstrates that a negative thermal gradient leads to a greater proportional loss in pack performance than is gained by a positive thermal gradient when compared to the homogeneous temperature case. As shown in Figure 5.7 h, applying greater negative thermal gradients greatly increases the EoD SoC deficit, while positive thermal gradients lead to correspondingly smaller decrease in the EoD SoC deficit. When comparing the 20-45 and 45-20 cases the EoD SoC deficit is reduced from 13.2 % in the 45-20 case to 3.2 % in the 20-45 case, explaining the 1.6 % difference in capacity between the cases. Finally, the effect of the different thermal gradients on the mean current deviation from nominal and maximum applied current for each cell, as shown in Figure 5.7 e and f respectively is considered. The mean and maximum variation is increased as the thermal gradient becomes increasingly negative, due to the increased overall branch resistance further from the terminals in the negative cases. Conversely increasingly positive thermal gradients lead to smaller mean and maximum deviations.

Consequently, a significant increase in the accessible pack capacity when compared to the homogeneous case might be expected. However, while the portion of pack capacity and energy which is accessible is increased in the 20-45 case, this is by only 0.38 % and 0.43 % respectively, as shown in Figure 5.7 e. The magnitude of the gain in performance is small, as while the thermal gradient does tend to equalise the branch resistances in the positive thermal gradient case, the cell impedance follows an Arrhenius relationship. Therefore there is a greater increase in cell impedance when cooling Cells 1-3 than the corresponding reduction when heating Cells 4-6, relative to a mean temperature of 32.5 °C. This in

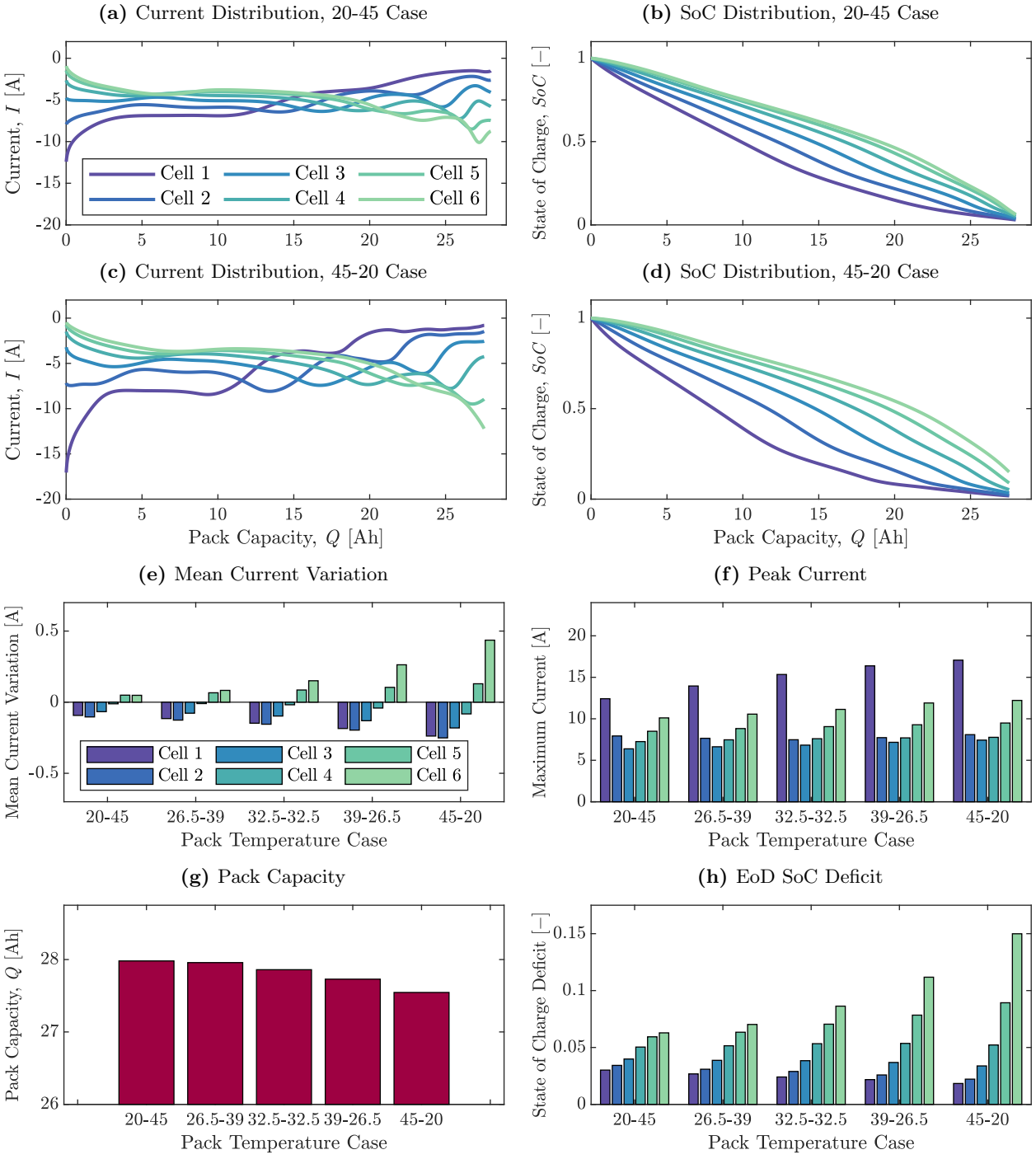


Figure 5.7: Experimentally measured current and SoC distributions for a U-topology 1S6P pack under heterogeneous temperature conditions. All measurements taken during a 1 C discharge. a) Current distribution for 20-45 case. b) SoC distribution for 20-45 case. c) Current distribution for 45-20 case. d) SoC distribution for 45-20 case. e) Mean current variation for all heterogeneous temperature cases. f) Peak current for all heterogeneous temperature cases. g) Pack capacity all heterogeneous temperature cases. h) EoD SoC deficit for all heterogeneous temperature cases.

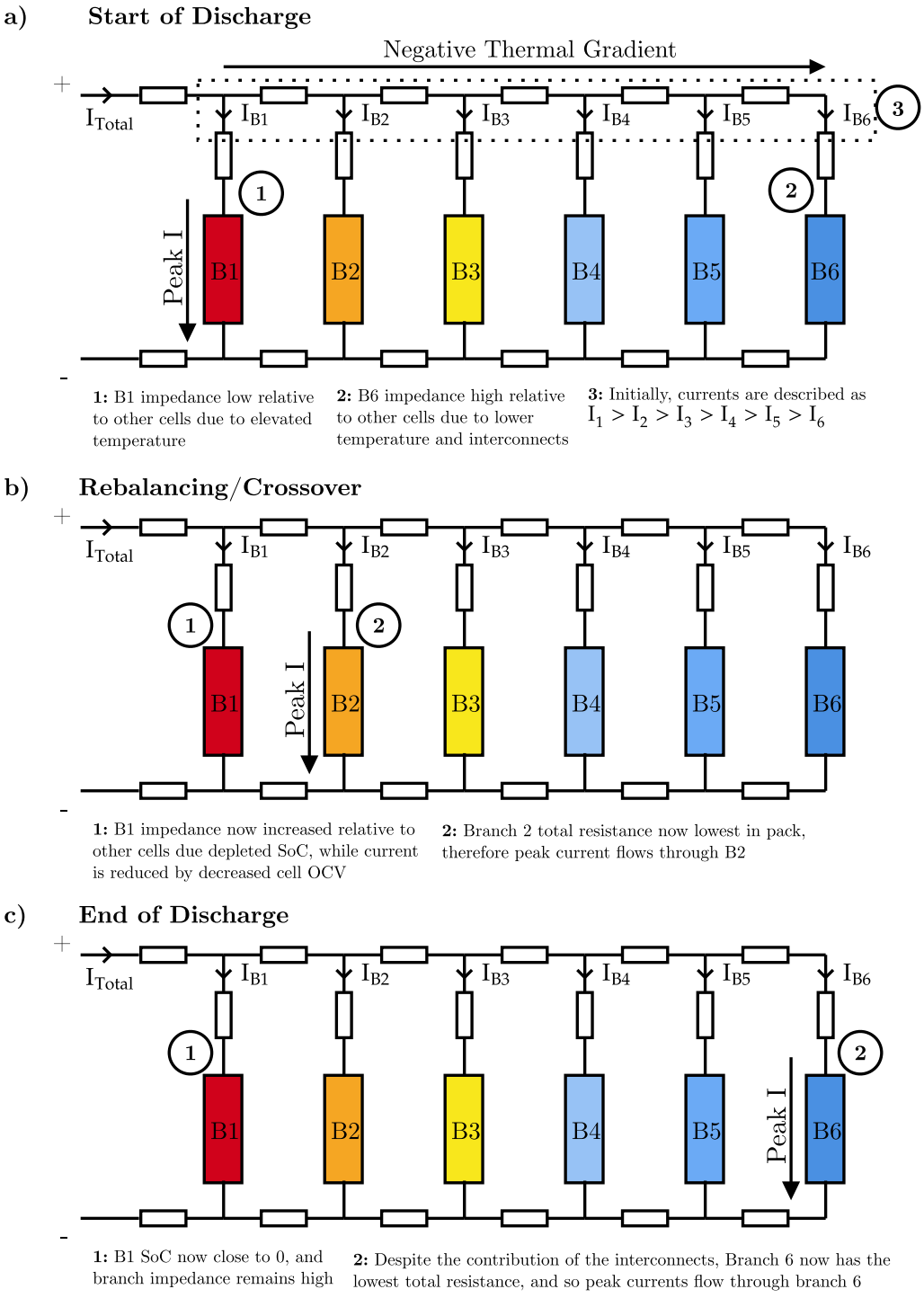


Figure 5.8: Schematic representation of current distribution during discharge for 1S6P pack under a negative thermal gradient. a) Start of discharge. b) During rebalancing (mid-discharge). c) End of discharge.

turn leads to higher overall resistances in the string and therefore greater losses due to Joule heating in the lower temperature cells. Nevertheless, equalising cell SoCs and currents is likely to have beneficial effects on pack lifetime by reducing the overall pack degradation rate by more evenly spreading the accessed capacity between the cells. Additionally, decreasing end of discharge SoC deficit implies that a positive thermal gradient is beneficial for equalising cell depth-of-discharge in parallel strings, and as the depth-of-discharge of a cell is a known stress factor during degradation this is likely to lead to benefits in terms of overall pack lifetime.

A schematic representation of this effect for a parallel string under a negative thermal gradient is shown in Figure 5.8. In the homogeneous case at start of discharge the cell impedance is approximately equal, and any unequal branch resistances are caused by stacking of interconnection resistances. In the heterogeneous case with a negative thermal gradient this effect remains, but the cells in the early branches of the pack have a reduced impedance compared to pack mean, due to their elevated temperature. Therefore, while the initial trends are similar to a homogeneous case, the magnitude of current splitting is increased with a negative applied thermal gradient.

The final two linear thermal gradient cases, the 26.5-39 and 39-26.5 cases (+12.5 °C and -12.5 °C thermal gradients, mean temperature of 32.5 °C) are not shown here. However the same trends are observed, where directionality of the applied thermal gradient leads to increasing or decreasing of the current and SoC splitting effects, with a smaller magnitude than in the ± 25 °C thermal gradient cases. The final cases considered, the 20-45-20 and 45-20-45 cases, are aimed to approximate the scenario in which either only the exterior or core respectively of the pack are cooled, leading to development of a 'pyramidal' thermal gradient. The pyramidal gradients in the 20-45-20 case lead to a reduction in both the mean and maximum current deviations alongside a reduction in the overall pack capacity compared to the 32.5-32.5 case, due to the substantial cooling of Cell 6, which substantially reduces the accessible capacity in the cell. Conversely the 45-20-45 case leads to an increase in current variation but a reduced loss of accessible capacity.

Considering the current split at start-of-discharge, it is possible to derive an analytical expression for the current split, similar to that of Wu et al. [141]. In a 'Z' topology pack, the currents passing through the branches closest to the string terminals are initially higher, this will lead to accelerated depletion in the SoC of these cells compared to the nominal rate of depletion for the entire pack. KVL states that the voltages around any closed circuit loop must sum to zero, and therefore as the terminal voltage at any instant is constant for each string branch, for each branch the terminal potential minus the total of the cell OCV and all branch overpotentials must equal zero. Using this law, an analytical system of simultaneous equations for the branch currents of the selected topologies can be derived, assuming the interconnection resistance, R_{IC}, is constant, as shown in Equations 5.2-5.7

$$V_s - OCV_1 - (R_{Cell,1} + R_S) \cdot I_1 + R_{IC} \cdot I_{Total} = 0 \tag{5.2}$$

$$V_s - OCV_2 - (R_{Cell,2} + R_S) \cdot I_2 + 2 \cdot R_{IC} \cdot (I_2 + I_3 + I_4 + I_5 + I_6) = 0 \tag{5.3}$$

$$V_s - OCV_3 - (R_{Cell,3} + R_S) \cdot I_3 + 2 \cdot R_{IC} \cdot (I_2 + 2I_3 + 2I_4 + 2I_5 + 2I_6) = 0 \tag{5.4}$$

$$V_s - OCV_4 - (R_{Cell,4} + R_S) \cdot I_4 + 2 \cdot R_{IC} \cdot (I_2 + 2I_3 + 3I_4 + 3I_5 + 3I_6) = 0 \tag{5.5}$$

$$V_s - OCV_5 - (R_{Cell,5} + R_S) \cdot I_5 + 2 \cdot R_{IC} \cdot (I_2 + 2I_3 + 3I_4 + 4I_5 + 4I_6) = 0 \tag{5.6}$$

Table 5.2: Comparison of analytical and experimentally measured initial current distribution for 20-20 case, 1 C discharge.

Branch	**1**	**2**	**3**	**4**	**5**	**6**
Analytical Current [A]	-13.37	7.04	-4.00	-2.48	-1.72	-1.39
Experimental Current [A]	-13.15	-7.36	-4.26	-2.54	-1.61	-1.19
Error [%]	1.7	-4.4	-6.1	-2.0	6.9	16.2

$$V_s - OCV_6 - (R_{Cell,6} + R_S) \cdot I_6 + 2 \cdot R_{IC} \cdot (I_2 + 2I_3 + 3I_4 + 4I_5 + 5I_6) = 0 \tag{5.7}$$

Where V_s is the terminal voltage, R_{Cell} is the cell internal resistance, R_s is the current sense resistor values, OCV_i is the cell OCV and I_i is the corresponding branch current for $i = \{1, 2 \ldots, 6\}$. Solving these equations for the 20-20 case at the start of discharge, assuming that $R_s = R_{IC} = 1$ mΩ and $R_{Cell,i} = $ const. $= 7.2$ mΩ (approximate mean $R_{Cell,i}$ at SoC = 100 %, 20 °C) yields values for the initial instantaneous current, shown in Table 5.2.

When compared to the experimentally measured currents in the 20-20 case, there was a maximum error of 16.2 % for branch 6 (noting that the absolute error is low at 0.20 A). In general, the error in prediction increased for cells further from the string terminals, likely due to stacked errors in resistance estimation and the fact that R_{CT} is current dependent. However, considering that it was assumed $R_{Cell,i}$, R_s and R_{IC} are constant, there is relatively good agreement between the analytical and experimental values. However while it is possible to predict the initial current split, due to the dependence of cell OCV and internal resistance on SoC and temperature, solving for an entire discharge would require lookup tables, and it is more effective moving forwards to utilise a full ECN model to predict current splitting effects.

5.4.3 Z-Topology: Homogeneous and Heterogeneous Temperature Cases

In this section, the experimental results for the Z-topology 1S6P pack configuration are now considered. The basic reasoning for the distribution of currents is identical to that discussed for the U-topology case, and for a more detailed explanation the reader is referred to Section 5.4.1. As such, a more limited set of cases are explored in detail, to highlight the differences in behaviour between the topology cases. In the homogeneous case, Figure 5.9 a shows the current split per cell for the homogeneous temperature 32.5-32.5 case, and the current distribution is in general more even than in the U-topology case. As can be seen, there are only small differences in initial current, with the difference between Cell 1 and 6 initially being approximately 2 times, as compared to the order of magnitude difference in the U-topology. This is due to the almost identical total path resistances between the branches, with only small variations in cell impedance, contact resistance and minor variations between resistors and busbars affecting the current distribution. While the simple assumption might however be that the branch currents should be identical, this is not the case. As shown previously by Wu et al. [141], who derived an analytical expression for the initial cell currents. This relationship is defined by Equations 5.8-5.10, for a 1S3P Z-topology, using a similar approach to that taken in Section 5.4.1 for the U-topology.

$$V_s - OCV_1 - (R_{Cell,1} + R_S) \cdot I_1 + R_{IC} \cdot (2 \cdot I_1 + I_2) = 0 \tag{5.8}$$

$$V_s - OCV_2 - (R_{Cell,2} + R_S) \cdot I_2 + R_{IC} \cdot (I_1 + 2 \cdot I_2 + I_3) = 0 \tag{5.9}$$

$$V_s - OCV_3 - (R_{Cell,3} + R_S) \cdot I_3 + R_{IC} \cdot (I_2 + 2 \cdot I_3) = 0 \tag{5.10}$$

Where V_s is the terminal voltage, R_{Cell} is the cell internal resistance, R_s is the current sense resistor values, OCV_i is the cell OCV and I_i is the corresponding branch current for $i = \{1, 2, 3\}$. This effect is due to the unequal overpotential in each branch, as whilst the path resistances are approximately equal, the current through each interconnection is not identical, resulting in initially unbalanced current flows as demonstrated in Equations 5.8-5.10. As the initial cell currents in the Z-configuration are not equal and the SoC of the cells in the string will be depleted at initially different rates. If the initial rate is different, over time the cell SoCs will diverge and therefore a continuing distribution of currents from the nominal value will be seen. Extending the analysis of Wu et al. [141] to the 1S6P case investigated here, it was found that the current is split symmetrically into cell pairs, with the relationship given by Equation 5.11.

$$(I_1 = \ I_6) < (I_2 = \ I_5) < (I_3 = I_4) \tag{5.11}$$

This relationship is for the ideal case where all cells are identical in capacity, OCV response and impedance, and thus there is still variation between the cell pairs identified (Figure 5.9 a). Nevertheless, a broad pairing of cell currents as stated is seen. Increasing the mean temperature leads again to an increasing magnitude of current split, as the increase in temperature again leads to decreased contribution to the total path resistance by the cell internal impedance. As such the relative importance of the parasitic resistances is increased. In these cases, the broad pairing of cell currents is still observed. The effect of this homogenisation of currents can be seen in Figure 5.9 c and e, showing the maximum cell current and pack capacity respectively. Figure 5.9 c shows that increasing the pack mean temperature has a minimal effect on the magnitude of the maximum current, while a minimal effect was also seen on the mean current deviation from nominal. It is noted that while the cell currents are theoretically paired, in practice small variations in the cell capacity, impedance and parasitic resistances mean that small differences are observed between the nominally paired branches.

Considering the accessible capacity, increasing the mean temperature does increase the accessible capacity, due to the smaller losses and EoD SoC deficit, however the magnitude of this effect is smaller than in the U-topology case, with only a 2.2 % gain in string capacity between the 20-20 and 45-45 cases. It is also noted that the total accessible capacity in the Z-topology 45-45 case is approximately 3 % lower than in the U-topology case. This is likely due to the location of cutoff voltage measurement now being 'across' the pack and therefore a greater portion of the parasitic overpotentials are measured, limiting the accessible capacity in the Z-topology. The SoC deficit at EoD for all cells in the homogeneous case was over 5 %, which compares unfavourably to the U-topology case, where the EoD SoC deficit was under 5 % in cells 1-3 in the 20-20 case, and under 6 % in all cells in the 45-45 case.

Next, the linear thermal gradients applied to the Z-topology are considered. Unlike the U-topology case, the cell currents are in this case approximately symmetric. Previously when considering the homogeneous temperature cases, cell currents were observed to approximately pair, however, as shown in Figure 5.9 b, application of a 25 °C thermal gradient to the Z-topology string decouples the cell

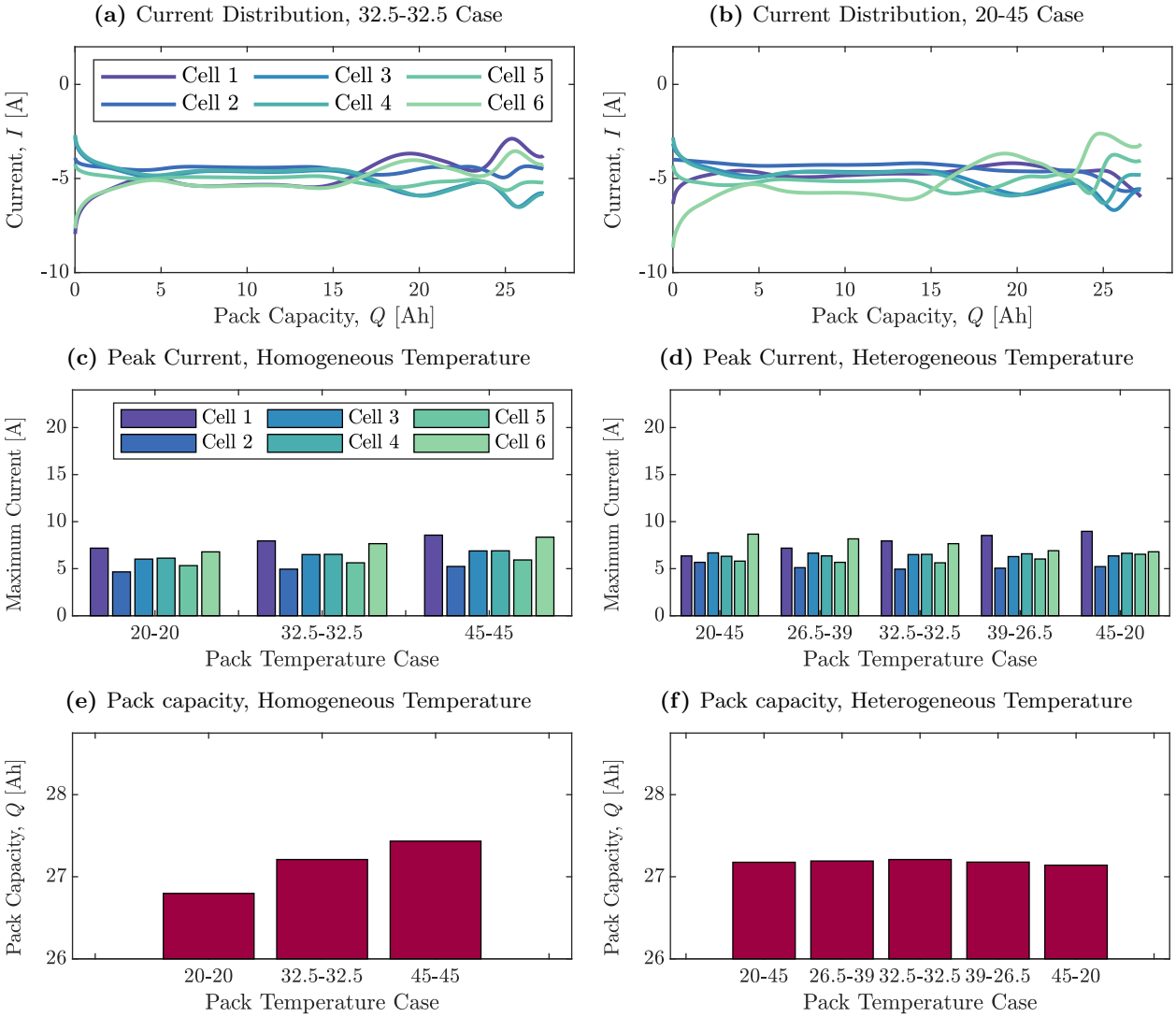


Figure 5.9: Experimentally measured current and SoC distributions for a Z-topology 1S6P pack under all temperature conditions. All measurements taken during a 1 C discharge. a) Current distribution for 32.5-32.5 case. b) Current distribution for 20-45 case. c) Peak current for all homogeneous temperature cases. d) Peak current for all heterogeneous temperature cases. e) Pack capacity for all homogeneous temperature cases. f) Pack capacity for all heterogeneous temperature cases.

current pairs, leading to increasingly unbalanced currents compared to the homogeneous cases. This is due to the applied thermal gradient leading to differences in temperature, and therefore cell impedance, between the symmetric cell pairs. Considering the maximum current (Figure 5.9 d) applying a thermal gradient does unbalance the cell currents, due to the decoupling between previously paired cell currents, compared to the homogeneous temperature case. However, the maximum current is still significantly lower than seen in the U-topology case. As expected, the results are broadly symmetrical between the 20-45 and 45-20 cases, implying that the nomenclature of 'positive' and 'negative' thermal gradients has no relevance to the Z-topology. Finally, the thermal gradients applied have a minimal effect on the accessible capacity of the pack, as shown in Figure 5.9 f. This is due to the cell impedances having a smaller relative impact in the Z-topology, as the total branch resistance is higher as each branch includes a nominally equal number of interconnection resistances, 6 per branch, compared to the U-topology where for example branch 1 includes 1 interconnection and branch 6 includes 11, meaning the significance of the cell impedance is much greater in branch 1. When thermal gradients are present in the Z case, symmetry therefore means that a reduction in branch impedance is compensated by an increase in total branch impedance in the symmetric branch, and therefore the direction of the thermal gradient has no impact.

5.5 Interim Discussion

So far, the effect of changing the homogeneous temperature and thermal gradient applied to two possible string topologies has been considered and experimentally investigated. Based on these results, it can be concluded that the thermal conditions within the string have a highly significant impact on the current and SoC distributions, as well as the accessible capacity of the string. For example, increasing the mean temperature in the homogeneous cases for both topologies investigated leads to percentage point gains in overall capacity. Analysis of total branch resistances over a full discharge has shown the impacts of cell impedance changes caused by unequal SoC distributions on the overall current distribution development. This highlights the coupled nature of impedance, current and SoC within parallel connected cell strings. As it has been mathematically shown that if interconnection resistances are finite, a current distribution will exist, this implies that there will always be some degree of heterogeneity in any parallel connected system, for all topologies (excepting a 1S2P symmetrical system).

Thermal gradients on the other hand lead to generally negative effects on the current and SoC balance and pack capacity in the Z-topology, however in the U-topology thermal gradients may be classified into 'positive' and 'negative' thermal gradients with reference to Cell 1 in the string. The negative gradients identified lead to a reduction in performance in terms of the above metrics, while the positive gradients lead to small improvements. The implication for the U-topology however is for the TMS, which will in any practical system lead to thermal gradient formation (e.g. due to working fluid temperature increases or airflow direction), and as such should always aim to introduce a positive gradient where possible. This will lead to a small gain in capacity, but more importantly reduce variability between cell operating regimens, therefore improving the consistency of cell degradation.

Due to the symmetry in the Z-topology case, the effect of thermal gradients is much more minimal, due to the relatively higher resistance of each branch reducing the impact of the cell impedance. However, this in turn leads to an overall reduction in capacity in the Z-topology, due to the increased parasitic

resistive loss in each branch leading to a greater SoC deficit at EoD. The next objectives of this work were to investigate the optimal thermal configuration to achieve the highest pack performance, while reducing heterogeneities within the pack. Additionally, the role of both the interconnect resistance ratio and variations of the interconnection resistances can be investigated, using the ECN model derived in Section 4.5.

5.6 Model Outline and Validation

The model used to investigate variations in the temperature conditions was previously derived and validated in Section 4.5, with the express aim of optimising the model to describe behaviour within parallel cell strings. As such, the model was previously validated against experimental results for the U-topology packs presented in Section 5.4 and showed generally good agreement between the simulated and experimentally measured results in all cases.

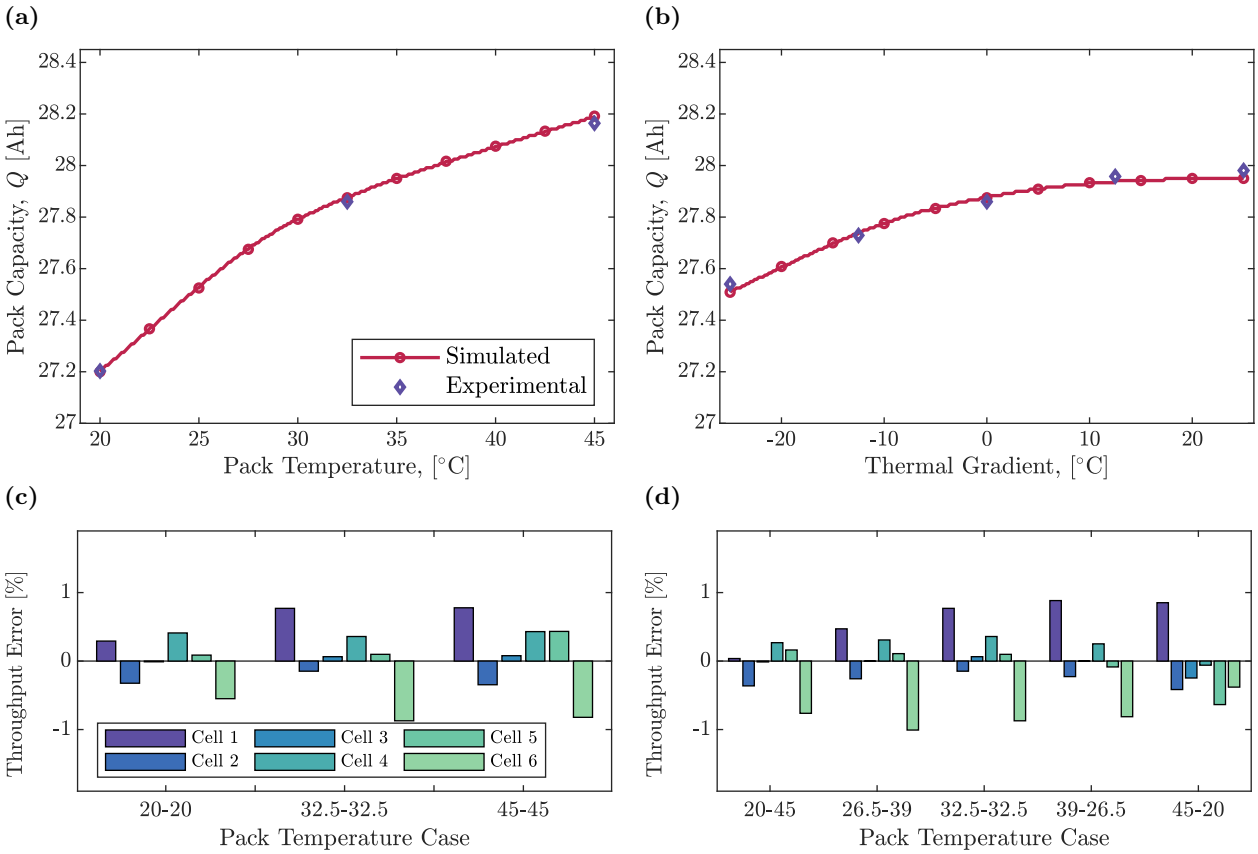


Figure 5.10: Validation of 1S6P model. a) Experimentally measured and simulated pack capacities, homogeneous temperature (251 simulated points, 20.0 - 45.0 °C, step size 0.1 °C. b) Experimentally measured and simulated pack capacities, homogeneous temperature (251 simulated points, mean temperature 32.5 °C, -25.0 - +25.0 °C thermal gradient, step size 0.1 °C. c) Simulated cell current throughput error, homogeneous temperature cases. c) Simulated cell current throughput error, heterogeneous temperature cases.

In order to further validate the model capacity predictions, the model was run to simulate a range of both homogeneous pack temperature and applied thermal gradients with a mean temperature of 32.5-32.5 for the U-topology case. Figure 5.10 a and b show the simulated results for 251 simulation runs in each case over the experimentally investigated windows with a parameter step size of 0.17 °C for the homogeneous and thermal gradient cases respectively. As can be seen in comparison to the experimentally measured pack capacity in each case there was good agreement between the model

Table 5.3: Percentage error in model capacity predictions.

Case	**20-20**	**32.5-32.5**	**45-45**	**20-45**	**26.5-39**	**32.5-32.5**	**39-26.5**	**45-20**
Error [%]	-0.103	0.055	0.098	-0.112	-0.64	0.045	0.001	-0.148

predictions and measured capacities.

Table 5.3 shows that there was good agreement between the model predictions and measured pack capacities in all cases, with the error maintained below approximately 0.15 %. The cellwise errors in capacity prediction are shown in Figure 5.10 c and d for the homogeneous and thermal gradient cases respectively, and it can be seen that the error is maintained below 1 % in all cases, with an approximately even split between under- and over-prediction of the cell utilised capacity. The errors in capacity prediction, both at the cell and pack level, were deemed acceptable for further investigation of string behaviour, with the errors expected to be principally caused by the initial modelling assumption that all cells possessed identical capacity and impedance behaviour. As shown in Section 5.3.2, this was not the case, with up to a 0.7 % spread in capacity and 8 % spread in $R_{DC|10s}$ identified. Nevertheless, the errors introduced by this assumption remain small overall, and the relative accuracy of the model is not significantly reduced.

5.7 The Effects of Heterogeneities: Modelling Study

5.7.1 The Effects of Thermal Conditions

Having ensured the model performance predictions retained accuracy for the parallel string configurations experimentally investigated, the effect of composite thermal variations was investigated. This consisted of simulating a number of scenarios with variation in both thermal gradient magnitude and string mean temperature. For the purposes of analysis and comparison, the 32.5-32.5 case with no applied thermal gradient is taken as a reference, and where appropriate deviations are calculated relative to this case. The range of input conditions considered in the first case for the U-topology ranged from a string mean temperature of 15 °C to 45 °C with a thermal gradient of ± 20 °C (leading to a maximum and minimum cell temperature of 55 and 5 °C respectively. All simulations investigating thermal conditions were carried out using the previously parameterised resistance model for the busbars experimentally investigated. In each case, the effects of current rate were also varied, with rates of 0.5, 1 and 2 C considered.

The simulated pack capacity for the U-topology case at the 3 selected rates, each simulated under 256 combinations of thermal gradient and mean temperature, is shown in Figure 5.11 a to c for each rate respectively. Application of thermal gradients in the U-topology case leads to a reduction in capacity in the negative case and increases in capacity in the positive case, confirming the previously experimentally derived results presented in Section 5.4. Again, this occurs due to the differential cell impedance induced by cases under thermal gradients, which in turn changes the total branch impedance. Increasing the branch impedance leads to an overall reduction in accessible capacity in the string branch, however the relative impact of increasing the branch impedance is greater the further from the string terminals the relevant cell is placed. In the case where the thermal gradient is positive, the cells closest to the string terminals have a higher impedance and therefore the branch impedances are increasingly even. Conversely, a negative thermal gradient will lead to low temperature cells being

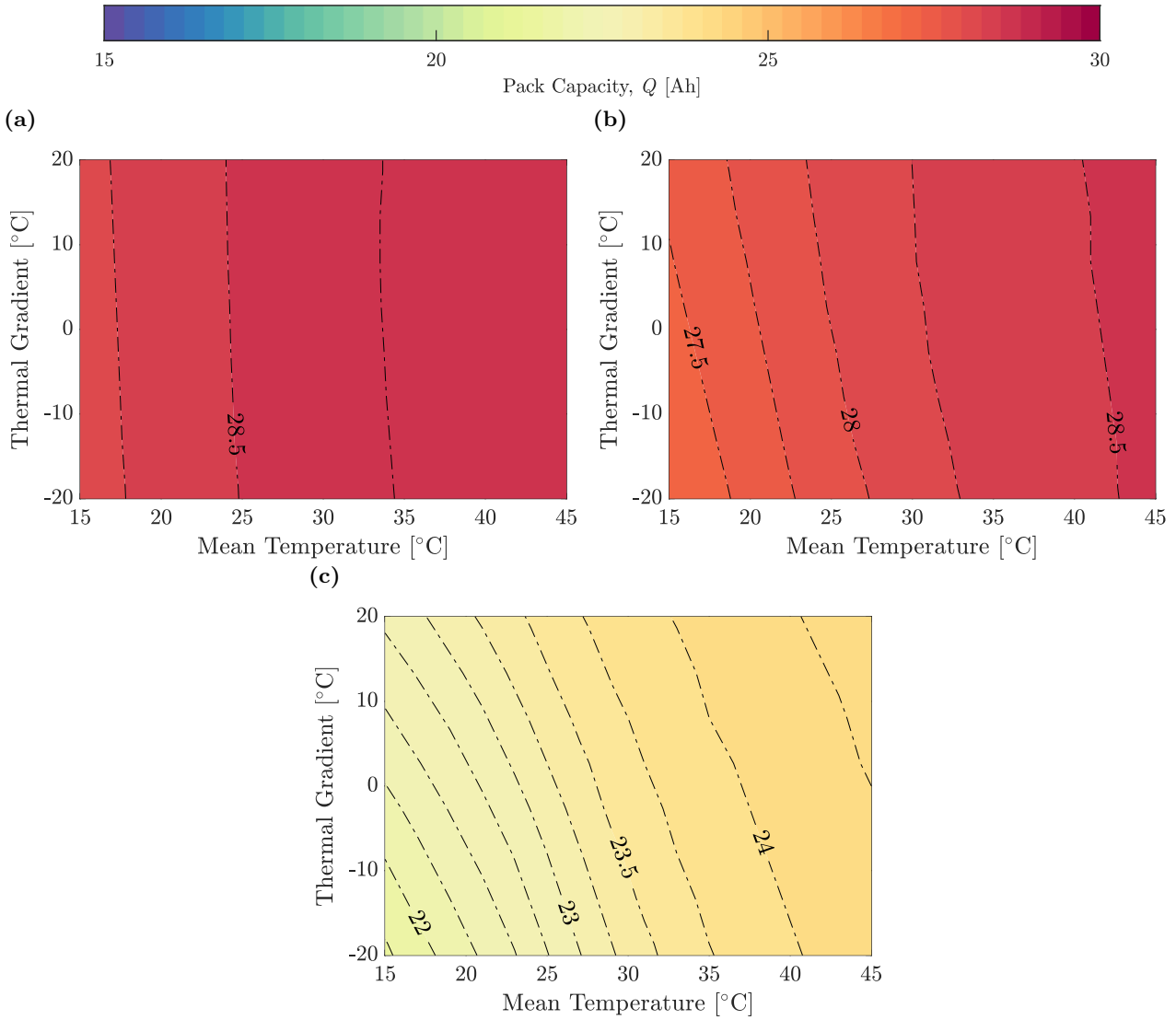


Figure 5.11: Contour plots of simulated 1S6P U-topology pack accessible capacity under -20 - +20 °C thermal gradients and 15 - 45 °C mean temperatures. a) 0.5 C discharge. b) 1 C discharge. c) 2 C discharge.

placed further from the string terminals, increasing the branch impedance and reducing the capacity which can be accessed from those cells.

As shown by Figure 5.11, increasing the applied rate decreases the accessible pack capacity overall by up to 20 % when comparing the 0.5 C case to the 2 C case. Additionally, the degree of capacity loss induced by reduced mean temperatures and therefore higher cell impedances is increased, with thermal gradients having an increasing impact at higher rates. Under a 0.5 C constant current discharge (Figure 5.11 a) applied thermal gradients have a negligible impact on the simulated pack capacity. However, under a 2 C constant current discharge (Figure 5.11 c) applying thermal gradients of ± 20 °C has a significant impact on the accessible capacity of the string. As an example, it is predicted that a pack of mean temperature of 31 °C and applied thermal gradient of -20 °C has the same accessible performance as a pack at 25.0 °C mean temperature and applied thermal gradient of +20 °C achieving the same performance with a 6 °C reduction in mean cell temperature. From these simulations it can be concluded that thermal gradients do have a significant impact on pack performance in the U-topology case, however that impact is generally only seen at higher rates.

Previously in Section 5.4, the reason for loss of performance was found to be inaccessible capacity in the cells furthest from the terminals, with thermal gradients inhibiting the ability to access this capacity before the pack lower voltage cutoff. Under thermal gradients, especially at lower mean temperatures, the difference between cell impedances increases, due to the non-linearity of the cell impedance response with respect to temperature. When higher current rates are applied to the pack, the relative importance of overpotentials is increased, due to the higher total currents. While the cell overpotential also increases, the dominant overpotential comes from the interconnections, as each passes the current to multiple cells.

Therefore, at higher rates the difference between the cell OCV and pack terminal voltage is greater, leading to a greater overall drop in pack capacity. In the case of a positive thermal gradient, total branch resistances are equalised, leading to greater accessible capacity than the 0 °C thermal gradient case, while the converse is true with a negative thermal gradient. The cell tested and modelled in this work, the Kokam 5 Ah, is a high-power cell and therefore is designed to sustain high rates. As such, the 2 C discharge case is relatively moderate for the cell, and it can be expected that for a high energy cell similar effects would occur at lower rates. In general it is expected that the effects of thermal gradients on pack performance will be greater at low temperatures and higher rates, with the direction of the thermal gradient influencing if the effect is positive or negative for a 'U' topology.

Still considering the U-topology case, Figure 5.12 a-f shows the cell accessible capacity for Cells 1-6 respectively for the range of thermal gradients and mean temperatures investigated. As shown, the current throughput through Cells 1-4 is relatively insensitive to the applied thermal gradient. In comparison, Cells 5 and 6 are highly sensitive to the applied thermal gradient, with a 7 % reduction in current throughput in Cell 6 in extreme cases (-20 °C thermal gradient, 15 °C mean temperature) compared to the base case. As such it can be concluded that the capacity loss seen in the U-topology pack under negative thermal gradients is principally driven by the loss of accessible capacity in the cells furthest from the string terminals. Therefore it is not expected that this effect would be present in the Z-topology case.

The underlying causes of this capacity loss for the U-topology at higher rates can be examined further by considering detailed results from two extremes of the 2 C simulation case. Figure 5.13 a and b show the current and current throughput distributions for the pack at 15.0 °C mean temperature and applied thermal gradient of -20 °C while Figure 5.13 c and d show the same metrics at 45.0 °C mean temperature and applied thermal gradient of +20 °C. In the first case, despite overall similar current profiles and SoC distributions, EoD is reached earlier in the low temperature case, due to the increased overpotentials and therefore earlier reaching of the lower voltage limit for the pack, leading to a reduction in overall capacity.

Considering the Z-topology case shown in Figure 5.14 a-c for the 3 rates investigated, as previously shown experimentally, thermal gradients have a minimal effect on the accessible capacity, due to both the symmetry and the therefore equal branch impedance. This leads to relatively smaller changes in the branch impedance when thermal gradients lead to changes in cell impedances. As such, the effect of thermal gradients on the Z-topology pack capacity is minimal and the principal effect driving capacity is the overall mean temperature of the pack, which reduces losses when increased and therefore increases accessible capacity. Figure 5.14 a and c show the accessible capacity under a 0.5 C and 2 C rate respectively, showing the sensitivity of the Z-topology pack to mean temperature increases with

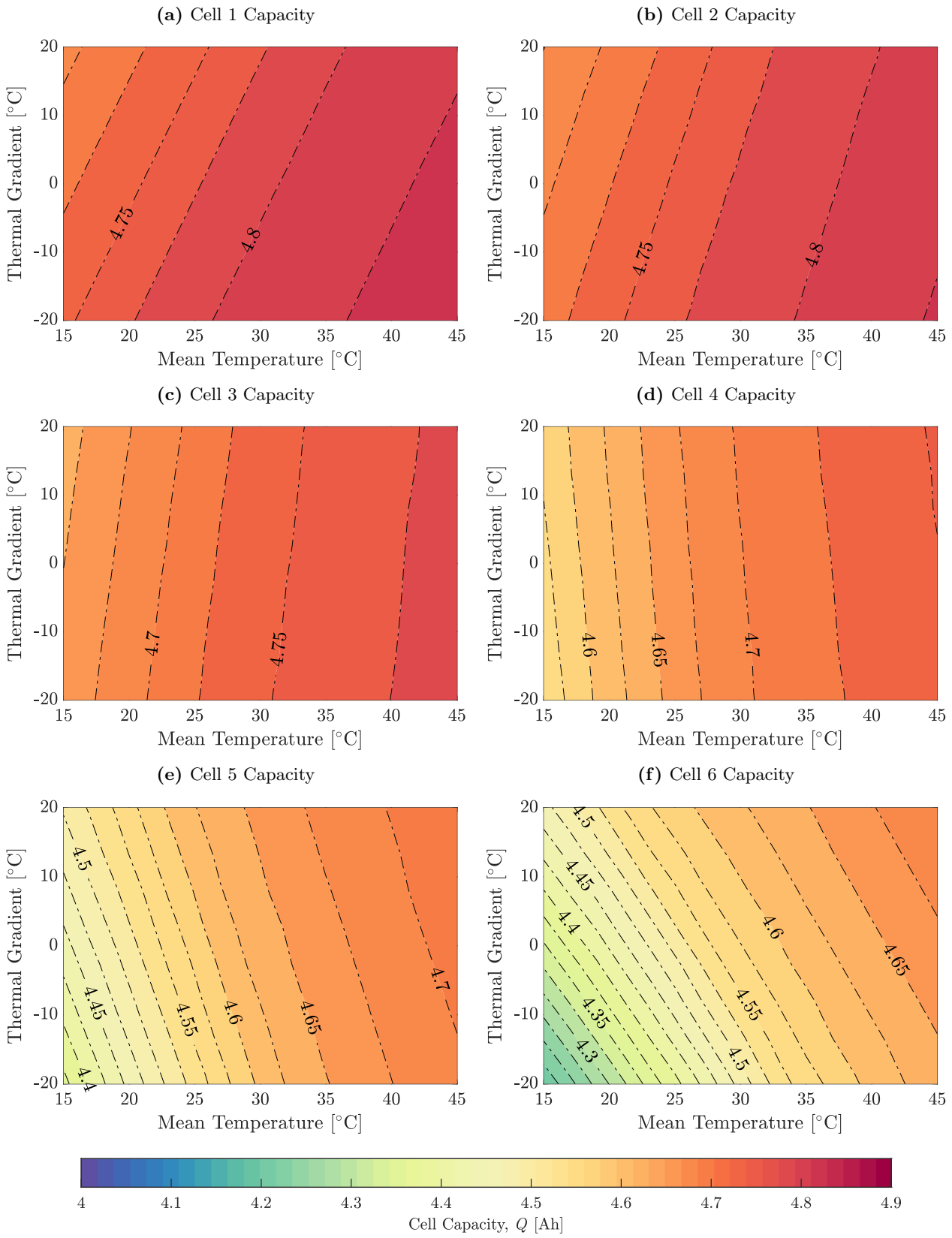


Figure 5.12: Contour plots of simulated 1S6P U-topology pack capacity under -20 - +20 °C thermal gradients and 15 - 45 °C mean temperatures, 1 C discharge. a) Cell 1 accessible capacity. b) Cell 2 accessible capacity. c) Cell 3 accessible capacity. d) Cell 4 accessible capacity. e) Cell 5 accessible capacity. f) Cell 6 accessible capacity.

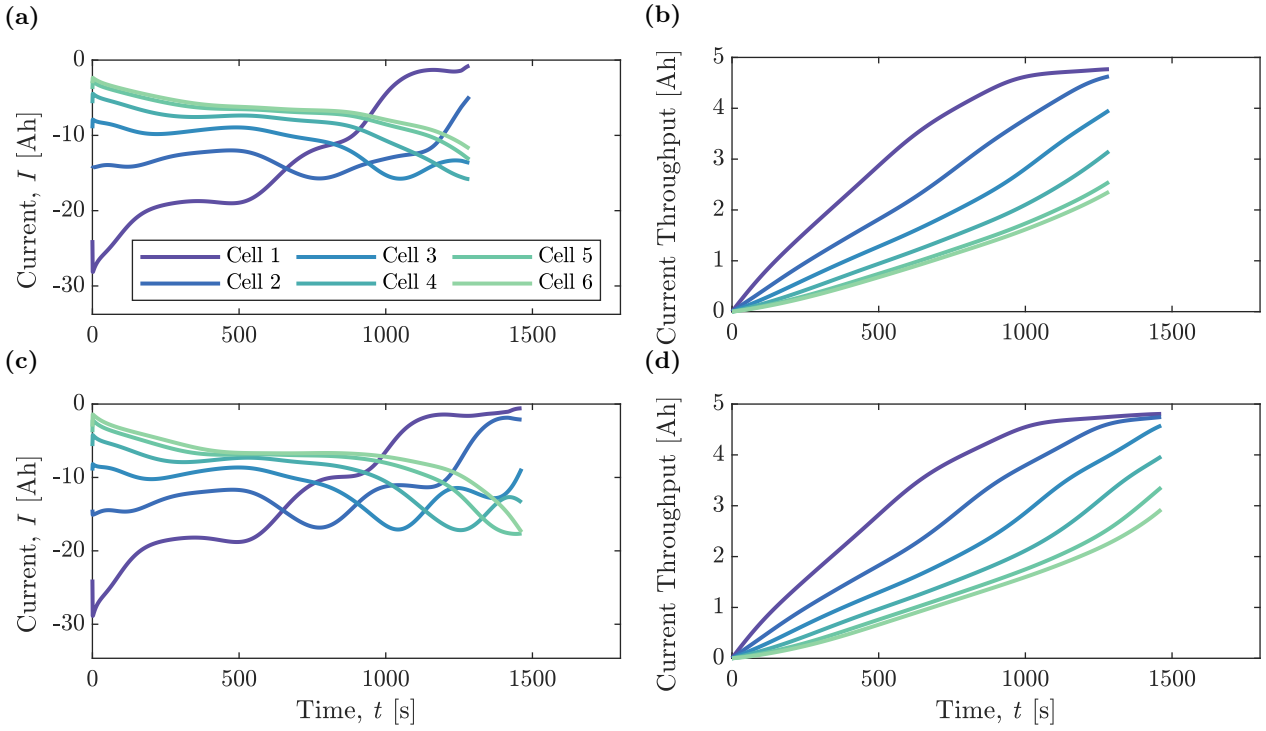


Figure 5.13: Example simulated current and SoC distributions. a) Current distribution for T_m = 15 °C, $\Delta T = -20$ °C. b) SoC distribution for T_m = 15 °C, $\Delta T = -20$ °C. c) Current distribution for T_m = 45 °C, $\Delta T = +20$ °C. e) SoC distribution for T_m = 45 °C, $\Delta T = +20$ °C

increasing rate.

5.7.2 The Effects of Variable Interconnection Resistance

Another possible impact on overall capacity is varying the interconnection resistance (and therefore IRR) between each cell. In a real system, this could occur either due to fault conditions or unequal length busbar connections. In this section the effects of increased interconnection resistance on overall pack capacity is considered. An idealised string was considered, with the branch resistors (R_S) held constant at 1 mΩ. The investigated circuit is shown in Figure 5.15, and the pack response at 1 C was simulated for 51 variations in branch resistance for each interconnection resistor, $R_{IC,n}$. In each case the selected resistor value was varied from 0.1 mΩ to 20 mΩ, for a total of 306 simulated pack configurations per temperature breakpoint.

The effect of varying differing interconnection resistances can be seen in Figure 5.16 for the U-topology pack at 32.5 °C. At 32.5 °C, the cell total impedance at 50 % SoC is approximately 7.5 mΩ, and this value is used when commentating on the IRR. As expected, increasing the resistance $R_{IC,1}$ has the greatest overall impact on pack capacity, with a rapid drop in accessible pack capacity above a resistance value of 6 mΩ. In contrast, increasing the resistance $R_{IC,6}$ has a minimal impact on overall pack capacity, as in this case only branch 6 of the string is affected by the increased resistance. As the applied current is constant in all cases, this leads to an increase in the current passed by the other cells in the string, somewhat compensating for the loss in accessible capacity from Cell 6.

In an LIB, impedance decreases non-linearly with increasing temperature, and therefore as the mean temperature of a pack increases, the relative impact of increasing the interconnection resistance is enhanced. This is due to the increasing contribution of the interconnection resistance to the total

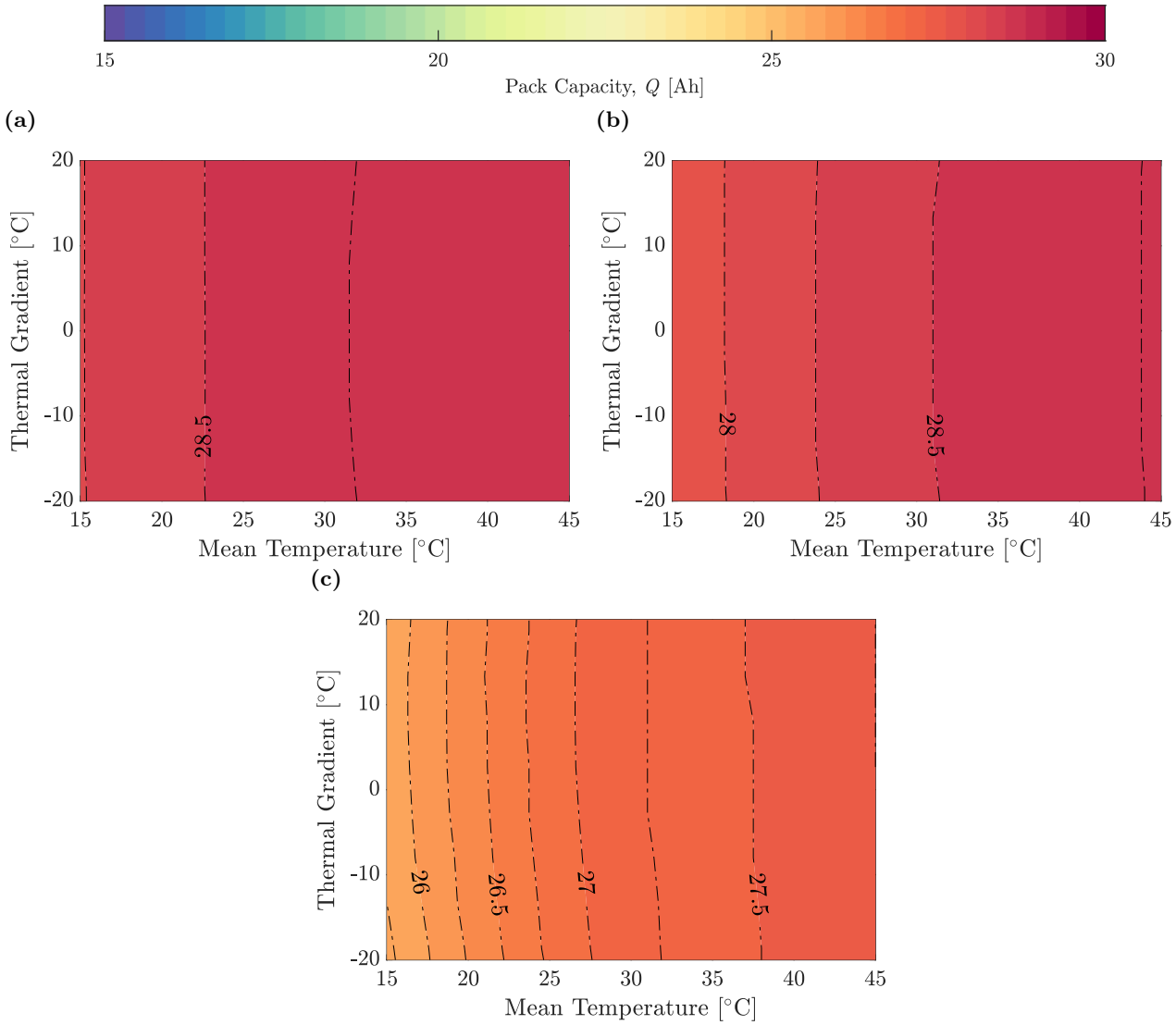


Figure 5.14: Contour plots of simulated 1S6P Z-topology pack capacity -20 - +20 °C thermal gradients and 15 - 45 °C mean temperatures. a) 0.5 C discharge. b) 1 C discharge. c) 2 C discharge.

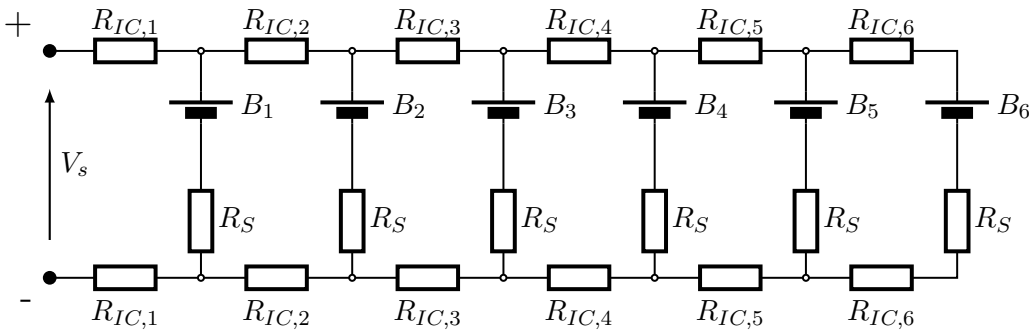


Figure 5.15: Circuit diagram for variable R_{IC} simulations

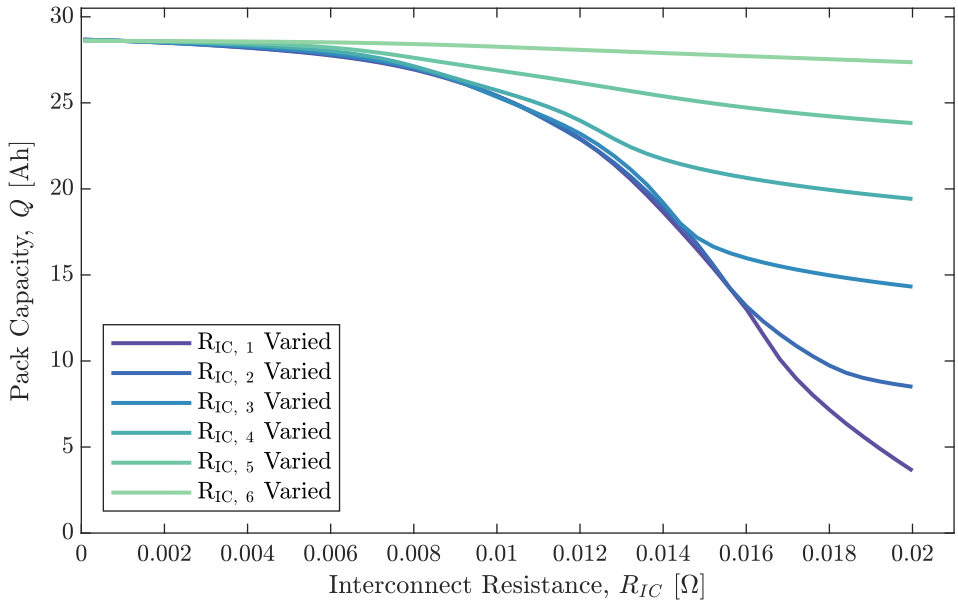


Figure 5.16: Pack capacity for U-topology with variable $R_{IC,n}$, where $n = \{1, 2, \ldots, 6\}$. In each case $R_{IC,n}$ is varied from 0.1 mΩ to 20 mΩ. All simulations under a 1 C discharge.

branch resistance which in turn is a key factor driving the current distribution. Thus, the U-topology strings are, in general, more sensitive to variations in interconnection resistance close to the pack terminals, with the effect of increased interconnection resistance increased at elevated temperature.

5.7.3 The Effects of Variable Branch Resistances

In order to emulate the effects of either cell resistance variation or high contact resistances, a set of simulations with varied branch resistance (R_S) were considered. In this case the idealised string was considered, with the interconnection resistors (R_{IC}) held constant at 1 mΩ. The investigated circuit is shown in Figure 5.17, and the pack response at 1 C was simulated for 51 variations in resistance for each branch resistor, $R_{S,n}$. In each case the selected resistor value was varied from 0.1 mΩ to 50 mΩ, for a total of 306 simulated pack configurations per temperature breakpoint. Considering the range of resistances selected, Taheri et al. [209] measured contact resistances in bolted connections of an order of 10 mΩ, while Brand et al. [211] measured contact resistances varying from the order of 10 mΩ for aluminium press contacts to 0.01 mΩ for copper at high contact pressures. Brand et al. [211] also investigated welded using spot, ultrasonic and laser welded contacts. Measured contact resistances ranged from 0.15 to 0.32 mΩ, depending on the weld size, shape and number of points. Therefore the range selected for investigation is appropriate to investigate the effects of variable contact resistances,

especially given that fault conditions may lead to significantly increased contact resistances [140].

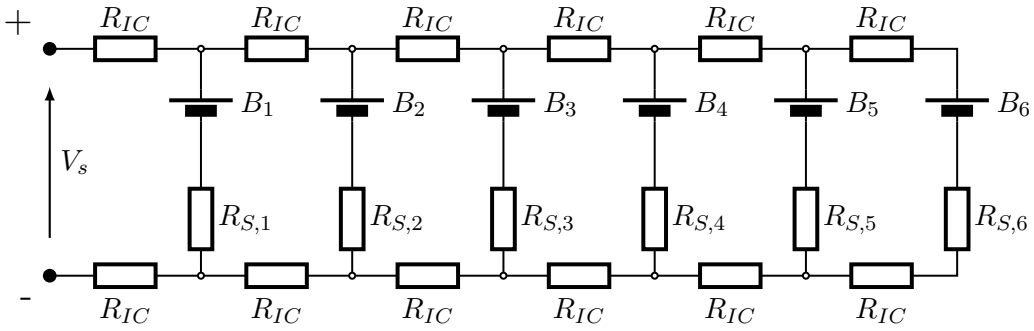


Figure 5.17: Circuit diagram for variable R_S simulations

The effects of varying differing branch resistances can be seen in Figure 5.18 a and b for the U- and Z-topology pack at 32.5 °C respectively. As can be seen in Figure 5.18 a, the loss in overall pack capacity is dependant on the position of the varied resistor, with changes in the resistance of branch 1 leading to a maximum loss in pack capacity of 2.5 % for $R_{S,1} = 50$ mΩ. In contrast, the same change in $R_{S,6}$ leading to a 6 % pack capacity loss. Due to the relative position of the varied resistors, increasing the resistance of branch 1 has a smaller overall impact on the pack capacity as initially the increased resistance serves to balance the overall branch impedances. Varying $R_{S,6}$ begins to have a significant impact of the pack capacity above approximately 10 mΩ, while for the $R_{S,1}$ case the impact is not significant until $R_{S,1}$ equals 35 mΩ. In comparison, for the Z-topology as shown in Figure 5.18 b, less sensitivity to the position of the increased branch resistance is seen. However, while the effect on overall pack capacity is less sensitive, for the Z-topology the capacity loss under all variations is higher than for the $R_{S,1}$ and $R_{S,2}$ variations in the U-topology. Additionally, the onset of rapid capacity loss in the Z-topology case occurs more rapidly in all cases except when compared to the $R_{S,5}$ and $R_{S,6}$ U-topology variation cases, occurring for all variations at approximately 20 mΩ.

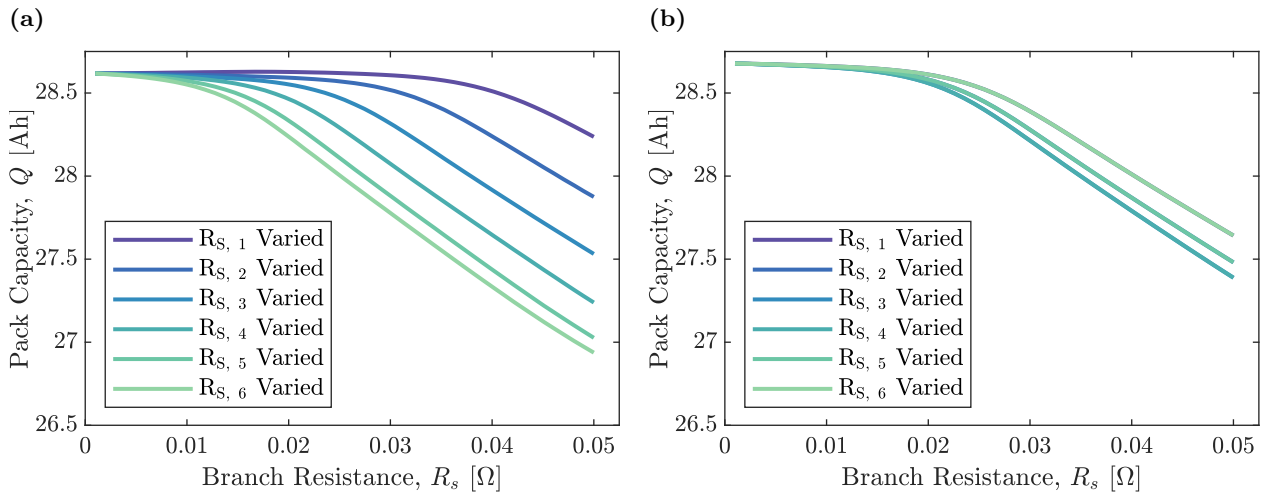


Figure 5.18: Pack capacity for U- and Z-topology with variable $R_{S,n}$, where $n = \{1, 2, \ldots, 6\}$. In each case $R_{S,n}$ is varied from 0.1 mΩ to 50 mΩ. All simulations under a 1 C discharge at 32.5 °C. a) U-topology. b) Z-topology

For the U-topology, the causes for the overall capacity loss in each case can be seen in Figure 5.19 a-f, which shows the cell current throughput for cells 1-6 respectively. The further from the string terminals the increased branch resistance occurs, the greater and earlier the impact on the accessible

capacity of the relevant cell is. For example increasing $R_{S,1}$ does not lead to significant impacts on Cell 1 accessible capacity until the impedance has increased to 30 mΩ, and the loss in accessible capacity in Cell 1 is a maximum of 10 %. In comparison, varying $R_{S,6}$ leads to a more rapid onset of cell capacity loss above $R_{S,6}$ equals 10 mΩ, with a maximum loss in accessible capacity of 38 %. This effect can be explained by considering the location of the relevant branch impedance. In the U topology case, where the increased branch impedance is close to the terminals, the overall effect is to equalise the total resistance of branch 1 with that of branches further from the terminals. As previously identified in Figure 5.19 d, the EoD total branch resistances are of the order of 25 mΩ. As can be seen in Figure 5.19 a, the accessible capacity of Cell 1 begins to decrease rapidly after the branch resistance exceeds approximately 20 mΩ. The value at which this curve inflects corresponds with the branch resistance exceeding the maximum resistance of branch 6. Meanwhile for Cell 6, shown in Figure 5.19 f, the curve inflects almost immediately, as in this case there is no rebalancing of branch resistances and instead the increased resistance is simply acting to 'block' access to energy in Cell 6. It is also noted that in all cases the accessible capacity of all other branches is marginally increased, compensating somewhat for the loss in accessible capacity in the branch with increased resistance.

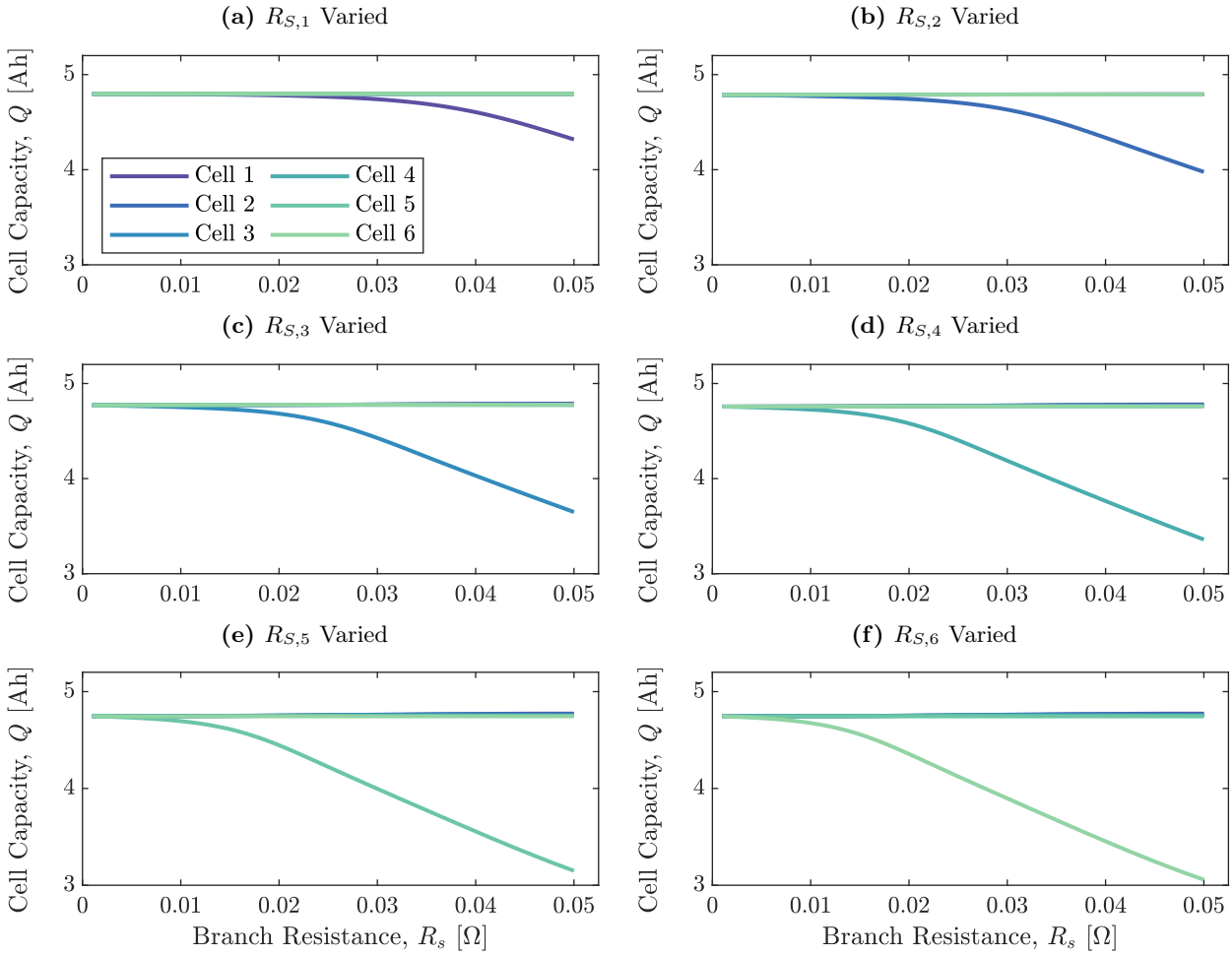


Figure 5.19: Cell accessible capacity for U-topology with variable $R_{S,n}$, where $n = \{1, 2, \ldots, 6\}$. In each case $R_{S,n}$ is varied from 0.1 mΩ to 50 mΩ, at a homogeneous temperature of 32.5 °C. All simulations under a 1 C discharge. a) $R_{S,1}$ varied. b) $R_{S,2}$ varied. c) $R_{S,3}$ varied. d) $R_{S,4}$ varied. e) $R_{S,5}$ varied. f) $R_{S,6}$ varied.

Finally, the effect of mean temperature on the accessible capacity is considered, as shown in Figure 5.20 a-f, which shows the effect of varying branch resistances $R_{S,1}$ - $R_{S,6}$ respectively at 3 temper-

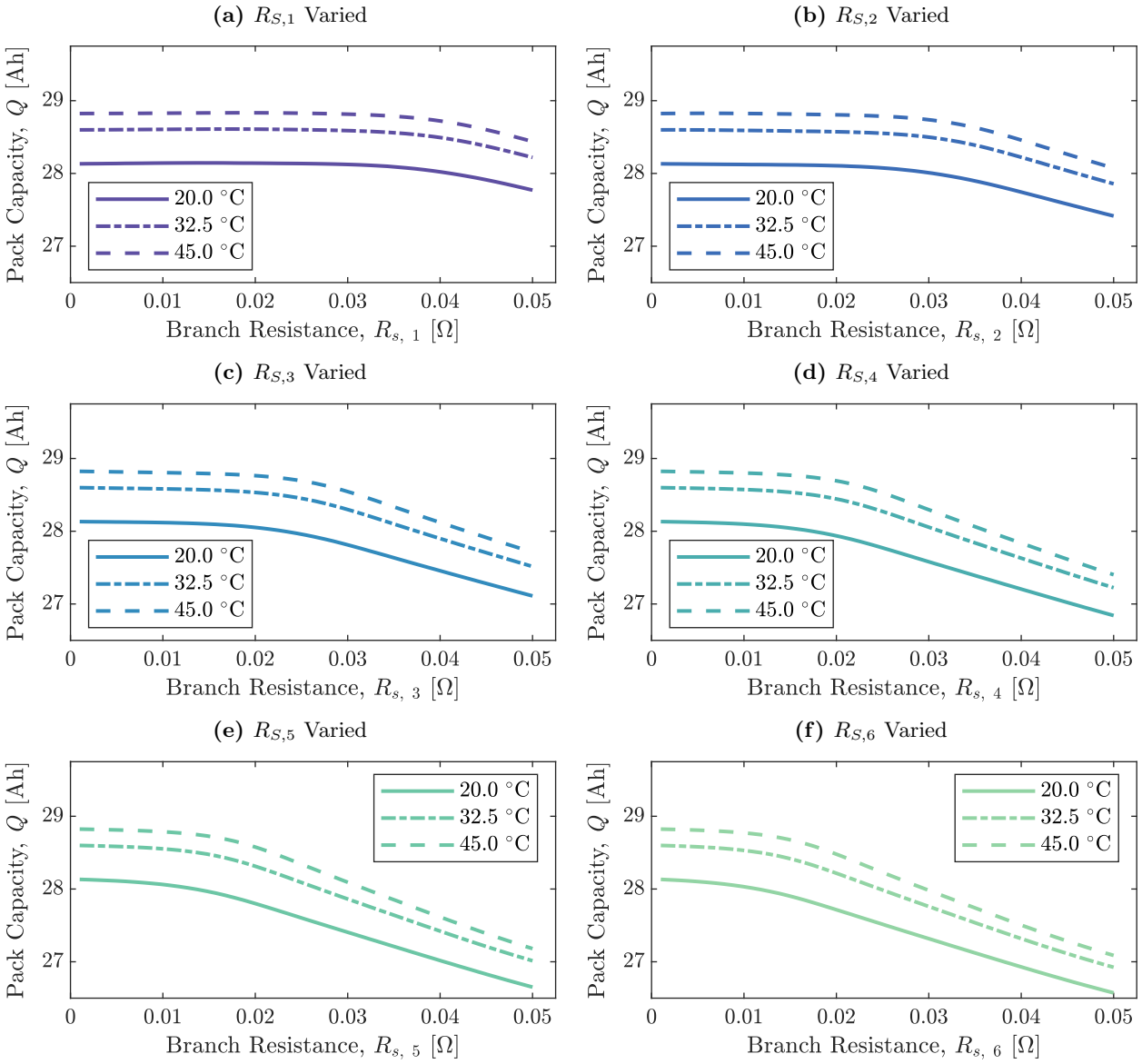


Figure 5.20: Pack accessible capacity for U-topology with variable $R_{S,n}$, where $n = \{1, 2, \ldots, 6\}$. In each case $R_{S,n}$ is varied from 0.1 mΩ to 50 mΩ. All simulations under a 1 C discharge, with T_m = 20, 32.5 and 45 °C. a) $R_{S,1}$ varied. b) $R_{S,2}$ varied. c) $R_{S,3}$ varied. d) $R_{S,4}$ varied. e) $R_{S,5}$ varied. f) $R_{S,6}$ varied.

ature breakpoints, 20.0, 32.5 and 45.0 °C. This set of simulations shows that increasing the mean temperature of the pack leads to overall greater accessible capacity due to the reduced cell impedance. However, increasing the mean temperature also delays the onset of rapid loss of accessible capacity in each case. This is due to the reduced overall branch resistance delaying the onset of rapid reduction in branch accessible capacity, due to the reduced cell impedance at increased temperature.

This effect is caused by the decreased contribution of the cell resistance to the overpotentials in the pack at higher temperatures. This in turn means that the drop of the pack voltage below the lower voltage cutoff is delayed. By delaying this point, a greater degree of rebalancing is possible at EoD, where the high resistance branch experiences a high peak current and the amount of capacity extracted from each cell is equalised.

5.8 Conclusion

Using the parallel string 1S6P test bench developed and introduced in Section 4.3, an experimental investigation into the effects of varying the mean temperature, thermal gradient applied and pack topology were investigated, for a range of thermal conditions and two topologies, the 'U'- and 'Z'-topologies. The experimental investigation identified the causes of performance loss in parallel strings compared to the summed capacity of the constituent cells, with both thermal conditions and topology having a significant impact on pack accessible capacity. The SoC deficit at end-of-discharge was identified as the principal cause of capacity loss, which in turn is driven by cell impedance variations induced by temperature, as cell impedance is a strong function of cell temperature. Therefore, changing the mean temperature of the string in both the U- and Z-topology cases had a significant impact on the overall accessible pack capacity. Increasing the mean temperature of a parallel connected pack increases the relative importance of interconnection resistances, due to the consequently increased IRR.

In conjunction, thermal gradients were identified as having generally negative effects on accessible capacity and homogeneity. However, thermal gradients have also been shown to have small but positive impacts on pack performance in the positive case for the U-topology. Therefore, if a U-topology is required, the thermal management system should be such that a positive rather than negative thermal gradient is applied. The positive thermal gradient case leads to increasing cell temperature further from the string terminals and therefore lower cell impedances. This acts to equalise total branch impedances and therefore increase the consistency of cell degradation. Because of symmetry in the Z-topology case, the effect of thermal gradients is much more minimal. This is caused by the higher resistance of each branch, as there are an equal number of interconnection resistances per branch, reducing the overall impact of the cell impedance. In the symmetric Z-topology case, due to the approximately equal branch impedances, current heterogeneities are induced by unequal overpotentials in each branch, in turn caused by the unequal current flows through different segments of the busbars. However, this in turn leads to an overall reduction in capacity in the Z-topology, due to the increased parasitic resistive loss in each branch leading to a greater SoC deficit at EoD.

In order to further assess the impacts of heterogeneous conditions within parallel strings, the previously parameterised ECN model was validated for the 1S6P string. A range of simulations were carried out, with variations in thermal conditions, topology and both interconnection and branch resistance considered. For the U-topology, increased interconnection resistances far from the terminals led to a significant capacity loss when the increased interconnection resistance was approximately equal to the nominal cell impedance. In comparison, placing the increased resistance close to the terminals allowed an increase of approximately 5 times the nominal cell impedance before significant impacts were predicted. Meanwhile increasing the total resistance of branch 1 to approximately 8 times the nominal cell impedance before significant reduction in capacity was predicted. In comparison, increasing the resistance of branch 6 led to significant capacity loss above an increase of approximately the nominal cell impedance, although increasing the pack temperature was shown to delay the onset of loss of accessible capacity. In general therefore, for a U-topology, it is critical to ensure that resistances in branches further from the terminals are controlled.

Considering the effects of thermal conditions, it was found that the U-topology was significantly more sensitive to both the mean temperature and thermal gradients, as well as to heterogeneities in the

interconnection and branch resistance. In this case, increasingly negative thermal gradients are seen to lead to a reduction in overall pack capacity at a given mean temperature. Conversely, increasingly positive thermal gradients lead to relative increases. In contrast, for the Z-topology, thermal gradients were found to have no significant impact on the overall performance of the pack due to the topological symmetry. In both cases, increasing the applied current rate increases the sensitivity of the pack to heterogeneous temperatures. At higher C-rates, branch currents and therefore overpotentials are higher, and as a consequence thermally driven changes in cell impedance lead to relatively larger changes in accessible capacity.

In conclusion, generally a Z-topology is preferable under most operating conditions to a U-topology, with the Z-topology being less sensitive to thermal variations and in most cases to branch resistance variations. However, this reduced sensitivity comes at the cost of increased overall reduction in accessible capacity due to the equal and higher branch resistances in the Z-topology case. Despite this, it is clear that a Z-topology is preferable for most operating cases. However, in this chapter the impacts of thermal and topological heterogeneities on the lifetime of parallel cell strings has not been considered and will be addressed in Chapter 6.

Chapter 6

The Effects of Thermal Heterogeneities on Pack Lifetime

The work presented in this chapter is entirely the authors own except as otherwise acknowledged here. The OCV diagnostic model was derived from work by Birkl et al. [25], [87], as introduced in Chapter 4, implemented with the kind assistance of Ryan Prosser. Elements of the pack test bench were developed with support of others in the Electrochemical Science and Engineering group, as previously acknowledged in Chapter 4. All other experimental testing, modelling and analysis was carried out solely by the author. The work presented in this Chapter is under preparation for publication as *The effects of thermal heterogeneities on aging within parallel-connected Lithium Ion batteries*, Max Naylor Marlow, Jingyi Chen and Billy Wu, 2021, *In Preparation.*

6.1 Introduction

In Chapter 5, the effects of thermal gradients, topology, operating rate and resistance heterogeneities on parallel string performance was investigated, both experimentally and using an equivalent circuit modelling framework. However, the effects of varied conditions on the lifetime of parallel strings was not assessed in detail and is a significant gap in the literature. In this chapter the effects of thermal heterogeneities on the useful lifetime of packs is investigated and assessed. The overall aims of this section of the work were as follows:

- Experimentally investigate the impacts of thermal gradients on parallel string lifetime.
- Understand and generalise the impacts of increasingly heterogeneous thermal conditions on lifetime.

Prior to testing, several hypotheses surrounding the effects of thermal gradients on parallel string lifetime were considered, and the experimental study was planned to address the following:

- Thermal gradients have been shown in Chapter 5 to be favourable or unfavourable to instantaneous performance of a U-topology pack.
- Heterogeneous conditions will have a negative effect of pack lifetime when compared to homogeneous temperature packs. This effect is expected to be balanced with the accelerated degradation

rates induced by higher average operating temperatures.

- Different thermal gradients will induce different degradation modes in cells within parallel strings, due to heterogeneities in temperature and differential current peaks and throughput over life.

6.2 Key Literature

In recent years, researchers have published a range of studies detailing the effects of operating conditions [141], cell-to-cell variations [9], [180], topology [154], [162] and thermal gradients [9], [162]–[164] on the instantaneous performance of cells and packs. However, there is limited literature addressing the lifetime implications of such heterogeneous conditions. The critical works, principally published in the last 3 years, are discussed in detail here and any research gaps are identified.

Gogoana et al. [146] experimentally investigated 6 1S2P packs with deliberately mismatched DC resistances in their pack construction, with 2 packs each at approximately 0 %, 10 % and 20 % mismatch, and linked the lifetime of the resultant packs to the resistance mismatch using an SEI layer growth model. It was found that towards the end of discharge, cells in a mismatched pack may experience abnormally high currents which may lead to sudden and accelerated degradation of the system. The proposed degradation model suggests that maximum charging current experienced by a cell has a strong influence on the degradation rate and therefore current balancing in parallel strings is critical to maintain pack lifetime. Whilst the C-rate during aging was 4.5 C, the selected cell in this work was rated for a maximum continuous discharge rate of 32 C. However, the study did not control the cell temperature or experimentally investigate the effects of high rate operation which may promote alternative degradation modes, such as active material loss.

Considering the effect of thermal gradients on degradation rates in parallel cell strings, Liu et al. [9] used a model based approach to investigate the effects on a 1S6P pack, modelling SEI layer growth as the sole degradation mechanism leading to both capacity loss and power fade. It was found that the degradation rate of the string is strongly linked to the applied thermal gradient. The study predicted a 10 % increase in rate of loss of pack output energy when comparing a -25 °C thermal gradient to a + 25 °C thermal gradient, indicating that while previous work presented in Chapter 5 indicates a positive thermal gradient will reduce operating heterogeneities, it may lead to accelerated degradation. However, this work did not experimentally validate these results and the degradation model is not able to capture alternative degradation modes which may be promoted by high peak currents in parallelised packs. Cavalheiro et al. [152] investigated a 1S5P pack configured as a cell stack with the outer surfaces of cells 1 and 5 convectively cooled, and compared the degradation rate to a single cell under the same nominal cycling procedure. Highly non-uniform degradation occurred in the string, degrading significantly faster than the baseline cell (7 % greater capacity loss at 2215 cycles). This effect was attributed to the higher mean cycling temperatures of the pack cells compared to the baseline single convectively cooled cell, with a peak temperature rise 12.5 °C higher in the parallel string case. However, active cooling of the string was identified as potentially leading to greater thermal gradients at lower mean temperatures, which was not investigated. Additionally, no detailed analysis of the underlying mechanisms causing differential degradation was presented, and thus detailed studies of aging within packs are required.

Shi et al. (Shi et al., 2016) investigated the effects of imbalanced currents on large format LFP cells in

a 1S2P configuration, comparing a homogeneous and heterogeneous temperature case. It was found that in the heterogeneous case with an approximately 30 °C thermal gradient, the degradation rate was more than double that of the homogeneous case. Over 1000 cycles, the initial deviation in currents was higher for the heterogeneous pack, and this diverged with cycle number, while the homogeneous temperature pack also diverged but by a significantly smaller amount. The retained capacity of the homogeneous temperature pack was higher, with an approximately 50 % reduction in capacity loss at 1000 cycles, while the rate of degradation of the individual cells within the homogeneous pack was approximately equal, with slightly higher rates of degradation seen in the cell closest to the pack terminals. In the heterogeneous case, degradation rates of the overall pack were higher, to be expected of a pack at higher mean temperature. The cell capacities diverged over time, with the higher temperature cell degrading faster, leading to a 9 % difference in cell reference capacity at EoL. Interestingly, the high temperature cell within the parallel string degraded slower than a reference cell cycled under identical conditions outside of a parallel string, while the low temperature cell in the string degraded faster than both the reference single cell and both cells within the homogeneous pack of identical temperature. This differential aging in both cases was attributed to the imbalanced currents present in the parallel strings, in particular the high peaks identified at start and end of discharge, which was hypothesised to lead to significant loss of lithium inventory. However, the small range of scenarios investigated in this case limits the detailed conclusions which may be drawn. Song et al. [212] investigated differential degradation within 1S2P parallel strings and found that a 20 °C thermal gradient lead to divergent behaviour within the string, with increasing cell-to-cell capacity deficits identified, and concluded that increasing thermal gradients lead to accelerated degradation, although this was not compared to a reference measurement for single cells. It was also concluded that if thermal boundary conditions are similar, convergence is expected for cells with either convex or linear degradation curves, whilst divergence is expected with a concave degradation curve, with the overall shape of the degradation curve dictating the regime. However, the study was confined to modelling, and the empirical degradation model used only accounts for SEI layer growth, excluding other possible degradation mechanisms.

Investigating the effects of increasing parallelisation on pack performance by testing a range of increasingly parallel packs, Gong et al. [170] concluded that increasing parallelisation reduces the degree of heterogeneity experienced by strings, particularly reducing peak currents at the end of discharge. This was suggested to be a factor prolonging lifetime of highly parallel packs, with reduced impacts from low capacity or high impedance cells. However, this study only assessed regrouped degraded cells rather than directly cycling packs, and as a consequence does not provide information about the development of heterogeneities during cycling. Additionally, the interconnection resistance is unspecified, whilst the pack topology studied is fully symmetric. It is expected that increased parallelisation of U-topology packs for example will lead to increasingly heterogeneous behaviour due to the stacking effect of interconnections leading to unbalanced branch resistances. Ultimately, this highlights the system-specific nature of pack heterogeneous behaviour and the need to draw general insights.

Baumann et al. [149] investigated 1S2P coupled cells harvested from an aged EV battery pack, and found that after aging in-service, significant increases to parameter spread occurred, with a mean increase in capacity spread of 0.5 %, and of internal resistance of 3.54 %, with several cell pairs resistance spread increasing to over 10 %. Further cycling of selected modules indicated that rather than converging due to self-balancing over time, the heterogeneities in cell performance increased, with

no general trend of convergence. This disagrees with results presented by Song et al. [212]. However no general conclusions were able to be drawn due to the application and design specific nature of heterogeneous aging, and further experimental study was recommended. While work by Offer et al. [140] identified large and potentially hazardous current variations induced by cell interconnections, it is possible that during aging, the effects of heterogeneous cell impedances will outweigh the initial current heterogeneities induced by interconnections and become the dominant factor driving current distribution within parallel strings.

Therefore, a significant question remains, which is if the aging trajectories of cells within parallel strings are convergent or divergent during cycling, what drives the convergent or divergent nature of this behaviour? Divergent behaviour is undesirable as it may lead to extreme currents in areas of packs, leading to reduced lifetime, extreme peak currents and safety concerns, as identified by several authors [139], [162]. Several authors have tried to address this question, however the results presented in the literature remain inconclusive and somewhat contradictory. For example, Pastor-Fernandez et al. [171], who cycled cells with deliberately induced SoL deviations in cell capacity found that during cycling, cell capacity converged due to the differential currents and therefore current throughputs induced. Meanwhile, Yang et al. [145] indicate that when thermal conditions are consistent and degradation follows the commonly seen linear or convex pathway, initially diverging cells will converge to identical capacities during cycling. However previous works discussed have indicated that thermal gradients within packs will lead to divergent cell performance over time [9], [185], [212]. As such, a comprehensive view of the influence of temperature is required, as direct comparisons between multiple homogeneous and heterogeneous temperature cases in the literature are limited. Additionally, comprehensive datasets for pack aging under heterogeneous conditions are rarely if even available in the literature, and therefore remains a significant research gap.

6.3 Cell Selection and Grouping

As previously identified by both work in Chapter 5 and other authors [9], [62], [149], [173], [180], small variations in cell capacity and impedance may potentially lead to significant variations in lifetime performance. In order to minimise any potential influence of cell-to-cell variations on the thermal effects selected for investigation, the differences in capacity and resistance between the cells within each pack were minimised. An initial set of 19 cells from the same batch, which had been stored under identical conditions were characterised, and the cell capacity was measured at 0.04 C with the cell charged to 4.2 V at 1 C using a CC-CV charging protocol with a cutoff current of 0.01 C (50 mA), then rested for 60 mins before discharging to 2.7 V. In each case, the cells were characterised in a thermal chamber (Binder KB53) at 20.0 °C. The cells were then charged to 50 % SoC (referenced to the 0.04 C measured capacity of the cell) allowed to equilibrate overnight, before a single EIS spectra was taken at 50 % SoC. The EIS measurement was taken with an RMS current of 0.2 A from 2500 to 0.01 Hz, with 10 frequencies logarithmically spaced per decade.

The resultant spectra are shown in Figure 6.1 a, with the inset showing the ohmic intercept and high frequency semicircle. As can be seen, the impedance spectra from the fresh cells were highly consistent, indicating there is minimal variability in cell impedance at SoL. Once obtained, the resultant EIS data was processed and fitted and the ohmic or series resistance, R_0, obtained from the real axis intercept. The fitted R_0 values are shown in Figure 6.1 c, with a mean R_0 value of 1.283 mΩ. The measured cell

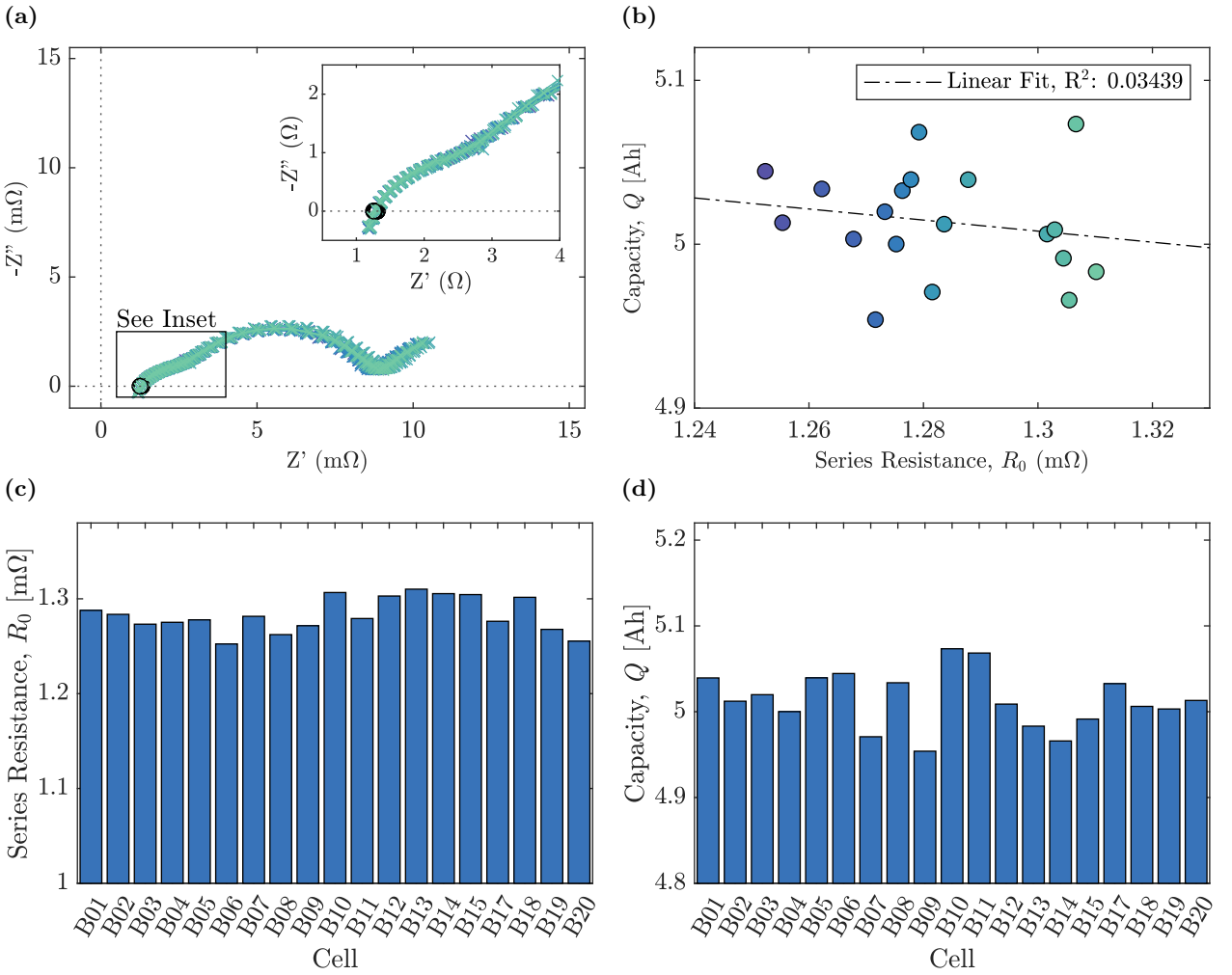


Figure 6.1: Measured capacity and impedance of cell batch. a) Cell impedance at 50 % SoC, 20 °Cfor all 19 cells. b) Resistance and capacity scatter plot for all 19 cells. c) Fitted R_0 values for all cells. d) Measured capacity for all cells at 0.04 C.

capacity values are shown in Figure 6.1 d, with a mean capacity at 0.04 C of 5.014 Ah, marginally above the nominal cell value of 5 Ah. Once the cell capacity and R_0 were measured, the cells could then be grouped to minimise variation in capacity and series resistance. A scatter plot of the R_0 and capacity values, shown in Figure 6.1 b, shows the minimal correlation ($R^2 = 0.03439$) between the SoL R_0 and capacity values. Although not plotted here, a similar trend is observed for R_{SEI} and R_{CT}, and the consistency of the cell SoL impedances can be seen in Figure 6.1 b.

In order to group the cells, the capacity and series resistance were considered for grouping. As shown in Figure 6.1 b, there was a marginally higher resistance group of six cells, and these cells were discarded from selection. The next highest resistance cell was then removed to leave twelve cells to produce six 1S2P packs, and the cells were then sequentially grouped by their corresponding R_0 values to leave six pairs, shown in Figure 6.2 a-f. As can be seen, the resultant deviations in both capacity and impedance were small, with all resistance differences minimised to below 0.45 % (5.72 $\mu\Omega$) and capacity differences to below 0.85 % (42.3 mAh), excepting pair 3 which showed a larger deviation of 1.314 % (65.6 mAh). Despite this, the spread at SoL was deemed acceptable and the cell pairings were subsequently used as shown.

Of the remaining cells from the batch, the group of 4 cells with approximately 5 Ah capacity and 1.31

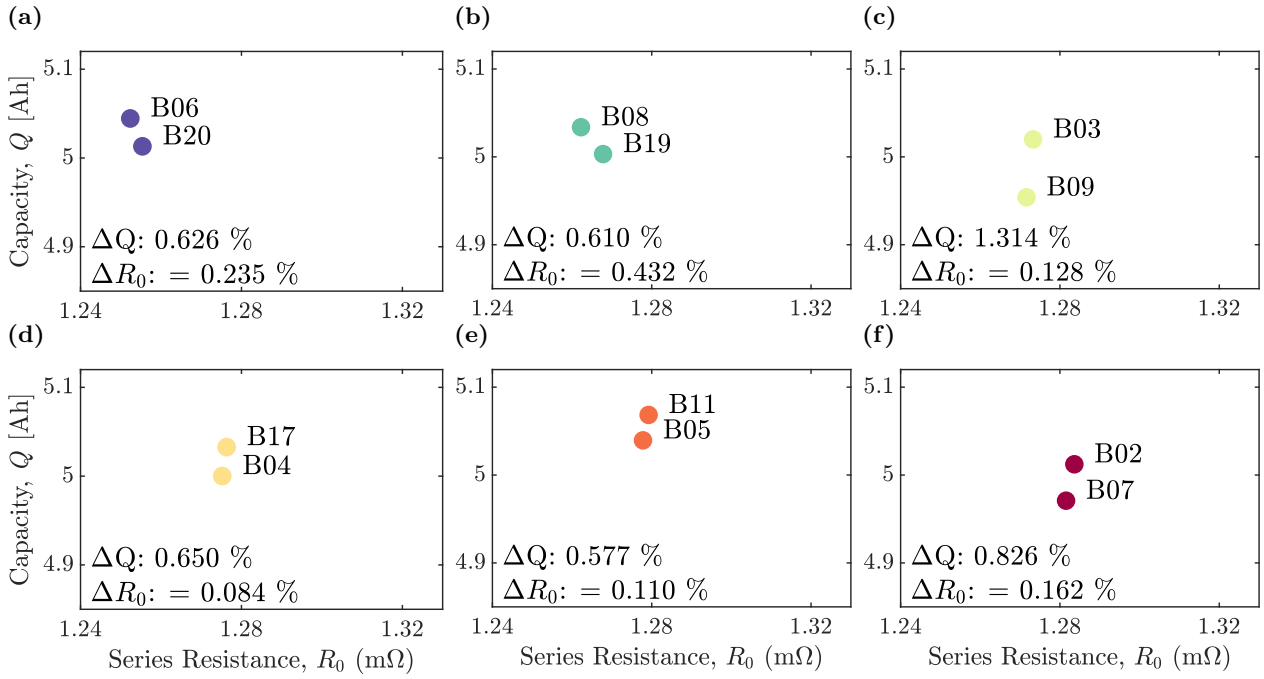


Figure 6.2: Allocated cell pairs for 1S2P aging experiments, showing ΔR and ΔQ. a) Pair 1. b) Pair 2. c) Pair 3. d) Pair 4 e) Pair 5. f) Pair 6.

mΩ R_0 were used for single cell baseline testing, and the remaining lowest R_0 cell was set aside to be used to provide an EIS baseline over a full temperature range, as based on the single spectra EIS results shown in Figure 6.1 a, the impedance response of all cells from the batch at SoL was highly consistent. To provide a baseline cell for comparison during cell disassembly, a final cell was selected and torn down for imaging. The final selected cells and their assigned purposes from the batch are summarised in Table 6.1. Overall, out of the initial batch of 19 cells, 16 were cycled for 2000 cycles either as individual cells or as part of 1S2P packs, 2 were used for reference impedance and teardown characterisation, and 1 cell remained spare.

Table 6.1: Cell IDs for full batch and allocation to experiments

Cell ID	Selected Use	Cycling Temperature [°C]
01	Fresh EIS Baseline	N/A
02	Pack 6 Cell 1	38.8
03	Pack 3 Cell 1	20.0
04	Pack 4 Cell 2	32.5
05	Pack 5 Cell 2	20.0
06	Pack 1 Cell 1	20.0
07	Pack 6 Cell 2	26.3
08	Pack 2 Cell 1	45.0
09	Pack 3 Cell 2	45.0
10	Fresh Teardown	N/A
11	Pack 5 Cell 1	45.0
12	Single Cell Cycling	20.0
13	Single Cell Cycling	32.5
14	Unused	N/A
15	Single Cell Cycling	45.0
17	Pack 4 Cell 1	32.5
18	Single Cell Cycling	20.0-45.0 TG
19	Pack 2 Cell 2	45.0
20	Pack 1 Cell 2	20.0

6.4 Experimental Methods and Data Analysis

In order to experimentally investigate the effect of varied thermal conditions, a 1S2P parallel U-configuration pack was selected as a test case, as this represented the smallest unit pack size which captures the physical effects in question. This increased the number of possible permutations of thermal conditions that could be investigated given the limits on available testing resources. The electrical topology, shown in Figure 6.3 was selected to replicate the conditions previously investigated in Chapter 5, with equal interconnection and current sense resistances of 1 mΩ used. For branch 2 the interconnection and current sense resistances $R_{IC,2}$ and $R_{S,2}$ were combined in practice into a single resistor of 2 mΩ to simplify assembly. After assembly, all busbars were calibrated using a Biologic VMP-3 potentiostat to accurately calibrate sense and busbar resistances, as discussed previously in Section 4.3.6.

The thermal gradients selected for investigation were 0, -12.5 and ± 25 °C. These values were se-

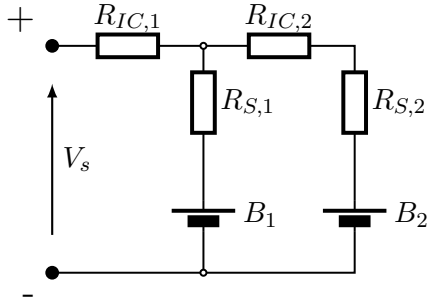


Figure 6.3: Circuit diagram of 1S2P packs used during aging experiments

Table 6.2: Pack aging thermal conditions and identifiers

Pair No.	Pack Name	B1 Temperature [°C]	B2 Temperature [°C]	Thermal Gradient [°C]	Mean Temperature [°C]
1	**P20.0/0.0**	20.0	20.0	0.0	20.0
2	**P45.0/0.0**	45.0	45.0	0.0	45.0
3	**P32.5/+25.0**	20.0	45.0	+25.0	32.5
4	**P32.5/0**	32.5	32.5	0.0	32.5
5	**P32.5/-25.0**	45.0	20.0	-25.0	32.5
6	**P32.5/-12.5**	38.8	26.3	-12.5	32.5

lected to both replicate previously identified values obtained by other researchers and to provide wide bounds for subsequent model validation. For example, Hosseinzadeh et al. [162] found a maximum thermal gradient of 29.4 °C in a 1S15P parallel string, while Cavalheiro et al. [152] measured a peak thermal gradient of 8 °C in a 1S5P convectively cooled cell stack. The final selected thermal cases are summarised in Table 6.2. Overall, 3 packs were cycled under a homogeneous temperature regime, at 20.0, 32.5 and 45.0 °C respectively, while 3 packs were cycled under thermal gradients with a constant mean temperature of 32.5 °C and applied thermal gradients of +25 °C, -12.5 °C and -25 °C, providing a range of thermal conditions for investigation. Thermal control of the 1S2P parallel cell strings was achieved using the test bench previously introduced in Section 4.3.

With the thermal conditions selected, cells were initially assessed and paired from a single batch, as described in detail in Section 6.3, to ensure consistency of performance at SoL. Once cell pairs were selected, at the SoL, each cell was individually characterised as follows, with all characterisation experiments using the previously introduced quick-change jigs taking place in a thermal chamber at a temperature of 20.0 °C. In all cases, cells were allowed to thermally equilibrate for 180 mins. All cell-level characterisation tests were carried out using a BaSyTec 60 A XCTS G2 battery cycler. For each cell, the capacity was measured at 0.04, 0.1, 0.5, 1, 2, and 3 C, referenced to the nominal cell capacity of 5 Ah. In each case, the cell was charged to 4.2 V at 1 C using a CC-CV charging protocol with a cutoff current of 0.01 C (50 mA), then rested for 60 mins before discharging to 2.7 V at the selected rate. HPPC measurements were taken using the modified HPPC protocol specified by Mulder et al. [213], which is designed to provide improved rate capability information compared to a standard HPPC measurement by combining multiple charge and discharge pulses at each SoC breakpoint. In the protocol used, 18 s charge and discharge pulses of 0.2, 1 and 3 C are applied, with a 60 second relaxation period between pulses before discharging at 0.25 C to the next SoC breakpoint and allowing the cell to rest for 1 hr. Finally, a discharge SRCV measurement was taken between 4.2 and 2.7 V with a slow scan rate of 2.5 mV/min. SRCV measurements were taken as a comparative diagnostic metric, with scope for future analysis. This scan rate was selected to provide an approximately 10 hr test, in line with the approximate rate of the 0.1 C discharge test used for ICA analysis. In all cases, data was logged at 1 Hz, excepting during HPPC pulses where the highest possible logging rate was used, 20 Hz or 1 mV voltage change.

After cell selection and grouping and cleaning of the cell tabs and pack contacts using Acetone and Isopropanol, the cells were assembled into packs. The contact resistance at each terminal was recorded using a Keithley 2182A Bench Digital Multimeter. In the event the total contact resistance exceeded 500 $\mu\Omega$, the pack terminals and tabs were cleaned again. Once contact resistances were minimised

below the threshold values, the cell-level SoL tests, excluding the HPPC measurement were repeated for the assembled packs. All pack-level experiments were carried out using a BaSyTec 50 A XCTS G1 battery cycler. After SoL characterisation, the packs were cycled using a constant current 2 C cycling regime, referenced to the nominal pack capacity of 10 Ah. During each cycling run, the packs were initially charged to 4.2 V using a 1 C CC-CV scheme with a 0.01 C (100 mA) cutoff, before being allowed to rest for 60 mins before start of cycling. After 125 cycles at 2 C, the packs were then recharacterized using a subset of the SoL measurements, with discharge capacity being measured at 0.1, 1, and 2 C measured using the same protocol as SoL measurements. Discharge SRCV measurements, using the same protocol as SoL were then taken. After pack-level characterisation, the packs were disassembled and the two individual cells from each pack characterised using the same protocols as at the pack-level, with the addition of the modified HPPC measurement to estimate cell DC resistance. All pack and cell level characterisation experiments were conducted at a constant temperature of 20.0 °C, controlled either using the pack temperature control rig or thermal chamber as required. These cycling and characterisation processes were then repeated for 16 subsequent breakpoints until each pack had experienced 2000 total 2 C cycles[1].

After final characterisation, a subset of cells was selected for EoL teardown to identify any morphological changes in the electrodes induced by cycling. The cells selected in this case, alongside a fresh cell from the same batch, were discharged to 2.7 V, with a CV hold to 0.01 C to ensure the cells were fully discharged. The cells were then opened using a ceramic scalpel to cut the pouch inside an Argon filled glovebox (MBraun LabMaster), and electrodes through the stack were sequentially removed as the stack was unwound. The harvested electrodes were then washed using DMC and vacuum dried at 55 °C for 1 hr to remove any excess solvent. Samples were then subsequently cut from the electrodes near the tabs and in the centre of the electrodes and imaged using Phenom ProX Scanning Electron Microscope, with an acceleration voltage of 10 kV, operating in backscatter mode. Additional optical microscopy images and photographs were taken of the torn-down cells and electrodes as appropriate.

For clarity, the details of the characterisation undertaken are summarised as follows:

1. **Cell Selection:** p-OCV (0.04 C); EIS (50 % SoC)
2. **SoL Cell Characterisation:** p-OCV (0.04 C); Capacity (0.1, 0.5, 1, 2, 3 C); SRCV; HPPC
3. **SoL Pack Characterisation:** p-OCV (0.04 C); Capacity (0.1, 0.5, 1, 2, 3 C); SRCV
4. **Cycling:** 125 CC cycles (2 C)
5. **Interim Pack Characterisation:** Capacity (0.1, 1, 2 C); SRCV
6. **Interim Cell Characterisation:** Capacity (0.1, 1, 2 C); SRCV, HPPC
7. **Final Pack Characterisation:** p-OCV (0.04 C); Capacity (0.1, 0.5, 1, 2, 3 C); SRCV
8. **Final Cell Characterisation:** p-OCV (0.04 C); Capacity (0.1, 0.5, 1, 2, 3 C); SRCV; HPPC; EIS (50 % SoC)

[1]Due to laboratory closures caused by the COVID-19 pandemic, a break time of approximately 3 months occurred between the initial 125 cycles and subsequent cycling. However, no appreciable impacts on overall cycling performance was observed, as the cells were stored at approximately 5 °C for the duration of the interruption to experiments to reduce any impacts of calendar aging

9. **Post-Mortem:** Cell teardown; Visual inspection; SEM imaging (Selected cells)

During cycling, steps 4-6 were repeated 16 times for a total of 2000 cycles applied to each cell. For interim cell-level characterisation, the packs were disassembled

To provide a comparative baseline for single cell lifetime performance, 4 single Kokam 5 Ah cells selected from the same batch were also cycled under the same nominal cycling regime (2 C for 2000 cycles), under a range of thermal conditions selected to match those experienced by the 1S2P packs. The thermal conditions selected are summarised in Table 6.3 and include cycling at the 3 major temperature breakpoints selected for the 1S2P study (20.0, 32.5 and 45.0 °C) alongside a single cell cycled with a 25 °C through plane thermal gradient at a mean temperature of 32.5 °C. In order to provide similar conditions to those experienced by the pack cells, the 1S6P test bench, introduced in Section 4.3, was repurposed to provide surface cooling during the single cell tests by removing the busbar interconnections and replacing the acrylic tab clamps with brass clamps with direct cycler connections, allowing the test bench to be used to cycle up to 6 individual cells. Prior to testing, a full set of EIS measurements of the cells were taken, using a Biologic VMP-3 potentiostat. The cells were placed in a thermal chamber (Binder KB23) and allowed to equilibrate at 20.0 °C for 24 hours, before being charged to 4.2 V using a CC-CV scheme with a cutoff current of 0.01 C (50 mA). The cells were then discharged to 2.7 V at a rate of 0.04 C to measure reference capacity. The cells were then recharged to 4.2 V using an identical CC-CV scheme, before being discharged a nominal 5 % SoC (250 mAh), and then were allowed to equilibrate for 4 hours. EIS measurements were then taken in galvanostatic mode from 1 kHz to 0.01 Hz, with 10 frequencies per decade used and an excitation RMS current of 250 mA applied.

Once the EIS characterisation was complete, the cells were initially characterised and discharge capacity measured at 0.1, 1 and 2 C, using identical test parameters to the 1S6P characterisation, while under surface temperature control at a temperature of 20.0 °C. All cycling and capacity characterisations were carried out using a Neware BTS-4000 20A battery cycler. At SoL, the cells were also removed from the test bench and placed inside a thermal chamber (Binder KB53) and a HPPC measurement, again using identical parameters to those used for the 1S2P cells. The cells were then cycled at 2 C charge and discharge for 100 cycles at the set temperatures, before the temperature was reduced in each case to 20.0 °C and the capacity characterisation repeated. Every 200 cycles, the cells were removed from the test bench and a HPPC measurement taken

Table 6.3: Single cell aging thermal conditions

Cell	Top Surface Temperature [°C]	Bottom Surface Temperature [°C]	Thermal Gradient [°C]	Mean Temperature [°C]
1	20.0	20.0	0.0	20.0
2	32.5	32.5	0.0	32.5
3	45.0	45.0	0.0	45.0
4	45.0	20.0	25.0	32.5

In order to provide a baseline for cell impedance performance with respect to temperature, B1101 was used to provide further detailed EIS measurements at SoL for reference. The cell impedance was measured at 5 temperature breakpoints with a 10 °C step from 10 to 50 °C. The parameters of the impedance measurements was identical to previously used for SoL characterisation of the cells selected

for single cell cycling, except the excitation current. This was increased from 200 to 500 mA for the 40 and 50 °C temperature breakpoints to improve the signal to noise ratio of the measurements, as the decreasing impedance at elevated temperature led to significant measurement noise due to the decreasing magnitude of the voltage response. Comparative measurements at these breakpoints between the two excitation currents showed no difference in measured impedance response, except the improved measurement stability.

Data analysis was carried out primarily in MATLAB 2020a, which was used to synchronise and analyse all data acquired. As previously discussed in Section 4.3, pack level current data was acquired using PicoLog TC-08 dataloggers, measuring differential voltages across current sense resistors. As multiple PCs were used to log the data, with an associated drift in the clocks between the PCs, battery cycler and PicoLog data were synchronised by locating the first logged application of current by the battery cycler and offsetting the PicoLog total current measurements to align with that timestamp. It was found that over long durations (weeks) the timing between PCs drifted by up to 10 s, but over the shorter individual experiments (<5 days), the drift within the experiments was negligible and could be neglected. During the degradation experiments, several intermittent power failures in the laboratory led to some brief irretrievable data losses from the pack current dataloggers, totalling to approximately 20 cycles of data per pack. This data is naturally excluded from the analysis of the synchronised data, including incomplete cycle data. For the heatmaps presented in Section 6.8, the gaps were filled with constant values from the last recorded full cycle, and as the lost data accounted for approximately 1-2 % of the total dataset, this was judged to have a negligible impact on overall findings. Appendix A identifies the missing data. For ICA analysis, the discharge data at 0.1 C was selected to provide the highest possible quality data and was analysed using LEAN algorithm, as derived by Feng et al. [78], and the degradation fitting model presented in Section 4.4.4. All processing and fitting of EIS data was carried out using the ZView software package from Scribner Associates.

6.5 Single Cell Reference Lifetime Performance

Initially the performance of the 4 single cells cycled at 2 C under different thermal conditions are assessed to provide a baseline against which to evaluate the performance of the parallel connected strings. Firstly, the capacity loss experienced by the 4 cells is presented in Figure 6.4 a and b, showing the dynamic (under 2 C discharge during cycling) and static measured capacity (0.1 C discharge) respectively. It is noted that the static capacity measurements do not measure the true capacity of the cells, and strictly measure pseudo-static or low rate capacity. However, an increase in capacity of less than 0.3 % is observed at SoL between measurements at 0.1 and 0.05 C, indicating that the 0.1 C measurements are a good approximation of the static capacity, as the cell impedance is low. The pseudo-static capacity measured at 0.1 C is hereby referred to as the static capacity. Figure 6.4 c shows the total current throughput per cell during the cycling experiment. The low temperature (20.0 °C) cell showed a rapid decrease in accessible capacity, compared to the higher temperature cycled cells, losing over 20 % accessible capacity over 2000 cycles despite experiencing a total current throughput 15 % lower. This was in comparison to 17 % dynamic capacity loss in the 32.5 °C and 13 % in the 45.0 °C cells. This difference may be explained by the decreased impedance of the cells cycled at high temperature, and in comparison, the static capacity trends are reversed. In this case the cell cycled at 45.0 °C, this experienced a 12 % loss in capacity measured at 0.1 C while the cells

cycled at 32.5 and 20.0 °C showed 7 and 5 % capacity loss respectively. It is noted that the increase in degradation rate was dramatically increased by the +12.5 °C increase in temperature from 32.5 °C when compared to the same increase from 20.0 °C, indicating that degradation was highly non-linear.

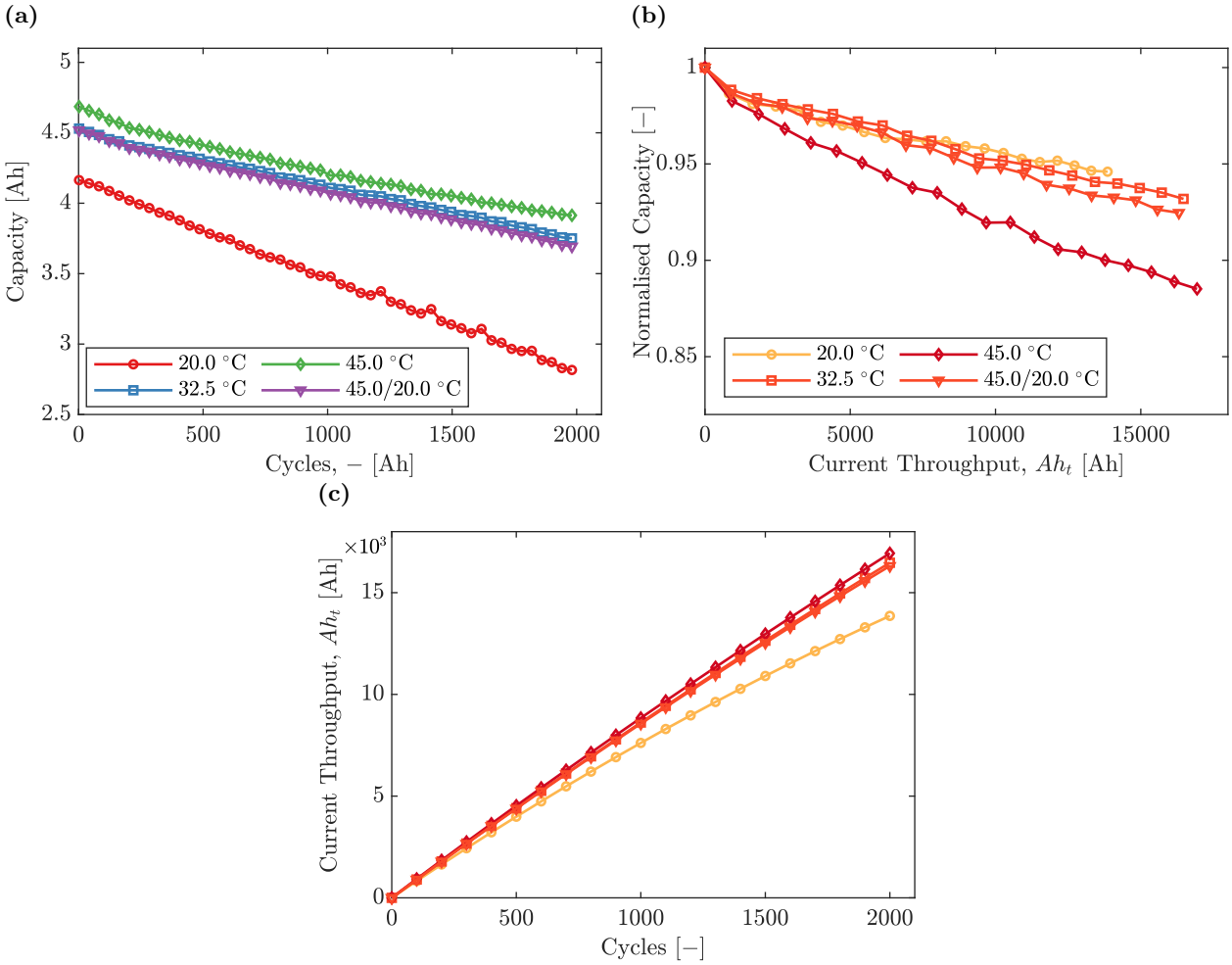


Figure 6.4: a) Dynamic discharge capacity during 2 C cycling for reference cells b) Static measured capacity at 0.1 C, 20 °C for all reference cells during aging. c) Total current throughput for all reference cells during aging.

Interestingly, while work from Troxler et al. [165] demonstrated that the impedance of cells under thermal gradients is decreased compared to isothermal cells, the accessible dynamic capacity of the cell cycled under a ± 25 °C thermal gradient was lower than the cell at the same mean temperature (32.5 °C). This is likely due to increasing amounts of inaccessible capacity within the cell, due to increased internal impedance in the colder layers of the cell, and can be considered similar to the underlying causes of capacity loss within parallel cell strings under thermal gradients presented in Chapter 5. This is evidenced by the 1.5 % greater static capacity loss seen at EoL.

As impedance change within parallel cell strings has been identified as a key factor dictating the degree of heterogeneity, the impedance growth of the baseline cells was measured at SoL and EoL. Figure 6.5 shows the impedance response for the 3 cells cycled at 20.0 (Figure 6.5 a and b), 32.5 (Figure 6.5 c and d) and 45.0 °C (Figure 6.5 e and f), with the left column of Figure 6.5 showing SoL whilst the right column shows the EoL EIS response. Note the scales in SoL and EoL plots are different for clarity. Only a subset of measurements are shown, again for clarity. From a qualitative inspection of the EIS spectra, the SoL performance of all cells are highly consistent, with minimal differences

observed excepting at low SoC values. However, the impedance growth over time is highly linked to temperature. Considering the EoL values for the 20.0 and 45.0 °C cells, a similar magnitude of impedance growth is observed, whilst impedance growth is lower in the 32.5 °C cell. Qualitatively in all cases R_{CT} dominates the cell impedance, whilst during aging the knee frequency is shifted lower.

In order to decouple the contribution of different cell processes to the overall cell impedance response, an equivalent circuit model (Figure 6.6 a) was used to extract the individual resistances using the ZView software package. The model uses 2 R-CPE pairs to distinguish between anode and cathode charge transfer processes, which are expected to have distinct time constants, with longer time constants contributed by the cathode [93]. Typical uncertainties in fitting were $<\pm$ 2 % for R_0 and R_{CT}, and $<\pm$ 10 % for R_{SEI}. The increased uncertainty in fit for R_{SEI} is expected as there is overlap between the contribution of R_{SEI} and R_{CT}, with R_{SEI} having a significantly smaller magnitude.

Figure 6.6 b, c and d show the SoL and EoL fitted resistances R_0, R_{SEI} and R_{CT} for all single cells cycled respectively. The initial values for all 3 fitted resistances are highly consistent, with R_0 and R_{SEI} exhibiting no appreciable SoC dependence. In comparison R_{CT} is highly SoC dependant, at SoL increasing by 3 times at 5 % SoC compared to 95 % SoC. After aging, whilst some changes are identified, the R_0 and R_{SEI} remained an order of magnitude smaller than R_{CT}, and thus the remaining analysis focusses on R_{CT} changes.

For all cycled cells, R_{CT} increased significantly, however the greatest increases were observed in the 20.0 °C cycled cell, with a 50 % greater increase in R_{CT} observed above 20 % SoC compared to the 45.0 °C case. Both the 32.5 and 45/20 °C cells show intermediate degrees of R_{CT} growth. Below 20 % SoC the increase in R_{CT} approximately matches the increase observed in the 20.0 °C cell. Previously both the dominance of the cathode R_{CT} on the full cell R_{CT} and the increased growth rates of cathode R_{CT} at low temperature were identified (Section 3.3.7). Therefore, the broad trend identified is expected, with low temperature cycling leading to accelerated R_{CT} growth due to accelerated cathode degradation caused by particle fracture and pulverisation, accelerated at low temperature. This behaviour is significant in parallel strings cycled at interim temperatures (i.e. above those typical for Lithium plating but below those causing highly accelerated SEI layer growth), as accelerated resistance growth in low temperature cells may lead to increasingly heterogeneous behaviour over time, which is explored further in Section 6.8.

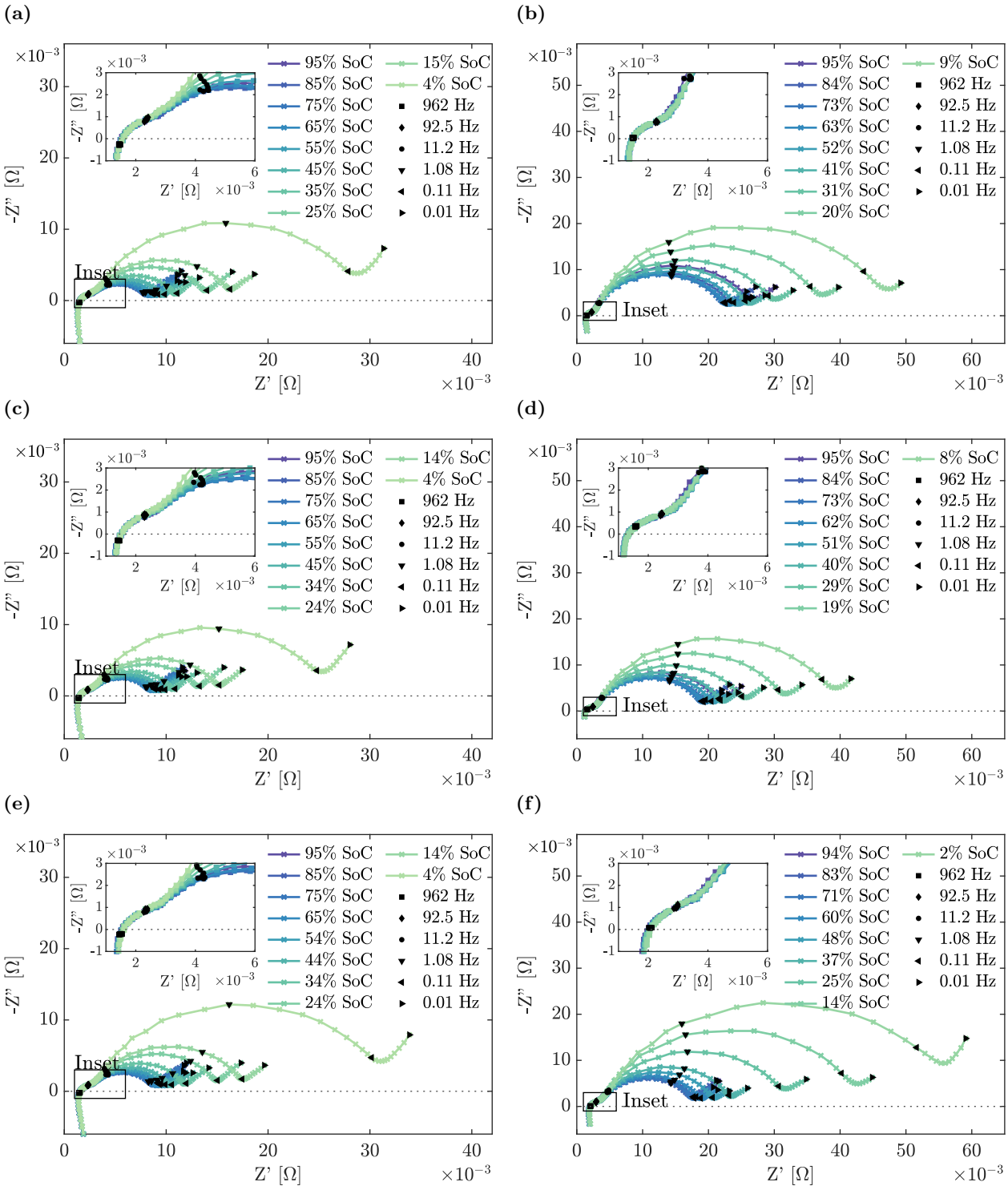


Figure 6.5: SoL and EoL EIS spectra for all reference cells, taken at 20 °C from 10 kHz-0.01 hZ, 250 mA excitation current. a) 20 °C cycled cell, SoL. b) 20 °C cycled cell, EoL. c) 32.5 °C cycled cell, SoL. d) 32.5 °C cycled cell, EoL. e) 45 °C cycled cell, SoL. f) 45 °C cycled cell, EoL.

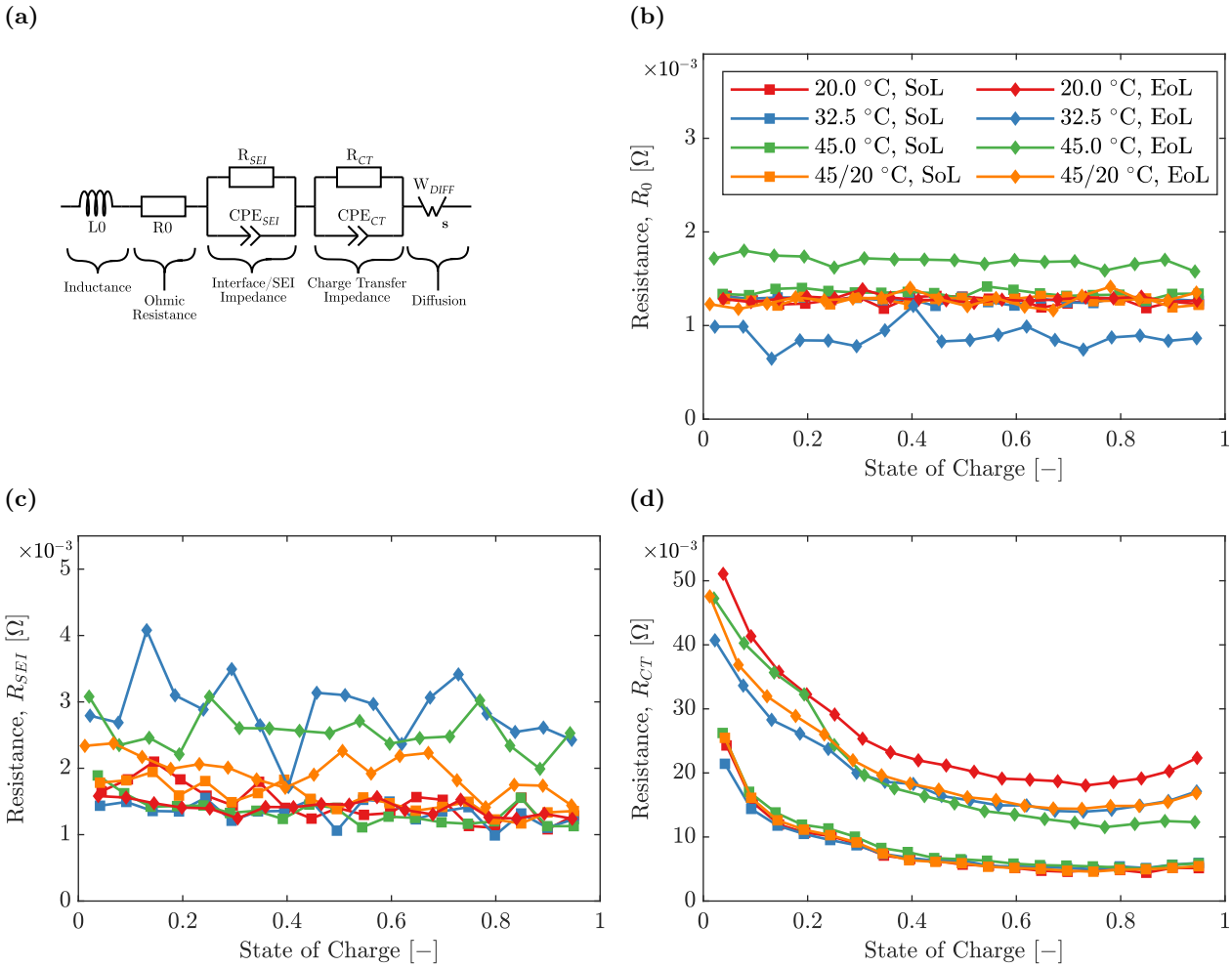


Figure 6.6: Fitted resistances for all reference cells at SoL and EoL. a) EIS fitting equivalent circuit model. b) Fitted R_0. c) Fitted R_{SEI}. d) Fitted R_{CT}.

6.6 Capacity Loss in Parallel Cell Strings

After completion of cycling, with 2000 cycles per pack studied, the capacity loss in the 3 homogeneous temperature 1S2P packs cycled at 2 C was considered. As shown in Figure 6.7 a, the rate of dynamic capacity loss is approximately linear when comparing the three homogeneous temperatures studied (20.0, 32.5 and 45.0 °C). The accessible capacity from the string is a function of several factors including the underlying cell static capacity, measured from 100 % SoC at low rate, the cell impedance and the cell OCV curve. Previously in Chapter 5, the cell impedance has been identified as driving current distributions within parallel strings. Increasing cell impedance at lower temperatures was shown to be the principal underlying cause of branch resistance change and therefore current heterogeneities during a single cycle. However, the interplay between these factors becomes more complex when considering performance over the lifetime of the string. There is also a significant deficit between the accessible capacity during dynamic cycling and the static reference capacity measured, as shown in Figure 6.7 b, measured at 0.1 C and 20 °C. For example, while P20.0/0.0 loses approximately 25 % accessible capacity over the 2000 cycles experienced, the static capacity loss between the cells is highly consistent at 20 °C. In comparison, P45.0/0.0 loses the least dynamic accessible capacity, 11 %, which is close to the static measured capacity loss, which has a mean value of 13 %. This implies that the SoC deficit, identified in Chapter 5 as a key factor in the reduction of accessible compared to reference capacity in parallel strings, is lower in the high temperature case, which again agrees with previously presented measurements.

Figure 6.7 c presents the mean difference in current throughput per cycle for each pack during discharge, defined as the mean current over the cycle in B1 minus the mean current in B2. As can be seen, there is generally a convergence in the homogeneous cases presented here, especially in the 2 lower temperature cases, with a reduction in current throughput difference of 80 % in P20.0/0.0 and 55 % in P32.5/0.0 , while a minimal reduction is seen in P45.0/0.0 . The noise in Figure 6.7 c is attributed to the minor variations in contact resistance between the cells in the string during the disassembly/reassembly process. While every effort was made to match contact resistances, it was not practically possible to exactly match all resistances in each case. Finally, the total current throughput for each cell in the homogeneous temperature case are shown in Figure 6.7 d, showing a building deficit between the cells, which may be attributed to the remaining SoC deficit at EoD (examined further in Section 6.8).

Figure 6.7 b shows that the deviation in reference capacity loss between the two pack cells is negligible for P20.0/0.0 and P32.5/0.0 while in P45.0/0.0 there is an appreciable building deficit in cell reference capacity during cycling, up to 1.5 % at EoL. Additionally, it is interesting to note that for P45.0/0.0, B2 has experienced a higher total current throughput despite seeing lower overall capacity loss. As previously identified, several critical stress factors are drivers of LIB degradation, and four key factors may be considered here; peak current rate, total current throughput, mean SoC and temperature. In the two lower temperature cases, peak currents (discussed in detail in Section 6.8) were observed to be lower than in the higher temperature case. In this study, the temperature between the cells was held constant, and the current throughput variation is small (<2.5 %), and so may be excluded from potential driving factors. Therefore, to explain the difference in capacity loss between B1 and B2 in the high temperature case, the mean SoC and peak current must be considered as the key stress factors.

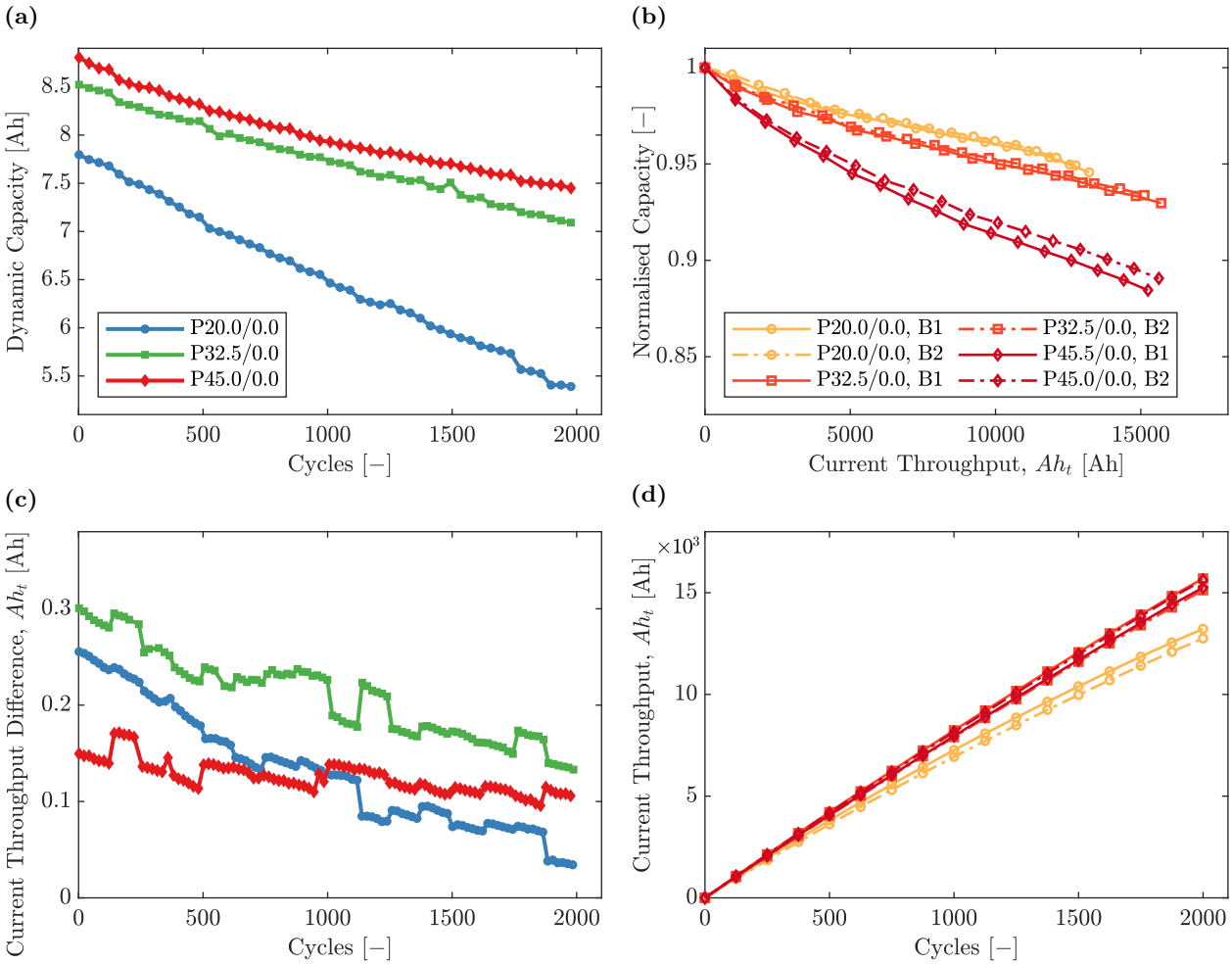


Figure 6.7: a) Dynamic discharge capacity during 2 C cycling for homogeneous temperature packs b) Static measured capacity at 0.1 C, 20 °C for all homogeneous temperature packs during aging. c) Current throughput deficit for all homogeneous temperature packs during aging. d) Total current throughput for all homogeneous temperature packs during aging.

In general, it is implied that at lower temperatures, the rate of static capacity loss within parallel strings is consistent, however at higher temperatures some deviation occurred, likely driven by the differential peak currents, mean current rates and cellwise current throughput totals. The importance of the total branch impedance, including the contact resistance, is also highlighted. If operating near the maximum safe rate for a cell, high peaking currents may lead to excessive local heating and safety hazards. In this case, a nominal applied rate of 2 C led to a peak current of approximately 2.8 C during discharge in the 32.5 and 45 °C homogeneous cases. The minimal difference between peak currents in the higher temperature cases is due to the non-linear decreases in cell impedance at higher temperatures. While the Kokam 5 Ah, an ultra-low impedance cell, is able to tolerate these rates, for high energy cells with lower maximum rated discharge rates this high peak rate may lead to overheating and both accelerated degradation and safety concerns. Previously, Offer et al. [140] highlighted the impacts of increased contact or weld resistances on a highly interconnected module topology, with a fault condition within some module connections leading to a current ratio of 6 between the highest and lowest loaded cells, compared to a factor of two in a no-fault module.

Having reviewed the degradation of the three packs under a homogeneous applied temperature, the four cases at the same mean temperature are next evaluated. The cycling thermal conditions are

summarised in Table 6.2, with 4 packs cycled at a mean temperature of 32.5 °C. As previously discussed in detail in Chapter 5, a negative thermal gradient was found to lead to an overall loss in performance compared to the positive case while also increasing the peak currents experienced by the first cell in the string for the U-topology. As shown in Figure 6.8 a, the dynamic performance of the strings investigated is dictated by the applied thermal gradient, with P32.5/+25.0 and P32.5/-25.0 experiencing an accelerated loss in overall accessible capacity when compared to P32.5/0.0. Decreasing the magnitude of the thermal gradient reduces the loss of accessible capacity by 65 %, implying that increasing magnitudes of thermal gradient are increasingly detrimental to both overall performance and pack lifetime. However, minimal difference is seen when comparing the positive and negative thermal gradient cases. Considering the static reference capacity loss (Figure 6.8 b), cells within the strings under thermal gradients experienced significant deviations in static capacity loss. This deviation is proportionate to the temperature of the cell in question. Again, no significant deviation in the rate of static capacity loss is seen when comparing the direction of the applied thermal gradient. Notably there is no appreciable difference in capacity loss rate when comparing B1 in P32.5/0.0, B2 in P32.5/-25.0 (both at 20.0 °C) and B2 in P32.5/-12.5 at 26.3 °C, while the rate of degradation accelerates significantly when comparing cells cycled above 32.5 °C. This implies that the degradation rate is non-linear with respect to temperature, and accelerates above approximately 32.5 °C.

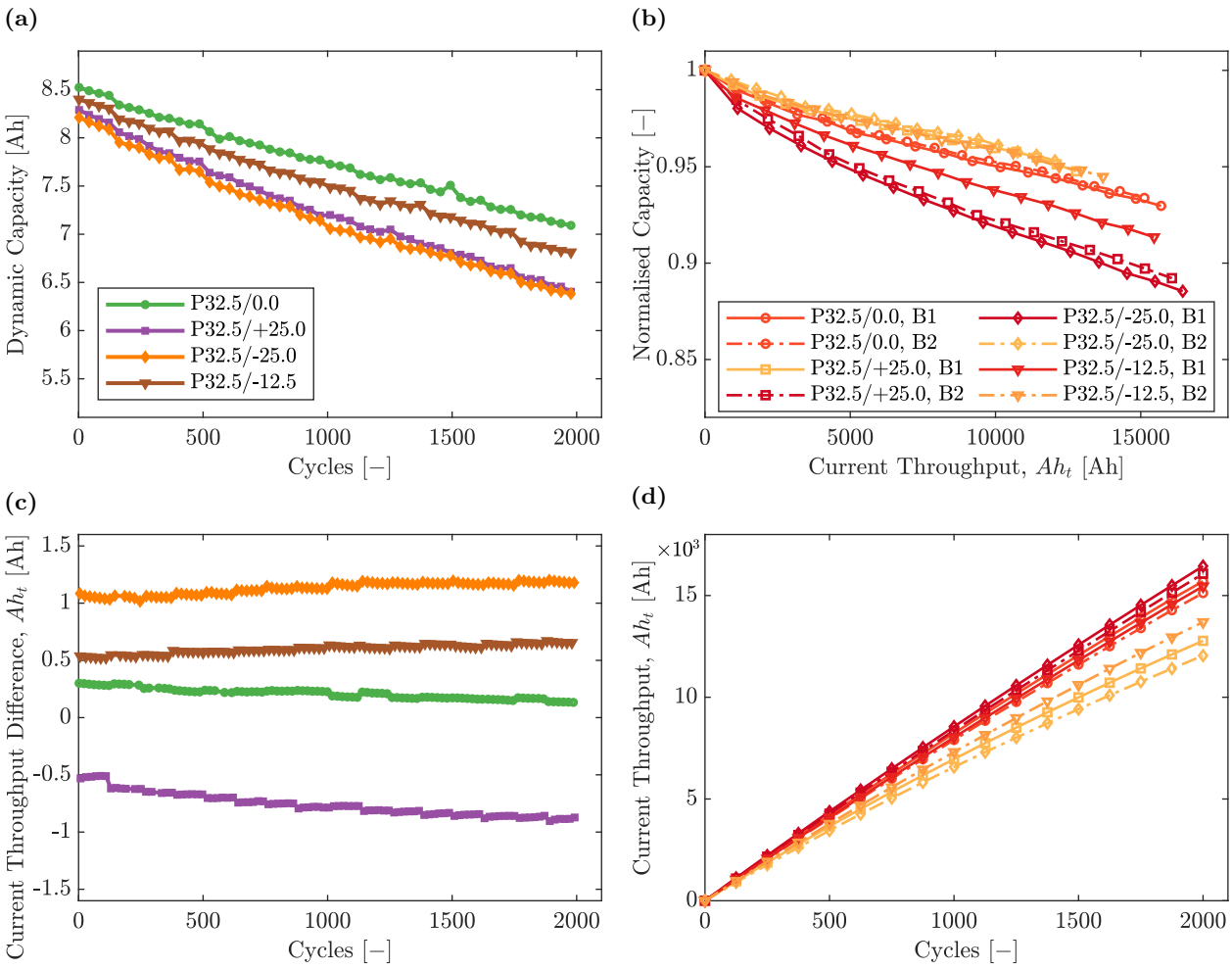


Figure 6.8: a) Dynamic discharge capacity during 2 C cycling for heterogeneous temperature packs b) Static measured capacity at 0.1 C, 20 °C for all heterogeneous temperature packs during aging. c) Current throughput deficit for all heterogeneous temperature packs during aging. d) Total current throughput for all heterogeneous temperature packs during aging.

Considering the current throughput deviation over time, cycle-to-cycle difference and total current throughput are shown in Figure 6.8 c and d respectively. When compared to the convergent behaviour in P32.5/0.0 the difference in current throughput per cell is divergent in all thermal gradient cases. In the positive thermal gradient case, P32.5/+25.0, the difference is negative as B2 at 45.0 °C experiences a higher mean current, and therefore is the limiting cell in the string. This effect is reversed in the negative thermal gradient cases. Considering the underlying case of the over time, the growth in cell resistance leads to an increasingly current throughput deficit for all cases with applied thermal gradients (discussed in detail in Section 6.8). Figure 6.8 d shows that over time the build-up of this deficit is significant and accelerates. This is despite all the cycled packs maintaining identical mean temperatures, with a deficits of up to 5000 Ah identified. In all cases, higher current throughputs are seen in the high temperature cells. In general, this is likely to exacerbate the already accelerated degradation of the high temperature cells, as increasing temperature and current throughput are stress factors to consider during cell degradation. Combined these effects is likely to increase the stress on high temperature cells leading to premature aging within the string.

6.7 Impedance Growth in Parallel Cell Strings

As has previously been discussed in Chapter 5, branch resistance is a key driver of heterogeneous behaviour within parallel strings, with the location and magnitude of resistance variations are highly influential in driving heterogeneous currents and SoC distributions. During the experimental study, current distributions and therefore SoC distributions in all packs were recorded and are explored in detail in this section. As previously discussed there were significant variations in the peak and mean currents seen by each cell within the 1S2P packs during cycling. Packs under thermal gradients exhibited divergent behaviour with increasing peak currents and divergent mean currents. This indicates that over time currents through the initially less-loaded cells are diminishing while those in the initially more-loaded cells are increasing. Over time, increasing SoC deficits are built up in the packs, leading to a loss of accessible capacity when compared to P32.5/0.0, the reference case.

Work presented in Chapter 5 has established that current and SoC heterogeneities are driven by differences in total branch resistance within a parallel string. In this study all resistances contributing to the total branch resistance were controlled and held constant, and therefore the cell impedance change was investigated. To provide a SoL reference, the impedance of a Kokam 5 Ah cell was measured at temperatures from 10 to 50 °C with 10 °C breakpoints. Figure 6.9 a shows a reference set of EIS spectra, taken at 50 % SoC. The impedance response exhibits 2 characteristic depressed semi-circles, associated with the SEI layer resistance (R_{SEI}) and charge transfer resistance (R_{CT}) respectively. The characteristic 'tail' associated with diffusion processes within the cell is also present. Figure 6.9 b-d show the fitted resistances, R_0, R_{SEI} and R_{CT} respectively. The fitting model used can be found in Figure 6.6 a. The total cell impedance decreases non-linearly with increasing temperature, due to sluggish kinetics and slower diffusion within the cell at lower temperatures, while an order of magnitude decrease in total cell impedance is seen over the full temperature range. R_0 and R_{SEI} are relatively insensitive to SoC variations, but decrease as cell temperature increases. Meanwhile, R_{CT} is strongly affected by the SoC and temperature. At SoL therefore, in the homogeneous temperature packs, R_{CT} will be the dominant factor driving the current distribution, with the non-linear increase in R_{CT} below 40 % SoC leading to rebalancing cell currents as discussed in Chapter 5. This rebalancing

effect occurs due to the non-linear increase in cell impedance at low SoC, with SoC deviation between cells caused by heterogeneous cell currents.

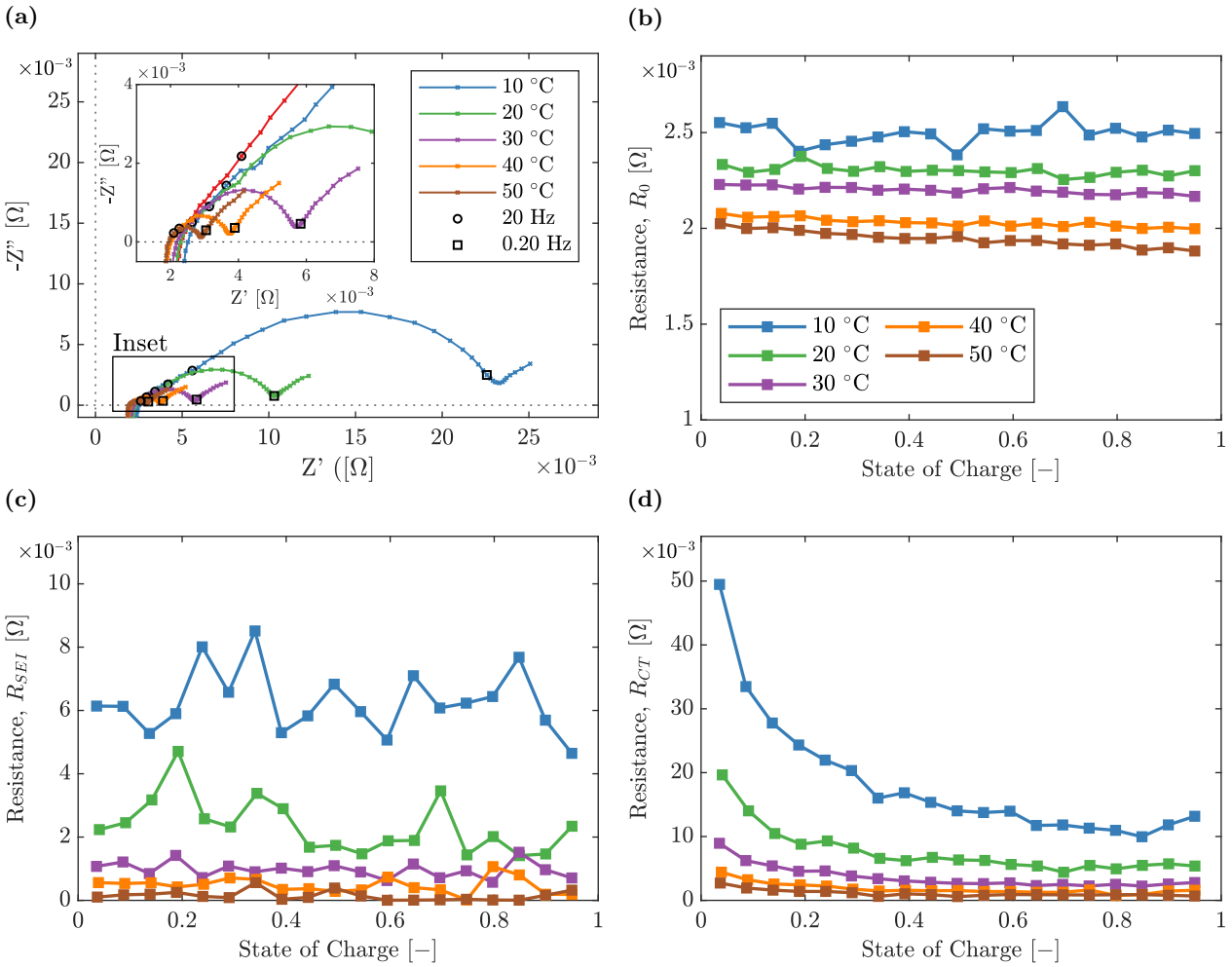


Figure 6.9: Reference SoL EIS measurements for Cell 01, including fitted resistances, taken at 10-50 °C from 10 kHz-0.01 hZ, 250 mA excitation current. a) Reference EIS spectra taken at 50 % SoC, with key frequencies marked. b) Fitted R_0. c) Fitted R_{SEI}. d) Fitted R_{CT}.

While EIS is a powerful diagnostic tool, it was not practical to acquire a full range of EIS measurements on each cell during cycling, due to channel availability and time limitations. Therefore, alternative measurements were taken to track cell resistance, using a HPPC pulse measurement. This had the advantages of taking only 25 % of the time of a full EIS scan while being run on a standard cycler channel. The disadvantage of HPPC measurements compared to EIS is that HPPC protocols measure the DC resistance of the cell rather than true AC impedance, As such decoupling of different cell processes is not straightforward. However, it is still possible to obtain indicative measurements of different processes, provided a prior understanding of the process time constants is obtained from EIS.

In Figure 6.9 a, two frequencies, 20 and 0.2 Hz, are highlighted. As can be seen, 20 Hz is approximately the frequency at which R_{CT} becomes the dominant process, while 0.2 Hz occurs at the knee, prior to diffusion dominating the overall cell impedance response. Therefore, the R_{DC} evaluations at the associated time breakpoints for these frequencies (0.05 and 5 s) are an approximation of the modulus of the cell impedance at this frequency. As such $R_{DC|0.05s}$ includes primarily the cell R_0 and R_{SEI} response, while $R_{DC|5.0s}$ includes R_0, R_{SEI} and R_{CT}. Due to limitations of the cycler current slew rate,

the highest rate pulse measurement it was possible to accurately obtain a DC resistance measurement was 0.05 s. Ideally, a shorter time breakpoint of approximately 0.01 s would be used to approximate the cell R_0 and R_{SEI} response, however this was not possible due to the aforementioned limitations in cycler performance.

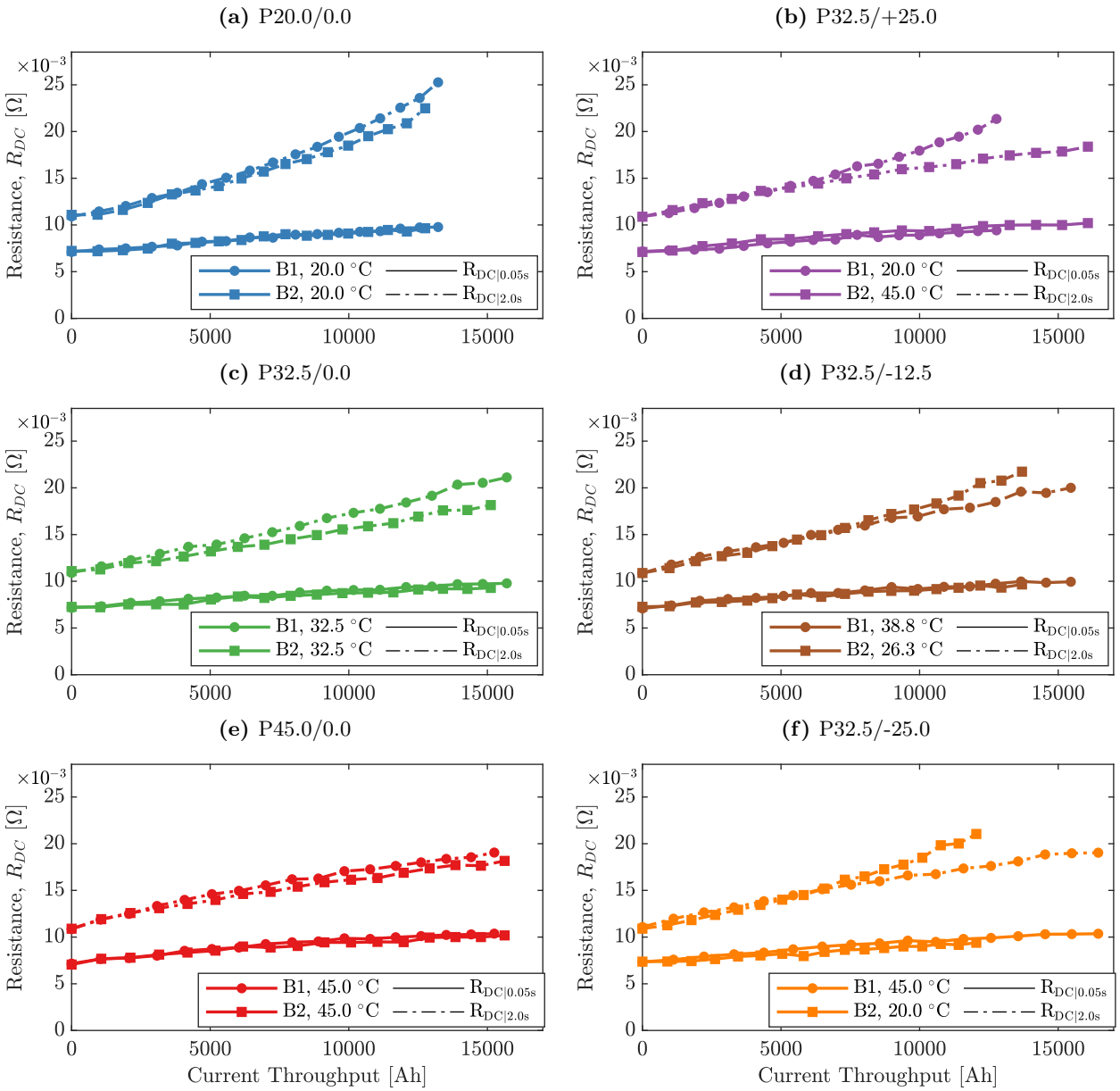


Figure 6.10: Growth in measured HPPC resistances, $R_{DC|0.05s}$ and $R_{DC|5.0s}$, for all packs. All HPPC measurements taken at 20 °C, 1 C pulse discharge. a) P20.0/0.0. b) P32.5/+25.0. c) P32.5/0.0. d) P32.5/-12.5. e) P45.0/0.0. f) P32.5/-25.0.

Figure 6.10 a-f presents the extracted HPPC resistance values $R_{DC|0.05s}$ and $R_{DC|5.0s}$ for B1 and B2 within each pack tested, at 50 % SoC. The magnitude of $R_{DC|0.05s}$ is approximately equal at SoL for all cells and is used to approximate R_0 and R_{SEI} . While the magnitude of $R_{DC|0.05s}$ is approximately 25 % above that measured using EIS, due to the hardware limitations mentioned, it serves as a useful approximation to track the lumped short time constant resistances over life. Meanwhile at SoL, $R_{DC|5.0s}$ is consistent between cells and accurately approximates the sum of R_0 and R_{SEI} and R_{CT}. As such, for tracking resistance changes over the lifetime, and providing some limited ability to distinguish between shorter and longer time constant resistive processes, the HPPC protocol as

defined was adequate.

As shown in Figure 6.10 a-f, the growth of $R_{DC|0.05s}$ is relatively insensitive to the pack or cell considered, with a linear growth in all cases of between 35 and 48 % over 2000 cycles. However, divergence is seen in the longer time constant DC resistance, $R_{DC|5.0s}$. Interestingly, the growth in $R_{DC|5.0s}$ is more significant and accelerates at lower temperatures, for example in, P20.0/0.0 (Figure 6.10 a). In comparison for P45.0/0.0 the growth in $R_{DC|5.0s}$ is decelerating (Figure 6.10 e). P32.5/0.0, the interim temperature case, shows approximately linear growth in $R_{DC|5.0s}$. This behaviour is unexpected as it is typically assumed that resistance growth rate increases at higher temperatures, as would be the case if SEI layer growth was the dominant mechanism of impedance growth. This implies that a) the rate of growth of R_{CT} is inversely proportional to temperature and/or b) the mechanism is independent of temperature but promoted by the cell operating conditions at low temperature. Further confirmation of these observations is seen in the packs cycled under thermal gradients. P32.5/+25.0 shows divergent growth in $R_{DC|5.0s}$, with significant divergence between B1 (at 20.0 °C) and B2 (at 45 °C) seen above 7.5 kAh current throughput, shown in Figure 6.10 b. This leads to an eventual difference in $R_{DC|5.0s}$ of 20 %, significantly increase heterogeneities within the pack. Similar behaviour is in P32.5/-12.5 and P32.5/-25.0 (Figure 6.10 d and f). The measured increase in $R_{DC|5.0s}$ for the cells at 20.0 °C in both packs under thermal gradients is 5-15 % lower than seen in the homogeneous 20.0 °C pack, indicating that the current rate may be stress factor relating to the growth in R_{CT}.

In order to provide confirmation of these observations, EIS measurements were taken at the SoL and EoL for each cell at 50 % SoC with respect to measured cell capacity at SoL and EoL. In all cases, the cell voltage at measurement was 3.78 ± 0.002 V. The measured spectra are shown in Figure 6.11 a-f. The trends highlighted by the DC resistance measurements presented are confirmed, with the depressed semicircle associated with R_{CT} dominant in all cells. First considering P20.0/0.0, significant divergence is seen in the magnitude below approximately 20 Hz, while the high frequency impedance response remains relatively constant, with negligible divergence seen between the cell pairs. Considering the homogeneous temperature cases (Figure 6.11 a, c and e) it can be seen that the magnitude of the R_{CT}-associated semicircle is inversely proportional to the applied temperature. Divergence between the spectra is seen in P20.0/0.0 and P32.5/0.0, however in P45.0/0.0 impedance is not seen to diverge significantly. The homogeneous temperature cases indicate R_0 may grow slightly at elevated temperatures. Impedance responses for P32.5/+25.0, P32.5/-12.5 and P32.5/+25.0 are shown in Figure 6.11 b, d and f , and broadly follows the same trends highlighted in the homogeneous cases. Again the lower temperature cells experience larger increases in R_{CT}, while the high temperature cells see greater growth in high frequency impedances. The impacts of this impedance change on pack behaviour is discussed in detail in Section 6.8.

After acquisition, the impedance spectra were fitted using the fitting model found in Figure 6.6 a. The changes in each associated resistance for each pack is presented in Figure 6.12 a-f, showing the normalised increase in R_0, R_{SEI} and R_{CT}. For P20.0/0.0 (Figure 6.12 a) the magnitude in R_{CT} increased of 4.8 and 3.8 times in B1 and B2 respectively. Meanwhile P45.0/0.0 shows an increases in R_{CT} of 2.6 and 2.3 times, and the divergence between cells reduces at higher temperatures. The trends observed in the homogeneous packs are replicated in the heterogeneous P32.5/+25.0, P32.5/-12.5 and P32.5/+25.0 packs, as shown in Figure 6.12 b, d and f. In all cases, the change in R_0 and R_{SEI} is negligible compared to the change in the fitted R_{CT} value, confirming that the impedance growth

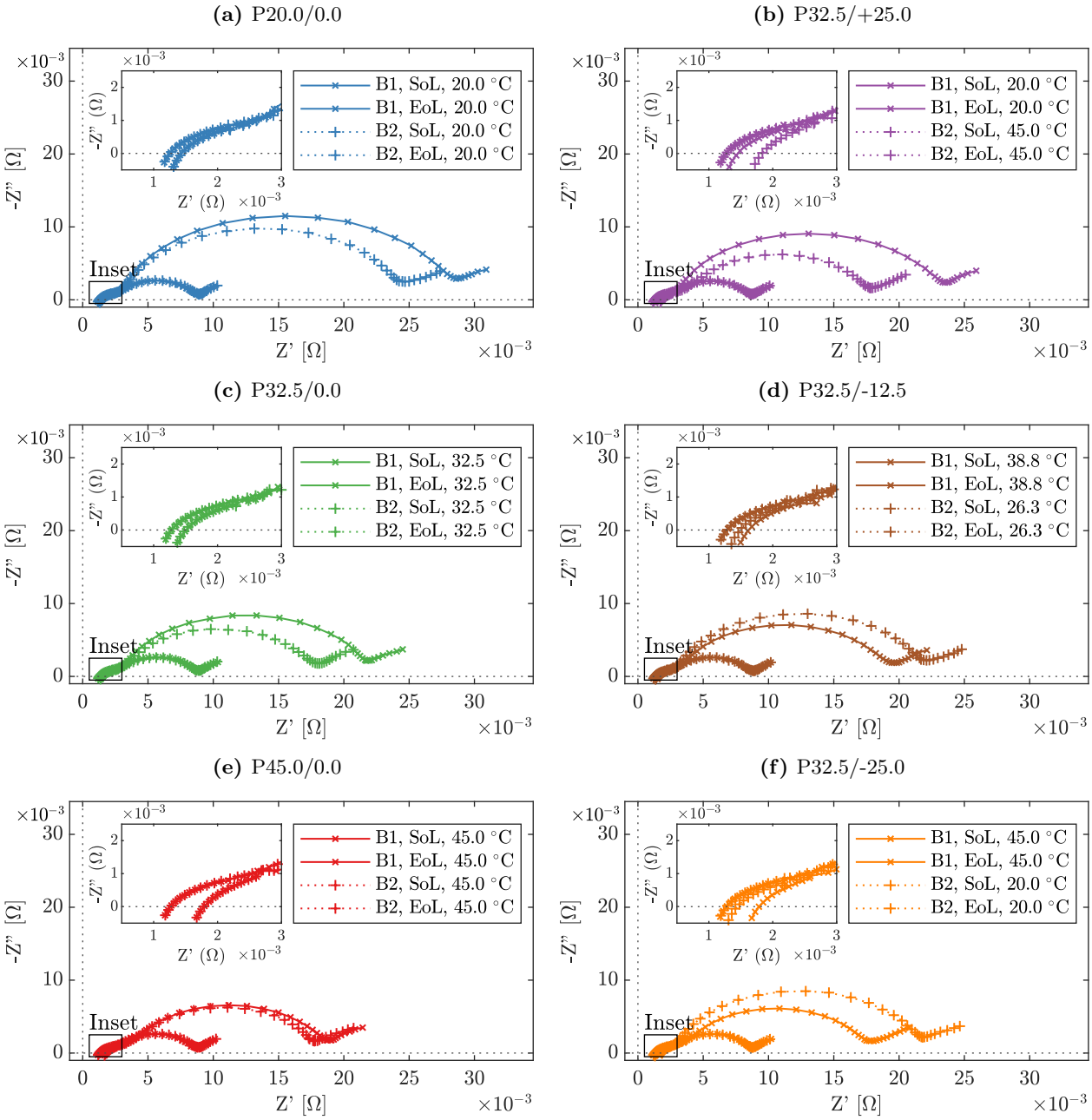


Figure 6.11: EIS Spectra at SoL and EoL for all packs, taken at 50 % SoC, 20 °C from 10 kHz-0.01 hZ, 250 mA excitation current. a) P20.0/0.0. b) P32.5/+25.0. c) P32.5/0.0. d) P32.5/-12.5. e) P45.0/0.0. f) P32.5/-25.0.

observed is dominated by changes to R_{CT}.

As a final confirmation of the behaviour of each impedance, the normalised resistance growth values for each fitted resistance and all 12 cells studied are presented in Figure 6.13 a-c for R_0, R_{SEI} and R_{CT}, plotted against the cycling temperature. No significant correlation with temperature is observed in R_0 (Figure 6.13 a). However, R_{SEI} growth (Figure 6.13 b) is observed to be clearly a thermally correlated process as expected, with significant increases above 40.0 °C. Meanwhile the rate of growth of R_{CT} (Figure 6.13 c) is negatively correlated with temperature, the rate of growth halving when cycling temperature increases from 20.0 to 45.0 °C.

Distribution of Relaxation Times (DRT) analysis by Zhu et al. [93] indicated that in NMC cathodes, the total charge transfer resistance is dominated by the cathode R_{CT}, which also increased significantly

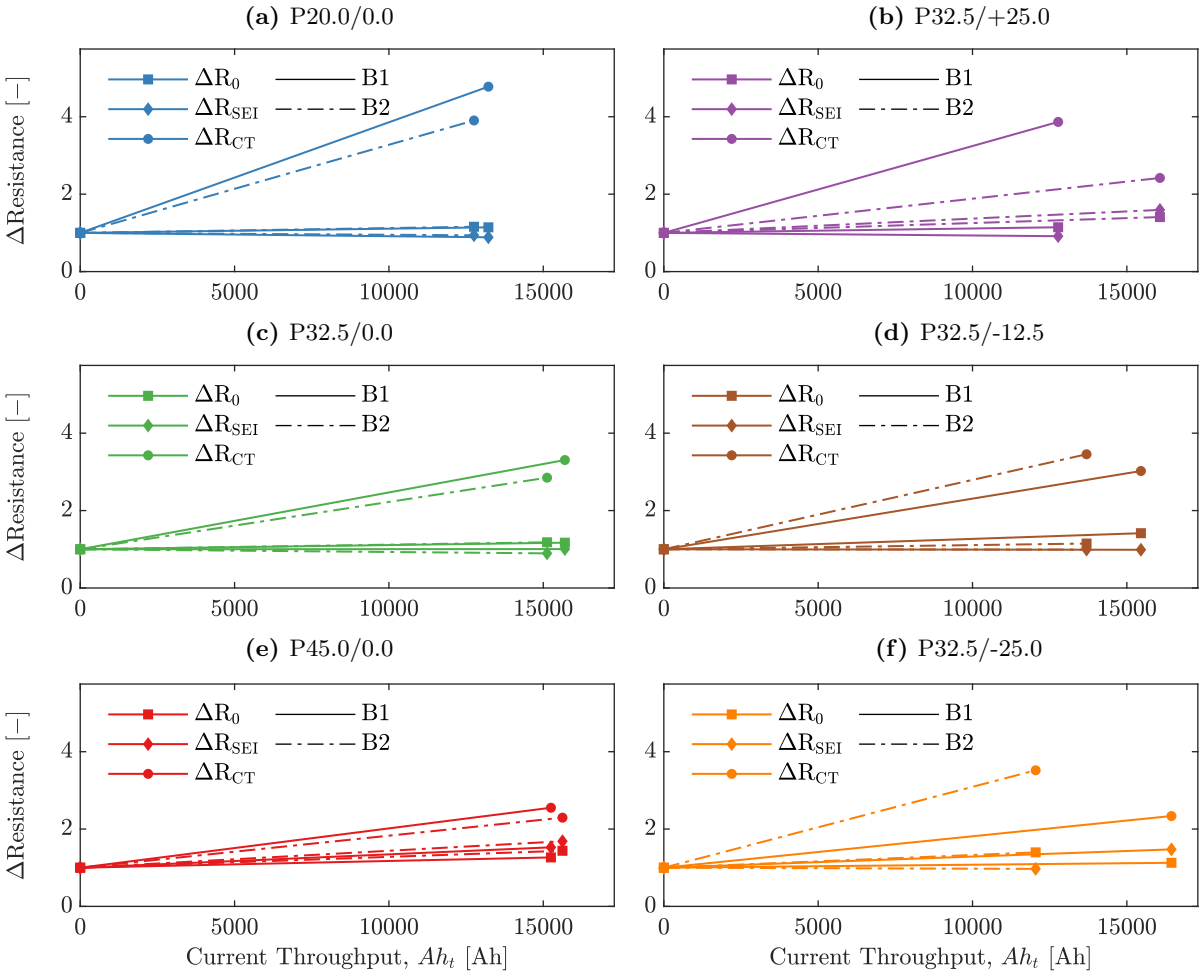


Figure 6.12: Proportional change in fitted resistances R_0, R_{SEI} and R_{CT}, for all packs. a) P20.0/0.0. b) P32.5/+25.0. c) P32.5/0.0. d) P32.5/-12.5. e) P45.0/0.0. f) P32.5/-25.0.

faster than the anode R_{CT}. This increase was found to be inversely proportional to temperature and it was proposed that the rise in R_{CT} is caused by particle fracture and consequent loss of electrochemically active material. Meanwhile, Zhang et al. [92] used EIS analysis of aged cells with inserted Lithium-metal reference electrodes to show that the impedance rise during cycling was predominantly caused by changes to the cathode R_{CEI} and R_{CT}. In comparison changes in anode impedance lead to minimal effects on the full cell, with growth in R_{CEI} the dominant change at the full cell level. Consequently, the impedance growth demonstrated in the cycled cells is likely dominated by cathode degradation leading to increases in cathode R_{CT}, and this is indicative of cathode capacity loss due to loss of electrochemically active sites in the cathode.

Further evidence of differing degradation mechanisms, and therefore resistance growth, was obtained by analysis of the relaxation time constants during HPPC measurements. During the HPPC measurements, cells were discharged by 10 % SoC at 0.25 C and then allowed to relax for 1 hr before application of current pulses. The relaxation time constant was estimated by analysing the voltage relaxation after removal of the discharge current, and extracting the time taken for the voltage to relax by 63.2 % of voltage difference between the start and end of relaxation, equating to approximately 1 time constant for voltage relaxation. As the time constants identified in EIS measurements indicate that that τ_{SEI} and τ_{CT} are both less than 10 s, it can be assumed that the dominant process during voltage relaxation is solid-state diffusion within the electrodes (although diffusion within

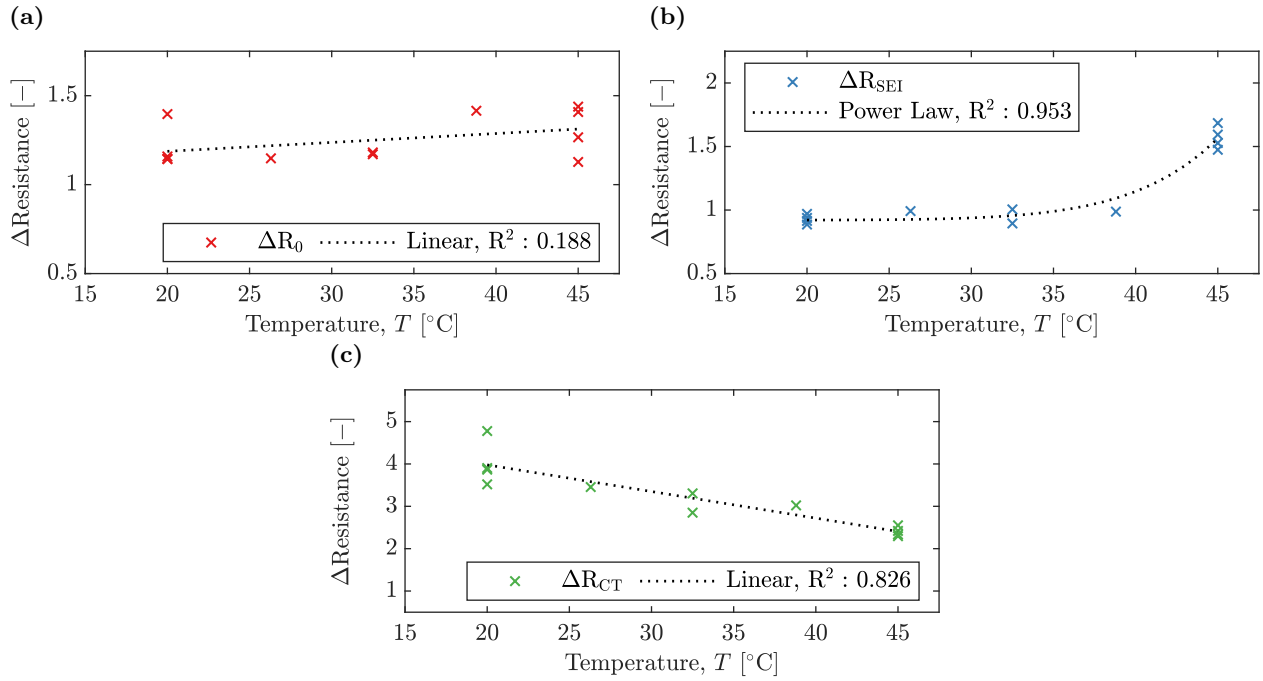


Figure 6.13: Proportional change in fitted resistances R_0, R_{SEI} and R_{CT} against temperature for all cells. b) R_0. a) R_{SEI}. c) R_{CT}.

the electrolyte may also play a role). This assumes that the low rate discharge has led to a linear concentration gradient forming. Increases to the relaxation time constant are indicative of decreasing diffusion coefficients within the cell.

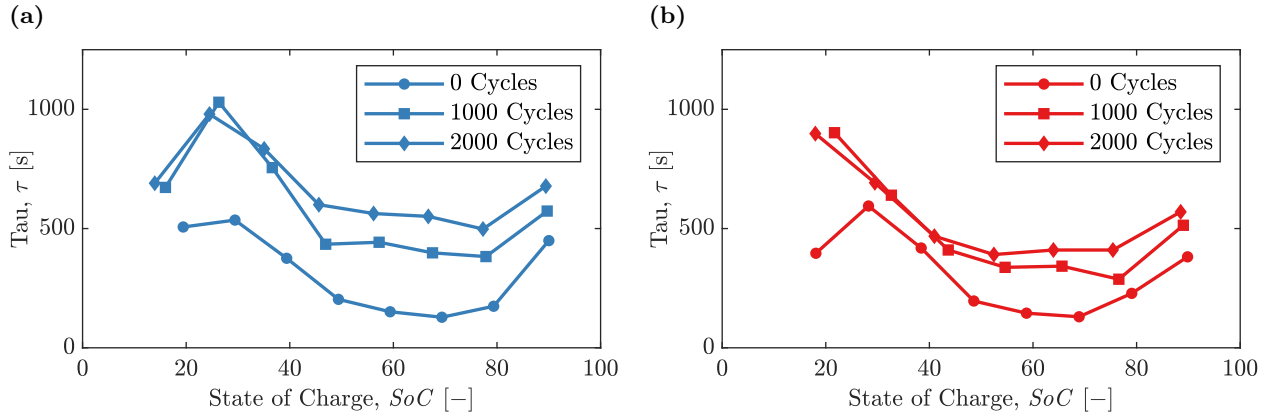


Figure 6.14: Development of $\tau_{Relaxation}$ during voltage relaxation in HPPC measurements, for selected cells. a) P20.0/0.0 B1. b) P45.0/0.0 B1.

Figure 6.14 shows the estimated relaxation time constants at SoL, mid-life and EoL for B1 in P20.0/0.0 and P45.0/0.0 (Figure 6.14 a and b respectively), indicative of the differing development of relaxation time constants. In the lower temperature cell, the relaxation time constant growth is significantly accelerated in comparison to the high temperature cell, with significantly greater increases observed in the mid-SoC range (40-80 % SoC). It is noted that the lower SoC time constant values do not drop in the high temperature cell (Figure 6.14 b) at low SoCs, as seen in the low temperature cell. This is likely caused by drift in the cell stoichiometry caused by the accelerated capacity loss in the higher temperature cell. Evidence for this stoichiometric drift is presented in Section 6.9, where LLI is identified in the low temperature cycled cells, and would lead to drift in electrode stoichiometry.

While it is not possible to directly attribute the mode of power fade via analysis of the relaxation time constants, the different behaviour over time is indicative of different degradation modes leading to power fade at 20.0 and 45.0 °C. However, greater changes to the relaxation time constant is indicative of diffusion limiting degradation within the cell, for example structural changes within the electrode.

Based on the analysis of SoL and EoL EIS results, the following trends are observed. The proposed mechanisms leading to power fade are discussed in detail in Section 6.10:

- Growth in R_{CT} is inversely proportional to temperature over the 20-45 °C temperature range studied.
- Growth in R_{CT} is accelerated in the low temperature packs in cells closer to the terminals which experience increased mean and peak currents, implying the growth mechanism is affected by increased mean/peak currents.
- Growth in R_{SEI} is correlated with increasing temperature, but negligible below 40 °C.
- Growth in R_0 is weakly correlated with increased temperature, however changes are negligible (10-20 times smaller), relative to those observed in R_{CT}.

Considering the impedance growth behaviour of the packs during cycling, the expected impacts on the heterogeneous current distributions are as follows, while the underlying mechanisms suggested to lead to the cell resistance changes are discussed in Section 6.10:

- In the lower temperature homogeneous cases, convergence of currents is expected due to the accelerated growth of R_{CT} in B1 increasing the total resistance of branch 1 and compensating for the increased branch resistance of branch 2, due to the interconnections.
- In the higher temperature homogeneous case, less convergence is expected as there is no consequential divergence in cell impedance over time, leading to minimal rebalancing of branch resistances.
- The growth in high frequency impedance is shown to be small in all investigated cases, therefore explaining the minor changes in peak discharge current observed, as the peak applied current occurs at the beginning of discharge, with high frequency impedance dominant.
- Packs under thermal gradients will exhibit divergent current behaviour, as the accelerated growth of R_{CT} at low temperature will eliminate any balancing effect of accelerated R_{SEI} growth in the higher temperature cells in the string.

6.8 Influence of Thermal Gradients on Heterogeneities

So far, both the capacity loss within the parallel strings and the impedance response changes have been considered in detail, alongside a limited analysis of the heterogeneity within the parallel strings. In this Section, the influence of capacity loss and impedance changes on the heterogeneous behaviour within the pack is analysed, with the aim of attributing specific changes in overall behaviour to cell-level changes within the pack, and subsequently identifying trends that may be generalised to other systems.

In the first case, heatmaps of the current distribution observed within the homogeneous temperature packs are presented in Figure 6.15, plotted against cycles and depth of discharge. The depth of discharge is defined as the current passed, divided by the total current throughput per cycle. Figure 6.15 a and b shows currents in B1 and B2 respectively for P20.0/0.0, while Figure 6.15 c-d and e-f show the same for P32.5/0.0 and for P45.0/0.0. Minor variations occurring every 125 cycles are caused by small variations in the contact resistance caused during repeat assembly and disassembly of the packs. Considering first the two lower temperature homogeneous cases, previously the dominant and accelerated growth of R_{CT} has been identified and is expected to cause convergence of pack currents. Initially as the packs are held at constant temperature the cell impedance is approximately equal at SoL, meaning the initial current distribution is dictated by the interconnection resistance. Subsequently during aging, accelerated growth in R_{CT} both at lower temperatures and in cells experiencing high peak currents leads to convergence, as branch resistances become more balanced. This trend is observed in both P20.0/0.0 and P32.5/0.0, with significant convergence of currents over the 2000 cycles studied. Using P20.0/0.0 as an example (Figure 6.15 a and b), initial current peaks in B1 are seen below 10 % DoD, with currents peaking at over 2.2 C. In this case, minimal rebalancing of currents is seen, which is attributed to the increased overall resistance at low temperatures leading to increased overpotentials and therefore less opportunity for rebalancing at higher DoDs. During aging, the current distribution is homogenised, with the initial high peak current region steadily decreasing in duration. In P32.5/0.0, identical trends are seen, but increased rebalancing is seen above 80 % DoD, due to the decreased cell impedance giving more opportunity for rebalancing of currents towards EoD.

In P45.0/0.0 (Figure 6.15 e and f) current convergence also occurs, however this is less significant than seen at lower temperatures. At high temperatures the cell impedance is reduced, due to the non-linearly decreasing impedance with respect to temperature and so at high temperatures, interconnect resistances have a correspondingly greater effect on the current distribution. Therefore, at high temperatures the degree of convergence is reduced. The convergence observed is principally in the initial region below 10 % DoD, and this is attributed to the increasing R_{SEI} in the high temperature pack during aging. Increases in R_{SEI} occur above 40 °C and lead to decreasing initial peak currents and therefore initial SoC deviation, as the high frequency branch impedance is increased at start of discharge.

Over the life of the pack, a small reduction in current heterogenity occurs due to the increasing cell impedance reducing the impact of the interconnection resistance on overall current distribution. However, the degree of convergence is reduced compared to the lower temperature packs, as the increase in impedance magnitude is smaller. More significant rebalancing occurs within the high temperature pack at low DoD values due to the decreased overpotentials allowing for more extensive rebalancing. As the overall current distribution is only partially convergent over time, this rebalancing remains at EoL.

Figure 6.16 a and b shows the peak current and mean current difference for each homogeneous temperature pack respectively. The noise seen in the measurements, concentrated in B1 for all cases is again caused by minor variations in the contact resistance between pack assemblies. This highlights the importance of consistent contact resistances in a U-topology parallel string. The peak currents typically occur within the first 5 s of the discharge and are not shown in the current distribution heatmaps such as Figure 6.15, as the colourmap is selected to provide contrast over the full DoD. In all cases, the

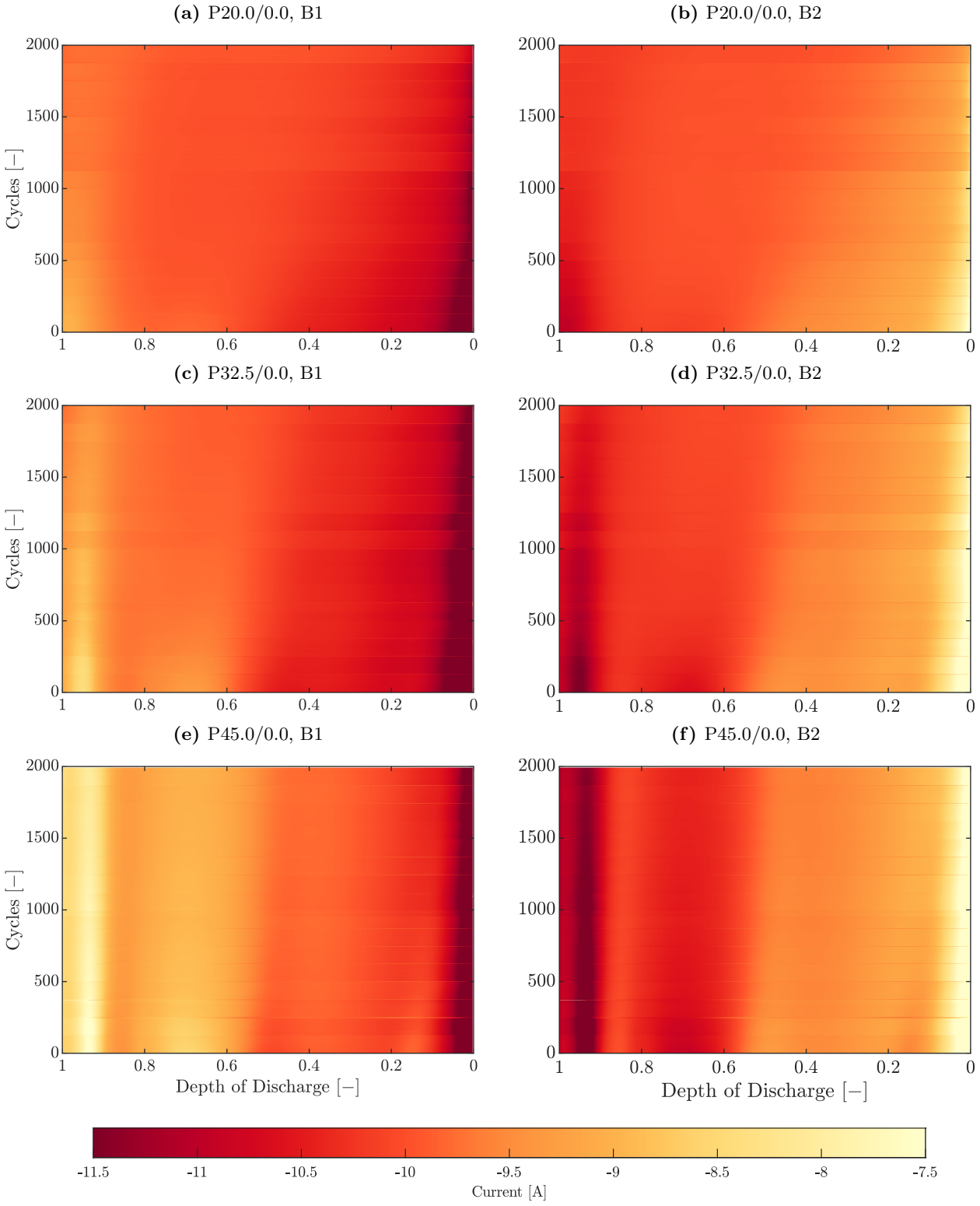


Figure 6.15: Heatmaps of current distribution within homogeneous temperature packs over lifetime. Depth of discharge defined as current passed divided by the total current throughput per cycle. a) P20.0/0.0 B1. b) P20.0/0.0 B2. c) P32.5/0.0 B1. d) P32.5/0.0 B2. e) P45.0/0.0 B1. f) P45.0/0.0 B2.

peak current reduces over the lifetime of the packs, due to the increasing cell impedance reducing the impact of the interconnection resistance on current distribution. Due to decreased overall impedance growth at higher temperatures the convergence in peak current is reduced. For all homogeneous packs, the peak currents are convergent over time, implying that for a homogeneous or close to homogeneous

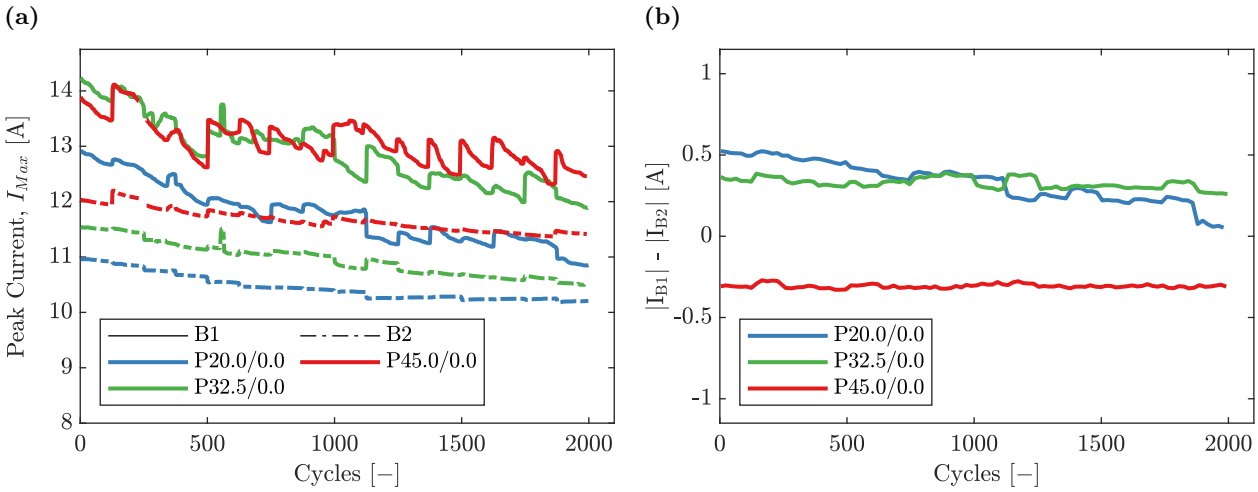


Figure 6.16: Peak and mean currents over lifetime for homogeneous temperature packs. a) Peak current. b) Mean current difference

temperature pack the operating currents will become more homogeneous. The mean current difference in P32.5/0.0 and P45.0/0.0 is relatively stable over life, due to reduced cell impedances and therefore overpotentials allowing for more extensive SoC rebalancing towards the EoD and therefore overall a smaller mean current difference.

Current distribution heatmaps for the heterogeneous temperature packs are then presented in Figure 6.17, plotted against cycles and DoD. Figure 6.17 a and b shows currents in B1 and B2 respectively for P32.5/+25.0, while Figure 6.17 c-d and e-f show the same for P32.5/-12.5 and for P32.5/-25.0. In P32.5/+25.0, the current is initially higher in B2, as the reduced cell impedance leads to a lower overall branch impedance in branch 2. Here, the overall current distribution is divergent during aging, as the accelerated impedance growth in B1 at low temperature and the lower cell impedance of B2 results in an increasing mismatch in branch resistances. Due to the changes in cell impedance, the resistance of branch 1 increased more rapidly during cycling. As shown in Figure 6.10, the measured cell DC resistance diverged at approximately 1000 cycles, and this increase in mismatch of branch resistances is observed in the current distribution above 1000 cycles.

In the converse case, P32.5/-25.0 (Figure 6.17 e and f), it can be seen that broadly the opposite behaviour is seen. Over the life of the pack the current distribution is divergent, again driven by the accelerated impedance growth seen in the low temperature cell. As shown clearly in Figure 6.17 e, the divergence in cell impedance occurring at approximately 1000 cycles has a more significant impact on the current distribution. This is due to the elimination of the interconnect resistances assisting in balancing the branch resistances as seen in the positive thermal gradient case, therefore leading to an increased impact of the divergent cell impedances above 1000 cycles. In the moderate negative thermal gradient pack, P32.5/-12.5 (Figure 6.17 c and d), while currents are somewhat divergent during aging, this is significantly reduced compared to ± 25.0 packs. This is attributed to the reduced difference in cell impedance induced by temperature, alongside the less significant divergence in cell impedances over the lifetime of the pack. In general, it can be concluded that larger magnitude thermal gradients will lead to increased impacts on the heterogeneities, provided the cell impedances are divergent within the pack. Conversely if cell impedances are convergent, heterogeneities in current will be reduced.

Figure 6.18 a and b show the peak and mean current differences respectively for the heterogeneous

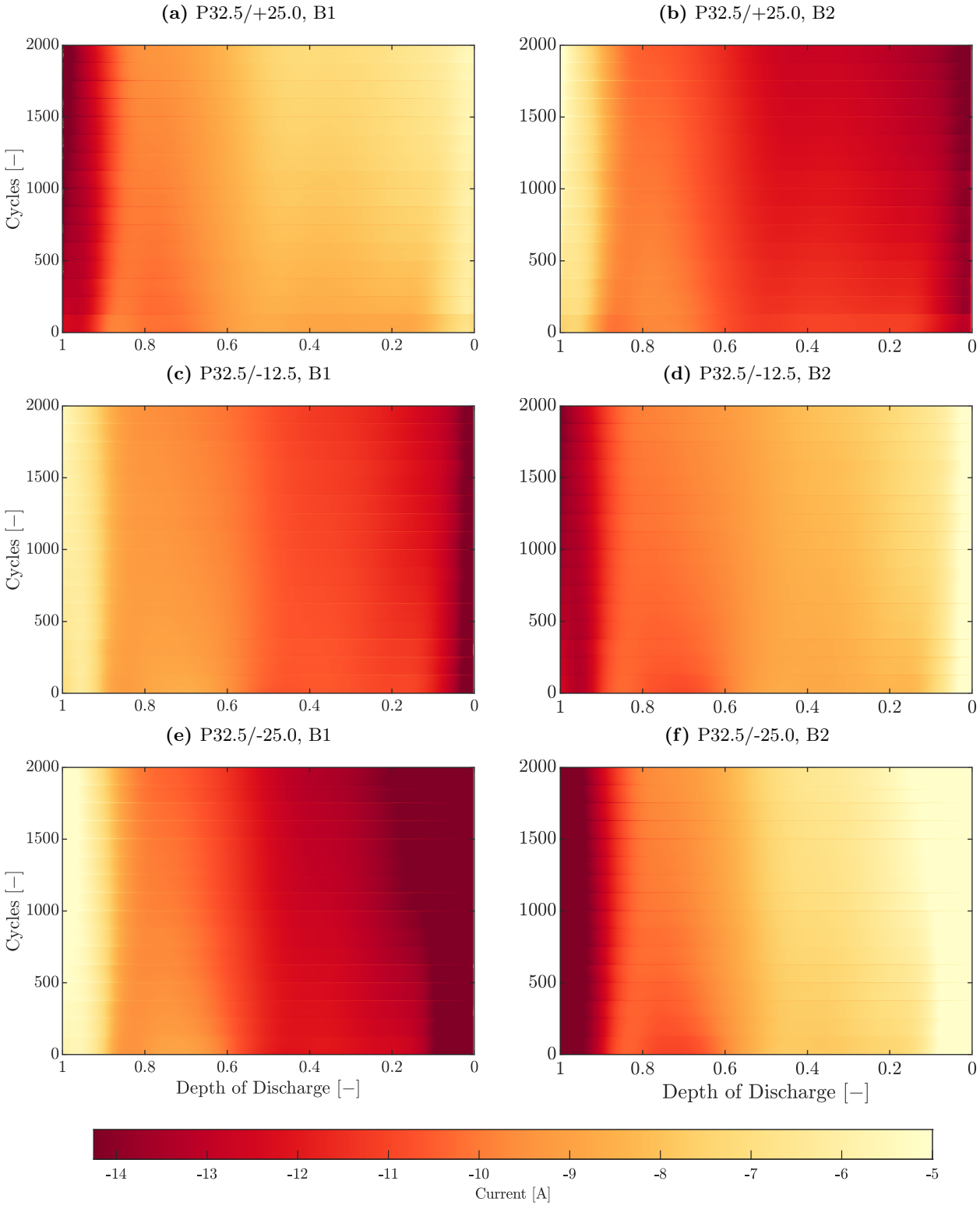


Figure 6.17: Heatmaps of current distribution within heterogeneous temperature packs over lifetime. Depth of discharge defined as current passed divided by the total current throughput per cycle. a) P32.5/+25.0 B1. b) P32.5/+25.0 B2. c) P32.5/-12.5 B1. d) P32.5/-12.5 B2. e) P32.5/-25.0 B1. f) P32.5/-25.0 B2.

temperature packs. In the negative thermal gradient packs, peak currents are significantly increased, to a peak of approximately 3.9 C in P32.5/-25.0. Comparatively in P32.5/+25.0 peak currents are 10 % lower than seen in P32.5/+25.0 highlighting the benefits of a positive over a negative thermal gradient. Due to the balancing effects seen on the total branch impedance, peak currents in P32.5/+25.0 are

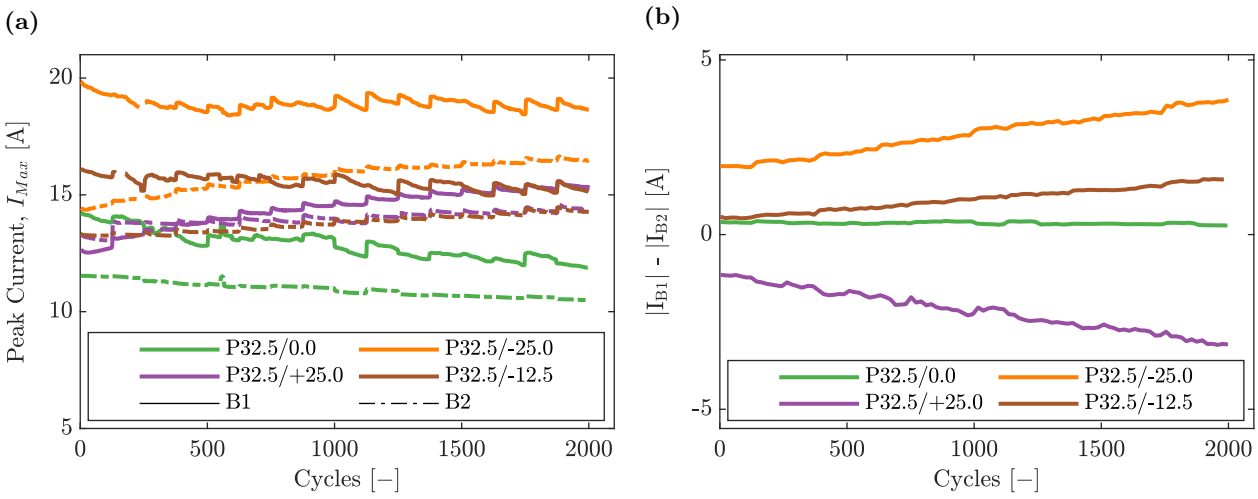


Figure 6.18: Peak and mean currents over lifetime for heterogeneous temperature packs. a) Peak current. b) Mean current difference

the most consistent out of the 6 packs tested. In the negative thermal gradient packs, the peak current converged to the higher (P32.5/-25.0) or mean (P32.5/-12.5) current values. This means the convergent behaviour of the peak current distribution observed in the homogeneous temperature packs switches to divergent behaviour when a thermal gradient is applied. This switch in behaviour is caused by differential impedance growth induced by the applied thermal gradients. In general, high peak currents may have detrimental effects on overall lifetime and safety, and accelerate rate-activated degradation processes such as particle fracture.

Considering the mean current difference between the cells (Figure 6.18 b) during aging, the thermal gradients lead to divergent mean currents. Highlighting the comparison of P32.5/0.0 and P32.5/-12.5, it can be seen that applying a -12.5 °C thermal gradient at an identical mean temperature changes the behaviour of the mean current significantly, switching behaviour from convergence to divergence. Again, increasing differences in mean current imply increasing deficits in current throughput over time, accelerating differential cell aging.

In Chapter 5, the SoC deficit at EoD was identified as a consequence of differential branch resistances caused by thermal gradients, in turn leading to a reduction in accessible capacity from the string. Therefore, the SoC deficit build-up over pack lifetime is shown in Figure 6.19 a and b for the homogeneous and heterogeneous temperature packs respectively. The SoC deficit is calculated based on the per-cycle current throughput and fitted values to the reference static capacity measurements at 0.1 C providing an estimate for cell static capacity at each cycle. These values were interpolated using a piecewise cubic polynomial ('*pchip*') algorithm, which was selected to avoid overshoots in the data fitting.

In the homogeneous temperature packs (Figure 6.19 a), the SoC deficit is initially greatest P20.0/0.0, as expected. Over time the SoC deficit increases, due to the increased cell impedances leading to a increased inaccessible capacity during aging, while due to the convergent current distribution the SoC deficit equalises. In P32.5/0.0 and P45.0/0.0 the initial deficit is smaller, due to the reduced total branch impedances. In P45.0/0.0 the SoC deficit is consistent throughout the pack life, due to the more extensive current rebalancing which occurs at EoD (increasing from 11 to 15 % SoC after 2000 cycles). In the heterogeneous cases (Figure 6.19 b), the SoC deficits are highly non-uniform,

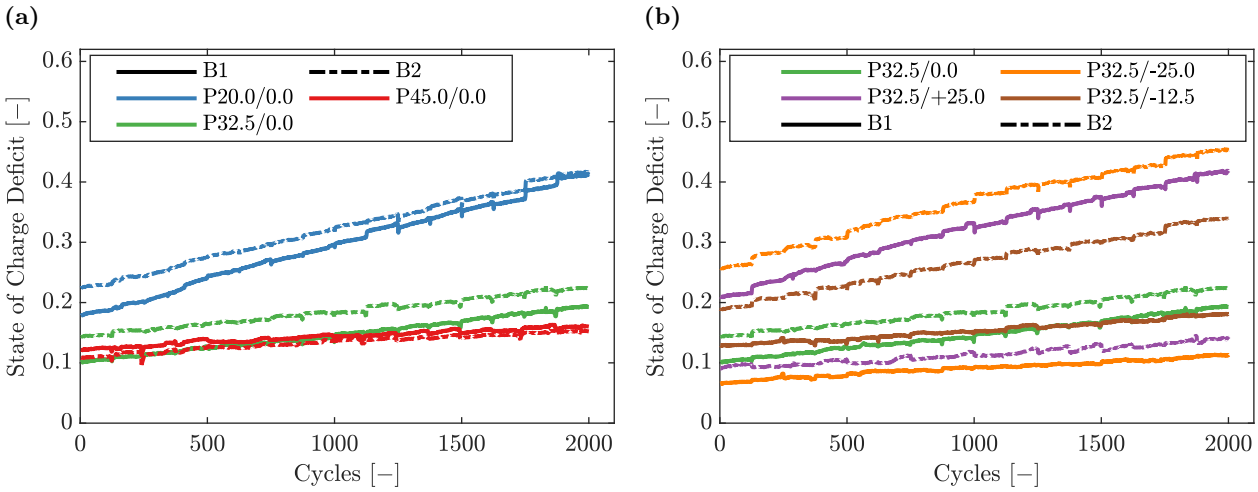


Figure 6.19: Estimated SoC deficit over lifetime for 1S2P packs. a) Homogeneous temperature packs. b) Heterogeneous temperature packs.

and are divergent in all cases. In each case the low temperature cell shows a large SoC deficit at EoD, for example in P32.5/-25.0, with a deficit of 45 % SoC in B2 at EoD, compared to 11 % in B1. In the the positive thermal gradient case (P32.5/+25.0) the deficit is reduced in B1, due to the overall reduction of the impact of the interconnection resistances on current distribution. In general it is implied that the reduction of capacity of a parallel string under an imposed thermal gradient compared to a homogeneous temperature can be principally attributed to reductions in accessible capacity in the cold cell.

To further examine the development of the SoC deficit within the parallel strings, heatmaps of the current throughput difference per cycle with respect to cycles and DoD are presented in Figure 6.20. Considering the behaviour of the 3 homogeneous temperature cases (Figure 6.20 a, c and e), it can be seen that in all cases a significant amount of rebalancing of current throughput is possible, with increasing rebalancing at higher temperatures. As a consequence, the current throughput deviation over time is reduced, leading to the reduced SoC deficits previously discussed. In comparison, in the cases with applied thermal gradients (Figure 6.20 b, d and f), the degree of rebalancing is reduced over the lifetime of the packs, due to the divergent cell impedances leading to a reduction in the amount of rebalancing of currents that can occur. In particular for P32.5/+25.0 and P32.5/-25.0, shown in Figure 6.20 b and f respectively, it can be seen that above 1000 cycles in both cases the EoD current throughput difference exceeds 1 Ah, or 10 % of the nominal SoL pack capacity. This leads to a significant loss of overall performance under theses operating conditions compared to the nominal capacity of the packs. Additionally, the region of significant current throughput deficit is increased in duration in both cases, implying that the mean SoC values of each cell will diverge with time. The SoC of a cell is a known degradation stress factor, with increasing SoC values accelerating calendar aging. As such this is a potential cause of accelerated degradation in the low temperature cells in a pack with a long in-service life, although this may be offset by the lower overall temperature, and a detailed investigation is outside the scope of this work.

To summarise the presented results, Figure 6.21 shows a simplified schematic representation of the effects of branch resistance growth on current (and subsequently SoC) distributions within a homogeneous temperature pack. As previously identified in Chapter 5, the principal driving factor behind

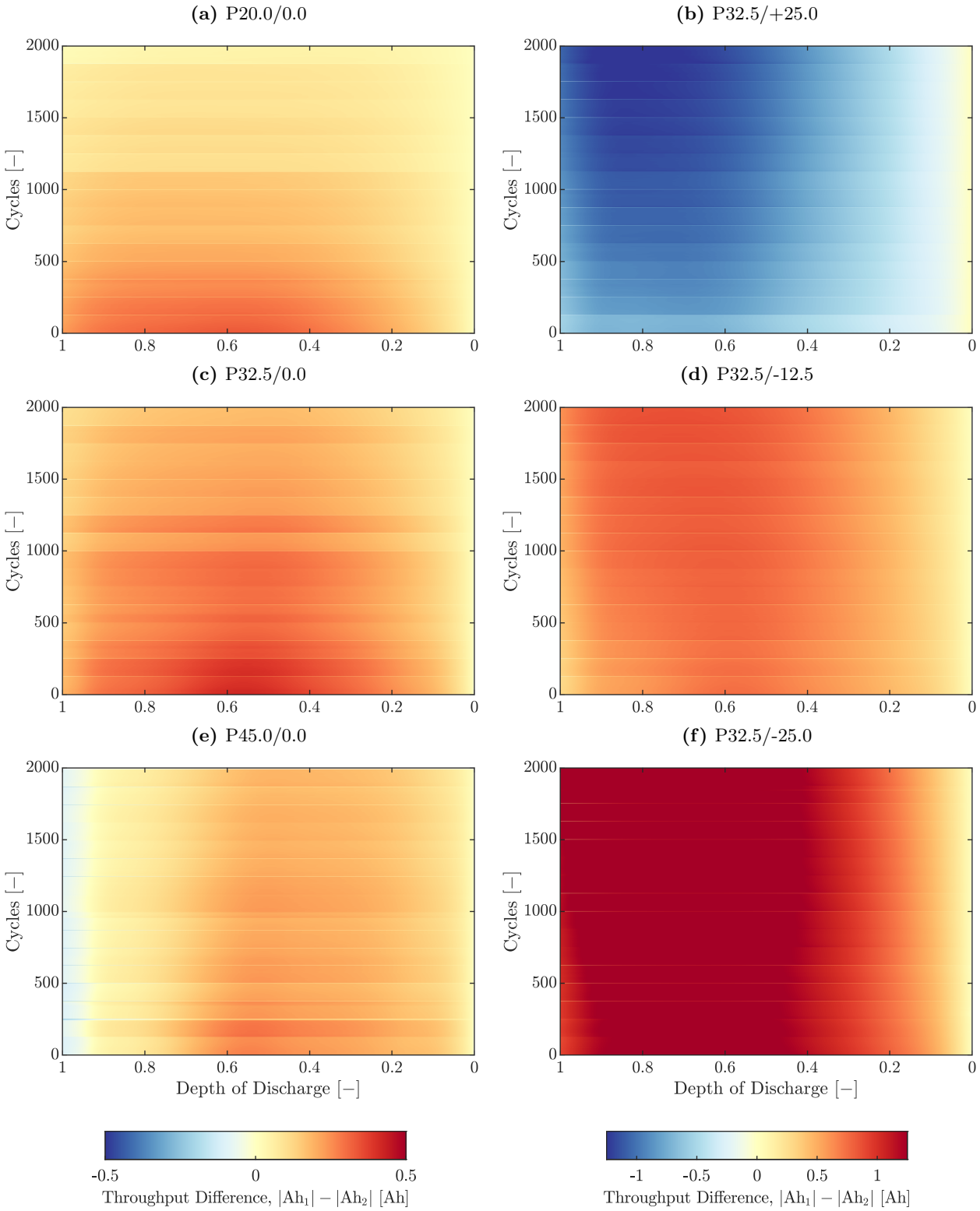


Figure 6.20: Heatmaps of current throughput deficit per cycle for all packs over lifetime. Depth of discharge defined as current passed divided by the total current throughput per cycle. a) P20.0/0.0. b) P32.5/+25.0. c) P32.5/0.0. d) P32.5/-12.5. e) P45.0/0.0. f) P32.5/-25.0. Note: Colourmaps differ for left (homogeneous temperature) and right (heterogeneous temperature) columns, to improve contrast.

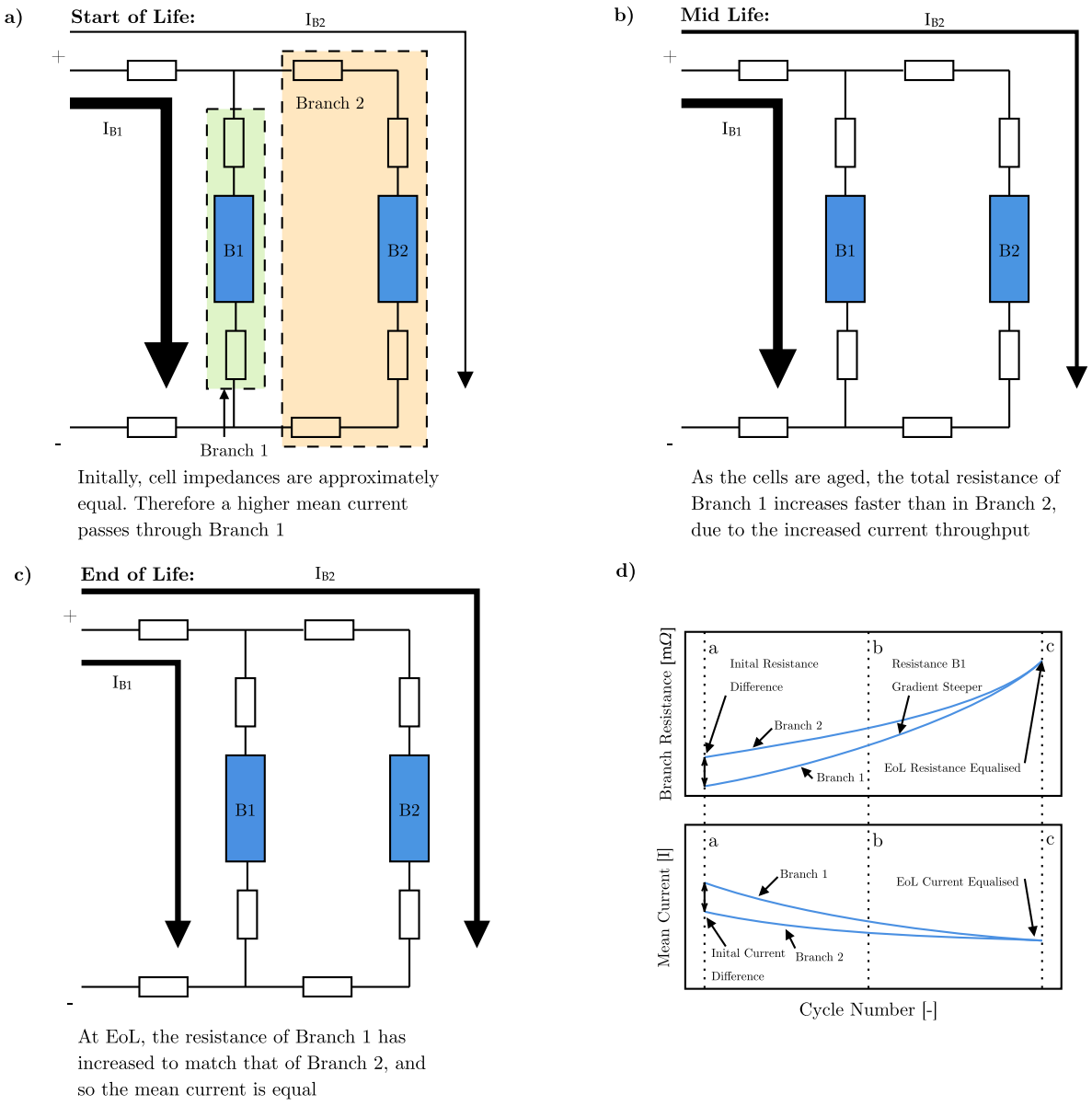


Figure 6.21: Schematic representation of homogenisation of current distribution during aging in homogeneous temperature packs. a) Start of life. b) Mid life. c) End of life. d) Schematic representation of total branch resistance and branch mean current during aging

current distribution in a parallel string is branch impedance change, however drift in cell OCV will also influence the current distribution. At SoL (Figure 6.21 a), branch 2 has a higher total resistance and therefore a higher peak current and greater total current throughput passes through B1. By EoL (Figure 6.21 c), increases to the impedance of B1 leads to an overall equalisation of branch resistance and therefore homogenises the current and SoC distribution observed. Whilst the branch resistance is not constant throughout a single discharge, Figure 6.21 d shows a simplified schematic representation of the cause and effects of resistance change in the homogeneous packs. Schematically represented is the start of discharge total branch resistance and the differing rates of branch resistance increase leading to homogenisation of currents.

Figure 6.22 in contrast shows a schematic representation of the effects of branch resistance growth in a heterogeneous temperature pack (in this case with a negative thermal gradient). In this case at SoL

(Figure 6.22 a), the elevated temperature of B1 leads to a greater difference in total branch resistance, and therefore a greater split in cell currents. However, due to the previously observed accelerated cell impedance growth at low temperatures (see Section 6.7), this effect is compounded over the life of the pack, as the total resistance of branch 2 grows faster than that of branch 1. Thus, by EoL (Figure 6.22 c), the mean current through branch 2 is reduced while branch 1 sees an increased mean current. Figure 6.22 d shows a schematic representation of this effect. At SoL (a), the difference in branch impedance is increased compared to the homogeneous temperature case, leading to a greater current split. During cycling the resistance growth of B2 is accelerated, leading to a greater difference in branch total impedance (c). By EoL, the branch resistances have significantly diverged, leading to an overall greater degree of heterogeneity.

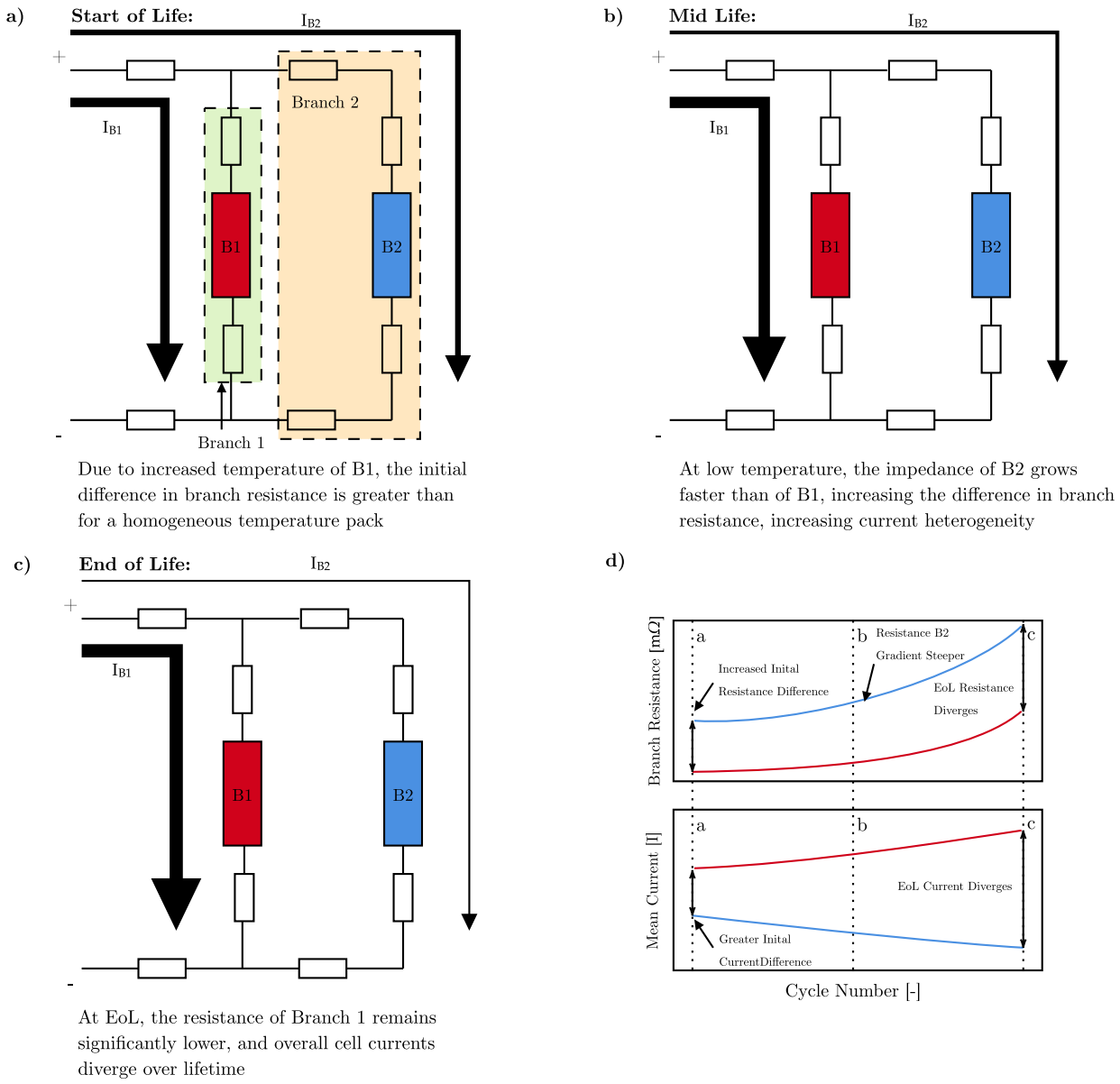


Figure 6.22: Schematic representation of heterogenisation of current distribution during aging in heterogeneous temperature packs. a) Start of life. b) Mid life. c) End of life. d) Schematic representation of total branch resistance and branch mean current during aging

An important note is that this expected behaviour is only valid for the interim temperatures studied (20-45 °C). These temperatures were selected to reflect the typical optimal temperature range for pack

operation, where significant SEI growth or Lithium plating may be avoided. EIS analysis has shown in Section 6.7 that below 40 °C, for the cell studied, SEI layer growth leading to resistance increases was minimal. It is expected that if the mean pack temperature was elevated further, SEI layer growth would dominate the overall cell impedance growth. As such, current and SoC distributions would converge during time, due to the greater impedance growth of the high temperature cell in the string. This highlights the importance of developing a holistic understanding of cell impedance growth over a range of interim temperature during design, in order to avoid inducing potentially hazardous current heterogeneities in aged packs.

6.9 Parallel String Cell Level Diagnostics

In order to further analyse the cell-level degradation observed during the pack cycling, and assess the contribution of various degradation modes to the overall loss of pack performance, OCV analysis was carried out on the 0.04 C reference discharge data obtained at each SoL and EoL for each cell to identify the dominant degradation modes occurring within each cell. For full details of the OCV analysis procedure and diagnostic model fitting are found in Section 4.4.4. Combined with identified degradation modes with both HPPC and EIS measurements, it is possible to diagnose the likely causes of degradation within the cells, and as a consequence identify the likely mechanisms underlying the degradation observed within the packs. In this Section the identified degradation modes are presented, whilst likely mechanisms are discussed in Section 6.10.

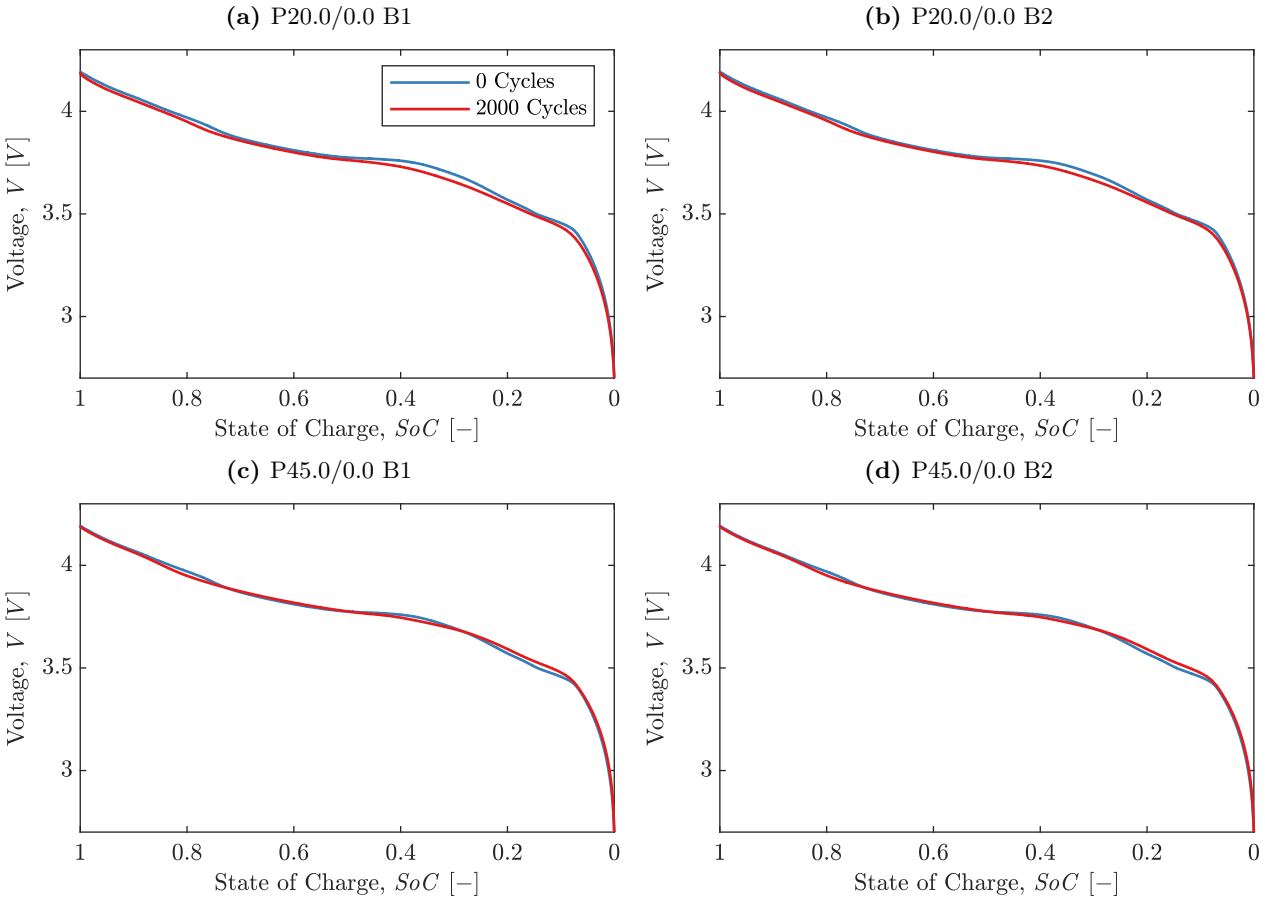


Figure 6.23: Example OCV measurements for P20.0/0.0 and P45.0/0.0 at SoL and EoL. a) P20.0/0.0 B1. b) P20.0/0.0 B2. c) P45.0/0.0 B1. d) P45.0/0.0 B2. All measurements taken at 20.0 °C and 0.04 C. Note that OCV is presented plotted against SoC.

Figure 6.23 a-d presents OCV curves at SoL and EoL for both cells in P20.0/0.0 and P45.0/0.0, which show examples of the change to the shape of the cell OCV response after 2000 cycles at both 20.0 and 45.0 °C. As shown, in the lower temperature (20.0 °C) cycled cells, a significant reduction in the cell OCV is observed at the location of the principal voltage plateau (at 3.75 V). Meanwhile, the SoC location of the principal plateau moves to higher SoC values. In contrast in the high temperature (45.0 °C) cycled cells, a limited reduction in the voltage of the principal plateau occurs. However, the SoC location of the principal plateau is shifted to lower SoC values in the higher temperature case. Contrasting the changes to the principal plateau shape and location, at low temperature the principal voltage plateau has reduced definition and is shifted to higher SoC values, indicative of loss of active cathode material within the cell. In contrast at high temperatures, the principal plateau definition and location is not changed as significantly, indicating that if loss of cathode material is occurring, this is combined with loss of lithium inventory which simultaneously changes the alignment of the electrodes.

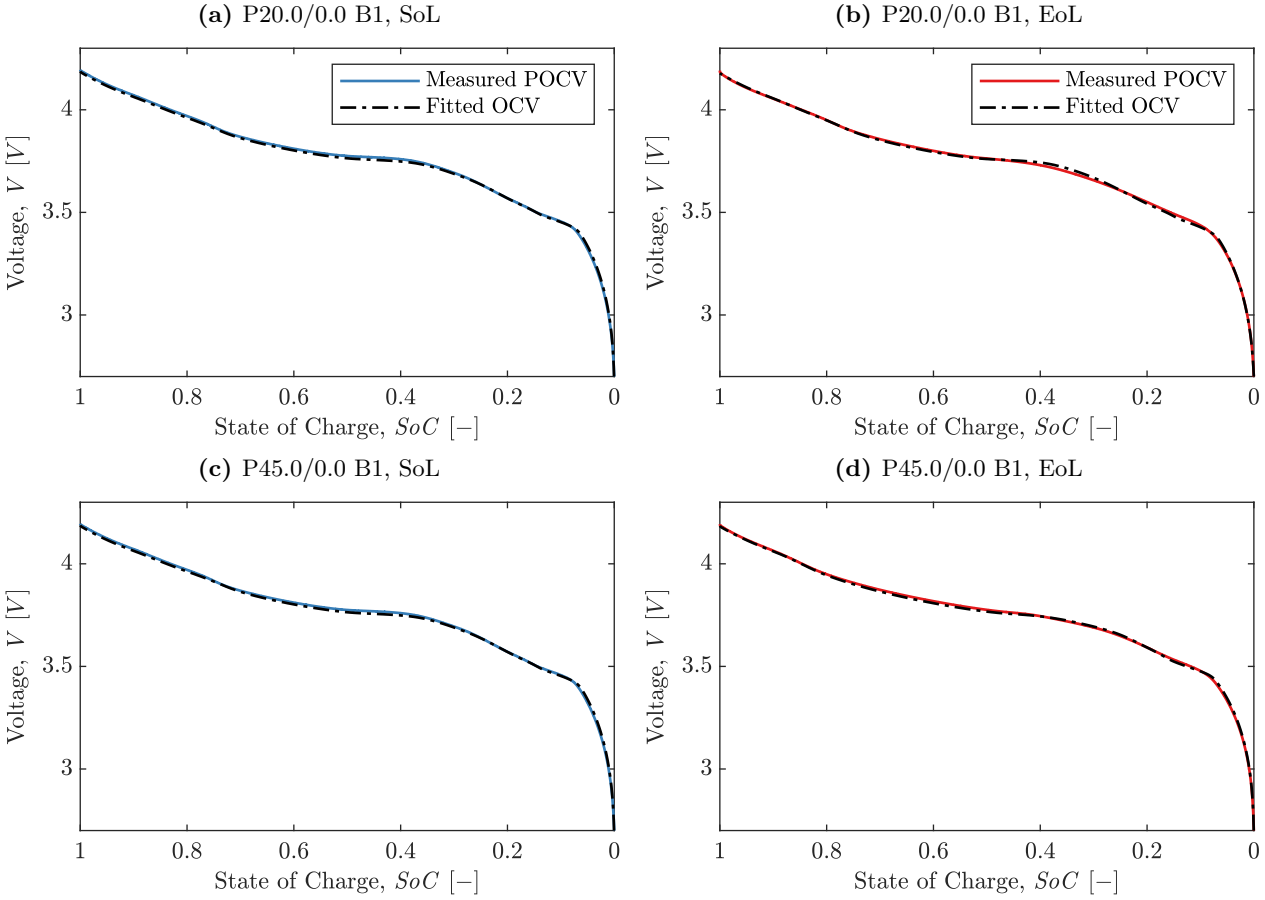


Figure 6.24: Example cell for P20.0/0.0 B1 and P45.0/0.0 B1 at SoL and EoL. a) P20.0/0.0 B1, SoL. b) P20.0/0.0 B1, EoL. c) P45.0/0.0 B1, SoL. d) P45.0/0.0 B1, EoL. All measurements taken at 20.0 °C and 0.04 C. Note that OCV is presented plotted against SoC, not capacity.

However, this analysis is qualitative, and using quantitative fitting of the cell OCV curve, it is possible to decouple the degree to which each degradation mode (LLI, $\mathrm{LAM_{An}}$ and $\mathrm{LAM_{Ca}}$) contribute to overall cell degradation. Example fits at SoL/EoL are shown in Figure 6.24 for B1 of P20.0/0.0 and P45.0/0.0, showing the high degree of fidelity of the OCV fitting model at both SoL and EoL. Considering the formal accuracy of the fitted OCV at SoL and EoL for each cell, which is shown in Figure 6.25 for all cycled cells, a RMSE error of <9 mV at SoL and <7 mV at EoL was achieved

by the model in all cases. As previously discussed in Section 4.4.4, errors in the OCV fit are likely due to the flat nature of the anode OCV curve. The voltage of graphite (the anode) versus lithiation in general does not significantly change over most graphite lithiation states, apart from during phase transitions occurring during graphite staging. As such changes to the shape of the anode curve (caused by LAM_{An} leading to a reduction in anode capacity) are more difficult for an OCV-type model to identify, which is a general limitation of the OCV fitting approach to cell degradation mode diagnosis. Nevertheless it is possible to sufficiently accurately identify degradation modes occurring within the cell using this approach.

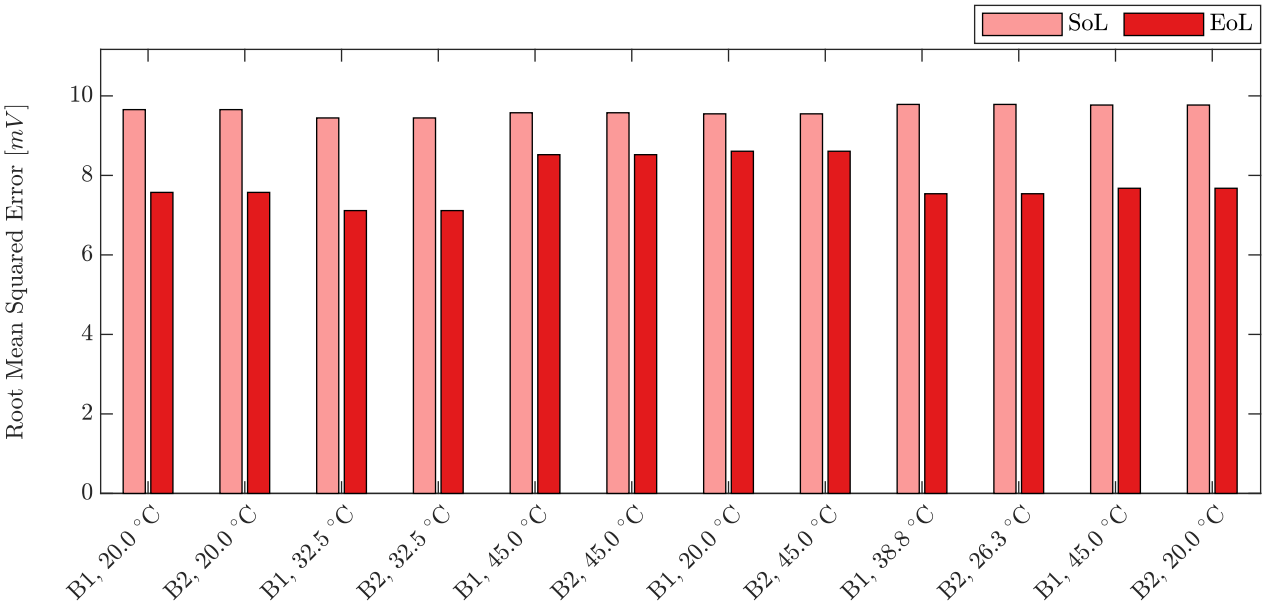


Figure 6.25: Root mean squared error for OCV fits for all cells.

Figure 6.26 shows the identified losses caused by each of the three identifiable degradation modes at EoL for each cell cycled. As can be seen in all cases the dominant degradation modes are LLI and LAM_{Ca}. LAM_{An} in general contributes a significantly smaller amount to the overall cell degradation. A clear trend may be observed, with the dominant degradation mode in all cells cycled at low temperature (<32.5 °C) being LAM_{Ca}, whilst at higher temperatures (>32.5 °C) LLI becomes the dominant degradation mode. At intermediate temperatures (32.5 °C) approximately equal amounts of LLI and LAM_{Ca} are observed. The degree of LLI is highly sensitive to temperature, as expected, ranging from 3.8 % LLI in P32.5/+25.0 B1 to 13.5 % LLI in P45.0/0.0 B1. Meanwhile increasing the cycling temperature leads to a more modest increase in loss of active material from both electrodes, with LAM_{Ca} increasing from 6.2 % in P32.5/+25.0 B1 to 10.1 % in P45.0/0.0 B1. The range of identified LAM_{An} was from 1.0 % in P45.0/0.0 B1 to 3.9 % in P32.5/-12.5 B1.

Figure 6.27 shows a clearer picture of how cell degradation modes change with respect to temperature. Figure 6.27 a shows the EoL SoH for each cell, and the EoL SoH ranges from 96 % to 86 %. As shown, the EoL SoH is well correlated with the cycling temperature, indicative of the dominance of temperature as a degradation stress factor. Considering the identified degradation modes with respect to temperature, as expected LLI is the dominant degradation mode at higher temperatures, and the amount of LLI identified is well correlated with temperature (Figure 6.27 b). Increasing temperature leads to increasing LLI, which is supported by the identified trends in R_{SEI} growth shown in Section 6.7 and corresponds to accelerated SEI layer growth at elevated temperatures, although LLI may also

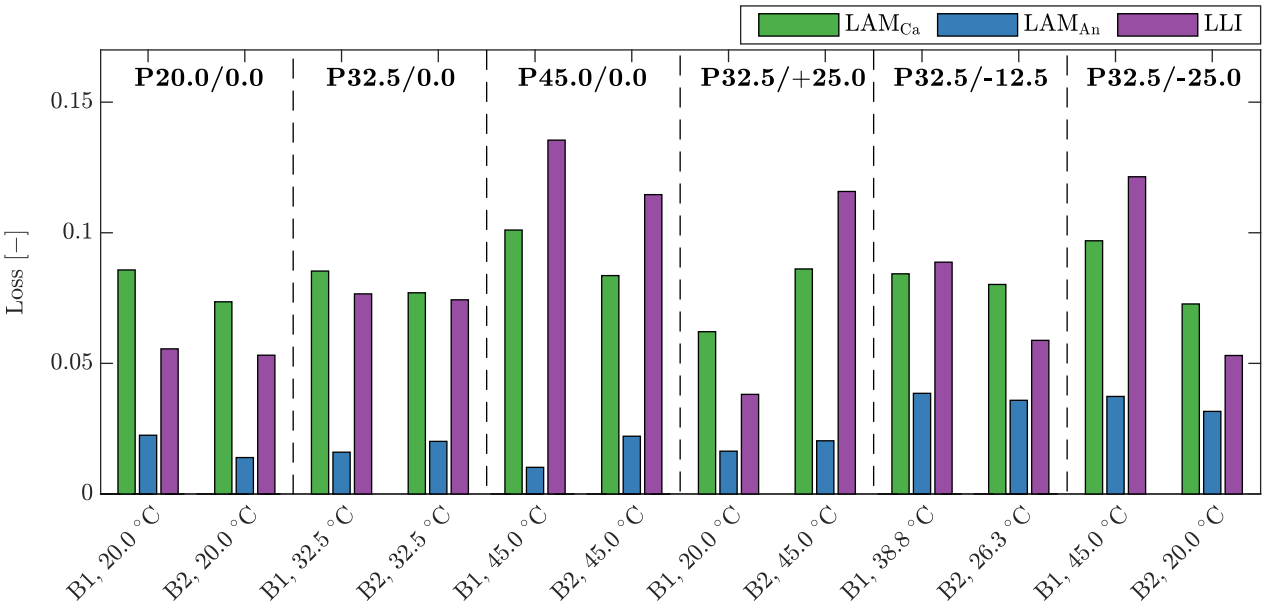


Figure 6.26: Fitted degradation modes identified using the OCV model for all cells

occur via loss of lithiated active material. However the OCV model is not capable of discrimination between loss of lithiated and delithiated active material.

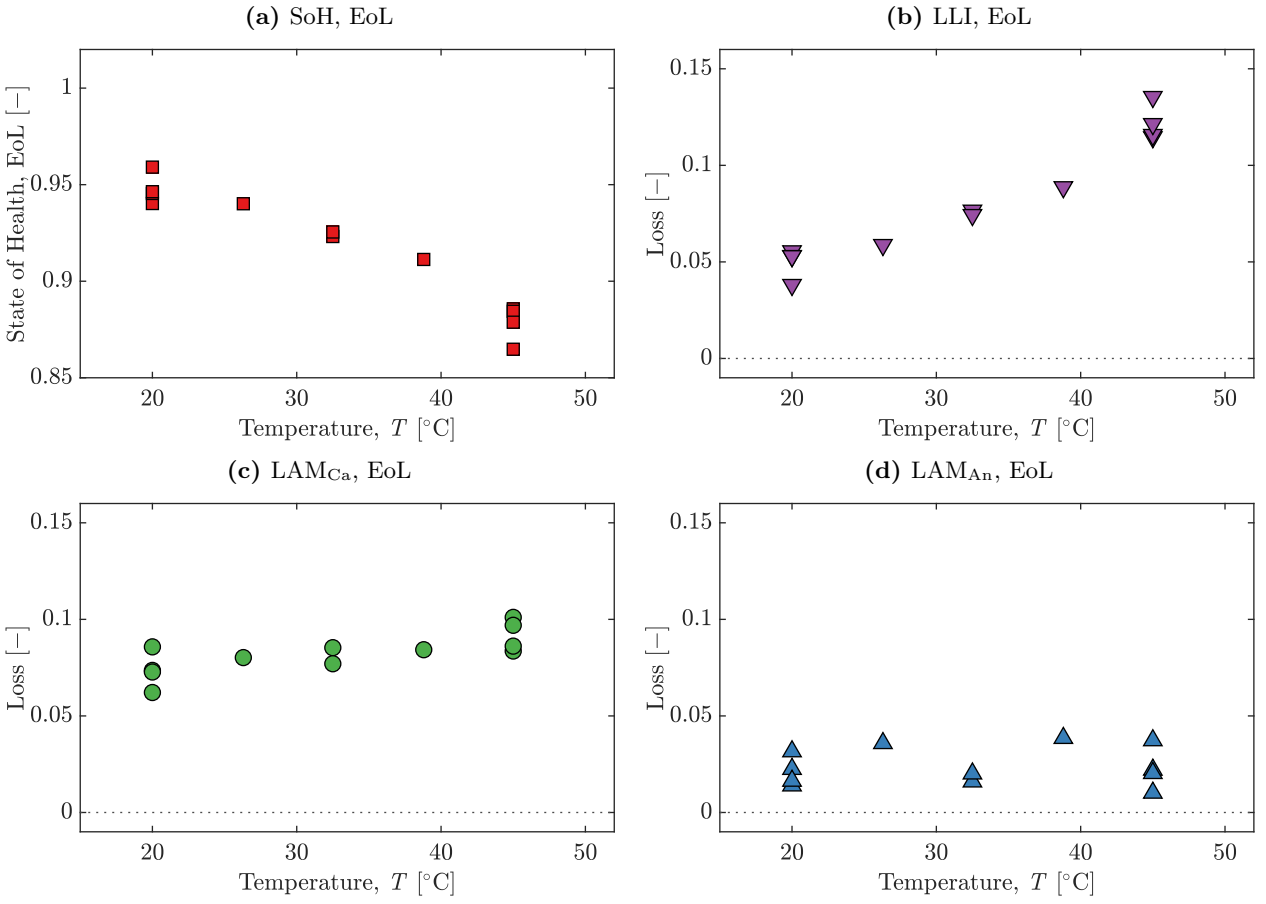


Figure 6.27: EoL SoH and identified degradation modes for all cells with respect to temperature. a) EoL SoH. b) EoL LLI. c) EoL LAM$_{Ca}$. d) EoL LAM$_{An}$.

Considering loss of active material in both electrodes, significantly more LAM$_{Ca}$ is observed than

LAM_{An} at all temperatures, with an insignificant correlation between the amount of LAM_{Ca}/LAM_{An} and temperature in all cases. However with increasing temperature the dominant degradation mode changes, with LAM_{Ca} dominant for temperatures of <32.5 °C, and LLI dominant at temperatures of >32.5 °C. In all cases the degree of LAM_{An} is significantly lower, and the contribution of LAM_{An} to overall cell degradation is limited. It is notable that in all packs cycled, the degree of LAM_{Ca} identified is greater in the cell experiencing higher peak currents, as identified in Section 6.8. This is indicative of higher peak currents leading to greater cathode damage, and is evident in the 3 packs cycled under homogeneous temperature conditions, where in all cases B1 experiences a higher degree of cathode damage. The greatest difference in the homogeneous temperature packs is found in P45.0/0.0, in which B1 experienced significantly higher peak currents at start of discharge during cycling than B2. This effect is discussed further in Section 6.10.

It is interesting to note that the EoL SoH of the cycled cells is well correlated with the degree of LLI, due to the initial electrode alignment (identified in Section 4.4.4). The initial excess electrode capacity and cell stoichiometry mean that loss of active material in both electrodes of the order identified does not lead to significant measurable loss of overall cell capacity. However LLI, which leads to changes in cell stoichiometry and thus electrode alignment, leads to significant changes to the accessible cell capacity. Increasing electrode slippage, caused by LLI, leads to immediately identifiable reductions in cell capacity, as this slippage limits the capacity of each electrode available over the constant cycling voltage range, and therefore LLI is the dominant cause of capacity loss during cycling. This effect can be explained by considering the effect of anode slippage versus the cathode. At SoL, the final rapid voltage drop seen in cell OCV below 10 % SoC is directly related to the rapidly increasing anode voltage at low anode litiation states. As the anode slips relative to the fixed cathode, the degree of anode lithiation is reduced for a given cathode lithiation. As such, even if both electrodes retain identical capacities, the amount of accessible capacity over the cell operating voltage window is reduced.

In order to provide independent evidence of the degradation mode identified via OCV fitting, a post-aging teardown of a single cell from each of the homogeneous packs (P20.0/0.0 and P45.0/0.0) was carried out. In both cases, B1 was selected for teardown, and an uncycled cell from the same batch was also disassembled to provide a reference baseline. In each case, the cell was opened in an Argon-filled glovebox, and the electrode stack unwound to reveal the electrodes. Electrodes were harvested from layers 1, 10, 20 and 25 (with 50 total anode/cathode pairs in the pack), and samples cut from the centre of the electrode. No qualitative morphological changes were observed in the electrodes through-thickness, while no significant morphological changes were observed in the harvested anodes compared to the baseline, supporting the previously identified limited anode loss of active material. Washing of the harvested anodes and limitations to the magnification of the instrument used meant it is not possible to assess the degree of SEI layer formation (which would lead to LLI) based on this postmortem.

Figure 6.28 presents scanning electron microscopy images obtained from samples at the centre of the cathodes. In Figure 6.28 a and b, for the uncycled cathode, two particle morphologies are observed. The cathode consists of spherical agglomerate particles (NMC) consisting of fine angular particles mixed with layered and faceted grain particles (LCO). Figure 6.28 c and d show the cathode from P20.0/0.0 B1, and cracks are highlighted in both particle morphologies. Highlighted feature 1 (Figure

6.28 c) shows intragranular cracks in the faceted particles, extending both through and in the layer planes. Feature 2 also shows evidence of crack formation in the agglomerate particles, while in other locations pit-holes and pulverisation of the agglomerates is observed. In the lower magnification image (Figure 6.28 d), deposition of debris, likely lost cathode material, is highlighted as feature 3. Considering P45.0/0.0 B1 (Figure 6.28 e and f), pit-holes and pulverisation of the agglomerate particles is also observed (feature 4), whilst fracture also occurred in the faceted morphology particles (feature 5). Deposition of debris in the binder is also observed in the low-magnification images (feature 6). This debris is likely lost active material from the cathode electrode particles, released during particle fracture and pulverisation. As this postmortem analysis is only able to qualitatively identify electrode morphological damage, it is not possible to qualitatively assess the relative amount of loss of cathode active material in each case. However, qualitatively, no significant differences were observed between harvested cathodes from cells cycled at low and high temperatures, supporting the results from OCV fitting that the amount of cathode active material loss is relatively independent of the cycling temperature.

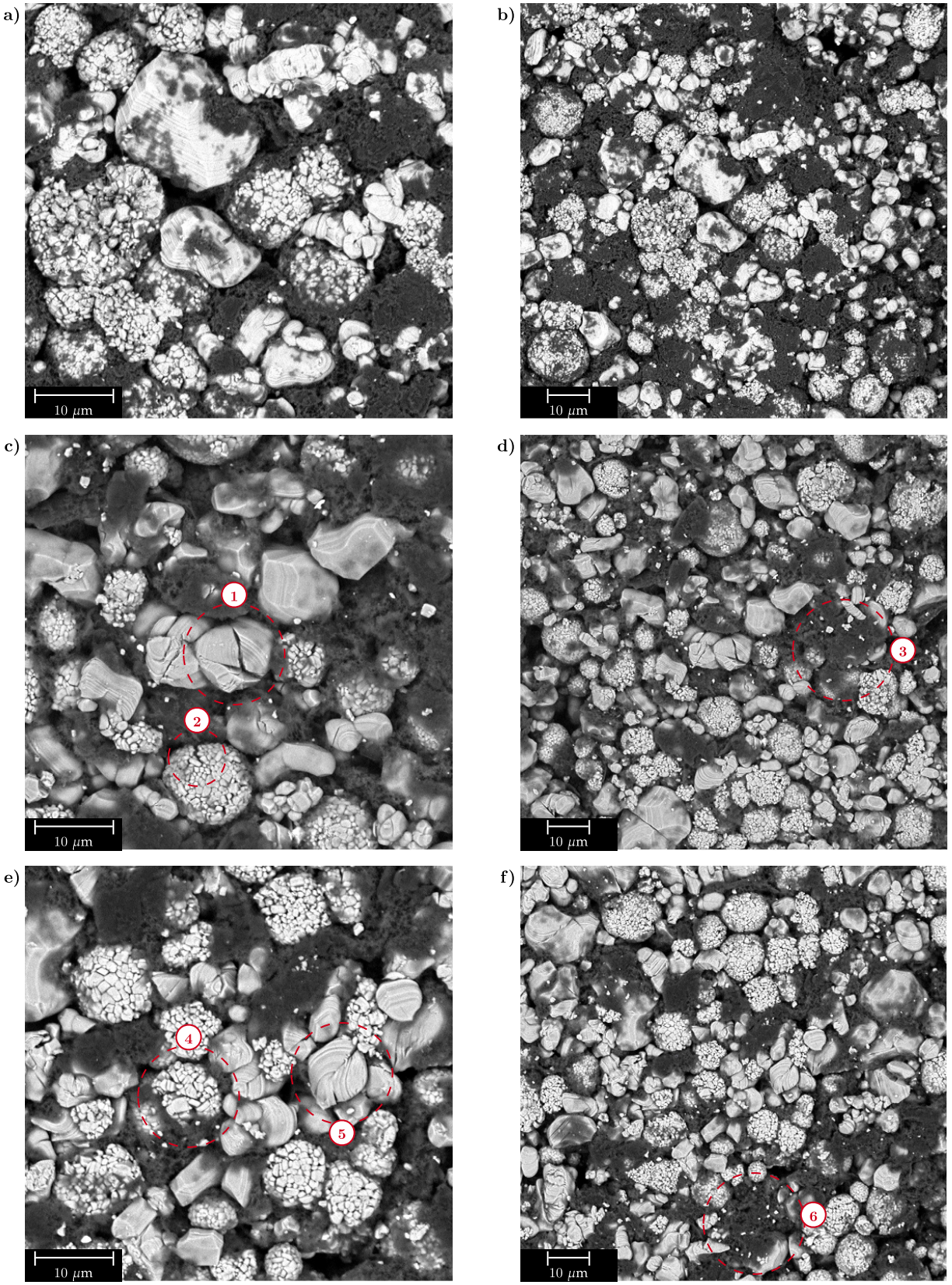


Figure 6.28: SEM images of cathodes from fresh and cycled cells, with features highlighted. All samples taken from the centre of cathode No. 25 (centre of electrode stack). 20 °C cycled cell selected is P20.0/0.0 B1, 45 °C cycled cell selected was P45.0/0.0 B1 a) Fresh cathode. b) Fresh cathode (low magnification). c) Cathode cycled at 20 °C. d) Cathode cycled at 20 °C. (low magnification). e) Cathode cycled at 45 °C. f) Cathode cycled at 45 °C. (low magnification). Highlighted features: 1) Fracture in LCO particle. 2) Fracture in NMC particle. 3) Debris deposited in binder. 4) Damage to NMC particle. 5) Fracture of LCO particle. 6) Debris deposited in binder.

6.10 Discussion and Proposed Degradation Mechanisms

Briefly recapping, the aims of this study were to a) identify the effects of thermal gradients and temperature conditions on parallel string lifetime, b) identify and explain the effects of thermal conditions on heterogeneity over the lifetime of parallel cell strings and c) draw generalised conclusions regarding best practice for parallel pack or module design. This discussion aims to draw conclusions regarding the underlying mechanisms leading to the heterogeneous behaviour during aging shown in Sections 6.6-6.9.

Considering the lifetime behaviour of the packs, in the homogeneous temperature cases, convergence of cell performance and operating conditions was observed. This was attributed to the increasingly heterogeneous resistance growth in the cells leading to a balancing of branch currents and therefore reducing the degree of current heterogeneity. In comparison, in the packs cycled under heterogeneous temperatures, i.e. thermal gradients, a divergence in cell operating conditions and cell performance was observed. This divergent current behaviour was caused by two principal factors, the first being the divergent cell impedance growth eliminating the rebalancing effects seen in the homogeneous temperature packs and the second being increasingly differing cell capacities.

Within packs with applied thermal gradients, at SoL there is initially a significant mismatch between branch resistances, due to the decreased cell impedance at elevated temperatures. Subsequently during aging, greater impedance growth is observed in the low temperature cells. In conjunction with the slower cell impedance growth in the elevated temperature cells, increasingly unequal branch resistances occur during operation. As a consequence, the behaviour of the packs under thermal gradients were observed to become more heterogeneous over cycling, with greater SoC deficits and consequently reduced accessible capacity. These deficits in turn lead to higher mean SoCs at the lower cutoff voltage in low temperature cells and reduced depths of discharge. While with the 5 Ah Kokam cells used, this did not lead to significant heterogeneous degradation, this would be a concern if a cell is more sensitive to the depth of discharge. Additionally, restricted depths of discharge within high SoC ranges may also accelerate degradation, due to the cell spending prolonged periods at high voltages. In the homogeneous cases, SoC deficits were also observed to increase but convergently, due to the increased cell impedances leading to increasingly rapid reaching of voltage limits due to increased cell overpotentials. The second principal cause of divergence in the heterogeneous packs was the diverging rates of cell capacity loss, induced by temperature differences, which induce a mismatch in cell voltages during discharge and consequently drive string currents through the low-resistance cells in the string.

When considering the underlying causes of the differential impedance growth and capacity loss, a parametric OCV model was quantitatively applied to identify the degradation modes promoted by the different operating conditions, revealing the underlying degradation modes leading to capacity loss in the cycled packs. In all cases, limited loss of active anode material was identified, with loss of active cathode and lithium inventory instead the dominant modes for all cells. In all cells a balance of $\mathrm{LAM_{Ca}}$ and LLI are observed. It is notable that for both $\mathrm{LAM_{Ca}}$ and $\mathrm{LAM_{An}}$ there is a limited correlation between the degree of each mode and temperature, indicating that the amount of each mode occurring is not significantly related to temperature under the pack operating regime (over the temperature range studied). However, this does not eliminate the possibility that the underlying mechanism leading to the degree of LAM changes with increasing or decreasing cell cycling temperature.

At the lower temperatures studies (<32.5 °C), the balance of LAM_{Ca} to LLI is biased in favour of LAM_{Ca}, with 6.1-8.5 % LAM_{Ca} identified in comparison to 3.7-5.3 % LLI in cell cycled at 20 °C. In comparison at higher temperatures (>32.5 °C), this balance is reversed with a greater degree of LLI than LAM_{Ca}, with 11.4-13.5 % LLI identified in comparison to 8.6-10.5 LAM_{Ca} at 45 °C. In the cells cycled at intermediate temperature (32.5 °C) there is a remarkably similar balance of LAM_{Ca} and LLI (7.5-8.0 % of both modes for both cells cycled at 32.5 °C). Further details of these results are presented in Section 6.9.

It is notable that the degree of capacity loss in all cells is well-correlated with the degree of LLI identified, which is expected as whilst LLI will lead to an immediate capacity loss in the cell due to the induced changes in stoichiometry. LAM_{An}/LAM_{Ca} will not lead to a loss of capacity until the excess anode or cathode present at SoL is consumed, and in the case of the cells cycled in this study the amount of LAM in both electrodes is smaller than the excess electrode available at SoL. Note that LAM in both cases may lead to a loss of accessible energy, due to the reduction in cell OCV induced, however this effect is expected to be relatively small.

Recapping the underlying mechanisms which can lead to LAM_{CA}, Birkl et al. [25] comprehensively reviewed and identified cause and effect chains leading to LAM_{CA}, and these can be broadly grouped as follows; firstly, fracture of electrode particles due to volumetric changes during cycling may lead to loss of active material through 'islanding' of areas of cathode particles, while binder decomposition may lead to loss of particle electrical contact and isolation of areas of the electrode, again reducing the amount of electrochemically active cathode available. Particle fracture in the cathode may be exacerbated by high temperatures which lead to high thermal stresses, although temperatures in this study are unlikely to significantly exacerbate this effect [214]. High current densities may also exacerbate particle fracturing, particularly at the electrode-separator interface [45], [46], [215]. However, improved conductivity in the electrolyte may offset this effect at higher temperatures, as improved diffusion kinetics within the electrolyte will reduce concentration gradients through-electrode, and therefore reduce local reaction current densities in the active particles. Consequently, peak stresses in the active particles will be reduced. As a layered metal oxide, the NMC particles may be considered a ceramic-type material, and as a consequence are more liable to fracture under tensile rather than compressive stresses, which are induced during deintercalation i.e. charging of the cathode. Particle fracture may in turn lead to loss of particle electrical contact due to fracture, whilst binder decomposition may lead to isolation of particles from the electrode electrical network, in effect removing the particle. While LAM caused by particle fracture is generally considered to primarily lead to capacity loss, electrical contact losses may also lead to increased resistances [216], [217].

Finally, direct damage to the cathode active material may lead to LAM_{CA} through dissolution of transition metals from the cathode, structural disordering of the cathode or via passivation through p-SEI formation. These mechanisms will lead to loss of electrochemically active sites and consequently capacity loss, and are all accelerated by increased temperature. Transition metal dissolution may occur through electrochemical oxidation of oxygen within the layered cathode [49], whilst nickel at high oxidation states may react when exposed to electrolyte, leading to Ni^{2+} becoming dissolved in the electrolyte and being deposited on the surface of both electrodes [38]. This deposition may further accelerate SEI layer growth at the anode. Meanwhile, as the electrolyte is typically fluoride containing, acid attack caused by hydrofluoric acid formed due to residual moisture may also dissolve transition

metal ions from the cathode [41]. All of the aforementioned mechanisms in turn will lead to LAM_{CA}. Dissolution of transition metal ions into the electrolyte may in turn lead to side-reactions occurring between the electrolyte and transition metal ions, and consequent deposition of precipitates on the surface of the cathode, forming a p-SEI (or CEI) layer in a similar manner to SEI layer formation at the anode surface [52].

Structural disordering or phase change of layered NMC cathodes occurs when the layered structure decomposes in disordered spinel and rock salt phases. This effect occurs at the particle surface, leading to passivation of the particle [38]. The formation of the disordered spinel and rock salt phases is more favourable in delithiated cathode material [39]. Structural changes in NMC particles have been shown to be unlikely to occur during delithiation, due to the higher potential of the $Co^{3+/4+}$ redox couple than that of the $Ni^{3+/4+}$ redox couple [41], [218]. This implies that if structural disordering is a dominant mechanism of cathode damage, it will be observed to occur principally during discharge of the cell (i.e. during cathode lithiation). Increased cathode charge transfer resistances will be observed after significant cathode phase changes, due to the slower ion exchange kinetics through the passivated surface and reduction in the availability of electrochemically active sites. Recent work by Dose et al. [219] indicated that increasing the full cell upper cutoff voltage above 4.1 V in an NMC811 cell led to significant and non-linear increases in both impedance growth and capacity loss rate. The upper cutoff potential is linked to accelerated transition metal dissolution, surface phase change and particle cracking, and therefore anode slippage may also contribute to the overall non-linear accelerated impedance rise at lower temperatures. This work implies that reduced depths of discharge at high SoC (and therefore increased average cell voltages) may lead to accelerated cathode damage and degradation.

Having considered the underlying degradation mechanisms that commonly occur within LIBs, it is useful to next consider the links between these mechanisms and degradation modes (which may be observed through OCV model-based diagnostics, such as presented in Section 6.9. Edge et al. [218] provide a comprehensive review of the state-of-the-art understanding of the links between modes and mechanisms for LIBs, summarised in Figure 6.29. Distinction is made between primary and secondary mechanisms, modes and cell-level effects, and due to the *in-situ* diagnostics applied in this work, main consideration is given to identification of primary mechanisms, as further detailed post-mortem analysis would be required to identify specific secondary mechanisms. Considering the interplay between degradation mechanisms, modes and effects, relevant information to this study may be summarised as follows;

- LLI may be caused by loss of lithiated active material in the anode or cathode (due to particle fracture), SEI/p-SEI layer formation (transition metal dissolution from the cathode may lead to deposition of transition metals on the anode, accelerating SEI layer growth), irreversible lithium plating at the anode, or Ni-Li site exchange (structural damage) in the cathode.

- Loss of active material in the anode may be caused by 'islanding' of areas of the anode, graphite exfoliation and electrolyte decomposition and loss.

- Loss of active material in the cathode may be caused by 'islanding' of areas of the cathode, Ni-Li site exchange and electrolyte decomposition and loss.

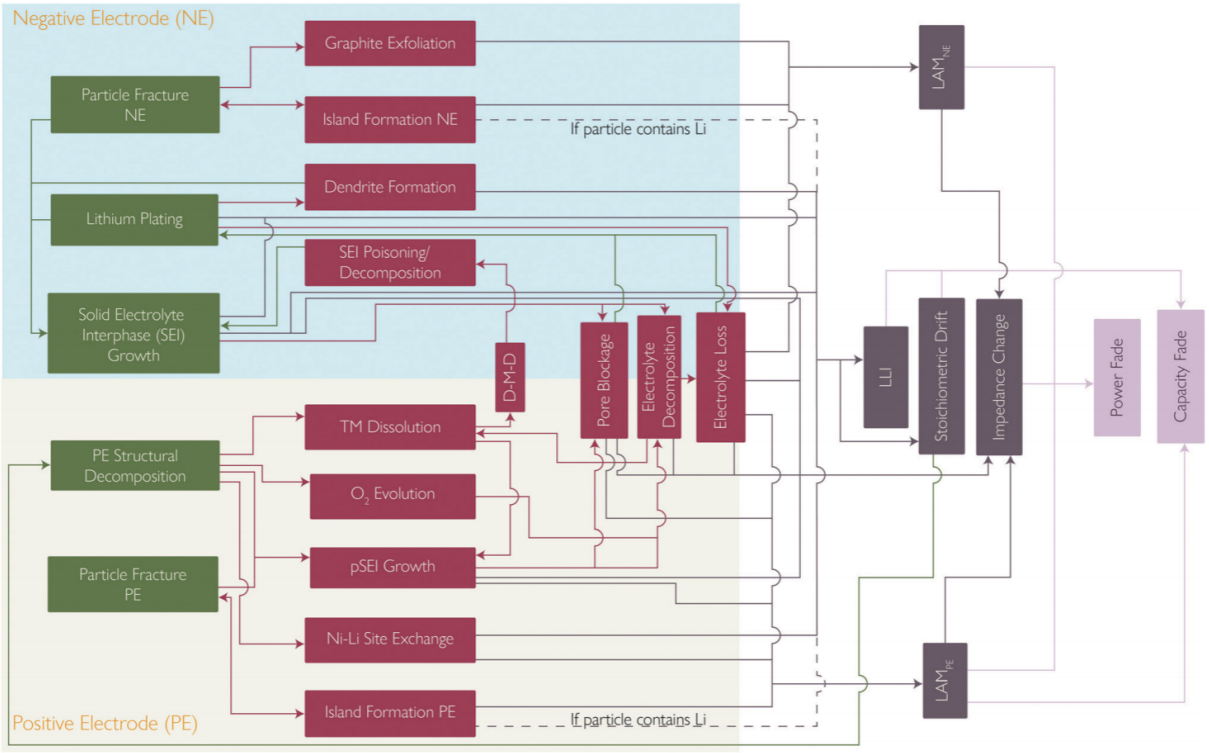


Figure 6.29: The complex interplay between the primary and secondary mechanisms explained in this review, showing how each contributes to a degradation. Distinction is made between primary and secondary degradation mechanisms, modes and consequences at the cell level [218]. CC-BY 3.0

- Impedance change may be caused by pore blockage at either electrode or loss of active material in either electrode (which leads to a reduction in overall active surface area and consequently greater impedance.

Having considered the mechanisms that may lead to the principal observed cathode degradation modes, suggested mechanisms leading to the behaviour observed in this study are proposed. Reviewing the principal identified degradation mechanisms identified in the cycled packs (Section 6.9), LAM_{Ca} was found to be the dominant mechanism at low (20 °C) temperature, whilst LLI was the dominant mechanism at high (45 °C) temperature for all cells. It is notable that similar amounts of LAM_{Ca} are observed in cells cycled over the full study temperature range, with a minimal positive correlation with temperature. While the Kokam 5 Ah is a blended cathode, NMC makes up the bulk of the cathode and so is considered the dominant particle type for discussion. It is important to note that in reality, most degradation modes considered will occur to some degree during cell cycling – the aim of this work is to identify the dominant mechanisms and how the dominant mechanism changes with respect to cycling conditions.

First considering mechanisms in the low temperature aged cells, it is proposed that the dominant LAM_{Ca} degradation mode is principally caused by accelerated particle fracture and consequent pulverisation of cathode particles. This mechanism may be summarised as follows:

- Close to the separator-cathode interface, local current densities are high due to concentration gradients through plane in the electrode. At low temperature, with slower kinetics and reduced charge carrier mobility, these concentration profiles may be steeper through-plane.

- Slow kinetics and reduced charge carrier mobility leads to preferential deintercalation from cathode particles close to the cathode-separator interface, and therefore increased local current densities. Consequently, higher tensile stresses are induced, and particle fracture occurs, leading to loss of active cathode via pulverisation and 'islanding' of sections of cathode particles.

- As the particles close to the separator are depleted, this process is progressively repeated through the electrode. Pulverisation of the cathode and consequent loss of electrochemically active sites at the cathode-separator interface will lead to increased R_{CT}, especially at low temperatures where it is kinetically less favourable to access particles deeper into the electrode.

As a consequence of fracture, active material in the cathode becomes 'islanded' and disconnected from the electrode electrical network, rendering areas of the electrode electrochemically inactive. As a secondary consequence of this process, the active area of the cathode is reduced, leading to an overall increase in cathode R_{CT}. Mechanical damage to cathode particles has been observed to lead to accelerated impedance growth at lower temperatures [93]. LLI also occurs in the low temperature aged cells, but to a lower degree than in higher temperature cycled cells. LAM_{Ca} may also occur as a consequence of cathode structural damage via Ni-Li site exchange or electrolyte loss, but neither of these mechanisms lead directly to accelerated impedance growth, leading to these mechanisms being less likely to be dominant at low temperature. Considering the rapid growth in cathode R_{CT} at low temperature it is most likely that the key underlying degradation mechanism in the low temperature cycled cells is cathode particle fracture, with a degree of SEI layer formation leading to LLI.

In comparison to the low temperature cells, the high temperature cells were shown to experience dominant LLI, with similar degrees of LAM_{Ca} to the low temperature cells. SEI layer growth has been shown to be highly positively correlated with cycling temperature, as increased temperatures accelerate the unwanted side reactions which lead to formation of the SEI. Therefore, it is likely that the significantly increased amount of LLI identified in the high temperature cells is caused by SEI layer formation and growth, induced by the elevated temperatures. However, a similar amount of LAM_{Ca} is identified in the high temperature cycled cells, but without an associated significant increase in cathode R_{CT} identified using EIS and HPPC measurements. This is notable and indicative of a change in the underlying mechanism leading to the observed LAM_{Ca} in the higher temperature cells when compared to the cells cycled at low temperature. In all cells, generally between 8-11 % LAM_{Ca} is identified using OCV fitting.

It is important to again note that these competing mechanisms at low and high temperature are likely occurring simultaneously to differing degrees, with the dominant mechanism gradually shifting as temperature increases. Indeed, post-mortem teardown images of cathodes cycled at elevated temperature (see Section 6.9 clearly show evidence of particle fracture. However by careful consideration of all the diagnostic evidence available (EIS, HPPC, OCV fitting and post-mortem imaging) it is possible to identify the most likely mechanisms underpinning degradation at all temperatures. Despite this, it is critical to consider that these conclusions are reached via indirect observations of cells in-situ, and therefore more detailed chemical post-mortem would be required to conclusively prove that the proposed mechanisms are indeed occurring.

Overall, the above mechanisms are proposed to explain the observed behaviour of the cycled cells within the 6 packs tested. Generally, SEI layer growth has been considered to be the dominant mech-

anism for capacity loss and impedance growth, while lithium plating is considered a principal cause of safety concerns. However, this study identifies cathode degradation as the dominant degradation mode present at interim temperatures (20.0-32.5 °C) which would generally be considered in a 'safe' operating temperature range. Whilst LAM_{Ca} is measured at all temperatures studied, within the range of the study significant changes to the fundamental cell capacity due to LAM_{Ca} do not occur, due to the initial excess cathode present. If the study had continued to lower cell states of health, it would be expected that LAM_{Ca} would lead to significant changes to fundamental cell capacity, once the initial excess cathode was consumed. However, LAM_{Ca} leads to significant changes to cell kinetic performance, with significantly greater growth in cathode R_{CT} at lower temperatures. This increasing cathode polarisation leads to a loss in accessible cell capacity and is typically not considered. As a consequence, the need to consider cathode degradation in detail when selecting pack designs and operating modes is highlighted by this work. It is noted that while the mechanisms previously proposed are supported based on EIS, HPPC and OCV diagnostic measurements taken during pack cycling, more detailed post-mortem analysis of cycled cells is required to conclusively demonstrate the underlying mechanisms leading to cathode damage.

6.11 Conclusion

In this chapter, a comprehensive study of the effects of thermal gradients and temperature changes on the degradation of parallel strings has been presented, including a detailed examination of the development of heterogeneous currents within the studied packs. Additionally, detailed diagnostics were obtained at the single cell level by disassembling the parallel strings throughout their lifetime. This allowed comprehensive examination of the degradation modes occurring within the cells during cycling, and association these modes with both suggested underlying mechanisms and stress factors.

It was found that there were significant differences in static and dynamic capacity loss rates within homogeneous packs, with lower temperature cycled packs losing performance significantly more rapidly than those cycled at higher temperatures. This highlights the advantages of increased operating temperatures on instantaneous pack performance, due to the increased cell impedance at low temperature leading to increased SoC deficits at EoD. Conversely the low temperature cycled packs exhibited minimal static capacity loss. OCV diagnostic analysis identified this behaviour as a consequence of the degradation modes induced by the cycling temperature. Whilst at both high and low temperatures significant degradation was caused by loss of active material in the cathode, at high temperatures the degree of loss of lithium inventory was greater than the loss of active material in the cathode.

Due to the excess cathode present at SoL, LAM_{Ca} did not lead to appreciable capacity fade at the cell level at the levels identified. This explained the differences in measured static capacity loss between the temperatures, despite the similar overall total loss of active cathode material. If pack aging had continued, it is expected that LAM_{Ca} would eventually lead to considerable capacity fade once the excess cathode is consumed. It is proposed that the greater increases in cell impedance seen at low temperatures were caused by particle fracture and pulverisation due to high peak currents leading to an overall loss in electrochemically active cathode surface area. Meanwhile the loss of cathode active material at high temperature is more likely caused by structural damage to the cathode, accelerated by high temperatures. This proposed mechanism would explain the similar levels of cathode degradation observed at all temperatures, whilst also accounting for the different rates of growth of cathode charge

transfer resistance observed at high and low temperatures.

Considering the impacts of cell level capacity loss and impedance growth on heterogeneous behaviour within the cell strings, it was found that in the homogeneous temperature cases the current distribution converged over lifetime. This effect was due to heterogeneous impedance growth in the parallel strings, likely induced by differential peak currents, with greater peak currents observed in the cells closest to the string terminals. As a consequence, over the 2000 cycles applied, current heterogeneities were almost eliminated in the 20.0 °C string, while due to the lower apparent cell impedance and therefore greater influence of the interconnection resistances, significant heterogeneity remained in the 45.0 °C cycled string albeit with decreasing magnitude over life. In comparison, in the strings exposed to large thermal gradients, divergence of the cell current distribution over time was observed. This was attributed to the differential impedance growth between the low and high temperature cells within the string reinforcing the initially different apparent branch impedances.

Due to the accelerated impedance growth in the lower temperature cells in the heterogeneous packs, the already higher apparent cell impedance led to increasing SoC deficits between cells during cycling. As a consequence, the current distributions observed increased in heterogeneity, whilst dynamic performance was lost when compared to the reference case at the same mean temperature. This is a significant conclusion, as typically impedance growth would be assumed by pack designers to increase at high temperature. However, in this study growth in impedance at low temperature of the NMC-111 cathode has been shown to drive growing heterogeneities within parallel connected strings, with cells considered in the optimal pack temperature range of 15-35 °C [129], [131] experiencing significant cathode-driven impedance growth. This effectively blocks access to capacity in the low temperature cells in the string, increasing the EoD SoC deficit and ultimately leading to decreased performance over life, even when cell-level capacity loss is relatively minimal. It is noted that this effect will be more pronounced at higher C-rates, as at low rate increased impedance growth smaller EoD SoC deficits will be observed despite increased impedance growth. Therefore, while minimum operating temperatures up to now have typically been set to avoid the onset of Lithium plating, consideration of interim-temperature cathode impedance growth is needed to reduce avoidable performance loss over life. This also highlights the need for pack designers to holistically consider cell-level degradation effects during specification development and thermal management design.

Whilst this study aimed to provide a comprehensive overview of degradation within parallel cell strings, some limitations remain. For example, only constant current rather than constant power or drive cycled operating conditions were considered under a single current rate. Cell temperatures were maintained via surface cooling and held independently. It is known that surface cooling leads to accelerated cell degradation when compared to tab cooling, whilst in real battery packs cell temperature is likely to be coupled rather than independent due to limitations in thermal management. Additionally, only a single topology was investigated with limited parallelisation. As a consequence, future work is suggested to include:

- Further investigation of the impedance growth properties of NMC cathode cells at low temperature, and integration of these effects into pack level degradation modelling.
- Investigation of the effects of constant power or drive cycle loading conditions on lifetime when compared to constant current loading.

- Investigation of the effects of different cooling strategies, for example tab cooling, and scenarios when cell temperatures are coupled as opposed to independent.
- Further modelling of the effects of applied rate, charging strategy and topology on heterogeneity development and lifetime.
- Parameterisation of an empirical or semi-empirical degradation model with the aim of carrying out a full sensitivity study of the above parameters.

Application of significant thermal gradients to the packs led to loss of both instantaneous and lifetime performance compared to homogeneous temperature packs at the same mean temperature, highlighting the need to design for minimisation of thermal gradients. This effect is likely non-linear, with a -12.5 °C thermal gradient leading to a 10 % increase in dynamic capacity loss compared to a 27 % increase with a -25 °C thermal gradient applied at the same mean temperature. However further experimental investigation or modelling would be required to conclusively demonstrate non-linearity. As most systems will have thermal gradients, due to practical limitations in thermal management, the need to minimise and consider the direction of the resultant thermal gradient is highlighted. In terms of heterogeneous current behaviour, it was shown that negative thermal gradients led to significant increases in both peak currents and greater heterogeneity over life, and therefore design for positive thermal gradients is preferable, especially in cases where this is a low cost design choice (for example by selecting the direction of air or coolant flow). It was also shown that decreasing the (negative) thermal gradient by 50 % led to a 66 % reduction in mean current difference and a 25 % reduction in peak current, highlighting both the non-linear effects of increasing thermal gradients and therefore the importance of minimising thermal gradients to reduce safety concerns and prolong pack lifetime.

In general, this work provides insights into the behaviour of parallel cell strings over lifetime. It has been shown that increasing parallel string temperatures over the temperature range studied is advantageous due to decreasing inaccessible capacity, albeit at the cost of an increased influence of the interconnection impedance on current distributions and accelerated capacity loss. Nevertheless, it is clear that operating at lower temperatures has significant costs in performance terms despite reduced degradation rates. In general, it is therefore preferable to operate at interim temperatures to maximise performance while retaining cell capacity over life.

Chapter 7

Conclusions and Future Work

The aim of this work was to improve the understanding of both performance loss and aging within parallel connected LIB packs and explore the effects of pack-level heterogeneities in both cases. In the case of aging it was intended to perform a detailed study of aging within parallel-connected LIBs. In doing so it was necessary to develop tools to both experimentally control pack thermal boundary conditions and diagnose degradation modes within cells. Whilst the many permutations of both pack topology and thermal boundaries are possible, by investigation of two model systems, a 1S2P and 1S6P pack, underpinning insights in dynamic behaviour has been created which allows for the conclusions of this work to translate into other system configurations. Summary conclusions of the work presented in this thesis and their relationship to the initial research questions (Chapter 1) are as follows.

Experimental Tools and Models Developed

The main experimental tools developed, two pack test benches, were instrumental in underpinning the investigations in this work by allowing controlled experimental studies to be carried out. The models developed allowed detailed investigation of both the coupling between different causes of heterogeneity and identification of degradation modes within aged cells, allowing definition of a mechanistic model to describe the effects experimentally observed. Summarising the conclusions of this work in brief:

- Review of the existing academic literature has shown that test benches for controlling thermal boundary conditions at the pack level are seldom seen and often do not control individual cell temperatures [145], [163], [164], [168]. The repercussion of this is that conclusions from pack level studies in the literature are highly dependent on their thermal boundary conditions and thus results in inconsistent findings. Therefore, a test bench was developed to carry out long-term aging experiments on 6 1S2P parallel connected LIB packs. Additionally, a separate test bench was developed for use in investigation of the instantaneous performance of a 1S6P pack.
- Review of the existing literature shows a multitude of diagnostic models for identification of degradation modes within LIBs, however quantitative models are still limited, especially in the context of pack level studies. Therefore, a quantitative fitting tool was implemented, based on work by Birkl et al, [25], [87] to identify degradation modes within LIBs by tracking changes to the cell OCV over the lifetime of LIBs. This model uses a relatively simple parameterisation procedure, using half cell OCV curves to identify electrode capacities and stoichiometry at SoL.

The model was shown to be sufficiently accurate to identify dominant degradation modes (LLI, LAM_{An}, LAM_{Ca}) when validated using synthetic data generated using the OCV model operating in 'forward' mode.

- Whilst many detailed models for use in battery packs are available, a simple 1-RC ECN model was selected to investigate the effects of thermal and resistive heterogeneities within parallel connected LIBs. The model was validated in comparison to experimentally derived current and SoC distributions for a 1S6P pack and shown to be sufficiently accurate to simulate pack-level behaviour. When applied to the 1S6P pack studied, the model was able to predict individual cell current throughput with a maximum of $\pm$ 1 % error, and overall pack capacity with a maximum of $\pm$ 0.2 % error.

The Effects of Heterogeneities on Pack Performance:

Through a combination of experimental and modelling studies presented in Chapter 5, it was possible to develop understanding of the causal links coupling resistive and thermal heterogeneities within parallel connected LIBs, alongside the underlying causes of performance loss when moving from single cells to full packs. Summarising the conclusions of this work in brief:

- Review of the academic literature showed that instantaneous performance loss within parallel connected LIBs may be attributed to many possible heterogeneous effects within a pack, including cell-to-cell variations [162], [180], resistance heterogeneities [9], [139], [159] and thermal gradients [9], [163], [164], [168]. Whilst the effects of cell-to-cell variations have been explored in some detail, as have resistive variations, the effects of thermal gradients on performance have not been well explored. Additionally, experimental studies are often limited in providing underpinning insights and controllability to allow translation across different pack architectures, providing motivation for this work.

- Using the 1S6P test case, experimental measurements and simulations explored the impacts of thermal gradients on instantaneous performance within parallel-connected LIBs configured in both a U- and Z-topology. This analysis identified the SoC deficit at EoD as the principal cause of reduced capacity in parallel connected cell strings compared to the sum of the capacities of the naked cells. When under load, current heterogeneities lead to significant SoC distributions building within parallel strings, and as a consequence non-linear cell impedance changes lead to eventual SoC deficits at EoD/EoC. While both interconnection overpotentials and the cell OCV profile contribute to heterogeneous behaviour, the cell impedance was found to be the dominant cause.

- The orientation of a thermal gradient relative to the electrical topology of parallel connected cells was shown to have significant impacts on the instantaneous performance of a parallel connected pack, with reversal of a Δ25 °C thermal gradient in a U-topology pack leading to a 1.6 % increase in pack accessible capacity under a CC load while reducing heterogeneities in cell current and SoC. This effect is caused by non-linear cell impedance changes either balancing or unbalancing branch resistances, dependant on thermal gradient direction. Therefore, during design, consideration should be made for orientation of the TMS relative to the electrical topology of the pack.

- Meanwhile it was found that the impacts of parasitic resistances on overall pack performance increased at higher temperatures, due to the increased IRR with lower cell impedance, leading to more heterogeneous current and SoC distributions. Therefore at higher temperatures the impacts of interconnection overpotentials are more significant. Additionally it was shown that under fault conditions, the impacts of any fault leading to increased interconnection or branch resistance are highly location dependant. Additional consideration should also be taken regarding the magnitude of interconnection resistances and pack topology to maximise performance.

- Comparing the U- and Z- topology, experimental investigation and simulations showed that in general the Z-topology is less sensitive to thermal and resistive heterogeneities, however at the cost of marginally reduced capacity due to increased branch resistance losses. In the Z-topology case, interconnection overpotentials are more balanced, leading to less heterogeneous current and SoC distributions. If a U-topology is required, the importance of maintaining consistent branch resistances further from the terminals is highlighted, as these branches have an increased impact on overall performance.

The Effects of Thermal Heterogeneities on Cell and Pack Lifetime

A key motivation of this work was to link pack level heterogeneities to degradation mechanisms occuring within cells of packs, and their influence on overall lifetime and behaviour. The lifetime study presented in Chapter 6 combined with the diagnostic model developed allowed linking of pack level thermal heterogeneities to cell level degradation modes, and enabled the proposal of a mechanistic model explaining their causal links. Summarising the conclusions of this work in brief:

- A review of the literature showed that the aging trajectory of parallel connected LIBs is not well explored. Within a pack, convergent rates of capacity loss and power fade is desirable, as divergent capacity or power fade will lead to accelerated loss of overall performance. However the literature is contradictory over whether induced heterogeneities will lead to convergent [171], [212] or divergent [9], [149], [152], [185], aging. Whilst the literature study indicated that thermal heterogeneities lead to divergent aging, detailed analysis of induced degradation modes via thermal heterogeneities are lacking alongside comprehensive experimental analysis, providing the motivation for this work.

- Aging of packs under controlled thermal gradients comprehensively demonstrated divergent aging under applied thermal gradients, with potential non-linear increases in divergent aging with increasing thermal gradients. The direction of the applied thermal gradient did not have a significant impact on either degradation rate or divergence, however in more highly parallelised systems, directionality is likely to be significant.

- Heterogeneous current distributions over the lifetime of the cycled packs were tracked, and it was shown that under homogeneous thermal conditions, cell currents are convergent. However, application of thermal gradients led to divergent cell current distributions. Detailed analysis of resistance growth within the packs showed that in the heterogeneous temperature packs, differing degradation modes within the cells occured, leading to divergent cell impedance growth and consequently more heterogeneous current distributions. In contrast, in the homogeneous

temperature packs, convergent impedance growth led to increasingly homogeneous current distributions.

- Under the temperature range studied (20-45 °C), cell impedance growth was measured at SoL and EoL using EIS, and tracked throughout the life of each cell using HPPC measurements. The growth in charge transfer resistance was found to be negatively correlated with temperature. The dominant resistance growth was in the charge transfer resistance, which for NMC cells has been shown to be dominated by the cathode charge transfer resistance. Under the operating temperatures studied, SEI layer growth was less significant, highlighting the need for consideration of cathode power fade even at 'safe' intermediate temperatures.
- Identification of degradation modes present within the cycled cells using the diagnostic model developed indicated a switch in dominant degradation mode from LAM_{Ca} at low temperature to LLI at high temperatures. Similar degrees of LAM_{Ca} are identified at all temperatures. It is proposed that LAM_{Ca} at low temperatures was principally caused by particle fracture, due to high local current densities at the cathode-separator interface. At lower temperatures, slowed solid and liquid phase diffusion lead to increased concentration gradients within electrode particles, and therefore higher tensile stresses leading to fracture. Meanwhile it is proposed that LAM_{Ca} at higher temperatures was caused by structural damage in the cathode particles, explaining the differences in rate of growth of cathode charge transfer resistance. However, further materials-level characterisation would be required to confirm these proposed mechanisms.
- Finally, a comprehensive dataset was experimentally obtained for a model 1S2P system aged to relatively high cycle numbers under a range of thermal boundary conditions. This dataset included comprehensive characterisation of both the packs and individual cells at 17 breakpoints over 2000 full DoD cycles. It is believed this dataset is unique in the literature and will be made available to other researchers for both pack and diagnostic model validation.

The contents of this thesis therefore present a comprehensive study investigating the effects of a range of heterogeneities on parallel connected LIB performance and aging. The underpinning insights generated thus have the potential to be translated into other battery pack architectures. Key contributions include the description of the root cause of convergent and divergent cell lifetime behaviour under homogeneous and heterogeneous thermal conditions. Mechanistic diagnostics of the cell performance allowed for the conclusion that, within the intermediate temperature range studied, that the cathode polarisation resistance dynamics are the key factor. This is a conclusion which has thus far been overlooked in the battery pack literature and serves as motivation for future modelling studies.

7.1 Future Work

Within the time constraints of the 3-year funded PhD project the author feels that significant progress has been made in improving the understanding heterogeneities within parallel connected LIBs, particularly during aging under heterogeneous temperature. However there remain some areas open to explore which were not possible to visit in detail during the project, as follows:

- **Degradation Modelling** – Whilst the ECN model used was a useful tool to predict instantaneous performance loss, it was not possible to fully parameterise a degradation model to use

alongside the ECN model, due to time and equipment constraints. The literature surrounding parallel string heterogeneities would benefit from detailed sensitivity studies carried out using computationally inexpensive models, with the aim of providing guidelines to pack designers. Whilst cathode polarisation resistance increases were experimentally identified as a major cause of heterogeneity, few models can effectively describe these effects. Therefore, physics-based models describing cathode degradation effects would be highly beneficial for further improving the understanding of heterogeneous operating conditions within packs.

- **Series Connected Cells** – Within this project, series connected LIBs were not investigated due to equipment limitations. However, investigation of the effects of heterogeneities on aging within series or mixed series-parallel connected LIB packs would be highly beneficial to industry. The framework provided by the test benches developed would be suitable for carrying out this future work with minimal modifications.

- **Load Cycles during Aging** – Due to time constraints, it was not possible to repeat pack aging tests under alternative loading conditions to CC. However, investigation of aging processes induced under constant power or realistic load cycles is highly recommended to identify the effects of heterogeneities on aging rates.

- **Impedance Growth within NMC Cathode Cells** – Further investigation of the temperature dependence of impedance growth within NMC cathode cells is warranted. The experimental study presented in Chapter 6 concluded that the temperature correlation of cathode impedance growth is critical to how ongoing heterogeneous current distributions develop within parallel connected cells and should be considered at the design stage when selecting operating temperatures for parallelised packs.

Bibliography

[1] M. Li, J. Lu, Z. Chen, and K. Amine, "30 Years of Lithium-Ion Batteries," *Advanced Materials*, vol. 30, no. 33, Aug. 2018, ISSN: 15214095. DOI: 10.1002/adma.201800561. [Online]. Available: https://onlinelibrary.wiley.com/doi/full/10.1002/adma.201800561%20https://onlinelibrary.wiley.com/doi/abs/10.1002/adma.201800561%20https://onlinelibrary.wiley.com/doi/10.1002/adma.201800561.

[2] K. Mizushima, P. C. Jones, P. J. Wiseman, and J. B. Goodenough, "LixCoO2 (0¡x¡-1): A new cathode material for batteries of high energy density," *Materials Research Bulletin*, vol. 15, no. 6, pp. 783–789, Jun. 1980, ISSN: 00255408. DOI: 10.1016/0025-5408(80)90012-4.

[3] M. Colin, A. Izadi-Najafabadi, A. O'Donovan, N. Albanese, N. Soulopolous, D. Doherty, M. Boers, R. Fisher, C. Cantor, J. Frith, S. Mi, and A. Grant, "BloombergNEF: Electric Vehicle Outlook 2020," BloombergNEF, Tech. Rep., 2020.

[4] J. Rickard, "Tesla Model 3: Battery Cell Internals and Disassembly," Electric Vehicle TV, Tech. Rep., 2019.

[5] R. A. Meyers (ed), *Batteries for Sustainability: Selected Entries from the Encyclopedia of Sustainability Science and Technology*. Springer Science+Business Media New York, 2012. DOI: 10.1007/978-1-4614-5791-6_2.

[6] J. Xiao, Q. Li, Y. Bi, M. Cai, B. Dunn, T. Glossmann, J. Liu, T. Osaka, R. Sugiura, B. Wu, J. Yang, J. G. Zhang, and M. S. Whittingham, "Understanding and applying coulombic efficiency in lithium metal batteries," *Nature Energy*, vol. 5, no. 8, pp. 561–568, Aug. 2020, ISSN: 20587546. DOI: 10.1038/s41560-020-0648-z. [Online]. Available: https://doi.org/10.1038/s41560-020-0648-z.

[7] A. Barai, K. Uddin, M. Dubarry, L. Somerville, A. McGordon, P. Jennings, and I. Bloom, "A comparison of methodologies for the non-invasive characterisation of commercial Li-ion cells," *Progress in Energy and Combustion Science*, vol. 72, pp. 1–31, May 2019, ISSN: 03601285. DOI: 10.1016/j.pecs.2019.01.001. [Online]. Available: https://www.sciencedirect.com/science/article/pii/S0360128518300996.

[8] V. Ruiz and F. Persio, *Standards for the Performance and Durability Assessment of Electric Vehicle Batteries - Possible Performance Criteria for an Ecodesign Regulation*. Joint Research Centre, European Commission, 2018, p. 68, ISBN: 978-92-79-94179-5. DOI: 10.2760/24743.

[9] X. Liu, W. Ai, M. Naylor Marlow, Y. Patel, and B. Wu, "The effect of cell-to-cell variations and thermal gradients on the performance and degradation of lithium-ion battery packs," *Applied Energy*, vol. 248, no. March, pp. 489–499, Aug. 2019, ISSN: 03062619. DOI: 10.1016/j.apenergy.2019.04.108. [Online]. Available: https://linkinghub.elsevier.com/retrieve/pii/S0306261919307810%20https://doi.org/10.1016/j.apenergy.2019.04.108.

[10] T. Bruen and J. Marco, "Modelling and experimental evaluation of parallel connected lithium ion cells for an electric vehicle battery system," *Journal of Power Sources*, vol. 310, pp. 91–101, 2016, ISSN: 03787753. DOI: 10.1016/j.jpowsour.2016.01.001. [Online]. Available: http://dx.doi.org/10.1016/j.jpowsour.2016.01.001.

[11] B. Lu, Y. Song, Q. Zhang, J. Pan, Y. T. Cheng, and J. Zhang, "Voltage hysteresis of lithium ion batteries caused by mechanical stress," *Physical Chemistry Chemical Physics*, vol. 18, no. 6, pp. 4721–4727, Feb. 2016, ISSN: 14639076. DOI: 10.1039/c5cp06179b. [Online]. Available: www.rsc.org/pccp.

[12] M. P. Mercer, C. Peng, C. Soares, H. E. Hoster, and D. Kramer, "Voltage hysteresis during lithiation/delithiation of graphite associated with meta-stable carbon stackings," *Journal of Materials Chemistry A*, vol. 9, no. 1, pp. 492–504, Jan. 2021, ISSN: 2050-7488. DOI: 10.1039/d0ta10403e. [Online]. Available: https://pubs.rsc.org/en/content/articlehtml/2021/ta/d0ta10403e%20https://pubs.rsc.org/en/content/articlelanding/2021/ta/d0ta10403e.

[13] V. Ruiz and F. Di Persio, "SAE J1798: Recommended practice for performance rating of electric vehicle battery modules," SAE International, Tech. Rep., 2008, p. 16.

[14] A. Lasia, *Electrochemical Impedance Spectroscopy and its Applications*. Springer Science+Business Media New York, 1999, vol. 1, pp. 271–292, ISBN: 978-1-4614-8932-0. DOI: 10.1007/978-1-4614-8933-7.

[15] E. Barsoukov and J. R. Macdonald, "Impedance Spectroscopy Theory, Experiment, and Applications," *Journal of Applied Electrochemistry*, vol. 125, p. 571, 2005, ISSN: 0013-4686. DOI: 10.1016/j.snb.2007.02.003. [Online]. Available: http://dx.doi.org/10.1016/j.electacta.2013.07.057.

[16] D. Linden and T. B. Reddy, *Handbook of Batteries: Fourth Edition*. McGraw Hill, 2011, ISBN: 5856420187. DOI: 10.5860/choice.33-2144.

[17] J.-P. Diard, B. L. Gorrec, and C. Montella, "Handbook of Electrochemical Impedance Spectroscopy - Diffusion Impedances," BioLogic, Tech. Rep. January, 2012, p. 30. DOI: 10.1017/CBO9781107415324.004. arXiv: arXiv:1011.1669v3. [Online]. Available: http://www.bio-logic.info/potentiostat-electrochemistry-ec-lab/apps-literature/eis-literature/hanbook-of-eis/.

[18] H. Leduc, R. Okamura, E. Kyeyune-Nyombi, K. Huynh, and S. Chung, "Real-Time Under-Load Electrochemical Impedance Spectroscopy (EIS) Analysis and Modeling," *ECS Meeting Abstracts*, vol. MA2020-02, no. 20, pp. 1584–1584, Nov. 2020, ISSN: 2151-2043. DOI: 10.1149/ma2020-02201584mtgabs. [Online]. Available: https://iopscience.iop.org/article/10.1149/MA2020-02201584mtgabs.

[19] W. Waag, S. Käbitz, and D. U. Sauer, "Experimental investigation of the lithium-ion battery impedance characteristic at various conditions and aging states and its influence on the application," *Applied Energy*, vol. 102, pp. 885–897, Feb. 2013, ISSN: 03062619. DOI: 10.1016/j.apenergy.2012.09.030. arXiv: 1605.05787. [Online]. Available: http://dx.doi.org/10.1016/j.apenergy.2012.09.030.

[20] BSI, *BS12405-2: 2012, electrically propelled road vehicles–test specification for lithium-ion traction battery packs and systems; part 2: High energy applications,"*, 2012.

[21] L. Gao, R. Dougal, S. Liu, and I. Introduction, "Active power sharing in hybrid battery/capacitor power sources," *Eighteenth Annual IEEE Applied Power Electronics Conference and Exposition, 2003. APEC '03.*, vol. 1, pp. 497–503, 2003. DOI: 10.1109/APEC.2003.1179259.

[22] J. R. Belt, "Battery Test Manual For Plug-In Hybrid Electric Vehicles," Laboratory, Idaho National, Tech. Rep., 2010. DOI: doi:10.2172/991910. arXiv: EXT-14-32849 [INL].

[23] R. Jackey, M. Saginaw, P. Sanghvi, J. Gazzarri, T. Huria, M. Ceraolo, and U. Pisa, "Battery Model Parameter Estimation Using a Layered Technique : An Example Using a Lithium Iron Phosphate Cell Pulse Tests to Measure Dynamic," *SAE International*, 2018. DOI: 10.4271/2013-01-1547.

[24] J. Vetter, P. Novák, M. R. Wagner, C. Veit, K. C. Möller, J. O. Besenhard, M. Winter, M. Wohlfahrt-Mehrens, C. Vogler, and A. Hammouche, "Ageing mechanisms in lithium-ion batteries," *Journal of Power Sources*, vol. 147, no. 1-2, pp. 269–281, Sep. 2005, ISSN: 03787753. DOI: 10.1016/j.jpowsour.2005.01.006.

[25] C. R. Birkl, M. R. Roberts, E. Mcturk, P. G. Bruce, and D. A. Howey, "Degradation diagnostics for lithium ion cells," *Journal of Power Sources*, vol. 341, pp. 373–386, Feb. 2017, ISSN: 0378-7753. DOI: 10.1016/j.jpowsour.2016.12.011. [Online]. Available: http://dx.doi.org/10.1016/j.jpowsour.2016.12.011.

[26] P. B. Balbuena and Y. Wang, *Lithium-Ion Batteries: Solid-electrolyte Interphase*. Imperial College Press, May 2004, p. 424, ISBN: 1860943624. DOI: 10.1142/p291. [Online]. Available: https://www.worldscientific.com/worldscibooks/10.1142/p291.

[27] E. Peled, "Advanced Model for Solid Electrolyte Interphase Electrodes in Liquid and Polymer Electrolytes," *Journal of The Electrochemical Society*, vol. 144, no. 8, p. L208, 1997, ISSN: 00134651. DOI: 10.1149/1.1837858. arXiv: arXiv:1011.1669v3. [Online]. Available: http://jes.ecsdl.org/cgi/doi/10.1149/1.1837858.

[28] P. Verma, P. Maire, and P. Novák, "A review of the features and analyses of the solid electrolyte interphase in Li-ion batteries," *Electrochimica Acta*, vol. 55, no. 22, pp. 6332–6341, Sep. 2010, ISSN: 00134686. DOI: 10.1016/j.electacta.2010.05.072.

[29] T. Waldmann, M. Wilka, M. Kasper, M. Fleischhammer, and M. Wohlfahrt-Mehrens, "Temperature dependent ageing mechanisms in Lithium-ion batteries - A Post-Mortem study," *Journal of Power Sources*, vol. 262, pp. 129–135, Sep. 2014, ISSN: 03787753. DOI: 10.1016/j.jpowsour.2014.03.112.

[30] A. Eddahech, O. Briat, E. Woirgard, and J. M. Vinassa, "Remaining useful life prediction of lithium batteries in calendar ageing for automotive applications," *Microelectronics Reliability*, vol. 52, no. 9-10, pp. 2438–2442, Sep. 2012, ISSN: 00262714. DOI: 10.1016/j.microrel.2012.06.085.

[31] S. Käbitz, J. B. Gerschler, M. Ecker, Y. Yurdagel, B. Emmermacher, D. André, T. Mitsch, and D. U. Sauer, "Cycle and calendar life study of a graphite—LiNi1/3Mn 1/3Co1/3O2 Li-ion high energy system. Part A: Full cell characterization," *Journal of Power Sources*, vol. 239, pp. 572–583, Oct. 2013, ISSN: 03787753. DOI: 10.1016/j.jpowsour.2013.03.045.

[32] D. Aurbach, "Review of selected electrode-solution interactions which determine the performance of Li and Li ion batteries," *Journal of Power Sources*, vol. 89, no. 2, pp. 206–218, Aug. 2000, ISSN: 03787753. DOI: 10.1016/S0378-7753(00)00431-6.

[33] S. S. Zhang, "A review on electrolyte additives for lithium-ion batteries," *Journal of Power Sources*, vol. 162, no. 2 SPEC. ISS. Pp. 1379–1394, Nov. 2006, ISSN: 03787753. DOI: 10.1016/j.jpowsour.2006.07.074.

[34] K. Xu, "Electrolytes and interphases in Li-ion batteries and beyond," *Chemical Reviews*, vol. 114, no. 23, pp. 11 503–11 618, Dec. 2014, ISSN: 15206890. DOI: 10.1021/cr500003w. [Online]. Available: https://pubs.acs.org/sharingguidelines.

[35] J. N. Zhang, Q. Li, Y. Wang, J. Zheng, X. Yu, and H. Li, "Dynamic evolution of cathode electrolyte interphase (CEI) on high voltage LiCoO2 cathode and its interaction with Li anode," *Energy Storage Materials*, vol. 14, pp. 1–7, Sep. 2018, ISSN: 24058297. DOI: 10.1016/j.ensm.2018.02.016.

[36] Y. Qian, P. Niehoff, M. Börner, M. Grützke, X. Mönnighoff, P. Behrends, S. Nowak, M. Winter, and F. M. Schappacher, "Influence of electrolyte additives on the cathode electrolyte interphase (CEI) formation on LiNi1/3Mn1/3Co1/3O2 in half cells with Li metal counter electrode," *Journal of Power Sources*, vol. 329, pp. 31–40, Oct. 2016, ISSN: 03787753. DOI: 10.1016/j.jpowsour.2016.08.023.

[37] D. L. Wood, J. Li, and S. J. An, "Formation Challenges of Lithium-Ion Battery Manufacturing," *Joule*, vol. 3, no. 12, pp. 2884–2888, Dec. 2019, ISSN: 25424351. DOI: 10.1016/j.joule.2019.11.002.

[38] R. Jung, M. Metzger, F. Maglia, C. Stinner, and H. A. Gasteiger, "Oxygen Release and Its Effect on the Cycling Stability of LiNi x Mn y Co z O 2 (NMC) Cathode Materials for Li-Ion Batteries," *Journal of The Electrochemical Society*, vol. 164, no. 7, A1361–A1377, 2017, ISSN: 0013-4651. DOI: 10.1149/2.0021707jes.

[39] M. D. Radin, S. Hy, M. Sina, C. Fang, H. Liu, J. Vinckeviciute, M. Zhang, M. S. Whittingham, Y. S. Meng, and A. Van der Ven, "Narrowing the Gap between Theoretical and Practical Capacities in Li-Ion Layered Oxide Cathode Materials," *Advanced Energy Materials*, vol. 7, no. 20, pp. 1–33, 2017, ISSN: 16146840. DOI: 10.1002/aenm.201602888.

[40] F. Lin, I. M. Markus, M. M. Doeff, and H. L. Xin, "Chemical and structural stability of lithium-ion battery electrode materials under electron beam," *Scientific Reports*, vol. 4, pp. 1–6, 2014, ISSN: 20452322. DOI: 10.1038/srep05694.

[41] E. Zhao, L. Fang, M. Chen, D. Chen, Q. Huang, Z. Hu, Q. B. Yan, M. Wu, and X. Xiao, "New insight into Li/Ni disorder in layered cathode materials for lithium ion batteries: A joint study of neutron diffraction, electrochemical kinetic analysis and first-principles calculations," *Journal of Materials Chemistry A*, vol. 5, no. 4, pp. 1679–1686, 2017, ISSN: 20507496. DOI: 10.1039/c6ta08448f.

[42] Y. Zhao, F. B. Spingler, Y. Patel, G. J. Offer, and A. Jossen, "Localized Swelling Inhomogeneity Detection in Lithium Ion Cells Using Multi-Dimensional Laser Scanning," *Journal of The Electrochemical Society*, vol. 166, no. 2, A27–A34, Jan. 2019, ISSN: 0013-4651. DOI: 10.1149/2.0011902jes. [Online]. Available: https://iopscience.iop.org/article/10.1149/2.0011902jes%20https://iopscience.iop.org/article/10.1149/2.0011902jes/meta.

[43] K. Takahashi and V. Srinivasan, "Examination of Graphite Particle Cracking as a Failure Mode in Lithium-Ion Batteries: A Model-Experimental Study," *Journal of The Electrochemical Society*, vol. 162, no. 4, A635–A645, Jan. 2015, ISSN: 0013-4651. DOI: 10.1149/2.0281504jes. [Online]. Available: https://iopscience.iop.org/article/10.1149/2.0281504jes%20https://iopscience.iop.org/article/10.1149/2.0281504jes/meta.

[44] P. Yan, J. Zheng, M. Gu, J. Xiao, J. G. Zhang, and C. M. Wang, "Intragranular cracking as a critical barrier for high-voltage usage of layer-structured cathode for lithium-ion batteries," *Nature Communications*, vol. 8, no. 1, pp. 1–9, Jan. 2017, ISSN: 20411723. DOI: 10.1038/ncomms14101. [Online]. Available: www.nature.com/naturecommunications.

[45] J. Christensen, "Modeling Diffusion-Induced Stress in Li-Ion Cells with Porous Electrodes," *Journal of The Electrochemical Society*, vol. 157, no. 3, A366, Feb. 2010, ISSN: 00134651. DOI: 10.1149/1.3269995. [Online]. Available: https://iopscience.iop.org/article/10.1149/1.3269995%20https://iopscience.iop.org/article/10.1149/1.3269995/meta.

[46] W. Ai, L. Kraft, J. Sturm, A. Jossen, and B. Wu, "Electrochemical Thermal-Mechanical Modelling of Stress Inhomogeneity in Lithium-Ion Pouch Cells," *Journal of The Electrochemical Society*, vol. 167, no. 1, p. 013 512, Oct. 2020, ISSN: 0013-4651. DOI: 10.1149/2.0122001jes. [Online]. Available: https://iopscience.iop.org/article/10.1149/2.0122001JES%20https://iopscience.iop.org/article/10.1149/2.0122001JES/meta.

[47] A. Tomaszewska, Z. Chu, X. Feng, S. O'Kane, X. Liu, J. Chen, C. Ji, E. Endler, R. Li, L. Liu, Y. Li, S. Zheng, S. Vetterlein, M. Gao, J. Du, M. Parkes, M. Ouyang, M. Marinescu, G. Offer, and B. Wu, "Lithium-ion battery fast charging: A review," *eTransportation*, vol. 1, p. 100 011, Aug. 2019, ISSN: 25901168. DOI: 10.1016/j.etran.2019.100011. [Online]. Available: https://www.sciencedirect.com/science/article/pii/S2590116819300116%7B%5C#%7Dbib34.

[48] S. Santhanagopalan, P. Ramadass, and J. (Zhang, "Analysis of internal short-circuit in a lithium ion cell," *Journal of Power Sources*, vol. 194, no. 1, pp. 550–557, Oct. 2009, ISSN: 03787753. DOI: 10.1016/j.jpowsour.2009.05.002.

[49] E. Billy, M. Joulié, R. Laucournet, A. Boulineau, E. De Vito, and D. Meyer, "Dissolution Mechanisms of LiNi1/3Mn1/3Co1/3O2 Positive Electrode Material from Lithium-Ion Batteries in Acid Solution," *ACS Applied Materials and Interfaces*, vol. 10, no. 19, pp. 16 424–16 435, 2018, ISSN: 19448252. DOI: 10.1021/acsami.8b01352.

[50] J. Wandt, A. Freiberg, R. Thomas, Y. Gorlin, A. Siebel, R. Jung, H. A. Gasteiger, and M. Tromp, "Transition metal dissolution and deposition in Li-ion batteries investigated by operando X-ray absorption spectroscopy," *Journal of Materials Chemistry A*, vol. 4, no. 47, pp. 18 300–18 305, Nov. 2016, ISSN: 20507496. DOI: 10.1039/C6TA08865A. [Online]. Available: www.rsc.org/MaterialsA.

[51] I. Buchberger, S. Seidlmayer, A. Pokharel, M. Piana, J. Hattendorff, P. Kudejova, R. Gilles, and H. A. Gasteiger, " Aging Analysis of Graphite/LiNi 1/3 Mn 1/3 Co 1/3 O 2 Cells Using XRD, PGAA, and AC Impedance," *Journal of The Electrochemical Society*, vol. 162, no. 14, A2737–A2746, Oct. 2015, ISSN: 0013-4651. DOI: 10.1149/2.0721514jes. [Online]. Available: https://iopscience.iop.org/article/10.1149/2.0721514jes%20https://iopscience.iop.org/article/10.1149/2.0721514jes/meta.

[52] D. Li, H. Li, D. Danilov, L. Gao, J. Zhou, R. A. Eichel, Y. Yang, and P. H. Notten, "Temperature-dependent cycling performance and ageing mechanisms of C6/LiNi1/3Mn1/3Co1/3O2 batteries," *Journal of Power Sources*, vol. 396, no. May, pp. 444–452, 2018, ISSN: 03787753. DOI: 10.1016/j.jpowsour.2018.06.035.

[53] R. Jung, F. Linsenmann, R. Thomas, J. Wandt, S. Solchenbach, F. Maglia, C. Stinner, M. Tromp, and H. A. Gasteiger, "Nickel, Manganese, and Cobalt Dissolution from Ni-Rich NMC and Their Effects on NMC622-Graphite Cells," *Journal of The Electrochemical Society*, vol. 166, no. 2, A378–A389, Feb. 2019, ISSN: 0013-4651. DOI: 10.1149/2.1151902jes. [Online]. Available: https://iopscience.iop.org/article/10.1149/2.1151902jes%20https://iopscience.iop.org/article/10.1149/2.1151902jes/meta.

[54] W. Choi and A. Manthiram, "Comparison of Metal Ion Dissolutions from Lithium Ion Battery Cathodes," *Journal of The Electrochemical Society*, vol. 153, no. 9, A1760, Jul. 2006, ISSN: 00134651. DOI: 10.1149/1.2219710. [Online]. Available: https://iopscience.iop.org/article/10.1149/1.2219710%20https://iopscience.iop.org/article/10.1149/1.2219710/meta.

[55] M. Winter, G. H. Wrodnigg, J. O. Besenhard, W. Biberacher, and P. Novák, "Dilatometric Investigations of Graphite Electrodes in Nonaqueous Lithium Battery Electrolytes," *Journal of The Electrochemical Society*, vol. 147, no. 7, p. 2427, 2000, ISSN: 00134651. DOI: 10.1149/1.1393548. [Online]. Available: https://iopscience.iop.org/article/10.1149/1.1393548%20https://iopscience.iop.org/article/10.1149/1.1393548/meta.

[56] D. Aurbach, "Electrode-solution interactions in Li-ion batteries: A short summary and new insights," in *Journal of Power Sources*, vol. 119-121, Elsevier, Jun. 2003, pp. 497–503. DOI: 10.1016/S0378-7753(03)00273-8.

[57] V. Agubra and J. Fergus, "Lithium ion battery anode aging mechanisms," *Materials*, vol. 6, no. 4, pp. 1310–1325, Mar. 2013, ISSN: 19961944. DOI: 10.3390/ma6041310. [Online]. Available: http://www.mdpi.com/1996-1944/6/4/1310.

[58] J. Cannarella, X. Liu, C. Z. Leng, P. D. Sinko, G. Y. Gor, and C. B. Arnold, "Mechanical Properties of a Battery Separator under Compression and Tension," *Journal of The Electrochemical Society*, vol. 161, no. 11, F3117–F3122, 2014, ISSN: 0013-4651. DOI: 10.1149/2.0191411jes.

[59] A. M. Grillet, T. Humplik, E. K. Stirrup, S. A. Roberts, D. A. Barringer, C. M. Snyder, M. R. Janvrin, and C. A. Apblett, "Conductivity Degradation of Polyvinylidene Fluoride Composite Binder during Cycling: Measurements and Simulations for Lithium-Ion Batteries," *Journal of The Electrochemical Society*, vol. 163, no. 9, A1859–A1871, Jul. 2016, ISSN: 0013-4651. DOI: 10.1149/2.0341609jes. [Online]. Available: https://iopscience.iop.org/article/10.1149/2.0341609jes%20https://iopscience.iop.org/article/10.1149/2.0341609jes/meta.

[60] J. W. Braithwaite, "Corrosion of Lithium-Ion Battery Current Collectors," *Journal of The Electrochemical Society*, vol. 146, no. 2, p. 448, 1999, ISSN: 00134651. DOI: 10.1149/1.1391627. [Online]. Available: https://iopscience.iop.org/article/10.1149/1.1391627%20https://iopscience.iop.org/article/10.1149/1.1391627/meta%20http://jes.ecsdl.org/cgi/doi/10.1149/1.1391627.

[61] C. L. Campion, W. Li, and B. L. Lucht, "Thermal Decomposition of LiPF[sub 6]-Based Electrolytes for Lithium-Ion Batteries," *Journal of The Electrochemical Society*, vol. 152, no. 12, A2327, Oct. 2005, ISSN: 00134651. DOI: 10.1149/1.2083267. [Online]. Available: https://iopscience.iop.org/article/10.1149/1.2083267%20https://iopscience.iop.org/article/10.1149/1.2083267/meta.

[62] K. Rumpf, M. Naumann, and A. Jossen, "Experimental investigation of parametric cell-to-cell variation and correlation based on 1100 commercial lithium-ion cells," *Journal of Energy Storage*, vol. 14, pp. 224–243, 2017, ISSN: 2352152X. DOI: 10.1016/j.est.2017.09.010. [Online]. Available: https://doi.org/10.1016/j.est.2017.09.010.

[63] R. R. Richardson, M. A. Osborne, and D. A. Howey, "Battery health prediction under generalized conditions using a Gaussian process transition model," *Journal of Energy Storage*, vol. 23, pp. 320–328, 2019. arXiv: 1807.06350. [Online]. Available: http://arxiv.org/abs/1807.06350.

[64] S. J. Harris, D. J. Harris, and C. Li, "Failure statistics for commercial lithium ion batteries: A study of 24 pouch cells," *Journal of Power Sources*, vol. 342, pp. 589–597, Feb. 2017, ISSN: 0378-7753. DOI: 10.1016/J.JPOWSOUR.2016.12.083.

[65] M. Dubarry, G. Baure, and A. Devie, "Durability and Reliability of EV Batteries under Electric Utility Grid Operations: Path Dependence of Battery Degradation," *Journal of The Electrochemical Society*, vol. 165, no. 5, A773–A783, Mar. 2018, ISSN: 0013-4651. DOI: 10.1149/2.0421805jes. [Online]. Available: https://iopscience.iop.org/article/10.1149/2.0421805jes%20https://iopscience.iop.org/article/10.1149/2.0421805jes/meta.

[66] G. Baure, A. Devie, and M. Dubarry, "Battery Durability and Reliability under Electric Utility Grid Operations: Path Dependence of Battery Degradation," *Journal of The Electrochemical Society*, vol. 166, no. 10, A1991–A2001, Jun. 2019, ISSN: 0013-4651. DOI: 10.1149/2.0971910jes. [Online]. Available: https://iopscience.iop.org/article/10.1149/2.0971910jes%20https://iopscience.iop.org/article/10.1149/2.0971910jes/meta.

[67] L. Su, J. Zhang, J. Huang, H. Ge, Z. Li, F. Xie, and B. Y. Liaw, "Path dependence of lithium ion cells aging under storage conditions," *Journal of Power Sources*, vol. 315, pp. 35–46, May 2016, ISSN: 03787753. DOI: 10.1016/j.jpowsour.2016.03.043.

[68] M. Dubarry, V. Svoboda, R. Hwu, B. Y. Liaw, and B. Yann Liaw, "Incremental Capacity Analysis and Close-to-Equilibrium OCV Measurements to Quantify Capacity Fade in Commercial Rechargeable Lithium Batteries," *Electrochemical and Solid-State Letters*, vol. 9, no. 10, A454, 2006, ISSN: 10990062. DOI: 10.1149/1.2221767. [Online]. Available: http://esl.ecsdl.org/cgi/doi/10.1149/1.2221767.

[69] B. Y. Liaw, K. L. Gering, S. V. Sazhin, C. J. Michelbacher, D. K. Jamison, M. Cugnet, and M. Dubarry, "Investigation of path dependence in commercial lithium-ion cells chosen for plug-in hybrid vehicle duty cycle protocols," *Journal of Power Sources*, vol. 196, no. 7, pp. 3395–3403, 2010, ISSN: 03787753. DOI: 10.1016/j.jpowsour.2010.05.058. [Online]. Available: http://dx.doi.org/10.1016/j.jpowsour.2010.05.058.

[70] M. Dubarry, C. Truchot, and B. Y. Liaw, *' Alawa : A Unique Mechanistic Model for Battery Diagnosis and Prognosis Case ID :* 2016.

[71] S. F. Schuster, M. J. Brand, C. Campestrini, M. Gleissenberger, and A. Jossen, "Correlation between capacity and impedance of lithium-ion cells during calendar and cycle life," *Journal of Power Sources*, vol. 305, pp. 191–199, 2016, ISSN: 03787753. DOI: 10.1016/j.jpowsour.2015.11.096. [Online]. Available: http://dx.doi.org/10.1016/j.jpowsour.2015.11.096.

[72] Y. Gao, C. Zhang, Y. Jiang, Q. Guo, J. Jiang, and W. Zhang, "Recognition of battery aging variations for LiFePO4 batteries in 2nd use applications combining incremental capacity analysis and statistical approaches," *Journal of Power Sources*, vol. 360, pp. 180–188, 2017, ISSN: 03787753. DOI: 10.1016/j.jpowsour.2017.06.007. [Online]. Available: http://dx.doi.org/10.1016/j.jpowsour.2017.06.007.

[73] D. P. Finegan, A. Quinn, D. S. Wragg, A. M. Colclasure, X. Lu, C. Tan, T. M. Heenan, R. Jervis, D. J. Brett, S. Das, T. Gao, D. A. Cogswell, M. Z. Bazant, M. Di Michiel, S. Checchia, P. R. Shearing, and K. Smith, "Spatial dynamics of lithiation and lithium plating during high-rate operation of graphite electrodes," *Energy and Environmental Science*, vol. 13, no. 8, pp. 2570–2584, Aug. 2020, ISSN: 17545706. DOI: 10.1039/d0ee01191f. [Online]. Available: https://pubs.rsc.org/en/content/articlehtml/2020/ee/d0ee01191f%20https://pubs.rsc.org/en/content/articlelanding/2020/ee/d0ee01191f.

[74] M. Dubarry, C. Truchot, and B. Y. Liaw, "Synthesize battery degradation modes via a diagnostic and prognostic model," *Journal of Power Sources*, vol. 219, pp. 204–216, Dec. 2012. DOI: 10.1016/j.jpowsour.2012.07.016. [Online]. Available: http://dx.doi.org/10.1016/j.jpowsour.2012.07.016.

[75] N. A. Samad, Y. Kim, J. B. Siegel, and A. G. Stefanopoulou, "Battery Capacity Fading Estimation Using a Force-Based Incremental Capacity Analysis," *Journal of The Electrochemical Society*, vol. 163, no. 8, A1584–A1594, 2016, ISSN: 0013-4651. DOI: 10.1149/2.0511608jes. [Online]. Available: http://jes.ecsdl.org/lookup/doi/10.1149/2.0511608jes.

[76] D. Wang, Q. Miao, and M. Pecht, "Prognostics of lithium-ion batteries based on relevance vectors and a conditional three-parameter capacity degradation model," *Journal of Power Sources*, vol. 239, pp. 253–264, 2013, ISSN: 03787753. DOI: 10.1016/j.jpowsour.2013.03.129.

[77] C. Weng, Y. Cui, J. Sun, and H. Peng, "On-board state of health monitoring of lithium-ion batteries using incremental capacity analysis with support vector regression," *Journal of Power Sources*, vol. 235, pp. 36–44, 2013, ISSN: 03787753. DOI: 10.1016/j.jpowsour.2013.02.012.

[78] X. Feng, Y. Merla, C. Weng, M. Ouyang, X. He, B. Y. Liaw, S. Santhanagopalan, X. Li, P. Liu, L. Lu, X. Han, D. Ren, Y. Wang, R. Li, C. Jin, P. Huang, M. Yi, L. Wang, Y. Zhao, Y. Patel, and G. Offer, "A reliable approach of differentiating discrete sampled-data for battery diagnosis," *eTransportation*, vol. 3, p. 100 051, Feb. 2020, ISSN: 25901168. DOI: 10.1016/j.etran.2020.100051. [Online]. Available: https://www.sciencedirect.com/science/article/pii/S2590116820300084.

[79] I. Bloom, A. N. Jansen, D. P. Abraham, J. Knuth, S. A. Jones, V. S. Battaglia, and G. L. Henriksen, "Differential voltage analyses of high-power, lithium-ion cells 1. Technique and application," *Journal of Power Sources*, vol. 139, no. 1-2, pp. 295–303, Jan. 2005, ISSN: 03787753. DOI: 10.1016/j.jpowsour.2004.07.021.

[80] I. Bloom, J. Christophersen, and K. Gering, "Differential voltage analyses of high-power lithium-ion cells 2. Applications," *Journal of Power Sources*, vol. 139, no. 1-2, pp. 304–313, Jan. 2005, ISSN: 03787753. DOI: 10.1016/j.jpowsour.2004.07.022.

[81] I. Bloom, L. K. Walker, J. K. Basco, D. P. Abraham, J. P. Christophersen, and C. D. Ho, "Differential voltage analyses of high-power lithium-ion cells. 4. Cells containing NMC," *Journal of Power Sources*, vol. 195, no. 3, pp. 877–882, Feb. 2010, ISSN: 03787753. DOI: 10.1016/j.jpowsour.2009.08.019.

[82] H. M. Dahn, A. J. Smith, J. C. Burns, D. A. Stevens, and J. R. Dahn, "User-Friendly Differential Voltage Analysis Freeware for the Analysis of Degradation Mechanisms in Li-Ion Batteries," *Journal of The Electrochemical Society*, vol. 159, no. 9, A1405–A1409, Aug. 2012, ISSN: 0013-4651. DOI: 10.1149/2.013209jes. [Online]. Available: www.alglib.net.

[83] K. Ando, T. Matsuda, and D. Imamura, "Degradation diagnosis of lithium-ion batteries with a LiNi0.5Co0.2Mn0.3O2 and LiMn2O4 blended cathode using dV/dQ curve analysis," *Journal of Power Sources*, vol. 390, no. March, pp. 278–285, 2018, ISSN: 03787753. DOI: 10.1016/j.jpowsour.2018.04.043. [Online]. Available: https://doi.org/10.1016/j.jpowsour.2018.04.043.

[84] I. D. Campbell, M. Marzook, M. Marinescu, and G. J. Offer, "How Observable Is Lithium Plating? Differential Voltage Analysis to Identify and Quantify Lithium Plating Following Fast Charging of Cold Lithium-Ion Batteries," *Journal of The Electrochemical Society*, vol. 166, no. 4, A725–A739, Mar. 2019, ISSN: 0013-4651. DOI: 10.1149/2.0821904jes. [Online]. Available: https://iopscience.iop.org/article/10.1149/2.0821904jes%20https://iopscience.iop.org/article/10.1149/2.0821904jes/meta.

[85] V. Pop, H. J. Bergveld, P. P. L. Regtien, J. H. G. Op het Veld, D. Danilov, and P. H. L. Notten, "Battery Aging and Its Influence on the Electromotive Force," *Journal of The Electrochemical Society*, vol. 154, no. 8, A744, 2007, ISSN: 00134651. DOI: 10.1149/1.2742296.

[86] M. Dubarry, A. Devie, and B. Y. Liaw, "The Value of Battery Diagnostics and Prognostics," *J. Energy Power Sources*, vol. 1, no. 5, pp. 242–249, 2014. [Online]. Available: www.ethanpublishing.com.

[87] C. R. Birkl, E. McTurk, M. R. Roberts, P. G. Bruce, and D. A. Howey, "A Parametric Open Circuit Voltage Model for Lithium Ion Batteries," *Journal of The Electrochemical Society*, vol. 162, no. 12, A2271–A2280, 2015, ISSN: 0013-4651. DOI: 10.1149/2.0331512jes.

[88] R. Prosser, G. Offer, and Y. Patel, "Lithium-Ion Diagnostics: The First Quantitative In-Operando Technique for Diagnosing Lithium Ion Battery Degradation Modes under Load with Realistic Thermal Boundary Conditions," *Journal of The Electrochemical Society*, vol. 168, no. 3, p. 030 532, 2021, ISSN: 0013-4651. DOI: 10.1149/1945-7111/abed28.

[89] Z. Ma, Z. Wang, R. Xiong, and J. Jiang, "A mechanism identification model based state-of-health diagnosis of lithium-ion batteries for energy storage applications," *Journal of Cleaner Production*, vol. 193, pp. 379–390, 2018, ISSN: 09596526. DOI: 10.1016/j.jclepro.2018.05.074. [Online]. Available: https://doi.org/10.1016/j.jclepro.2018.05.074.

[90] B. Pan, D. Dong, J. Wang, J. Nie, S. Liu, Y. Cao, and Y. Jiang, "Aging mechanism diagnosis of lithium ion battery by open circuit voltage analysis," *Electrochimica Acta*, vol. 362, p. 137 101, 2020, ISSN: 00134686. DOI: 10.1016/j.electacta.2020.137101. [Online]. Available: https://doi.org/10.1016/j.electacta.2020.137101.

[91] T. Osaka, D. Mukoyama, and H. Nara, "Review—Development of Diagnostic Process for Commercially Available Batteries, Especially Lithium Ion Battery, by Electrochemical Impedance Spectroscopy," *Journal of The Electrochemical Society*, vol. 162, no. 14, A2529–A2537, Oct. 2015, ISSN: 0013-4651. DOI: 10.1149/2.0141514jes. [Online]. Available: https://iopscience.iop.org/article/10.1149/2.0141514jes%20https://iopscience.iop.org/article/10.1149/2.0141514jes/meta.

[92] Y. Zhang and C.-Y. Wang, "Cycle-Life Characterization of Automotive Lithium-Ion Batteries with LiNiO[sub 2] Cathode," *Journal of The Electrochemical Society*, vol. 156, no. 7, A527, May 2009, ISSN: 00134651. DOI: 10.1149/1.3126385. [Online]. Available: https://iopscience.iop.org/article/10.1149/1.3126385%20https://iopscience.iop.org/article/10.1149/1.3126385/meta.

[93] J. Zhu, M. Knapp, X. Liu, P. Yan, H. Dai, X. Wei, and H. Ehrenberg, "Low temperature separating lithium-ion battery interfacial polarization based on distribution of relaxation times (DRT) of impedance," *IEEE Transactions on Transportation Electrification*, pp. 1–1, Oct. 2020, ISSN: 2332-7782. DOI: 10.1109/tte.2020.3028475.

[94] C. Pastor-Fernández, K. Uddin, G. H. Chouchelamane, W. D. Widanage, and J. Marco, "A Comparison between Electrochemical Impedance Spectroscopy and Incremental Capacity-Differential Voltage as Li-ion Diagnostic Techniques to Identify and Quantify the Effects of Degradation Modes within Battery Management Systems," *Journal of Power Sources*, vol. 360, pp. 301–318, Aug. 2017, ISSN: 03787753. DOI: 10.1016/j.jpowsour.2017.03.042.

[95] Y. Zhang, Q. Tang, Y. Zhang, J. Wang, U. Stimming, and A. A. Lee, "Identifying degradation patterns of lithium ion batteries from impedance spectroscopy using machine learning," *Nature Communications*, vol. 11, no. 1, pp. 1–6, Dec. 2020, ISSN: 20411723. DOI: 10.1038/s41467-020-15235-7. [Online]. Available: https://doi.org/10.1038/s41467-020-15235-7.

[96] B. Wu, V. Yufit, Y. Merla, R. F. Martinez-Botas, N. P. Brandon, and G. J. Offer, "Differential thermal voltammetry for tracking of degradation in lithium-ion batteries," *Journal of Power Sources*, vol. 273, pp. 495–501, Jan. 2015, ISSN: 03787753. DOI: 10.1016/j.jpowsour.2014.09.127. [Online]. Available: https://www.sciencedirect.com/science/article/pii/S0378775314015389%20http://www.sciencedirect.com/science/article/pii/S0378775314015389.

[97] Y. Merla, B. Wu, V. Yufit, N. P. Brandon, R. F. Martinez-Botas, and G. J. Offer, "Novel application of differential thermal voltammetry as an in-depth state-of-health diagnosis method for lithium-ion batteries," *Journal of Power Sources*, vol. 307, pp. 308–319, Mar. 2016, ISSN: 03787753. DOI: 10.1016/j.jpowsour.2015.12.122. [Online]. Available: https://www.sciencedirect.com/science/article/pii/S0378775315307345%7B%5C#%7Dfig1.

[98] ——, "Extending battery life: A low-cost practical diagnostic technique for lithium-ion batteries," *Journal of Power Sources*, vol. 331, pp. 224–231, Nov. 2016, ISSN: 03787753. DOI: 10.1016/j.jpowsour.2016.09.008. [Online]. Available: https://www.sciencedirect.com/science/article/pii/S0378775316311715.

[99] A. J. Smith, J. C. Burns, S. Trussler, and J. R. Dahn, "Precision Measurements of the Coulombic Efficiency of Lithium-Ion Batteries and of Electrode Materials for Lithium-Ion Batteries," *Journal of The Electrochemical Society*, vol. 157, no. 2, A196, Dec. 2010, ISSN: 00134651. DOI: 10.1149/1.3268129. [Online]. Available: https://iopscience.iop.org/article/10.1149/1.3268129%20https://iopscience.iop.org/article/10.1149/1.3268129/meta.

[100] D. A. Stevens, R. Y. Ying, R. Fathi, J. N. Reimers, J. E. Harlow, and J. R. Dahn, "Using High Precision Coulometry Measurements to Compare the Degradation Mechanisms of NMC/LMO and NMC-Only Automotive Scale Pouch Cells," *Journal of The Electrochemical Society*, vol. 161, no. 9, A1364–A1370, 2014, ISSN: 0013-4651. DOI: 10.1149/2.0971409jes.

[101] J. C. Burns, D. A. Stevens, and J. R. Dahn, "In-Situ Detection of Lithium Plating Using High Precision Coulometry," *Journal of The Electrochemical Society*, vol. 162, no. 6, A959–A964, 2015, ISSN: 0013-4651. DOI: 10.1149/2.0621506jes.

[102] L. D. Ellis, J. P. Allen, I. G. Hill, and J. R. Dahn, "High-Precision Coulometry Studies of the Impact of Temperature and Time on SEI Formation in Li-Ion Cells," *Journal of The Electrochemical Society*, vol. 165, no. 7, A1529–A1536, 2018, ISSN: 0013-4651. DOI: 10.1149/2.1091807jes.

[103] R. Carter, B. Huhman, C. T. Love, and I. V. Zenyuk, "X-ray computed tomography comparison of individual and parallel assembled commercial lithium iron phosphate batteries at end of life after high rate cycling," *Journal of Power Sources*, vol. 381, pp. 46–55, Mar. 2018, ISSN: 0378-7753. DOI: 10.1016/J.JPOWSOUR.2018.01.087.

[104] M. H. Lipu, M. Hannan, A. Hussain, M. Hoque, P. J. Ker, M. Saad, and A. Ayob, "A review of state of health and remaining useful life estimation methods for lithium-ion battery in electric vehicles: Challenges and recommendations," *Journal of Cleaner Production*, vol. 205, pp. 115–133, 2018, ISSN: 09596526. DOI: 10.1016/j.jclepro.2018.09.065. [Online]. Available: https://linkinghub.elsevier.com/retrieve/pii/S0959652618327793.

[105] X. Han, L. Lu, Y. Zheng, X. Feng, Z. Li, J. Li, and M. Ouyang, "A review on the key issues of the lithium ion battery degradation among the whole life cycle," *eTransportation*, vol. 1, p. 100 005, Aug. 2019, ISSN: 25901168. DOI: 10.1016/j.etran.2019.100005.

[106] S. B. Sarmah, P. Kalita, A. Garg, X. D. Niu, X. W. Zhang, X. Peng, and D. Bhattacharjee, "A Review of State of Health Estimation of Energy Storage Systems: Challenges and Possible Solutions for Futuristic Applications of Li-Ion Battery Packs in Electric Vehicles," *Journal of Electrochemical Energy Conversion and Storage*, vol. 16, no. 4, Nov. 2019, ISSN: 23816910. DOI: 10.1115/1.4042987. [Online]. Available: http://asmedigitalcollection.asme.org/electrochemical/article-pdf/16/4/040801/6036074/jeecs%7B%5C_%7D16%7B%5C_%7D4%7B%5C_%7D040801.pdf.

[107] M. Doyle, T. F. Fuller, and J. Newman, "Modeling of Galvanostatic Charge and Discharge of the Lithium/Polymer/Insertion Cell," *Journal of The Electrochemical Society*, vol. 140, no. 6, pp. 1526–1533, 1993, ISSN: 0013-4651. DOI: 10.1149/1.2221597.

[108] C. Zhang, K. Li, S. McLoone, and Z. Yang, "Battery modelling methods for electric vehicles - A review," in *2014 European Control Conference, ECC 2014*, Institute of Electrical and Electronics Engineers Inc., Jul. 2014, pp. 2673–2678, ISBN: 9783952426913. DOI: 10.1109/ECC.2014.6862541.

[109] T. F. Fuller, M. Doyle, and J. Newman, "Simulation and Optimization of the Dual Lithium Ion Insertion Cell," *Journal of The Electrochemical Society*, vol. 141, no. 1, pp. 1–10, 1994, ISSN: 0013-4651. DOI: 10.1149/1.2054684.

[110] D. Zhang, B. N. Popov, and R. E. White, "Modeling Lithium Intercalation of a Single Spinel Particle under Potentiodynamic Control," *Journal of The Electrochemical Society*, vol. 147, no. 3, p. 831, 2000, ISSN: 00134651. DOI: 10.1149/1.1393279.

[111] S. G. Marquis, V. Sulzer, R. Timms, C. P. Please, and S. J. Chapman, "An asymptotic derivation of a single particle model with electrolyte," *arXiv*, vol. 166, no. 15, A3693–A3706, 2019, ISSN: 23318422. DOI: 10.1149/2.0341915jes. arXiv: 1905.12553.

[112] T. R. Tanim, C. D. Rahn, and C. Y. Wang, "State of charge estimation of a lithium ion cell based on a temperature dependent and electrolyte enhanced single particle model," *Energy*, vol. 80, pp. 731–739, Feb. 2015, ISSN: 03605442. DOI: 10.1016/j.energy.2014.12.031.

[113] S. J. Moura, F. B. Argomedo, R. Klein, A. Mirtabatabaei, and M. Krstic, "Battery State Estimation for a Single Particle Model with Electrolyte Dynamics," *IEEE Transactions on Control Systems Technology*, vol. 25, no. 2, pp. 453–468, Mar. 2017, ISSN: 10636536. DOI: 10.1109/TCST.2016.2571663.

[114] Y. Merla, B. Wu, V. Yufit, R. Martinez-Botas, and G. Offer, "An easy-to-parameterise physics-informed battery model and its application towards lithium-ion battery cell design, diagnosis, and degradation," *Journal of Power Sources*, vol. 384, 2018, ISSN: 03787753. DOI: 10.1016/j.jpowsour.2018.02.065.

[115] G. L. Plett, "Extended Kalman filtering for battery management systems of LiPB-based HEV battery packs - Part 1. Background," *Journal of Power Sources*, vol. 134, no. 2, pp. 252–261, Aug. 2004, ISSN: 03787753. DOI: 10.1016/j.jpowsour.2004.02.031.

[116] ——, "Extended Kalman filtering for battery management systems of LiPB-based HEV battery packs - Part 2. Modeling and identification," *Journal of Power Sources*, vol. 134, no. 2, pp. 262–276, Aug. 2004, ISSN: 03787753. DOI: 10.1016/j.jpowsour.2004.02.032.

[117] ——, "Extended Kalman filtering for battery management systems of LiPB-based HEV battery packs - Part 3. State and parameter estimation," *Journal of Power Sources*, vol. 134, no. 2, pp. 277–292, Aug. 2004, ISSN: 03787753. DOI: 10.1016/j.jpowsour.2004.02.033.

[118] S. Nejad, D. T. Gladwin, and D. A. Stone, "A systematic review of lumped-parameter equivalent circuit models for real-time estimation of lithium-ion battery states," *Journal of Power Sources*, vol. 316, pp. 183–196, Jun. 2016, ISSN: 0378-7753. DOI: 10.1016/J.JPOWSOUR.2016.03.042.

[119] Y. Zhao, Y. Patel, T. Zhang, and G. J. Offer, "Modeling the Effects of Thermal Gradients Induced by Tab and Surface Cooling on Lithium Ion Cell Performance," *Journal of The Electrochemical Society*, vol. 165, no. 13, A3169–A3178, 2018, ISSN: 0013-4651. DOI: 10.1149/2.0901813jes.

[120] A. Cordoba-Arenas, S. Onori, Y. Guezennec, and G. Rizzoni, "Capacity and power fade cycle-life model for plug-in hybrid electric vehicle lithium-ion battery cells containing blended spinel and layered-oxide positive electrodes," *Journal of Power Sources*, vol. 278, pp. 473–483, 2015, ISSN: 03787753. DOI: 10.1016/j.jpowsour.2014.12.047.

[121] J. Wang, P. Liu, J. Hicks-Garner, E. Sherman, S. Soukiazian, M. Verbrugge, H. Tataria, J. Musser, and P. Finamore, "Cycle-life model for graphite-LiFePO4 cells," *Journal of Power Sources*, vol. 196, no. 8, pp. 3942–3948, 2011, ISSN: 03787753. DOI: 10.1016/j.jpowsour.2010.11.134. [Online]. Available: http://dx.doi.org/10.1016/j.jpowsour.2010.11.134.

[122] R. B. Wright, C. G. Motloch, J. R. Belt, J. P. Christophersen, C. D. Ho, R. A. Richardson, I. Bloom, S. A. Jones, V. S. Battaglia, G. L. Henriksen, T. Unkelhaeuser, D. Ingersoll, H. L. Case, S. A. Rogers, and R. A. Sutula, "Calendar- and cycle-life studies of advanced technology development program generation 1 lithium-ion batteries," *Journal of Power Sources*, vol. 110, no. 2, pp. 445–470, Aug. 2002, ISSN: 03787753. DOI: 10.1016/S0378-7753(02)00210-0.

[123] M. Schimpe, M. E. von Kuepach, M. Naumann, H. C. Hesse, K. Smith, and A. Jossen, "Comprehensive Modeling of Temperature-Dependent Degradation Mechanisms in Lithium Iron Phosphate Batteries," *Journal of The Electrochemical Society*, vol. 165, no. 2, A181–A193, 2018, ISSN: 0013-4651. DOI: 10.1149/2.1181714jes.

[124] W. Wu, S. Wang, W. Wu, K. Chen, S. Hong, and Y. Lai, "A critical review of battery thermal performance and liquid based battery thermal management," *Energy Conversion and Management*, vol. 182, pp. 262–281, Jan. 2019, ISSN: 01968904. DOI: 10.1016/j.enconman.2018.12.051.

[125] G. Offer, Y. Patel, A. Hales, L. Bravo Diaz, and M. Marzook, "Cool metric for lithium-ion batteries could spur progress," *Nature*, vol. 582, no. 7813, pp. 485–487, Jun. 2020, ISSN: 14764687. DOI: 10.1038/d41586-020-01813-8. [Online]. Available: https://www.nature.com/articles/d41586-020-01813-8.

[126] A. Hales, L. B. Diaz, M. W. Marzook, Y. Zhao, Y. Patel, and G. Offer, "The Cell Cooling Coefficient: A Standard to Define Heat Rejection from Lithium-Ion Batteries," *Journal of The Electrochemical Society*, vol. 166, no. 12, A2383–A2395, 2019, ISSN: 0013-4651. DOI: 10.1149/2.0191912jes.

[127] J. Kim, J. Oh, and H. Lee, "Review on Battery Thermal Management System for Electric Vehicles," *Applied Thermal Engineering*, vol. 149, no. November 2018, pp. 192–212, Feb. 2018, ISSN: 13594311. DOI: 10.1016/j.applthermaleng.2018.12.020. [Online]. Available: https://linkinghub.elsevier.com/retrieve/pii/S135943111835614X.

[128] W. Tong, K. Somasundaram, E. Birgersson, A. S. Mujumdar, and C. Yap, "Thermo-electrochemical model for forced convection air cooling of a lithium-ion battery module," *Applied Thermal Engineering*, vol. 99, pp. 672–682, Apr. 2016, ISSN: 13594311. DOI: 10.1016/j.applthermaleng.2016.01.050. [Online]. Available: http://dx.doi.org/10.1016/j.applthermaleng.2016.01.050.

[129] Y. Chung and M. S. Kim, "Thermal analysis and pack level design of battery thermal management system with liquid cooling for electric vehicles," *Energy Conversion and Management*, vol. 196, pp. 105–116, Sep. 2019, ISSN: 01968904. DOI: 10.1016/j.enconman.2019.05.083.

[130] Z. Rao, Z. Qian, Y. Kuang, and Y. Li, "Thermal performance of liquid cooling based thermal management system for cylindrical lithium-ion battery module with variable contact surface," *Applied Thermal Engineering*, vol. 123, pp. 1514–1522, Aug. 2017, ISSN: 13594311. DOI: 10.1016/j.applthermaleng.2017.06.059.

[131] G. Xia, L. Cao, and G. Bi, "A review on battery thermal management in electric vehicle application," *Journal of Power Sources*, vol. 367, pp. 90–105, Nov. 2017, ISSN: 03787753. DOI: 10.1016/j.jpowsour.2017.09.046.

[132] P. Taheri and M. Bahrami, "Temperature Rise in Prismatic Polymer Lithium-Ion Batteries: An Analytic Approach," *SAE International Journal of Passenger Cars - Electronic and Electrical Systems*, vol. 5, no. 1, pp. 164–176, 2012, ISSN: 19464622. DOI: 10.4271/2012-01-0334.

[133] I. A. Hunt, Y. Zhao, Y. Patel, and J. Offer, "Surface Cooling Causes Accelerated Degradation Compared to Tab Cooling for Lithium-Ion Pouch Cells," *Journal of The Electrochemical Society*, vol. 163, no. 9, A1846–A1852, 2016, ISSN: 0013-4651. DOI: 10.1149/2.0361609jes.

[134] L. Wei, Z. Lu, F. Cao, L. Zhang, X. Yang, X. Yu, and L. Jin, "A comprehensive study on thermal conductivity of the lithium-ion battery," *International Journal of Energy Research*, vol. 44, no. 12, pp. 9466–9478, Oct. 2020, ISSN: 0363-907X. DOI: 10.1002/er.5016. [Online]. Available: https://onlinelibrary.wiley.com/doi/10.1002/er.5016.

[135] Z. Li, J. Zhang, B. Wu, J. Huang, Z. Nie, Y. Sun, F. An, and N. Wu, "Examining temporal and spatial variations of internal temperature in large-format laminated battery with embedded thermocouples," *Journal of Power Sources*, vol. 241, pp. 536–553, 2013, ISSN: 03787753. DOI: 10.1016/j.jpowsour.2013.04.117. [Online]. Available: http://dx.doi.org/10.1016/j.jpowsour.2013.04.117.

[136] U. S. Kim, J. Yi, C. B. Shin, T. Han, and S. Park, "Modelling the thermal behaviour of a lithium-ion battery during charge," *Journal of Power Sources*, vol. 196, no. 11, pp. 5115–5121, 2011, ISSN: 03787753. DOI: 10.1016/j.jpowsour.2011.01.103.

[137] C. Forgez, D. Vinh Do, G. Friedrich, M. Morcrette, and C. Delacourt, "Thermal modeling of a cylindrical LiFePO4/graphite lithium-ion battery," *Journal of Power Sources*, vol. 195, no. 9, pp. 2961–2968, May 2010, ISSN: 03787753. DOI: 10.1016/j.jpowsour.2009.10.105.

[138] W. Zhao, G. Luo, and C.-Y. Y. Wang, "Effect of tab design on large-format Li-ion cell performance," *Journal of Power Sources*, vol. 257, pp. 70–79, 2014, ISSN: 03787753. DOI: 10.1016/j.jpowsour.2013.12.146. [Online]. Available: http://dx.doi.org/10.1016/j.jpowsour.2013.12.146.

[139] E. Hosseinzadeh, J. Marco, and P. Jennings, "Combined electrical and electrochemical-thermal model of parallel connected large format pouch cells," *Journal of Energy Storage*, vol. 22, no. February, pp. 194–207, 2019, ISSN: 2352-152X. DOI: 10.1016/J.EST.2019.02.004. [Online]. Available: https://www.sciencedirect.com/science/article/pii/S2352152X18305929?via%7B%5C%%7D3Dihub.

[140] G. J. Offer, V. Yufit, D. A. Howey, B. Wu, and N. P. Brandon, "Module design and fault diagnosis in electric vehicle batteries," *Journal of Power Sources*, vol. 206, pp. 383–392, 2012, ISSN: 03787753. DOI: 10.1016/j.jpowsour.2012.01.087. [Online]. Available: http://dx.doi.org/10.1016/j.jpowsour.2012.01.087.

[141] B. Wu, V. Yufit, M. Marinescu, G. J. Offer, R. F. Martinez-Botas, and N. P. Brandon, "Coupled thermal-electrochemical modelling of uneven heat generation in lithium-ion battery packs," *Journal of Power Sources*, vol. 243, pp. 544–554, 2013, ISSN: 03787753. DOI: 10.1016/j.jpowsour.2013.05.164.

[142] N. Ganesan, S. Basu, K. S. Hariharan, S. M. Kolake, T. Song, T. Yeo, D. K. Sohn, and S. Doo, "Physics based modeling of a series parallel battery pack for asymmetry analysis, predictive control and life extension," *Journal of Power Sources*, vol. 322, pp. 57–67, Aug. 2016, ISSN: 0378-7753. DOI: 10.1016/J.JPOWSOUR.2016.05.005. [Online]. Available: http://dx.doi.org/10.1016/j.jpowsour.2016.05.005.

[143] C. Zhang, Y. Jiang, J. Jiang, G. Cheng, W. Diao, and W. Zhang, "Study on battery pack consistency evolutions and equilibrium diagnosis for serial- connected lithium-ion batteries," *Applied Energy*, vol. 207, pp. 510–519, Dec. 2017, ISSN: 0306-2619. DOI: 10.1016/J.APENERGY.2017.05.176.

[144] L. Zhou, Y. Zheng, M. Ouyang, and L. Lu, "A study on parameter variation effects on battery packs for electric vehicles," *Journal of Power Sources*, vol. 364, pp. 242–252, 2017, ISSN: 03787753. DOI: 10.1016/j.jpowsour.2017.08.033. [Online]. Available: http://dx.doi.org/10.1016/j.jpowsour.2017.08.033.

[145] N. Yang, X. Zhang, B. Shang, and G. Li, "Unbalanced discharging and aging due to temperature differences among the cells in a lithium-ion battery pack with parallel combination," *Journal of Power Sources*, vol. 306, pp. 733–741, Feb. 2016, ISSN: 0378-7753. DOI: 10.1016/J.JPOWSOUR.2015.12.079. [Online]. Available: https://www.sciencedirect.com/science/article/pii/S0378775315306911.

[146] R. Gogoana, M. B. Pinson, M. Z. Bazant, and S. E. Sarma, "Internal resistance matching for parallel-connected lithium-ion cells and impacts on battery pack cycle life," *Journal of Power Sources*, vol. 252, pp. 8–13, 2014, ISSN: 0378-7753. DOI: 10.1016/j.jpowsour.2013.11.101. [Online]. Available: http://dx.doi.org/10.1016/j.jpowsour.2013.11.101.

[147] S. Miyatake, Y. Susuki, T. Hikihara, S. Itoh, and K. Tanaka, "Discharge characteristics of multicell lithium-ion battery with nonuniform cells," *Journal of Power Sources*, vol. 241, pp. 736–743, Nov. 2013, ISSN: 03787753. DOI: 10.1016/j.jpowsour.2013.05.179.

[148] M. Brand, D. Quinger, G. Walder, A. Jossen, and M. Lienkamp, "Ageing inhomogeneity of long-term used BEV-batteries and their reusability for 2nd-life applications," in *26th Electric Vehicle Symposium 2012, EVS 2012*, vol. 1, 2012, pp. 525–531, ISBN: 9781622764211.

[149] M. Baumann, L. Wildfeuer, S. Rohr, and M. Lienkamp, "Parameter variations within Li-Ion battery packs – Theoretical investigations and experimental quantification," *Journal of Energy Storage*, vol. 18, no. April, pp. 295–307, 2018, ISSN: 2352152X. DOI: 10.1016/j.est.2018.04.031. [Online]. Available: https://doi.org/10.1016/j.est.2018.04.031.

[150] C. Campestrini, P. Keil, S. F. Schuster, and A. Jossen, "Ageing of lithium-ion battery modules with dissipative balancing compared with single-cell ageing," *Journal of Energy Storage*, vol. 6, pp. 142–152, May 2016, ISSN: 2352152X. DOI: 10.1016/j.est.2016.03.004.

[151] M. Fleckenstein, O. Bohlen, M. A. Roscher, and B. Bäker, "Current density and state of charge inhomogeneities in Li-ion battery cells with LiFePO4 as cathode material due to temperature gradients," *Journal of Power Sources*, vol. 196, no. 10, pp. 4769–4778, May 2011, ISSN: 03787753. DOI: 10.1016/j.jpowsour.2011.01.043.

[152] G. M. Cavalheiro, T. Iriyama, G. J. Nelson, S. Huang, and G. Zhang, "Effects of Nonuniform Temperature Distribution on Degradation of Lithium-Ion Batteries," *Journal of Electrochemical Energy Conversion and Storage*, vol. 17, no. 2, pp. 1–8, 2020, ISSN: 23816910. DOI: 10.1115/1.4045205.

[153] P. J. Osswald, S. V. Erhard, A. Noel, P. Keil, F. M. Kindermann, H. Hoster, and A. Jossen, "Current density distribution in cylindrical Li-Ion cells during impedance measurements," *Journal of Power Sources*, vol. 314, pp. 93–101, 2016, ISSN: 03787753. DOI: 10.1016/j.jpowsour.2016.02.070. [Online]. Available: http://dx.doi.org/10.1016/j.jpowsour.2016.02.070.

[154] F. A. Lebel, N. Lebreux, M. Dubois, and J. P. Trovao, "Effect of Current Path on Parallel Lithium-Ion Cells in Electric Vehicles Battery Packs," *2017 IEEE Vehicle Power and Propulsion Conference, VPPC 2017 - Proceedings*, vol. 2018-Janua, pp. 1–5, 2018. DOI: 10.1109/VPPC.2017.8330864.

[155] J. Lv, S. Lin, W. Song, M. Chen, Z. Feng, Y. Li, and Y. Ding, "Performance of LiFePO4 batteries in parallel based on connection topology," *Applied Energy*, vol. 252, p. 113 407, Oct. 2019, ISSN: 03062619. DOI: 10.1016/j.apenergy.2019.113407.

[156] W. Diao, M. Pecht, and T. Liu, "Management of imbalances in parallel-connected lithium-ion battery packs," *Journal of Energy Storage*, vol. 24, no. January, p. 100 781, 2019, ISSN: 2352152X. DOI: 10.1016/j.est.2019.100781. [Online]. Available: https://doi.org/10.1016/j.est.2019.100781.

[157] S. Neupert and J. Kowal, "Inhomogeneities in Battery Packs," *World Electric Vehicle Journal*, vol. 9, no. 20, 2018. DOI: 10.3390/wevj9020020.

[158] Y. Zhang, J. Zheng, S. Lin, F. Bai, W. H. Tanveer, S. Cha, X. Wu, and W. Feng, "Nonuniform current distribution within parallel-connected batteries," *International Journal of Energy Research*, vol. 42, no. 8, pp. 2835–2844, 2018, ISSN: 1099114X. DOI: 10.1002/er.4039.

[159] T. Grün, K. Stella, and O. Wollersheim, "Influence of circuit design on load distribution and performance of parallel-connected Lithium ion cells for photovoltaic home storage systems," *Journal of Energy Storage*, vol. 17, pp. 367–382, 2018, ISSN: 2352152X. DOI: 10.1016/j.est.2018.03.010. [Online]. Available: https://doi.org/10.1016/j.est.2018.03.010.

[160] D. U. Sauer and H. Wenzl, "Comparison of different approaches for lifetime prediction of electrochemical systems-Using lead-acid batteries as example," *Journal of Power Sources*, vol. 176, no. 2, pp. 534–546, Feb. 2008, ISSN: 03787753. DOI: 10.1016/j.jpowsour.2007.08.057.

[161] F. Baronti, R. Di Rienzo, N. Papazafiropulos, R. Roncella, and R. Saletti, "Investigation of series-parallel connections of multi-module batteries for electrified vehicles," in *2014 IEEE International Electric Vehicle Conference, IEVC 2014*, IEEE, Dec. 2014, pp. 1–7, ISBN: 9781479960750. DOI: 10.1109/IEVC.2014.7056173. [Online]. Available: http://ieeexplore.ieee.org/document/7056173/.

[162] E. Hosseinzadeh, S. Arias, M. Krishna, D. Worwood, A. Barai, D. Widanalage, and J. Marco, "Quantifying cell-to-cell variations of a parallel battery module for different pack configurations," *Applied Energy*, vol. 282, p. 115 859, Jan. 2021, ISSN: 03062619. DOI: 10.1016/j.apenergy.2020.115859.

[163] M. P. Klein and J. W. Park, "Current Distribution Measurements in Parallel-Connected Lithium-Ion Cylindrical Cells under Non-Uniform Temperature Conditions," *Journal of The Electrochemical Society*, vol. 164, no. 9, A1893–A1906, Jul. 2017, ISSN: 0013-4651. DOI: 10.1149/2.0011709jes. [Online]. Available: http://jes.ecsdl.org/lookup/doi/10.1149/2.0011709jes.

[164] A. Fill, T. Mader, T. Schmidt, R. Llorente, and K. P. Birke, "Measuring test bench with adjustable thermal connection of cells to their neighbors and a new model approach for parallel-connected cells," *Batteries*, vol. 6, no. 1, pp. 1–16, 2020, ISSN: 23130105. DOI: 10.3390/batteries6010002.

[165] Y. Troxler, B. Wu, M. Marinescu, V. Yufit, Y. Patel, A. J. Marquis, N. P. Brandon, and G. J. Offer, "The effect of thermal gradients on the performance of lithium-ion batteries," *Journal of Power Sources*, vol. 247, pp. 1018–1025, Jun. 2014, ISSN: 03787753. DOI: 10.1016/j.jpowsour.2013.06.084.

[166] N. Yang, X. Zhang, G. Li, A. Cai, and Y. Xu, "Effects of Temperature Differences Among Cells on the Discharging Characteristics of Lithium-Ion Battery Packs with Series/Parallel Configurations during Constant Power Discharge," *Energy Technology*, vol. 6, no. 6, pp. 1067–1079, 2018, ISSN: 21944296. DOI: 10.1002/ente.201700650.

[167] H. H. Huang, H. Y. Chen, K. C. Liao, H. T. Young, C. F. Lee, and J. Y. Tien, "Thermal-electrochemical coupled simulations for cell-to-cell imbalances in lithium-iron-phosphate based battery packs," *Applied Thermal Engineering*, vol. 123, pp. 584–591, 2017, ISSN: 13594311. DOI: 10.1016/j.applthermaleng.2017.05.105. [Online]. Available: http://dx.doi.org/10.1016/j.applthermaleng.2017.05.105.

[168] I. Zilberman, S. Ludwig, M. Schiller, and A. Jossen, "Online aging determination in lithium-ion battery module with forced temperature gradient," *Journal of Energy Storage*, vol. 28, Apr. 2020, ISSN: 2352152X. DOI: 10.1016/j.est.2019.101170. [Online]. Available: https://doi.org/10.1016/j.est.2019.101170.

[169] M. S. Wu, C. Y. Lin, Y. Y. Wang, C. C. Wan, and C. R. Yang, "Numerical simulation for the discharge behaviors of batteries in series and/or parallel-connected battery pack," *Electrochimica Acta*, vol. 52, no. 3, pp. 1349–1357, 2006, ISSN: 00134686. DOI: 10.1016/j.electacta.2006.07.036.

[170] X. Gong, R. Xiong, and C. C. Mi, "Study of the Characteristics of Battery Packs in Electric Vehicles with Parallel-Connected Lithium-Ion Battery Cells," *IEEE Transactions on Industry Applications*, vol. 51, no. 2, pp. 1872–1879, Mar. 2015, ISSN: 00939994. DOI: 10.1109/TIA.2014.2345951. [Online]. Available: http://ieeexplore.ieee.org/document/6872532/.

[171] C. Pastor-Fernández, M. A. Gama-Valdez, W. D. Widanage, T. Bruen, and J. Marco, "A Study of Cell-to-Cell Interactions and Degradation in Parallel Strings: Implications for the Battery Management System," *Journal of Power Sources*, vol. 329, pp. 574–585, 2016, ISSN: 03787753. DOI: 10.1016/j.jpowsour.2016.07.121.

[172] Q. Fang, X. Wei, and H. Dai, "A study of parameter inconsistency evolution pattern in parallel-connected battery modules," *SAE International*, 2017, ISSN: 01487191. DOI: 10.4271/2017-01-1194.Copyright.

[173] M. J. Brand, M. H. Hofmann, M. Steinhardt, S. F. Schuster, and A. Jossen, "Current distribution within parallel-connected battery cells," *Journal of Power Sources*, vol. 334, pp. 202–212, Dec. 2016, ISSN: 0378-7753. DOI: 10.1016/J.JPOWSOUR.2016.10.010. [Online]. Available: https://linkinghub.elsevier.com/retrieve/pii/S0378775316313921.

[174] A. Fill, S. Koch, A. Pott, and K. P. Birke, "Current distribution of parallel-connected cells in dependence of cell resistance, capacity and number of parallel cells," *Journal of Power Sources*, vol. 407, no. September, pp. 147–152, 2018, ISSN: 03787753. DOI: 10.1016/j.jpowsour.2018.10.061. [Online]. Available: https://doi.org/10.1016/j.jpowsour.2018.10.061.

[175] L. Chang, C. Zhang, T. Wang, Z. Yu, N. Cui, B. Duan, and C. Wang, "Correlations of cell-to-cell parameter variations on current and state-of-charge distributions within parallel-connected lithium-ion cells," *Journal of Power Sources*, vol. 437, no. June, p. 226 869, Oct. 2019, ISSN: 03787753. DOI: 10.1016/j.jpowsour.2019.226869. [Online]. Available: https://linkinghub.elsevier.com/retrieve/pii/S0378775319308626.

[176] A. Fill, S. Koch, and K. P. Birke, "Analytical model of the current distribution of parallel-connected battery cells and strings," *Journal of Energy Storage*, vol. 23, no. December 2018, pp. 37–43, 2019, ISSN: 2352152X. DOI: 10.1016/j.est.2019.02.031. [Online]. Available: https://doi.org/10.1016/j.est.2019.02.031.

[177] M. Dubarry, A. Devie, and B. Y. Liaw, "Cell-balancing currents in parallel strings of a battery system," *Journal of Power Sources*, vol. 321, pp. 36–46, Jul. 2016, ISSN: 03787753. DOI: 10.1016/j.jpowsour.2016.04.125. [Online]. Available: http://dx.doi.org/10.1016/j.jpowsour.2016.04.125%20https://www.sciencedirect.com/science/article/pii/S0378775316305092.

[178] Y. Li, B. Lan, and J. Luo, "Modeling and Simulation Evaluation of Current and Temperature Inconsistency in Parallel Connected Lithium-Ion Batteries," *Proceedings of 2018 International Conference on Information Systems and Computer Aided Education, ICISCAE 2018*, no. 201707020045, pp. 12–18, 2019. DOI: 10.1109/ICISCAE.2018.8666905.

[179] M. H. Hofmann, A. Noel, K. Czyrka, A. Jossen, F. B. Spingler, M. Steinhardt, and M. J. Brand, "Dynamics of current distribution within battery cells connected in parallel," *Journal of Energy Storage*, vol. 20, no. March, pp. 120–133, 2018, ISSN: 2352152X. DOI: 10.1016/j.est.2018.08.013. [Online]. Available: https://doi.org/10.1016/j.est.2018.08.013.

[180] K. Rumpf, A. Rheinfeld, M. Schindler, J. Keil, T. Schua, and A. Jossen, "Influence of Cell-to-Cell Variations on the Inhomogeneity of Lithium-Ion Battery Modules," *Journal of The Electrochemical Society*, vol. 165, no. 11, A2587–A2607, 2018, ISSN: 0013-4651. DOI: 10.1149/2.0111811jes. [Online]. Available: http://jes.ecsdl.org/lookup/doi/10.1149/2.0111811jes%20http://jes.ecsdl.org/content/165/11/A2587.full.pdf.

[181] F. An, J. Huang, C. Wang, Z. Li, J. Zhang, S. Wang, and P. Li, "Cell sorting for parallel lithium-ion battery systems: Evaluation based on an electric circuit model," *Journal of Energy Storage*, vol. 6, pp. 195–203, May 2016, ISSN: 2352-152X. DOI: 10.1016/J.EST.2016.04.007.

[182] F. An, H. Zhao, and P. Li, "Self-discharge rates in cells have a critical effect on the cycle life of parallel lithium-ion batteries," *RSC Advances*, vol. 8, no. 54, pp. 30 802–30 812, 2018, ISSN: 20462069. DOI: 10.1039/C8RA05403G.

[183] T. Bruen, J. Marco, and M. Gama, "Current variation in parallelized energy storage systems," *2014 IEEE Vehicle Power and Propulsion Conference, VPPC 2014*, vol. 2014, pp. 1–6, 2015. DOI: 10.1109/VPPC.2014.7007040.

[184] C. S. Westenhover, D. A. Wetz, M. J. Martin, C. G. Gnegy-Davidson, D. A. Dodson, and J. Heinzel, "Current sharing in parallel cell batteries cycled at high C rates," *2017 IEEE Electric Ship Technologies Symposium, ESTS 2017*, pp. 586–591, 2017. DOI: 10.1109/ESTS.2017.8069341.

[185] W. Shi, X. Hu, C. Jin, J. Jiang, Y. Zhang, and T. Yip, "Effects of imbalanced currents on large-format LiFePO4/graphite batteries systems connected in parallel," *Journal of Power Sources*, vol. 313, pp. 198–204, May 2016, ISSN: 03787753. DOI: 10.1016/j.jpowsour.2016.02.087. [Online]. Available: http://dx.doi.org/10.1016/j.jpowsour.2016.02.087.

[186] K.-C. Chiu, C.-H. Lin, S.-F. Yeh, Y.-H. Lin, C.-S. Huang, and K.-C. Chen, "Cycle life analysis of series connected lithium-ion batteries with temperature difference," *Journal of Power Sources*, vol. 263, pp. 75–84, Oct. 2014, ISSN: 0378-7753. DOI: 10.1016/J.JPOWSOUR.2014.04.034. [Online]. Available: https://www.sciencedirect.com/science/article/pii/S0378775314005229.

[187] K. Jalkanen, J. Karppinen, L. Skogström, T. Laurila, M. Nisula, and K. Vuorilehto, "Cycle aging of commercial NMC/graphite pouch cells at different temperatures," *Applied Energy*, vol. 154, pp. 160–172, Sep. 2015, ISSN: 03062619. DOI: 10.1016/j.apenergy.2015.04.110.

[188] A. Maheshwari, M. Heck, and M. Santarelli, "Cycle aging studies of lithium nickel manganese cobalt oxide-based batteries using electrochemical impedance spectroscopy," *Electrochimica Acta*, vol. 273, pp. 335–348, May 2018, ISSN: 00134686. DOI: 10.1016/j.electacta.2018.04.045.

[189] P. C. Tsai, B. Wen, M. Wolfman, M. J. Choe, M. S. Pan, L. Su, K. Thornton, J. Cabana, and Y. M. Chiang, "Single-particle measurements of electrochemical kinetics in NMC and NCA cathodes for Li-ion batteries," *Energy and Environmental Science*, vol. 11, no. 4, pp. 860–871, Apr. 2018, ISSN: 17545706. DOI: 10.1039/c8ee00001h. [Online]. Available: https://pubs.rsc.org/en/content/articlehtml/2018/ee/c8ee00001h%20https://pubs.rsc.org/en/content/articlelanding/2018/ee/c8ee00001h.

[190] V. Charbonneau, A. Lasia, and G. Brisard, "Impedance studies of Li+ diffusion in nickel manganese cobalt oxide (NMC) during charge/discharge cycles," *Journal of Electroanalytical Chemistry*, vol. 875, p. 113 944, Oct. 2020, ISSN: 15726657. DOI: 10.1016/j.jelechem.2020.113944.

[191] M. Brand, D. Quinger, G. Walder, A. Jossen, and M. Lienkamp, "Ageing inhomogeneity of long-term used BEV-batteries and their reusability for nd-life applications," in *EVS26 International Battery, Hybrid and Fuel Cell Electric Vehicle Symposium*, 2012.

[192] Kokam Co., *Kokam Superior Lithium Ion Polymer Material Safety Data Sheet*, Kyunggi-Do, 2009.

[193] ——, *Kokam SPLB11543140H5 Datasheet*, 2007.

[194] ——, *KOKAM SLPB Li-Ion/Polymer Cell Brochure*, 2017. [Online]. Available: kokam.com/data/Kokam%7B%5C_%7DCell%7B%5C_%7DBrochure%7B%5C_%7DV.3.pdf.

[195] C. Sole, N. E. Drewett, and L. J. Hardwick, "Insitu Raman study of lithium-ion intercalation into microcrystalline graphite," *Faraday Discussions*, vol. 172, no. 0, pp. 223–237, Dec. 2014, ISSN: 13645498. DOI: 10.1039/c4fd00079j.

[196] C. S. Kim, K. M. Jeong, K. Kim, and C. W. Yi, "Effects of capacity ratios between anode and cathode on electrochemical properties for lithium polymer batteries," *Electrochimica Acta*, vol. 155, pp. 431–436, Feb. 2015, ISSN: 00134686. DOI: 10.1016/j.electacta.2014.12.005.

[197] C. Mao, R. E. Ruther, J. Li, Z. Du, and I. Belharouak, "Identifying the limiting electrode in lithium ion batteries for extreme fast charging," *Electrochemistry Communications*, vol. 97, pp. 37–41, Dec. 2018, ISSN: 13882481. DOI: 10.1016/j.elecom.2018.10.007.

[198] M. Dubarry, N. Vuillaume, and B. Y. Liaw, "From single cell model to battery pack simulation for Li-ion batteries," *Journal of Power Sources*, vol. 186, no. 2, pp. 500–507, 2009, ISSN: 03787753. DOI: 10.1016/j.jpowsour.2008.10.051.

[199] S. J. Tong, A. Same, M. A. Kootstra, and J. W. Park, "Off-grid photovoltaic vehicle charge using second life lithium batteries: An experimental and numerical investigation," *Applied Energy*, vol. 104, pp. 740–750, 2013, ISSN: 03062619. DOI: 10.1016/j.apenergy.2012.11.046. [Online]. Available: http://dx.doi.org/10.1016/j.apenergy.2012.11.046.

[200] K. Uddin, A. Picarelli, C. Lyness, N. Taylor, and J. Marco, "An acausal Li-ion battery pack model for automotive applications," *Energies*, vol. 7, no. 9, pp. 5675–5700, 2014, ISSN: 19961073. DOI: 10.3390/en7095675.

[201] M. Ye, X. Song, R. Xiong, and F. Sun, "A Novel Dynamic Performance Analysis and Evaluation Model of Series-Parallel Connected Battery Pack for Electric Vehicles," *IEEE Access*, vol. 7, pp. 14 256–14 265, 2019, ISSN: 21693536. DOI: 10.1109/ACCESS.2019.2892394.

[202] S. Peng, C. Chen, H. Shi, and Z. Yao, "State of charge estimation of battery energy storage systems based on adaptive unscented Kalman filter with a noise statistics estimator," *IEEE Access*, vol. 5, pp. 13 202–13 212, 2017, ISSN: 21693536. DOI: 10.1109/ACCESS.2017.2725301.

[203] G. Liu, M. Ouyang, L. Lu, J. Li, and X. Han, "Analysis of the heat generation of lithium-ion battery during charging and discharging considering different influencing factors," in *Journal of Thermal Analysis and Calorimetry*, vol. 116, Kluwer Academic Publishers, Jan. 2014, pp. 1001–1010. DOI: 10.1007/s10973-013-3599-9. [Online]. Available: https://link.springer.com/article/10.1007/s10973-013-3599-9.

[204] K. E. Thomas and J. Newman, "Thermal Modeling of Porous Insertion Electrodes," *Journal of The Electrochemical Society*, vol. 150, no. 2, A176, Jan. 2003, ISSN: 00134651. DOI: 10.1149/1.1531194. [Online]. Available: https://iopscience.iop.org/article/10.1149/1.1531194%20https://iopscience.iop.org/article/10.1149/1.1531194/meta.

[205] X. F. Zhang, Y. Zhao, Y. Patel, T. Zhang, W. M. Liu, M. Chen, G. J. Offer, and Y. Yan, "Potentiometric measurement of entropy change for lithium batteries," *Physical Chemistry Chemical Physics*, vol. 19, no. 15, pp. 9833–9842, Apr. 2017, ISSN: 14639076. DOI: 10.1039/c6cp08505a. [Online]. Available: https://pubs.rsc.org/en/content/articlehtml/2017/cp/c6cp08505a%20https://pubs.rsc.org/en/content/articlelanding/2017/cp/c6cp08505a.

[206] A. A. Pesaran, "Battery thermal models for hybrid vehicle simulations," in *Journal of Power Sources*, vol. 110, Elsevier, Aug. 2002, pp. 377–382. DOI: 10.1016/S0378-7753(02)00200-8.

[207] B. Stiaszny, J. C. Ziegler, E. E. Krauß, J. P. Schmidt, and E. Ivers-Tiffée, "Electrochemical characterization and post-mortem analysis of aged LiMn 2O4-Li(Ni0.5Mn0.3Co 0.2)O2/graphite lithium ion batteries. Part I: Cycle aging," *Journal of Power Sources*, vol. 251, pp. 439–450, Apr. 2014, ISSN: 03787753. DOI: 10.1016/j.jpowsour.2013.11.080.

[208] M.-S. Wu, P.-C. J. Chiang, and J.-C. Lin, "Electrochemical Investigations on Advanced Lithium-Ion Batteries by Three-Electrode Measurements," *Journal of The Electrochemical Society*, vol. 152, no. 1, A47, Nov. 2005, ISSN: 00134651. DOI: 10.1149/1.1825385. [Online]. Available: https://iopscience.iop.org/article/10.1149/1.1825385%20https://iopscience.iop.org/article/10.1149/1.1825385/meta.

[209] P. Taheri, S. Hsieh, and M. Bahrami, "Investigating electrical contact resistance losses in lithium-ion battery assemblies for hybrid and electric vehicles," *Journal of Power Sources*, vol. 196, no. 15, pp. 6525–6533, 2011, ISSN: 03787753. DOI: 10.1016/j.jpowsour.2011.03.056.

[210] M. I. Ardani, Y. Patel, A. Siddiq, G. J. Offer, and R. F. Martinez-Botas, "Combined experimental and numerical evaluation of the differences between convective and conductive thermal control on the performance of a lithium ion cell," *Energy*, vol. 144, pp. 81–97, 2018, ISSN: 03605442. DOI: 10.1016/j.energy.2017.12.032.

[211] M. J. Brand, P. Berg, E. I. Kolp, T. Bach, P. Schmidt, and A. Jossen, "Detachable electrical connection of battery cells by press contacts," *Journal of Energy Storage*, vol. 8, pp. 69–77, 2016, ISSN: 2352152X. DOI: 10.1016/j.est.2016.09.011. [Online]. Available: http://dx.doi.org/10.1016/j.est.2016.09.011.

[212] Z. Song, X. G. Yang, N. Yang, F. P. Delgado, H. Hofmann, and J. Sun, "A study of cell-to-cell variation of capacity in parallel-connected lithium-ion battery cells," *eTransportation*, vol. 7, p. 100 091, Nov. 2021, ISSN: 25901168. DOI: 10.1016/j.etran.2020.100091.

[213] G. Mulder, K. Trad, K. D. Craemer, W. Porcher, M. Montaru, M. A. M. A. Marongiu, M. Oyarbide, N. Ehteshami, Y. Wu, A. Moretti, S. Passerini, H. Popp, F. Larsson, W. Kohs, e. J. Berckmans, and P. Kargl, "Test methods for improved battery cell understanding," VITO (SPICY)/ AIT (eCAIMAN) / FiveVB (AVL), Tech. Rep., 2017.

[214] S. Mohan, Y. Kim, J. B. Siegel, N. A. Samad, and A. G. Stefanopoulou, "A Phenomenological Model of Bulk Force in a Li-Ion Battery Pack and Its Application to State of Charge Estimation," *Journal of The Electrochemical Society*, vol. 161, no. 14, A2222–A2231, 2014, ISSN: 0013-4651. DOI: 10.1149/2.0841414jes.

[215] M. Zhu, J. Park, and A. M. Sastry, "Fracture Analysis of the Cathode in Li-Ion Batteries: A Simulation Study," *Journal of The Electrochemical Society*, vol. 159, no. 4, A492–A498, Feb. 2012, ISSN: 0013-4651. DOI: 10.1149/2.045204jes. [Online]. Available: https://iopscience.iop.org/article/10.1149/2.045204jes%20https://iopscience.iop.org/article/10.1149/2.045204jes/meta.

[216] M. Ebner, F. Marone, M. Stampanoni, and V. Wood, "Visualization and quantification of electrochemical and mechanical degradation in li ion batteries," *Science*, vol. 342, no. 6159, pp. 716–720, 2013, ISSN: 10959203. DOI: 10.1126/science.1241882.

[217] R. Xu, Y. Yang, F. Yin, P. Liu, P. Cloetens, Y. Liu, F. Lin, and K. Zhao, "Heterogeneous damage in Li-ion batteries: Experimental analysis and theoretical modeling," *Journal of the Mechanics and Physics of Solids*, vol. 129, no. 2019, pp. 160–183, 2019, ISSN: 00225096. DOI: 10.1016/j.jmps.2019.05.003.

[218] J. S. Edge, S. O'kane, R. Prosser, N. D. Kirkaldy, A. N. Patel, A. Hales, A. Ghosh, W. Ai, J. Chen, J. Yang, S. Li, M.-C. Pang, L. Bravo Diaz, A. Tomaszewska, M. Waseem Marzook, K. N. Radhakrishnan, H. Wang, Y. Patel, B. Wu, and G. J. Offer, "Lithium ion battery degradation: what you need to know," *Phys. Chem. Chem. Phys*, vol. 23, p. 8200, 2021. DOI: 10.1039/d1cp00359c.

[219] W. M. Dose, C. Xu, C. P. Grey, and M. F. De Volder, "Effect of Anode Slippage on Cathode Cutoff Potential and Degradation Mechanisms in Ni-Rich Li-Ion Batteries," *Cell Reports Physical Science*, vol. 1, no. 11, p. 100 253, Nov. 2020, ISSN: 26663864. DOI: 10.1016/j.xcrp.2020.100253.

Appendices

Appendix A

Identification of Missing Data

As previously mentioned in Chapter 6, power failures led to loss of a small portion of the tracked current distribution data. This missing data is tabulated in Table A.1.

Table A.1: Missing cycling cell current data per pack

Pack	**Missing Cycle Numbers**	**Number Missing**	**Missing Fraction** [%]
P20.0/0.0	341-343	2	0.1
P45.0/0.0	341-343	2	0.1
P32.5/-+25.0	206-219, 296-306	23	1.2
P32.5/0.0	204-216, 294-304, 551-565	38	1.9
P32.5/-25.0	148-160, 241-244	15	0.8
P32.5/-12.5	148-160, 237-240, 558-560	17	0.9

Appendix B

Permission to Reproduce Third-Party Works

Page	Type	Source	Copyright Holder	Permission Requested	Granted?
15	Figure 2.3	Waldmann et al. [25]	© The Authors, CC-BY	N/A	N/A
16	Figure 2.4	Waldmann et al. [25]	© The Authors, CC-BY	N/A	N/A
17	Figure 2.5	Waldmann et al. [29]	© Elsevier B.V.	19/01/2021	Yes
19	Figure 2.6 a	Christensen et al. [45]	© IOP Publishing, Ltd	24/01/2021	Yes
19	Figure 2.6 b, c	Ai et al. [46]	© The Authors, CC-BY	N/A	N/A
25	Figure 2.7	Dubary et al. [74]	© Elsevier B.V.	25/01/2021	Yes
27	Figure 2.8	Dubary et al. [25]	© The Authors, CC-BY	N/A	N/A
37	Figure 3.1	Offer et al. [125]	© Nature	19/01/2021	Yes
38	Figure 3.2	Kim et al. [127]	© Elsevier B.V.	19/01/2021	Yes
43	Figure 3.3	Lebel et al. [154]	© IEEE	N/A	N/A
44	Figure 3.4	Lv et al. [155]	© Elsevier B.V.	19/01/2021	Yes
45	Figure 3.5	Diao et al. [156]	© Elsevier B.V.	19/01/2021	Yes
45	Figure 3.6	Zhang et al. [158]	© John Wiley and Sons	19/01/2021	Yes
46	Figure 3.7	Baronti et al. [161]	© IEEE	N/A	N/A
47	Figure 3.8	Wu et al. [141]	© Elsevier B.V.	31/12/2020	Yes
48	Figure 3.9	Hosseinzadeh et al. [139]	© Elsevier B.V.	19/01/2021	Yes
49	Table 3.2	Hosseinzadeh et al. [162]	© Elsevier B.V.	19/01/2021	Yes
55	Figure 3.10	Hofmann et al. [179]	© Elsevier B.V.	19/01/2021	Yes
56	Figure 3.11	Wu et al. [141]	© Elsevier B.V.	31/12/2020	Yes
58	Figure 3.12	Liu et al. [9]	© Elsevier B.V.	19/01/2021	Yes
59	Figure 3.13	Chiu et al. [186]	© Elsevier B.V.	19/01/2021	Yes
60	Figure 3.14	Ganesan et al. [142]	© Elsevier B.V.	19/01/2021	Yes
61	Figure 3.15	Maheshwari et al. [188]	© Elsevier B.V.	19/01/2021	Yes
62	Figure 3.16	Zhu et al. [93]	© IEEE	N/A	N/A
184	Figure 6.29	Edge et al. [218]	© The Authors, CC-BY	N/A	N/A

Table B.1: Summary of copyright permissions.